ORNL-TM-3259

ENGINEERING DEVELOPMENT STUDIES FOR MOLTEN-SALT BREEDER REACTOR PROCESSING NO. 9

L. E. McNeese

OAK RIDGE NATIONAL LABORATORY
OPERATED BY UNION CARBIDE CORPORATION • FOR THE U.S. ATOMIC ENERGY COMMISSION

ORNL-TM-3259

Contract No. W-7405-eng-26

CHEMICAL TECHNOLOGY DIVISION

ENGINEERING DEVELOPMENT STUDIES FOR MOLTEN-SALT BREEDER REACTOR PROCESSING NO. 9

L. E. McNeese

DECEMBER 1972

OAK RIDGE NATIONAL LABORATORY
Oak Ridge, Tennessee 37830
operated by
UNION CARBIDE CORPORATION
for the
U. S. ATOMIC ENERGY COMMISSION

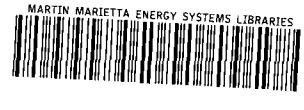

Reports previously issued in this series are as follows:

ORNL-TM-3053	Period ending December 1968
ORNL-TM-3137	Period ending March 1969
ORNL-TM-3138	Period ending June 1969
ORNL-TM-3139	Period ending September 1969
ORNL-TM-3140	Period ending December 1969
ORNL-TM-3141	Period ending March 1970
ORNL-TM-3257	Period ending June 1970
ORNL-TM-3258	Period ending September 1970

CONTENTS

CONTENTS (continued)

CONTENTS (continued)

SUMMARIES

FLOWSHEET ANALYSIS: ISOLATION OF PROTACTINIUM BY OXIDE PRECIPITATION

Two flowsheets that employ oxide precipitation for protactinium removal are described, and the effects of several operating parameters on the performance of the flowsheets have been investigated. In the first flowsheet, protactinium is selectively precipitated from MSBR fuel salt on a 3-day cycle. The resulting oxide and a small amount of fuel salt associated with it are hydrofluorinated in the presence of a secondary fluoride salt that is circulated through a fluorinator and a protactinium decay tank. A small fraction of the salt leaving the decay tank is returned to the primary reactor circuit to compensate for salt that is transferred to the decay tank along with the oxide. The uranium is removed from 10% of the fuel salt leaving the precipitator by fluorination or oxide precipitation, and rare earths are removed from the resulting salt by the metal transfer process. The purified salt leaving the metal transfer process is combined with the uranium removed earlier, and the resulting stream is returned to the reactor. A protactinium removal time of 5 days can be realized if 60% of the protactinium is separated from the salt in the precipitator, provided the fuel salt transfer rate to the decay tank is as low as 10 to 20 moles/day. For the same protactinium removal time, a protactinium removal efficiency of 80% would be required in the precipitator if the fuel salt transfer rate to the decay tank were as large as 3000 moles/day. The uranium inventory in the decay tank would be negligible.

In the second flowsheet, a fluorinator is not used for removal of uranium from the protactinium decay tank. Fuel salt is withdrawn from the reactor on a 3-day cycle and combined with a salt stream that is withdrawn from the protactinium decay tank. Part of the protactinium in the resulting salt stream is removed by precipitation, and the precipitate and associated salt are hydrofluorinated in the presence of processed fuel carrier salt leaving the metal transfer process. The resulting salt stream then passes through a decay tank, from which it

is fed to the protactinium precipitator in order to return the uranium to the reactor. Operation of the flowsheet is highly dependent on the fraction of the protactinium removed in the precipitator and on the amount of fuel salt that accompanies the oxide precipitate.

FLOWSHEET ANALYSIS: REFERENCE PROCESSING PLANT FLOWSHEET BASED ON FLUORINATION, REDUCTIVE EXTRACTION, AND THE METAL TRANSFER PROCESS

Operating conditions that will constitute the reference fluorination--reductive extraction--metal transfer flowsheet were selected, and additional calculations were performed to indicate the operating characteristics of the flowsheet. Essentially complete extraction of the protactinium is achieved with a 10-day processing cycle, a five-stage protactinium extractor, a lithium reductant addition rate of 200 equiv/day, and a uranium removal efficiency of 99% in the primary fluorinator. Rare earths are extracted from the fuel salt with removal times ranging from 16 to 50 days in a three-stage extractor. A three-stage extractor is also used for the selective transfer of the rare earths from the bismuth-plus-thorium phase and the extracted rare earths to a LiCl stream. The various waste salt streams produced by the processing system are combined into a single stream having the composition 76.3-12.3-9.8-0.64 mole % $LiF-ThF_4-BeF_2-ZrF_4$, 0.864 mole % trivalent rare-earth fluorides, and 0.114 mole % divalent rare-earth fluorides. The waste salt would be discarded from the processing system at the rate of 70 ft^3 every 220 days.

FLOWSHEET ANALYSIS: IMPORTANCE OF URANIUM INVENTORY IN AN MSBR PROCESSING PLANT

The MSBR processing flowsheets considered to date have resulted in uranium inventories in the processing plant that are quite low, usually less than 1% of the inventory in the reactor. Since several potential processing flowsheets may result in uranium inventories as large as 10% of the reactor inventory, the importance of increases in this inventory was examined. It was found that increasing the

processing plant inventory from 0 to 10% would increase the fuel cycle cost by only 0.03 mill/kWhr and would increase the system doubling time from 22 to 24.2 years. It was concluded that, while there are incentives for maintaining a low inventory, inventory values of 5 to 10% would not rule out an otherwise attractive processing system.

FLOWSHEET ANALYSIS: REMOVAL OF RARE-EARTH FISSION PRODUCTS FROM LiCl IN THE METAL TRANSFER PROCESS

Calculations were made to determine the effect of varying the concentration of lithium in the bismuth solution used for removing the trivalent rare earths from the LiCl in the metal transfer process; the reactor breeding ratio was found to decrease only slightly (from about 1.063 to about 1.060) as the lithium concentration in the bismuth was decreased from 5 at. % to approximately 1.67 at. %. Calculations were also carried out which indicate that a single-stage extractor has essentially the same removal efficiency for the divalent rare earths in the reference flowsheet as a two-stage contactor; thus the use of a single-stage contactor was adopted.

FROZEN-WALL FLUORINATOR DEVELOPMENT: EXPERIMENTS ON INDUCTION HEATING IN A CONTINUOUS FLUORINATOR SIMULATION

An experiment to demonstrate protection against corrosion by the use of a layer of frozen salt in a continuous fluorinator requires a corrosion-resistant heat source to be placed in the molten salt. High-frequency induction heating appears to be an acceptable heating method, and equipment has been installed for studying this method in a simulated fluorinator that uses a 31 wt % HNO_3 solution in place of molten salt. Experimental results on heat generation rates in the acid, in the pipe surrounding the acid column, and in the induction coil are presented for the first eight runs.

PREDICTED CORROSION RATES IN CONTINUOUS FLUORINATORS EMPLOYING FROZEN-WALL PROTECTION

Nickel is the preferred material of construction for fluorinators in MSBR processing plants since it exhibits greater resistance to attack by gaseous fluorine than other candidate materials. This resistance is due to the formation of a tightly adherent film of NiF_2, and it is proposed that a layer of frozen salt be used to prevent removal of the NiF_2 film via dissolution in the molten fluoride mixture that flows through the fluorinator. However, it is expected that the NiF_2 film will be removed periodically as the result of deviations from the desired mode of operation, and an analysis was carried out for estimating the resulting corrosion rate under such conditions. It was found that, if the NiF_2 film were destroyed 52 times per year, the average yearly corrosion rates at 450°C would be 2.9 mils and 0.97 mil for types 200 and 201 nickel respectively. It appears that either material will show satisfactory corrosion resistance if the NiF_2 film is destroyed less frequently than once per week.

PREDICTED PERFORMANCE OF CONTINUOUS FLUORINATORS

Previous data on the extent of removal of uranium from a molten fluoride salt in a 1-in.-diam, open-column fluorinator and recently obtained data on axial dispersion in open bubble columns were used to develop a mathematical model for predicting the performance of continuous fluorinators having diameters ranging from 6 to 12 in. The results of the analysis are encouraging since they suggest that single fluorination vessels of moderate size will suffice for removing uranium from MSBR fuel salt prior to the isolation of protactinium. The reference MSBR processing flowsheet requires fluorination of fuel salt at the rate of 170 ft^3/day and a uranium removal efficiency of 99%; the present analysis indicates that an 8-in.-diam fluorinator having a height of 17.8 ft will meet these requirements.

MEASUREMENT OF AXIAL DISPERSION COEFFICIENTS AND GAS HOLDUP IN OPEN BUBBLE COLUMNS

Measurements of gas holdup and axial dispersion were made in open bubble columns having diameters of 1, 1.5, 2, 3, and 6 in. for a range of operating conditions. The effects of changes in the viscosity and surface tension of the liquid, the superficial gas velocity, the gas inlet-orifice size, and the number of gas inlets were determined. These data, as well as data obtained previously, were used to develop correlations for predicting gas holdup and axial dispersion in open-column, gas-liquid contactors such as continuous fluorinators in which a molten fluoride salt is countercurrently contacted with a gaseous mixture of fluorine and UF_6.

SEMICONTINUOUS REDUCTIVE EXTRACTION EXPERIMENTS IN A MILD-STEEL FACILITY

We have continued to operate a facility in which semicontinuous reductive extraction experiments can be carried out in a mild-steel system. We are presently studying the mass transfer performance of an 0.82-in.-ID, 24-in.-long column packed with 1/4-in. molybdenum Raschig rings. Several experiments were carried out previously in which a salt stream containing UF_4 was countercurrently contacted with bismuth containing reductant over a range of operating conditions. In order to measure mass transfer rates in the column under closely controlled conditions and under conditions where the controlling resistance is not in the salt phase (as was the case in previous experiments), preparations were begun for experiments in which the rate of exchange of zirconium isotopes will be measured between salt and bismuth phases otherwise at chemical equilibrium. Techniques for the production and charging of ^{97}Zr (half-life, 16.8 hr) to the salt were developed, and about 7 mCi of ^{97}Zr was added to the salt in the feed tank. The first experiment using the ^{97}Zr tracer was interrupted by a leak in the salt exit line from the feed tank. Because damage to the feed tank and Calrod heaters on the vessel made salvage of the

tank impractical, a new vessel was fabricated and installed. Examination of a specimen from the original vessel revealed that, although some graphitization of the steel had occurred, no evidence of embrittlement was present.

DEVELOPMENT OF THE METAL TRANSFER PROCESS: OPERATION OF EXPERIMENT MTE-2

The second engineering experiment (MTE-2) for development of the metal transfer process was completed. This experiment was performed at 650°C in a 6-in.-diam carbon steel vessel that was divided into two compartments interconnected at the bottom by a pool of thorium-saturated molten bismuth. One compartment contained MSBR fuel carrier salt (72-16-12 mole % $LiF-BeF_2-ThF_4$) to which were added 7 mCi of ^{147}Nd and sufficient LaF_3 to produce a concentration of 0.3 mole %. The second compartment contained LiCl, a 35 at. % Li-Bi solution (in a cup), and a pump for circulating the LiCl through the cup at the rate of about 25 cm^3/min. Gas-lift sparge tubes were used to disperse droplets of bismuth in the salt phase and thereby improve contact of the phases. During a 3-month operating period, in which a total of 563 liters of LiCl was circulated through the cup containing the Li-Bi solution, more than 85% of the lanthanum and more than 50% of the neodymium were removed from the fluoride salt. No measurable accumulation of thorium in the Li-Bi solution (<10 ppm) was noted during this period. The observed values for the distribution coefficients for lanthanum, neodymium, thorium, and radium during the experiment were in general agreement with the expected values. From 70 to 100% of the quantities of the rare earths charged to the system could be accounted for throughout the experiment. A much greater decrease was observed in the concentration of lithium in the Li-Bi solution than was expected; the reason for this discrepancy has not been determined. Eight days before the end of the experiment, 1 vol % of fuel carrier salt was added to the LiCl in order to study the effect of contamination of the LiCl with fluoride salt. All of the objectives of the experiment were achieved.

DEVELOPMENT OF THE METAL TRANSFER PROCESS: DESIGN OF EXPERIMENT MTE-3

Design of the third engineering experiment for development of the metal transfer process has been initiated. This experiment (MTE-3) will use salt and bismuth flow rates that are 1% of the estimated flow rates required for processing a 1000-MW(e) reactor. Mechanical agitators will be used for promoting mass transfer between the salt and metal phases in the experiment. A mathematical analysis was carried out in order to select approximate equipment sizes and to determine operating conditions for the system. The experiment will use about 35 liters of MSBR fuel carrier salt, 6 liters of Th-Bi solution, 6 liters of LiCl, and about 5 liters of Li-Bi solution having an initial lithium content of about 5 at. %. The salt-metal contactor will be a 10-in.-diam, two-compartmented vessel having a mechanical agitator in each compartment.

DEVELOPMENT OF MECHANICALLY AGITATED SALT-METAL CONTACTORS

A program was initiated for the development of mechanically agitated salt-metal contactors as an alternative to packed columns presently under consideration for MSBR processing systems. This type of contactor is of particular interest for the metal transfer process since designs can be envisioned in which the bismuth phase would be a near-isothermal, internally recirculated, captive phase. It is believed that such designs will be less dependent on the technology for molybdenum fabrication than would a counterpart system based on packed columns. Preliminary tests on the hydrodynamics of mechanically agitated salt-metal contactors were carried out using mercury and water. Initially, tests were made using an agitator that was operated at the water-mercury interface in a manner designed to disperse the mercury in the water. However, results of these tests led us to conclude that the contactor should operate under conditions that minimize dispersion of the mercury. The Lewis contactor appears to have the greatest potential for achieving effective mass transfer rates with minimum dispersion of the phases. In this contactor, an agitator, located well away from the interface, is present in each phase. Each agitator is

operated in a manner such that the phases are mixed as vigorously as possible without actually dispersing one in the other. Information in the literature on mass transfer rates in Lewis-type contactors was reviewed. It was concluded that the mass transfer rate correlation developed by Lewis may be applicable to salt-bismuth systems, and that adequate mass transfer rates for MSBR processing applications should be obtained.

HYDRODYNAMICS OF PACKED-COLUMN OPERATION WITH HIGH-DENSITY FLUIDS

Studies of the hydrodynamics of packed column operation were continued, using fluids with high densities and a large density difference. Data were obtained in a 2-in.-diam, 24-in.-long column that was packed with 3/8-in. Teflon Raschig rings for determining the dependence of dispersed-phase holdup, pressure drop, and flooding on the viscosity of the continuous phase. An improved relationship was developed for predicting packed-column performance during the countercurrent flow of molten salt and bismuth. The effects of wetting of the packing by the metal phase on metal phase holdup, flooding, and pressure drop were also evaluated in a 2-in.-diam, 24-in.-long column packed with 3/8-in. copper Raschig rings that were wetted by the mercury. The interfacial area between the aqueous and mercury phases was decreased substantially when the packing was wetted, and the column throughput at flooding was about 40% greater than with nonwetted packing.

ANALYSIS OF MULTICOMPONENT MASS TRANSFER BETWEEN MOLTEN SALTS AND LIQUID BISMUTH DURING COUNTERCURRENT FLOW IN PACKED COLUMNS

The transfer of materials between a molten salt and liquid bismuth results in a condition where the fluxes of the transferring ions are dependent on both concentration gradients and electric potential gradients. This greatly complicates the mass transfer process and makes the design of continuous reductive extraction columns difficult. A mathematical analysis of mass transfer during reductive extraction processes

was carried out to facilitate interpretation of results from present and proposed experiments in packed columns and as an aid in using these data for the design of larger reductive extraction systems. A calculational procedure was developed for solving the resulting relations with as many as ten transferring materials. Provision was made for calculating rates of mass transfer between solvent and electrolyte phases for a range of operating conditions. In future work, particular attention will be paid to the influence of the electric field on the rate of mass transfer and to the differences that result from the case where mass transfer rates are assumed to be dependent only on concentration gradients.

STUDY OF THE PURIFICATION OF SALT BY CONTINUOUS METHODS

Salt purification studies using 66-34 mole % $LiF-BeF_2$ were terminated because of leaks that resulted in the loss of about half of the 14-liter salt charge. The composition of the remaining salt was adjusted to the approximate composition of the proposed MSBR fuel salt (72-16-12 mole % $LiF-BeF_2-ThF_4$). The newly prepared salt was then countercurrently contacted with a H_2--10% HF mixture in the packed column in order to remove oxide from the salt. Although a considerable quantity of oxide was removed from the salt, a significant quantity still remained in the column. In the two flooding runs and one iron fluoride reduction run that were carried out during this report period, the pressure drop across the column increased sufficiently to make operation of the system difficult. The column was then filled with molten salt, and an $HF-H_2$ stream was allowed to contact the static salt charge for a period of 18 hr in order to remove the oxide from the column. After this operation had been determined to be successful, eight additional iron fluoride reduction runs were completed. Operation of the system was smooth in each case, and the pressure drop across the column remained low. However, the results of iron analyses of the salt samples from the runs were inconsistent. This inconsistency was probably due to the low iron concentration in the system, although sample contamination was suspected in some cases.

1. INTRODUCTION

A molten-salt breeder reactor (MSBR) will be fueled with a molten fluoride mixture that will circulate through the blanket and core regions of the reactor and through the primary heat exchangers. We are developing processing methods for use in a close-coupled facility for removing fission products, corrosion products, and fissile materials from the molten fluoride mixture.

Several operations associated with MSBR processing are under study. The remaining parts of this report discuss:

1. the description and analysis of a flowsheet for isolating protactinium from MSBR fuel salt by oxide precipitation,
2. the description of the reference flowsheet for processing MSBR fuel salt by the fluorination--reductive extraction--metal transfer process,
3. an analysis of the importance of the uranium inventory in a processing plant,
4. the results of calculations related to the removal of rare earths from molten LiCl in the metal transfer process,
5. experiments conducted in a simulated continuous fluorinator for studying induction heating in molten salt,
6. predictions of the rate of corrosion of the nickel vessel in continuous fluorinators employing frozen-wall corrosion protection,
7. predictions of the extent of removal of uranium in continuous fluorinators,
8. measurement of axial dispersion coefficients and gas holdup in open bubble columns and the development of correlations for predicting these quantities,
9. experiments conducted in a mild-steel reductive extraction facility, to increase our understanding

of the rate at which uranium is extracted from molten salt into bismuth in a packed column,

10. operation of experiment MTE-2 for demonstrating the metal transfer process for the removal of rare earths from MSBR fuel carrier salt,

11. design of experiment MTE-3 for studying operation of the metal transfer process using salt and bismuth flow rates that are 1% of those expected for processing a 1000-MW(e) MSBR,

12. development of mechanically agitated salt-metal contactors,

13. studies of flooding, dispersed-phase holdup, and pressure drop during countercurrent flow of liquids having a large difference in densities in packed columns,

14. analysis of multicomponent mass transfer between molten salts and liquid bismuth during countercurrent flow in packed columns, and

15. studies of the purification of salt by continuous methods.

This work was carried out in the Chemical Technology Division during the period October through December 1970.

2. FLOWSHEET ANALYSIS: ISOLATION OF PROTACTINIUM BY OXIDE PRECIPITATION

M. J. Bell L. E. McNeese

Ross, Bamberger, and Baes[1] have shown that protactinium can be precipitated selectively as Pa_2O_5 from MSBR fuel salt by the addition of oxide to salt containing Pa^{5+}, and that Pa^{4+} can be readily oxidized to Pa^{5+} by hydrofluorination. Mailen[2] has measured the solubility of Pa_2O_5 in MSBR fuel salt that is saturated with UO_2 at temperatures between 550 and 650°C. Also, Bamberger and Baes[3] have found that uranium oxide can be precipitated from protactinium-free fuel salt as a UO_2-ThO_2 solid solution in which the concentration of UO_2 at equilibrium is dependent on the concentration of UF_4 in the salt. Bell and McNeese[4] have used the equilibrium data of Bamberger and Baes to calculate the performance of a countercurrent multistage uranium oxide precipitator and have found that greater than 99% of the uranium can be removed from fuel salt as a UO_2-ThO_2 solid solution that contains less than 10% ThO_2 by using only a few equilibrium stages in which the salt and oxide are countercurrently contacted. These results indicate that oxide precipitation may be an attractive alternative process to fluorination-reductive extraction for isolating protactinium and removing uranium from the fuel salt of an MSBR. Two flowsheets that employ oxide precipitation are described in the remainder of this section, and the effects of several operating parameters on the performance of the flowsheets are discussed.

2.1 Isolation of Protactinium by Oxide Precipitation, and Recovery of Uranium Daughters by Fluorination

Figure 1 presents a flowsheet and typical operating parameters for a process which employs oxide precipitation to isolate protactinium from MSBR fuel salt and fluorination to recover uranium produced by decay of the protactinium. Fuel salt is withdrawn from the reactor on a 3-day cycle, and protactinium is selectively removed by precipitation as Pa_2O_5. The precipitate and a small amount of salt associated with it are hydrofluorinated in the presence of a secondary salt that is circulated through

ORNL DWG 70-14086R1

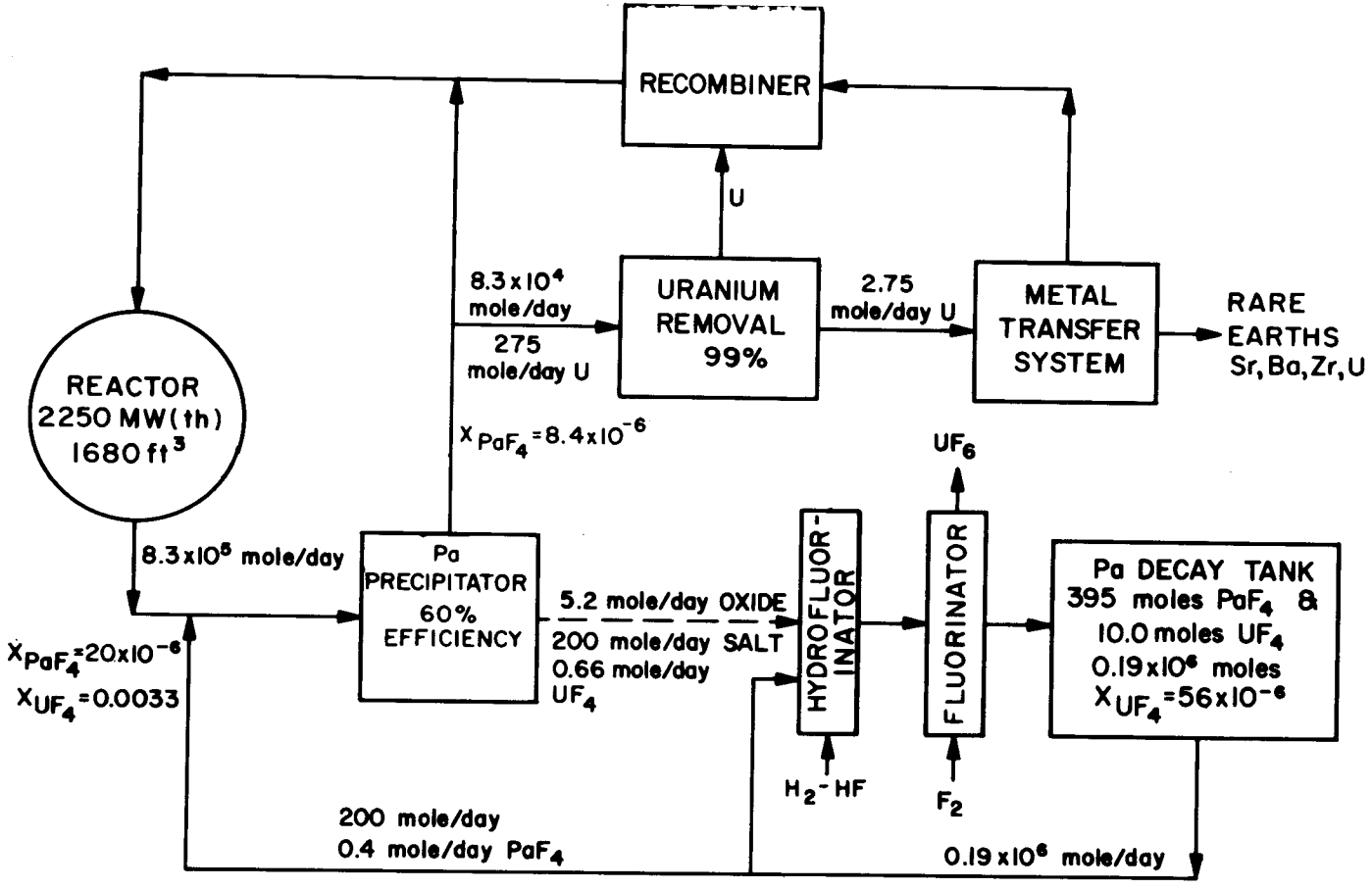

Fig. 1. Flowsheet for Isolating Protactinium by Fluorination-Oxide Precipitation and Removing Rare Earths by the Metal Transfer Process.

a fluorinator and a protactinium decay tank. A small fraction of the salt leaving the decay tank is returned to the primary reactor circuit to compensate for salt accompanying the oxide precipitate.

The main salt stream exiting from the precipitator vessel contains most of the fission products and uranium, plus 5 to 40% of the protactinium in the salt leaving the reactor. Ten percent of this stream is processed to recover a large fraction of the uranium, and rare earths are removed from the resulting salt by the metal transfer process. Purified salt leaving the metal transfer process is combined with the recovered uranium and then returned to the reactor. Removal of the uranium can be accomplished either by fluorination or by oxide precipitation.

A mathematical analysis of the protactinium isolation portion of the flowsheet was carried out using the nomenclature shown in Fig. 2. The following material balance relations can be written for protactinium:

$$FO = (F + FS)\cdot PEFF\cdot CP1 \quad , \tag{1}$$

$$CP2 = CP1\cdot(1 - PEFF) \quad , \tag{2}$$

$$(F + \lambda\cdot VR)\cdot CPR = P + F\cdot CP2 \quad , \tag{3}$$

$$\lambda\cdot(VR\cdot CPR + VT\cdot CPT) = P \quad , \tag{4}$$

and

$$FO + FS\cdot CP2 = (FS + \lambda\cdot VT)\cdot CPT \quad , \tag{5}$$

where

FO = flow rate of oxide leaving precipitator, moles/day,
FS = flow rate of salt accompanying oxide leaving precipitator, moles/day,
F = flow rate of salt leaving the reactor, moles/day,
PEFF = protactinium removal efficiency in precipitator,
λ = ^{233}Pa decay constant, day^{-1},
VR = volume of salt in reactor, moles,
VT = volume of salt in protactinium decay tank, moles,
CP = concentration of protactinium in salt at point denoted by suffix (defined below), mole fraction.

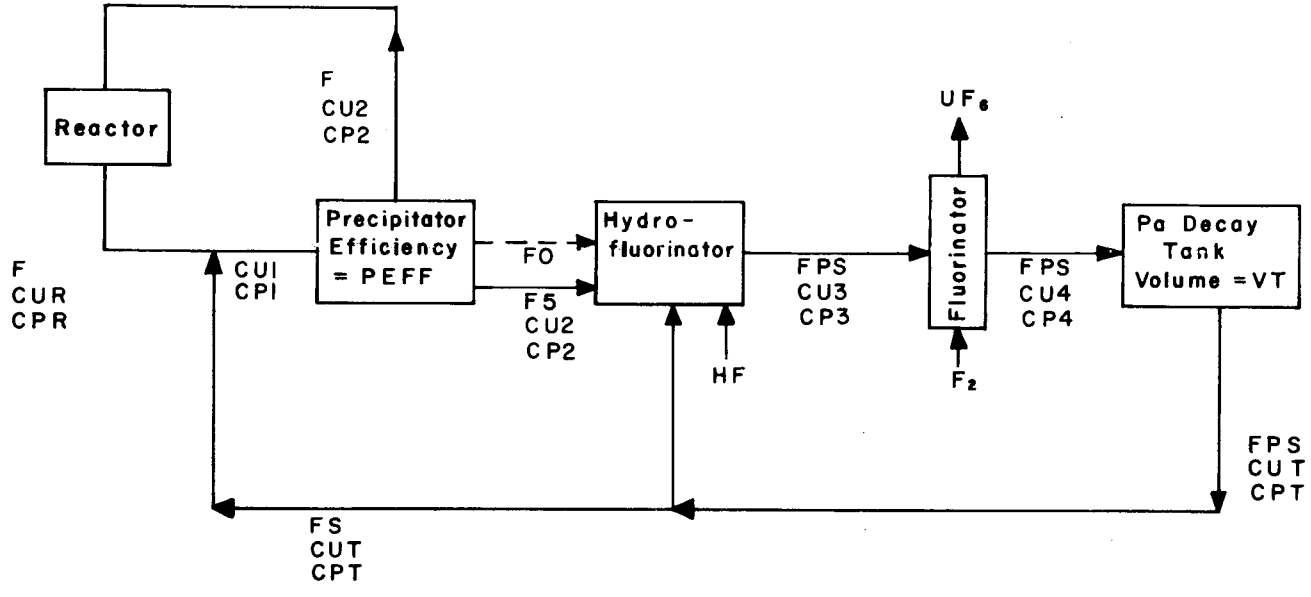

Fig. 2. Nomenclature Used in Mathematical Analysis of Flowsheet for Protactinium Isolation by Fluorination--Oxide Precipitation.

The suffixes 1, 2, 3, 4, R, and T refer to the following locations in the flowsheet: 1, entering precipitator; 2, entering hydrofluorinator; 3, leaving hydrofluorinator; 4, entering protactinium decay tank; R, leaving reactor; and T, leaving Pa decay tank. In the analysis, the quantities F, PEFF, P, VR, VT, and λ are known and the ratio FS/FO is specified. The quantities FO, FS, CP1, CP2, CPR, and CPT are to be determined. It should be noted that Eq. (4) implies that a negligible fraction of the total protactinium inventory is in the metal transfer system and assumes no removal of protactinium except by radioactive decay. However, as much as 5% of the protactinium inventory may be present in the metal transfer system in an actual processing plant. The equations to be solved are nonlinear because of the manner in which the unknown quantity FS enters the relations. The algorithm developed to solve Eqs. (1)-(5) involved assuming a value for FO, which fixes the value for FS and also reduces Eqs. (1)-(4) to a set of four linear algebraic equations that can be readily solved for the four unknown concentrations. Equation (5) is then used to improve the estimated value for FO, and the procedure is repeated until satisfactory convergence in the value of FO is obtained. After the concentrations of protactinium throughout the system and the quantities FO and FS have been determined, the concentrations of uranium throughout the system can be determined by the use of the following analogous set of material balance relations:

$$(F + FS)\cdot CU1 = F\cdot CUR + FS\cdot CUT \quad , \tag{6}$$

$$FS\cdot CU1 + (FPS - FS)\cdot CUT = FPS\cdot CU3 \quad , \tag{7}$$

$$CU4 = (1 - H)\cdot CU3 \quad , \tag{8}$$

and

$$FPS\cdot CU4 + \lambda\cdot VT\cdot CPT = FPS\cdot CUT \quad , \tag{9}$$

where

CU = concentration of uranium in salt at point denoted by suffix defined above, mole fraction,

H = uranium removal efficiency in fluorinator,

FPS = salt flow rate from hydrofluorinator, moles/day.

The quantities H and CUR are assumed to be fixed quantities. In making the analysis, it was assumed that the volumes of all vessels except the protactinium decay tank were negligible, and that the flow rates of the salt streams entering and leaving the fluorinator were equal.

The effects of several parameters on the performance of the flowsheet were calculated. As shown in Fig. 3, the protactinium removal time depends on the precipitator efficiency and the rate at which fuel salt is transferred to the protactinium decay tank along with the Pa_2O_5. A protactinium removal time of about 5 days can be realized if 60% of the protactinium is removed from the salt in the precipitator, provided the salt transfer rate to the protactinium decay tank is as low as 10 to 20 moles/day (a salt-to-oxide flow rate ratio of 2 to 4). If the salt-to-oxide flow rate ratio were as high as 600, a precipitator efficiency of about 80% would be required in order to obtain the same protactinium removal time. The uranium inventory in the decay tank depends on the efficiency of the fluorinator in the protactinium isolation loop and on the amount of fuel salt that is transferred to the protactinium decay tank along with the precipitate, as shown in Fig. 4. The uranium inventory in the decay tank will be only a small fraction of the uranium inventory in the reactor, and the associated inventory charge will be less than 0.001 mill/kWhr for a wide range of operating conditions.

2.2 Isolation of Protactinium by Oxide Precipitation Without the Use of Fluorination for Recovering ^{233}U Produced by Decay of ^{233}Pa

As shown in Fig. 5, the isolation of protactinium by oxide precipitation can also be carried out without the use of a fluorinator for recovering uranium that is produced by the decay of the ^{233}Pa. In this flowsheet, fuel salt is withdrawn from the reactor on a 3-day cycle and combined with a salt stream that is withdrawn from the protactinium decay tank. Part of the protactinium in the resulting salt stream is removed by precipitation as Pa_2O_5. The Pa_2O_5 precipitate is hydrofluorinated in the presence of salt exiting from the metal transfer system, and the resulting salt stream then passes through a decay tank, where part of the ^{233}Pa decays to ^{233}U. The salt stream leaving the protactinium

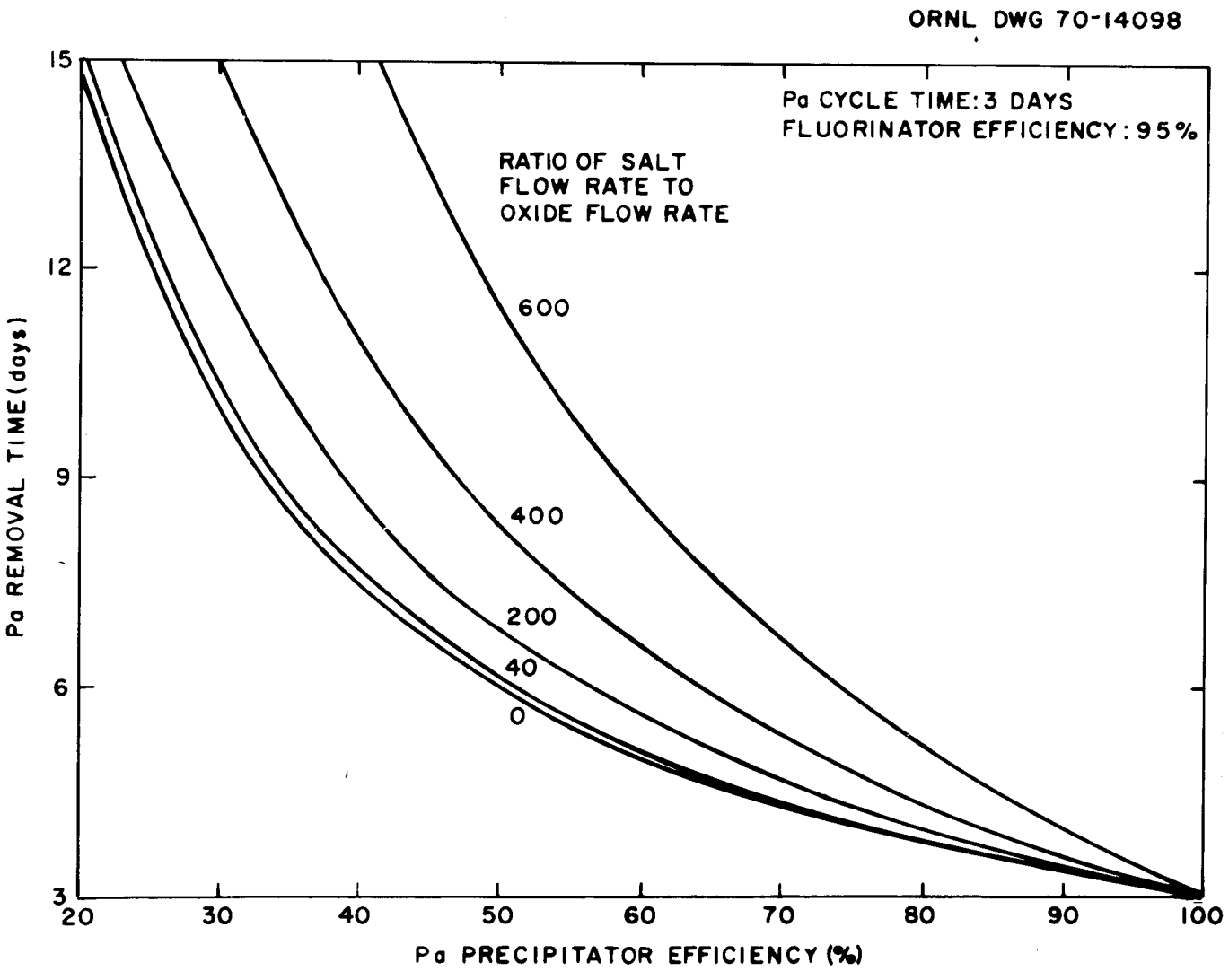

Fig. 3. Effects of Protactinium Precipitator Efficiency and Rate of Transfer of Salt with Precipitate on Protactinium Removal Time for Fluorination--Oxide Precipitation Flowsheet.

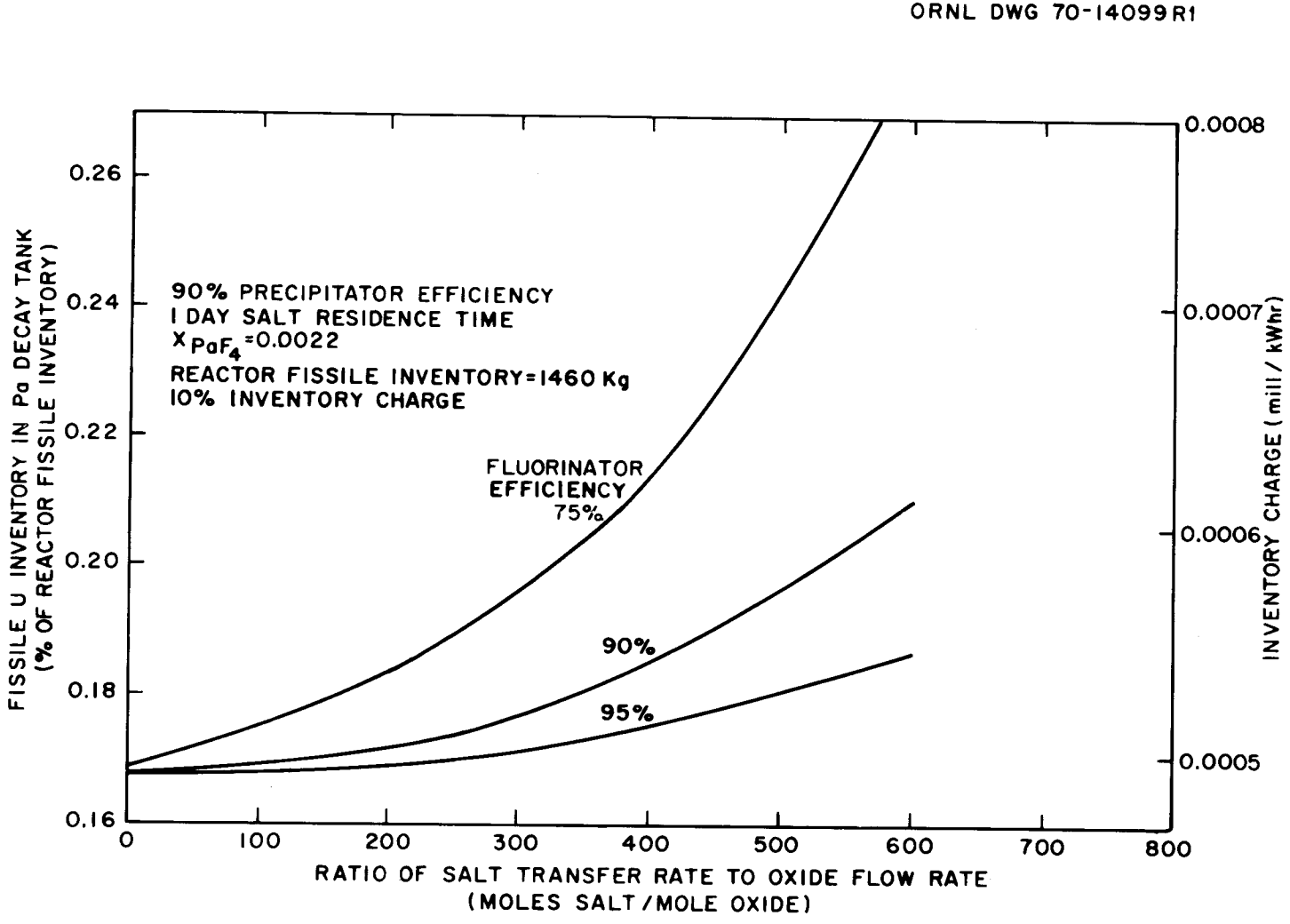

Fig. 4. Effects of Rate of Transfer of Salt-plus-Precipitate and Fluorinator Efficiency on Uranium Inventory in Protactinium Decay Tank for Fluorination--Oxide Precipitation Flowsheet.

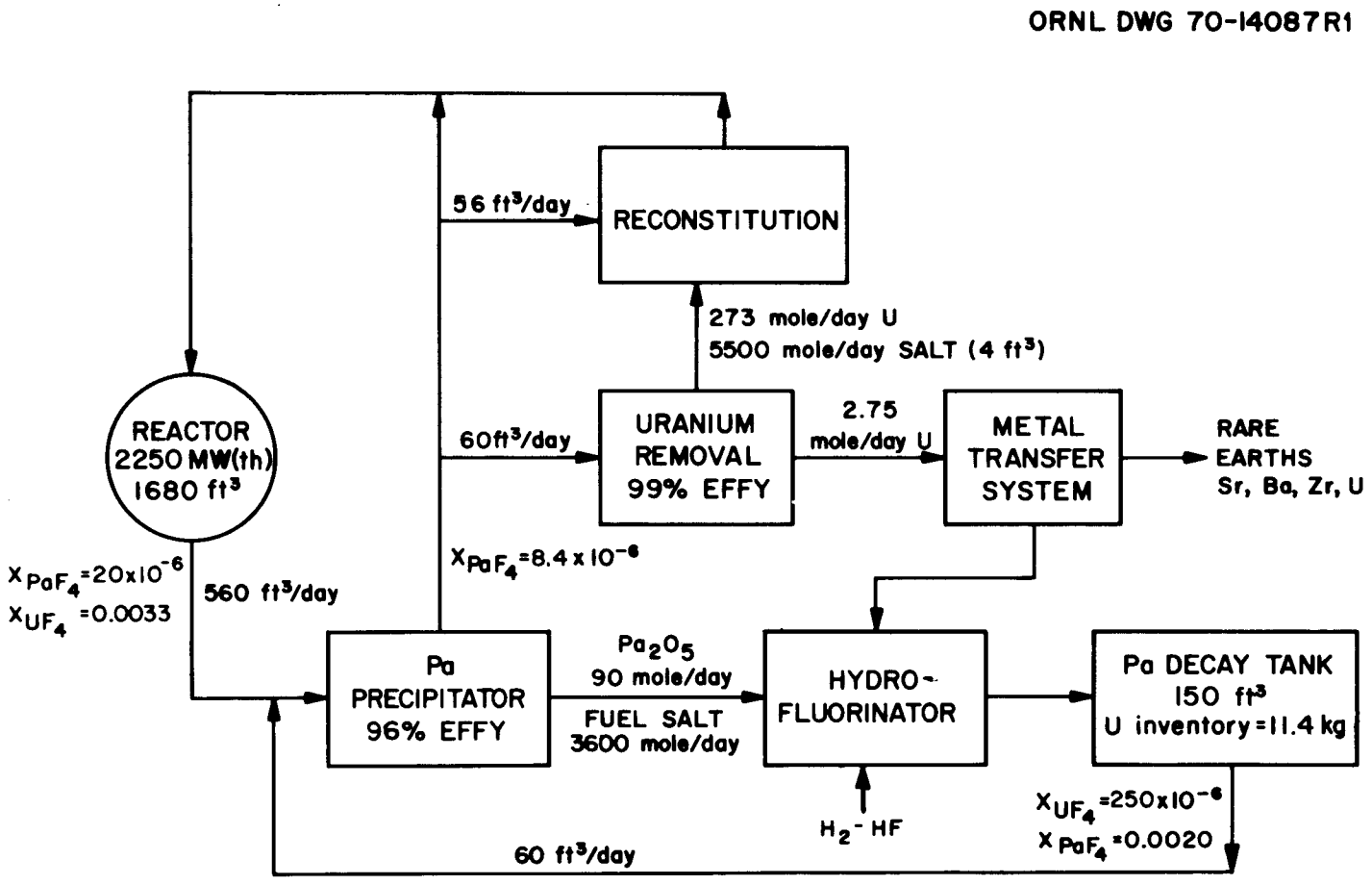

Fig. 5. Flowsheet for Isolating Protactinium by Oxide Precipitation and Removing Rare Earths by the Metal Transfer Process.

decay tank is combined with the salt entering the precipitator in order to return ^{233}U to the reactor without including a large quantity of ^{233}Pa.

A mathematical analysis was carried out for the protactinium isolation portion of the flowsheet, using the nomenclature shown in Fig. 6. The concentrations of protactinium at various points in the flowsheet are defined by the following material balance relations:

$$(FPS + F)\cdot CP1 = F\cdot CPR + FPS\cdot CPT \ , \tag{10}$$

$$FPS\cdot CP3 = FO + FS\cdot CP2 \ , \tag{11}$$

$$P = \lambda\cdot(VR\cdot CPR + VT\cdot CPT) \ , \tag{12}$$

$$FPS\cdot CP3 = (FPS + \lambda\cdot VT)\cdot CPT \ , \tag{13}$$

$$CP2 = (1 - PEFF)\cdot CP1 \ , \tag{14}$$

and

$$(FPS + F)\cdot CP1 = FO + (FPS + F)\cdot CP2 \ . \tag{15}$$

The quantities F, FPS, VR, VT, P, and λ are known; the ratio FS/FO is specified; and the values of CP1, CP2, CP3, CPR, CPT, FO, and FS are to be determined. The equations were linearized by assuming a value for FO, and Eqs. (10)-(14) were solved for the five unknown concentrations. Equation (15) was then used to improve the estimate of FO. As in the analysis for the earlier flowsheet, Eq. (12) implies that the protactinium inventory in the metal transfer system is a negligible fraction of the protactinium inventory in the total system. Changes in the flow rates of the salt streams through the precipitator and the hydrofluorinator as the result of precipitation and dissolution of oxide were neglected.

The concentrations of uranium in the system are defined by the following material balance relations:

$$(FPS + F)\cdot CU1 = F\cdot CUR + FPS\cdot CUT \ , \tag{16}$$

$$FPS\cdot CU3 = FS\cdot CU1 + (FPS - FS)\cdot CU4 \ , \tag{17}$$

ORNL DWG 72-13524

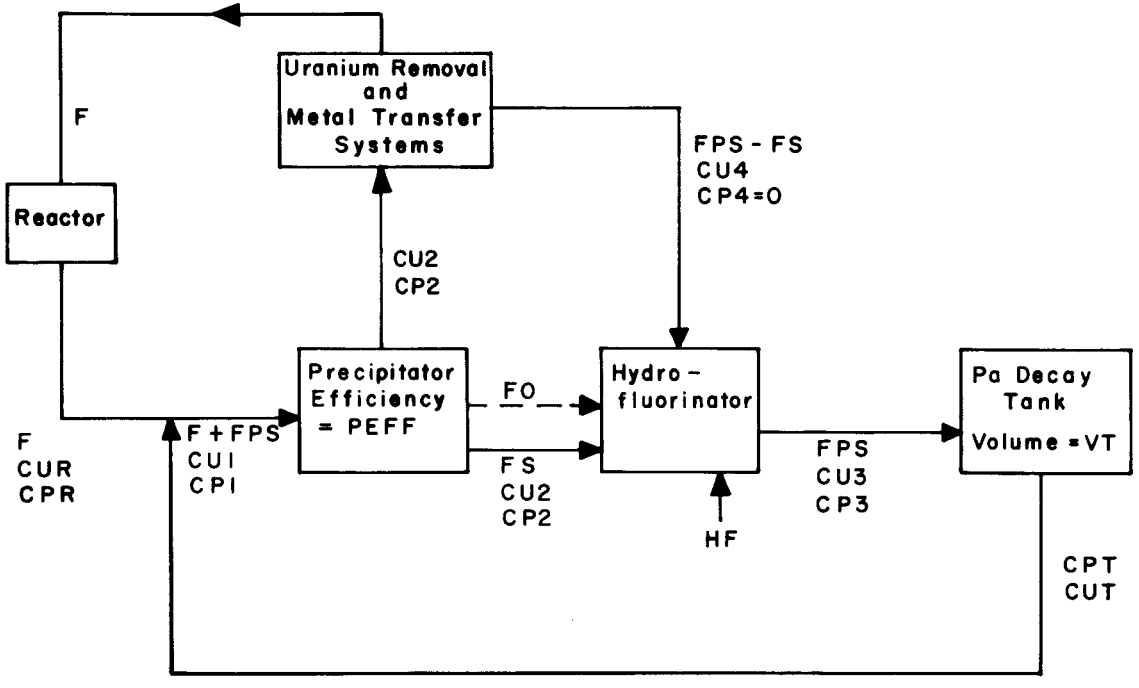

Fig. 6. Nomenclature Used in Mathematical Analysis of Flowsheet for Isolating Protactinium Without the Use of Fluorination for Recovering ^{233}U Produced by Decay of ^{233}Pa.

$$CU4 = (1 - H)\cdot CU1 \ , \tag{18}$$

and

$$FPS\cdot CU3 + \lambda\cdot VT\cdot CPT = FPS\cdot CUT \ , \tag{19}$$

where

H = uranium removal efficiency in the step prior to the metal transfer system,

and the other quantities are as defined previously.

The mathematical model describing operation of the protactinium isolation system was used to investigate the effects of several operating parameters on the performance of the flowsheet. The variation of protactinium removal time with changes in the precipitator efficiency and the fraction of the salt from the metal transfer system which is fed to the protactinium isolation system are shown in Fig. 7 for a protactinium processing cycle time of 3 days, a rare-earth processing cycle time of 30 days, a decay tank volume of 150 ft^3, and a salt-to-oxide molar ratio of 40 in the stream leaving the precipitator. Since the rate of flow of salt between the decay tank and the precipitator must be relatively large in order to limit the uranium inventory in the decay tank, high precipitator efficiencies are required with this flowsheet. A precipitator efficiency of about 96% would be necessary in order to obtain a protactinium removal time of 5 days. The uranium inventory in the protactinium decay tank is relatively sensitive to the amount of salt accompanying the oxide in the stream leaving the precipitator, as shown in Fig. 8. For a salt-to-oxide flow rate ratio of 50 (corresponding to a salt flow rate of ~ 5000 moles/day), the uranium inventory will be about 1% of the reactor fissile inventory and the associated inventory charge will be about 0.003 mill/kWhr. However, if separation of salt from the oxide is difficult and salt-to-oxide flow rate ratios of the order of several hundred are required (corresponding to a salt flow rate of about 5×10^4 moles/day), the uranium inventory in the protactinium decay tank will be about 5% of the reactor fissile inventory and the associated inventory charge will be about 0.015 mill/kWhr.

ORNL DWG 70-14097

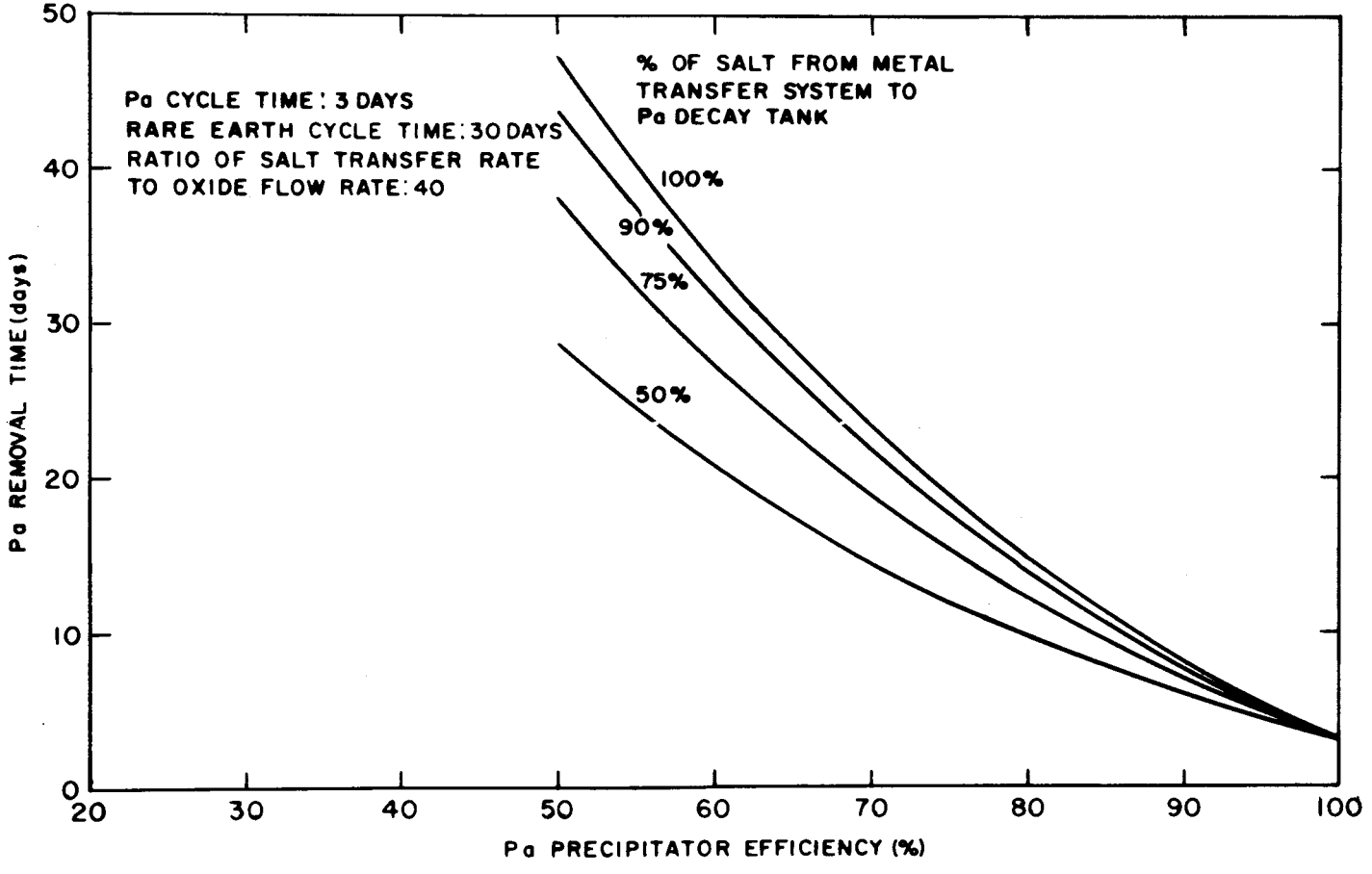

Fig. 7. Effects of Protactinium Precipitator Efficiency and the Fraction of Salt Fed from the Metal Transfer System to the Protactinium Removal System on Protactinium Removal Time.

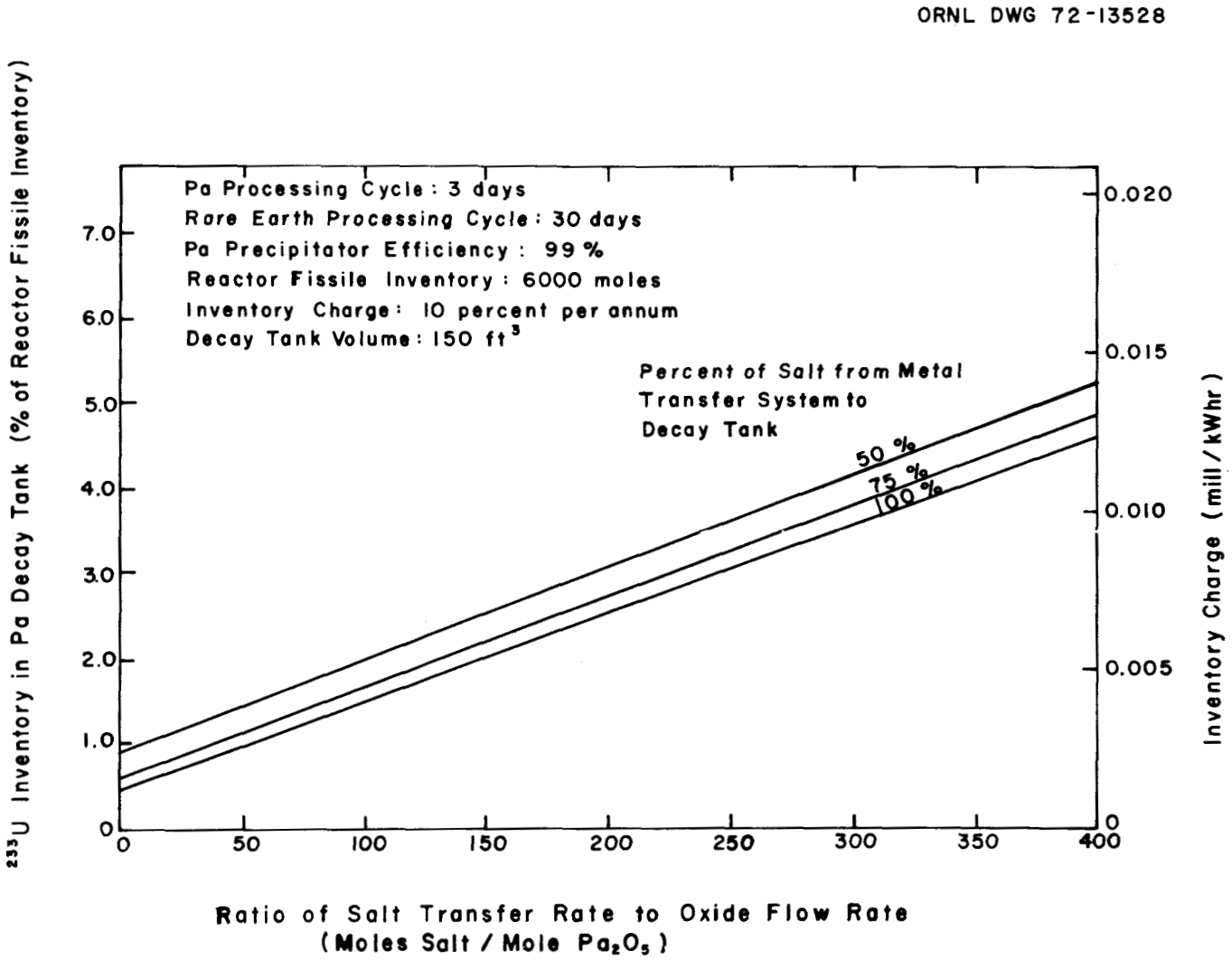

Fig. 8. Effects on Uranium Inventory of Salt-to-Pa_2O_5 Molar Ratio in Stream Leaving Precipitator and of the Percent of Salt Sent from Metal Transfer System to Decay Tank.

3. FLOWSHEET ANALYSIS: REFERENCE PROCESSING PLANT FLOWSHEET BASED ON FLUORINATION, REDUCTIVE EXTRACTION, AND THE METAL TRANSFER PROCESS

L. E. McNeese

Previously, we described an improved method for removing rare earths from the fuel salt of a single-fluid MSBR and presented calculated results on the system performance for a range of operating conditions.[5,6] More recently[7] we described an improved method for removing protactinium from fuel salt. This method is based on the use of fluorination for removing uranium and reductive extraction for removing protactinium. The isolated ^{233}Pa is held for decay to ^{233}U in a secondary molten fluoride salt. We also devised a method for combining the various wastes streams produced during the isolation of protactinium and during the removal of rare earths into a single stream.[7] During this report period, we combined these three processing methods into a single flowsheet and adopted a set of operating conditions that constitute the reference fluorination--reductive extraction--metal transfer flowsheet.

The reference flowsheet is shown in Fig. 9. For a 1000-MW(e) MSBR, fuel salt (71.7-16-12-0.33 mole % $LiF-BeF_2-ThF_4-UF_4$) is removed from the reactor at the rate of 0.88 gpm, which represents a 10-day processing cycle. The salt passes through a delay vessel, which results in an average decay period of 30 min, before being contacted with fluorine at the rate of 19.3 liters (STP)/min in a continuous fluorinator (employing frozen-wall corrosion protection) to remove 99% of the uranium from the salt stream. The fluorine feed rate is equivalent to 150% of that required for conversion of the UF_4 to UF_6. The fluoride salt stream leaving the fluorinator is contacted with a 28.3-liter/min hydrogen stream in order to remove dissolved fluorine from the salt and to reduce the valence of the residual uranium from 5+ to 4+. The salt stream is then contacted countercurrently with a 0.072-gpm bismuth stream containing 0.011 equiv of reductant per gram-mole of bismuth in a salt-metal contactor (which is equivalent to five theoretical stages) in order to extract the protactinium and uranium from the salt. The bismuth stream leaving

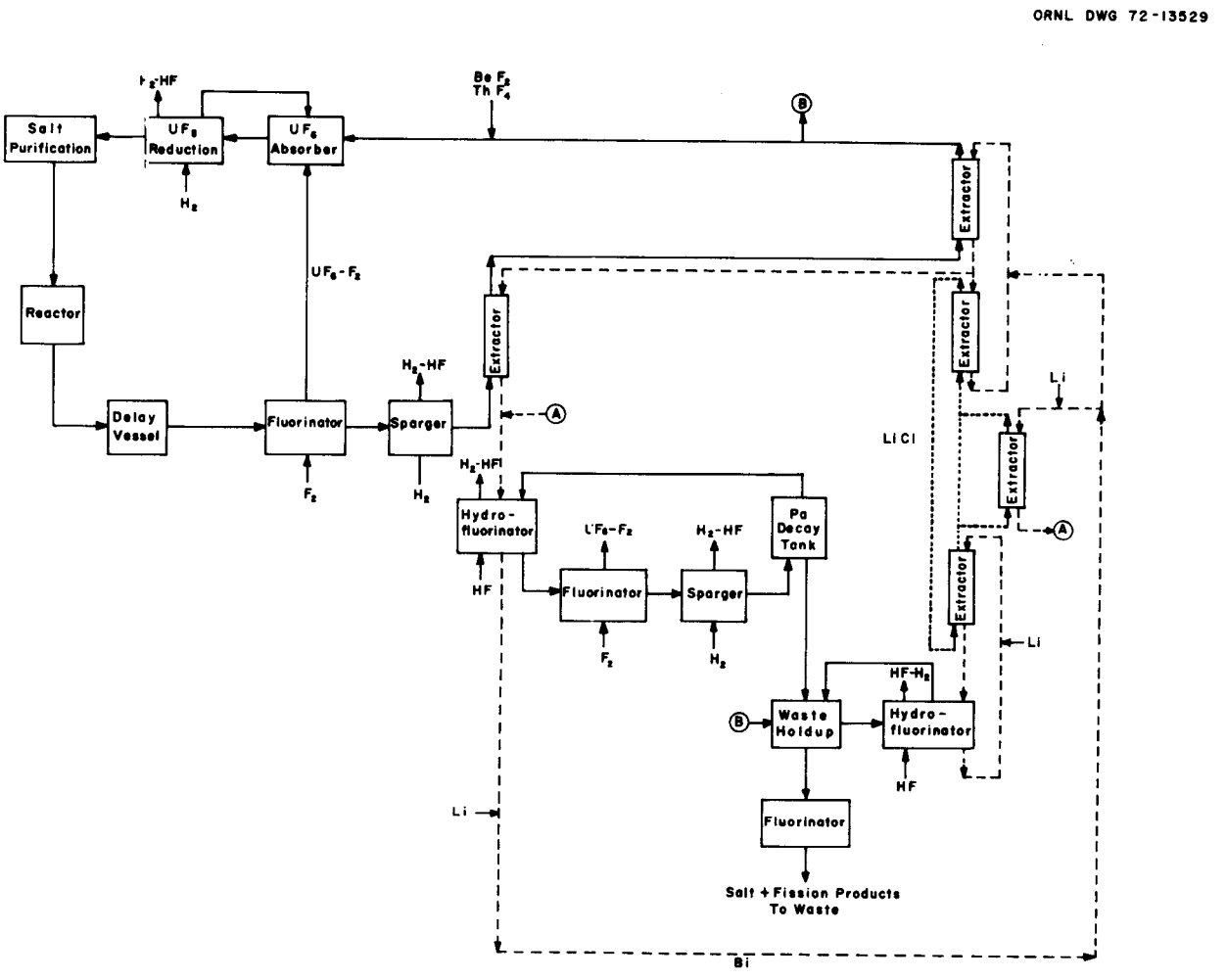

Fig. 9. Reference Flowsheet for Processing MSBR Fuel Salt via Fluorination, Reductive Extraction, and Metal Transfer.

the salt-metal contactor is subsequently contacted with an 11.8-liter/min HF stream in the presence of a 0.78-gpm secondary fluoride salt stream in order to transfer the extracted materials (protactinium, uranium, and zirconium) to the secondary salt. After leaving the hydrofluorinator, the secondary salt passes through a fluorinator, where 90% of the uranium is removed as UF_6 by contact with a 1.56-liter/min fluorine stream. (The assumed value for the fluorine utilization during this step is 17%.) The secondary salt is then contacted with a 2.8-liter/min hydrogen stream in order to remove dissolved fluorine and to reduce the valence of the residual uranium from 5+ to 4+. Finally, the salt passes through the protactinium decay tank, where most of the ^{233}Pa present in the reactor and processing plant is held for decay to ^{233}U. The 0.78-gpm secondary salt stream that is fed to the hydrofluorinator is taken from the protactinium decay tank.

The fuel carrier salt stream leaving the protactinium extraction column is essentially free of uranium, protactinium, and zirconium; however, its rare earth concentration is about the same as that in the reactor. This stream is fed countercurrent to a 12.3-gpm stream of bismuth containing lithium and thorium (0.011 equiv of reductant per mole of bismuth) in a three-stage contactor in order to extract fractions of the rare earths from the salt. The bismuth stream leaving the extractor contains the rare earths, thorium, and lithium; this stream is countercurrently contacted with a 33.3-gpm LiCl stream in a three-stage salt-metal contactor. Because of highly favorable distribution ratios, the rare earths, along with a negligible quantity of thorium, transfer to the LiCl. The trivalent rare earths are removed from the LiCl in a single-stage contactor by contact with an 8.1-gpm recirculating bismuth stream that contains 5 at. % lithium. The net flow rate of the Li-Bi solution through the contactor is 21.5 liters/day. Two percent of the LiCl stream exiting from the trivalent rare-earth contactor is fed to a two-stage salt-metal contactor, where the divalent rare earths are removed by contact with a 0.67-gpm recirculating bismuth stream that contains 50 at. % lithium. The net flow of the Li-Bi solution through the contactor is 2.2 liters/day. All of the extraction operations are carried out at 640°C.

The bismuth stream exiting from the divalent rare-earth contactor is fed to the hydrofluorinator below the protactinium extractor in order to add lithium to the protactinium decay tank at the rate of about 50 moles/day. With this addition, the composition of the salt in the decay tank is 79.6-17.7-2.12 mole % $LiF-ThF_4-ZrF_4$, 0.367 mole % divalent rare-earth fluorides, and 0.247 mole % of trivalent rare-earth fluorides. The salt has a liquidus temperature of about 600°C; at this temperature, the rare-earth fluoride concentration is well within solubility limits. Salt is removed from the protactinium decay tank at the average rate of 0.094 ft^3/day to eliminate the fluorides of lithium, thorium, zirconium, and the rare earths that accumulate in the secondary fluoride salt. About 0.12% of the fuel carrier salt leaving the rare-earth extractor is discarded as a means of removing LiF that is added during the extraction of protactinium and the rare earths. The discards of fuel carrier salt and secondary fluoride salt from the protactinium decay tank are made on a 220-day cycle. During each cycle, 20.7 ft^3 of the secondary fluoride salt and 44.2 ft^3 of the processed fuel carrier salt are transferred to the waste-salt holdup tank. The Li-Bi stream leaving the trivalent rare-earth stripper is hydrofluorinated in the presence of the resulting salt mixture during the 220-day period that is allowed for decay of the ^{233}Pa in the waste salt. The salt in the waste holdup tank would be fluorinated in order to recover the ^{233}U before the salt is discarded. The composition of the waste salt would be 76.3-12.3-9.8-0.64 mole % $LiF-ThF_4-BeF_2-ZrF_4$, 0.864 mole % trivalent rare-earth fluorides, and 0.114 mole % divalent rare-earth fluorides. Although the liquidus temperature of the salt is near 550°C, the salt temperature would have to be maintained at about 600°C to prevent precipitation of trivalent rare-earth fluorides. Waste salt would be discarded from the processing system at the rate of 70 ft^3 every 220 days.

The 0.072-gpm bismuth stream leaving the hydrofluorinator below the protactinium extractor is combined with reductant (200 moles of ^7Li per day), and the resulting stream is effectively returned to the protactinium extractor. The stream is actually combined with the 12.3-gpm bismuth stream that circulates through the rare-earth removal system,

and an equal quantity of material is removed and fed to the protactinium extractor; this mode of operation allows for the removal of materials that would tend to accumulate in the otherwise captive bismuth phase in the rare-earth removal system. A small quantity of bismuth (2.2 liters/day) is combined with sufficient ^{7}Li to produce a stream containing 50 at. % lithium for return to the divalent rare-earth extractor.

The processed fuel carrier salt remaining after discard of 0.12% of the salt stream exiting from the rare-earth extractor is combined with sufficient quantities of BeF_2 and ThF_4 (47.8 and 47 moles/day, respectively) to make up for the discard of these materials in the waste salt and burnup of thorium in the reactor. The resulting fuel carrier salt is then fed to the fuel reconstitution step, which is carried out in a vessel having two compartments. To the first compartment are fed the 63-37 mole % UF_6-F_2 stream from the fluorinators (at the flow rate of 20.9 liters/min), the processed fuel carrier salt (at the rate of 0.88 gpm), and a 1.7-gpm fuel salt stream that is recycled from the second compartment. The rate at which fuel salt is recycled from the second compartment is such that the quantity of UF_4 in the recycled fuel salt is sufficient to give an average uranium fluoride valence of 4.5 (an equimolar mixture of UF_4 and UF_5) in the resulting 2.58-gpm salt stream leaving the first compartment. The 2.58-gpm salt stream leaving the first compartment is contacted with a 12.8-liter/min hydrogen stream in the second compartment in order to reduce the UF_5 to UF_4. A hydrogen utilization of 50% is assumed during this operation. Fuel salt is withdrawn from the second compartment for return to the reactor at the rate of 0.88 gpm, and the remaining salt is recycled to the first compartment.

Before being returned to the reactor, the fuel salt is contacted with a 12.8-liter/min hydrogen stream to effect reduction of 1% of the UF_4 to UF_3. The salt is also contacted with nickel wool as a means of removing traces of bismuth from the salt before its return to the reactor.

The protactinium removal time obtained with the reference flowsheet is 10 days; the rare-earth removal times range from 16 to 50 days. The calculated value for the breeding ratio is about 1.065.

4. FLOWSHEET ANALYSIS: IMPORTANCE OF URANIUM INVENTORY IN AN MSBR PROCESSING PLANT

M. J. Bell L. E. McNeese

The MSBR processing flowsheets considered in the past have uniformly resulted in very low uranium inventories in the processing plant, that is, inventories below 1% of the uranium inventory in the reactor in most cases. Since several potential processing systems might result in uranium inventories as large as 5 to 10% of the reactor inventory, we have investigated the importance of increases in the uranium inventory. The major effects of an increased uranium inventory are: (1) an increase in inventory charges on fissile material, and (2) an increase in the reactor doubling time. The variation of each of these quantities with processing plant uranium inventory is shown in Fig. 10. The fissile inventory (which includes the ^{233}Pa in the processing plant) was assumed to be 1504 kg for the reference reactor and processing plant, the value of ^{233}U was taken to be \$14/g, and the capital charge rate was assumed to be 10% per year. The calculated system doubling time for the limiting case of a zero uranium inventory in the processing plant is 22 years. It is seen that a processing plant uranium inventory of 5% of the system fissile inventory would increase the fuel cycle cost by 0.015 mill/kWhr and would increase the system doubling time from 22 to 23.1 years. A uranium inventory of 10% of the system fissile inventory would result in a fuel cycle cost increase of 0.03 mill/kWhr and an increase in doubling time from 22 to 24.2 years. Thus, while there is incentive for maintaining a low uranium inventory in the processing plant, it does not appear that a uranium inventory as high as 5 to 10% of the system fissile inventory would rule out an otherwise attractive processing system.

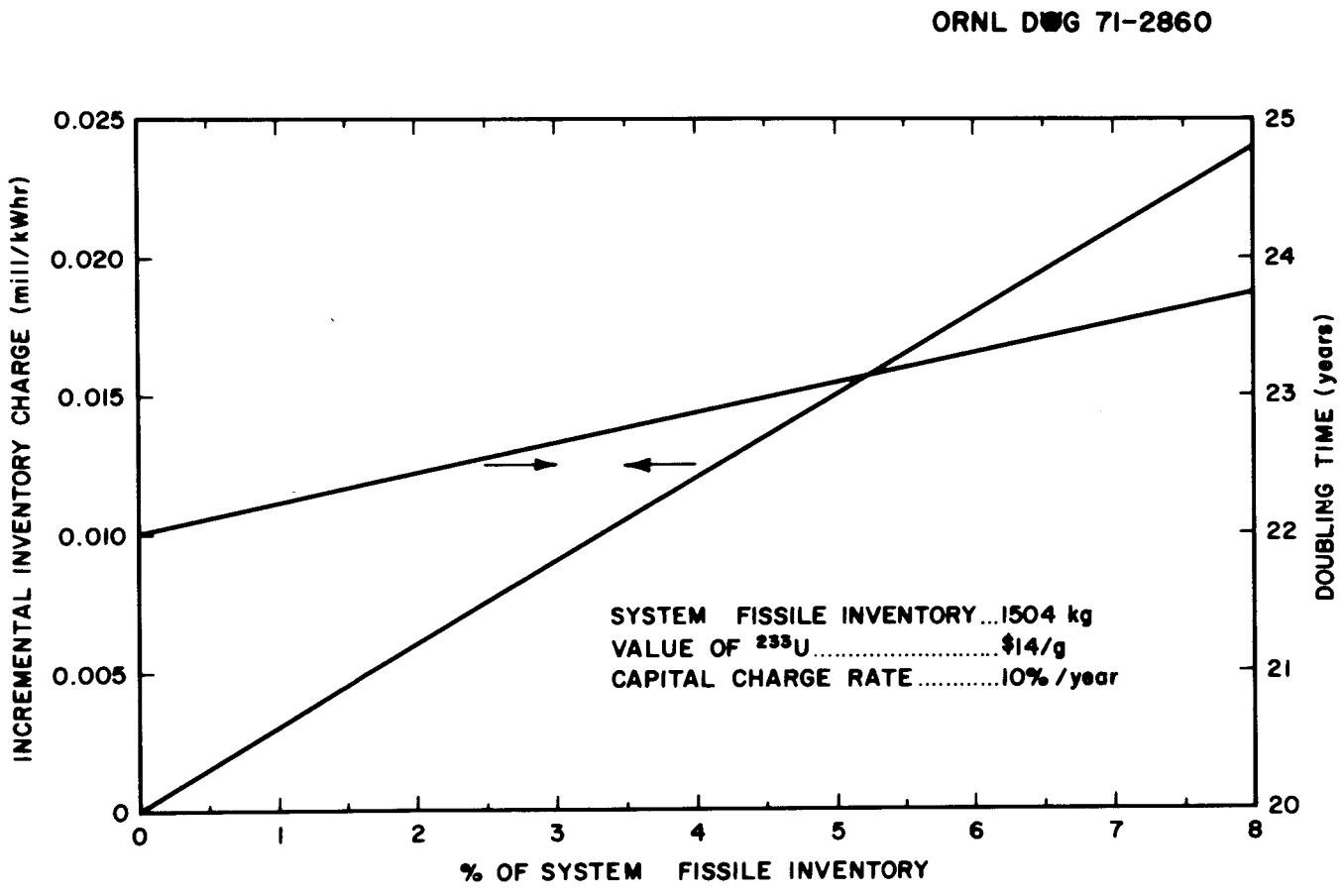

Fig. 10. Effects of ^{233}U Inventory in Processing Plant on System Doubling Time and Inventory Charges.

5. FLOWSHEET ANALYSIS: REMOVAL OF RARE-EARTH FISSION PRODUCTS FROM LiCl IN THE METAL TRANSFER PROCESS

M. J. Bell L. E. McNeese

A flowsheet has been described previously[8,9] for removing rare-earth fission products from MSBR fuel salt using the metal transfer process, which employs contact of LiCl with Li-Bi solutions for removing the rare earths and other fission products. In the reference flowsheet, the trivalent rare earths are removed by contacting LiCl at the rate of 33.4 gpm in a single equilibrium stage with an 8.1-gpm recirculating bismuth stream having a lithium concentration of 5 at. %. Bismuth containing extracted rare earths is withdrawn at the rate of 5.7 gal/day, and an equivalent amount of Li-Bi solution is added.

Early data indicated that mutual solubility problems might be encountered between thorium and trivalent rare earths in bismuth having a lithium concentration as high as 5 at. %. Although this has been found not to be the case,[10] we have made calculations to determine the effect that varying the lithium concentration in the lithium-bismuth alloy has on the thorium concentration in the metal and on the reactor performance. The results are presented in Fig. 11, which shows the effect of increasing the flow rate of the Li-Bi withdrawal stream while holding the amount of added reductant constant. The thorium concentration in the metal is reduced from 420 ppm at the reference withdrawal rate of 1000 moles/day to 140 ppm at the discard rate of 3000 moles/day. The effect on reactor performance is slight; the breeding ratio decreases from about 1.063 to about 1.060. It would be possible to compensate, in part, for this loss in breeding ratio by operating the trivalent rare-earth stripper as a once-through batch contactor having more than one stage.

In the reference flowsheet, the divalent rare-earth fission products are removed from the LiCl by contacting 2% of the LiCl leaving the trivalent rare-earth stripper with a 50 at. % Li-Bi solution at the flow rate of 0.56 gal/day in a two-stage contactor. To accommodate

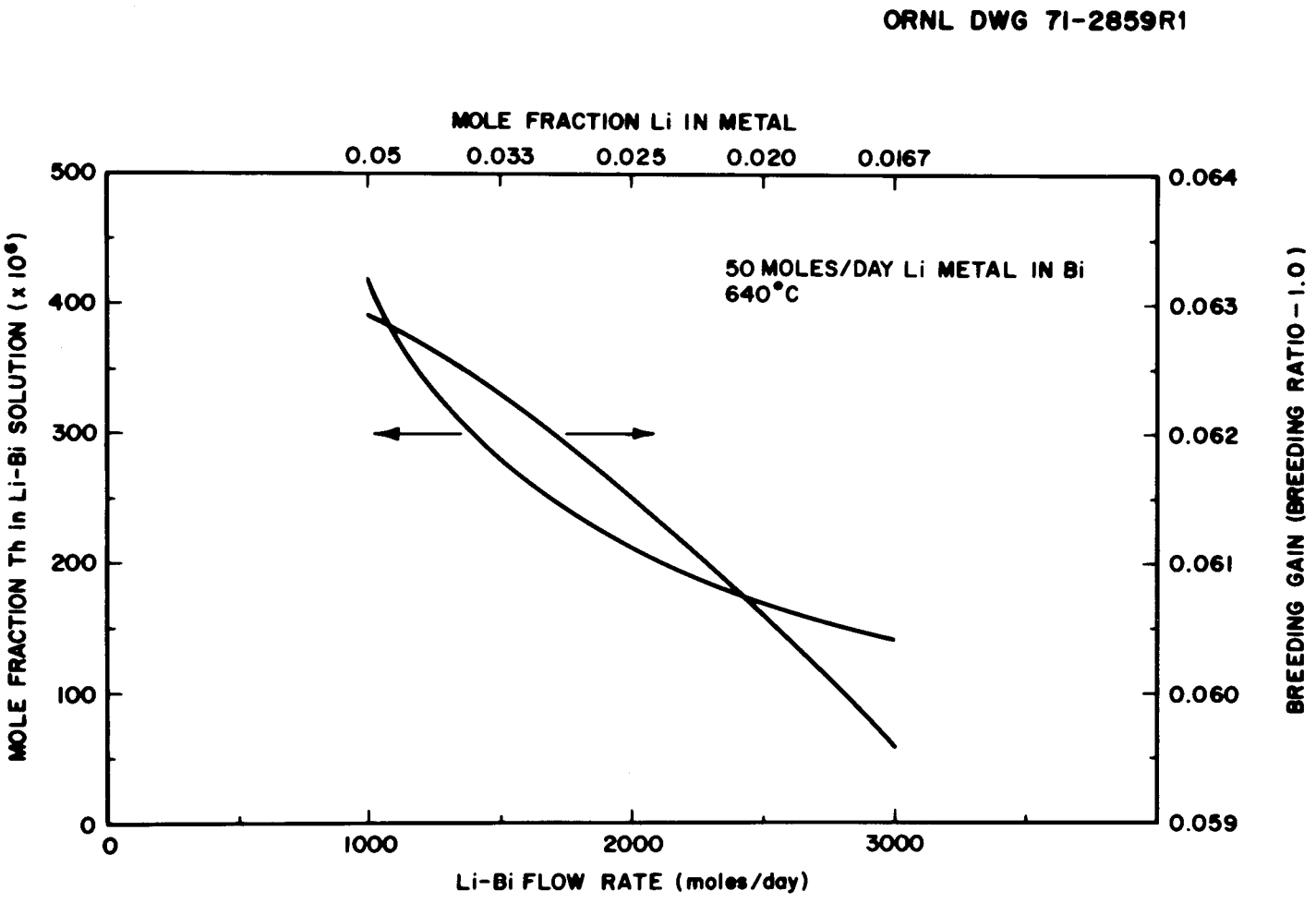

Fig. 11. Effect of Lithium-Bismuth Discard Rate on Thorium Concentration in Discard Stream and on MSBR Performance.

the high heat generation rates expected in the resulting Li-Bi solution, it is advantageous to operate the contactor as a continuous column through which the Li-Bi solution is recycled at a relatively high flow rate. A large fraction of the fission product decay heat could be dissipated by placing a decay tank in the recycle stream. However, this system would result in a contactor having only a single equilibrium stage. A calculation was made of the system performance for a flowsheet in which the divalent rare-earth contactor consisted of only one equilibrium stage. Removal times for the divalent rare earths were increased only slightly over those obtained with a two-stage column; the resulting decrease in the breeding gain of the reactor was negligible. Therefore, the mode of operation described above has been adopted as part of the reference MSBR processing flowsheet.

6. FROZEN-WALL FLUORINATOR DEVELOPMENT: EXPERIMENTS ON INDUCTION HEATING IN A CONTINUOUS FLUORINATOR SIMULATION

J. R. Hightower, Jr. C. P. Tung

An experiment to demonstrate protection against corrosion by the use of a layer of frozen salt in a continuous fluorinator requires the use of a corrosion-resistant heat source in the molten salt. High-frequency induction heating has been proposed as the source of heat, and the estimated performance[11] of a frozen-wall fluorinator having an induction coil embedded in the frozen salt near the fluorinator wall has indicated that this may be an acceptable heating method. However, there are uncertainties associated with the effect of bubbles that will be present in the molten salt on the heat generation rate and in the amount of heat that will be generated in the metal walls of the fluorinator. Equipment has been installed[12] for studying heat generation in a simulated frozen-wall fluorinator by induction methods. In the simulation, a 31 wt % HNO_3 solution with electrical properties similar to those of molten salts is used to simulate molten salt in the fluorinator vessel. Results of the first eight experiments with the fluorinator simulation are described in the remainder of this section.

6.1 Experimental Procedure

A simplified flow diagram for the continuous fluorinator simulation is shown in Fig. 12; the system is shown in greater detail in Fig. 13. The acid drain tank was filled with 28.4 kg of 31 wt % HNO_3 that was used during the initial operating period and also during the first eight runs that were carried out. In each run, the acid recirculation system was filled with acid by pressurizing the drain tank to about 6 psig with valve V-7 open (see Fig. 13). When the liquid level in the column (as indicated by the level in the sight glass) reached the level of the top of the jacketed pipe, valve V-7 was closed and the pressure in the drain tank was reduced to 1 atm. The acid recirculation pump and the cooling water were turned on, and all flow rates were adjusted to the desired

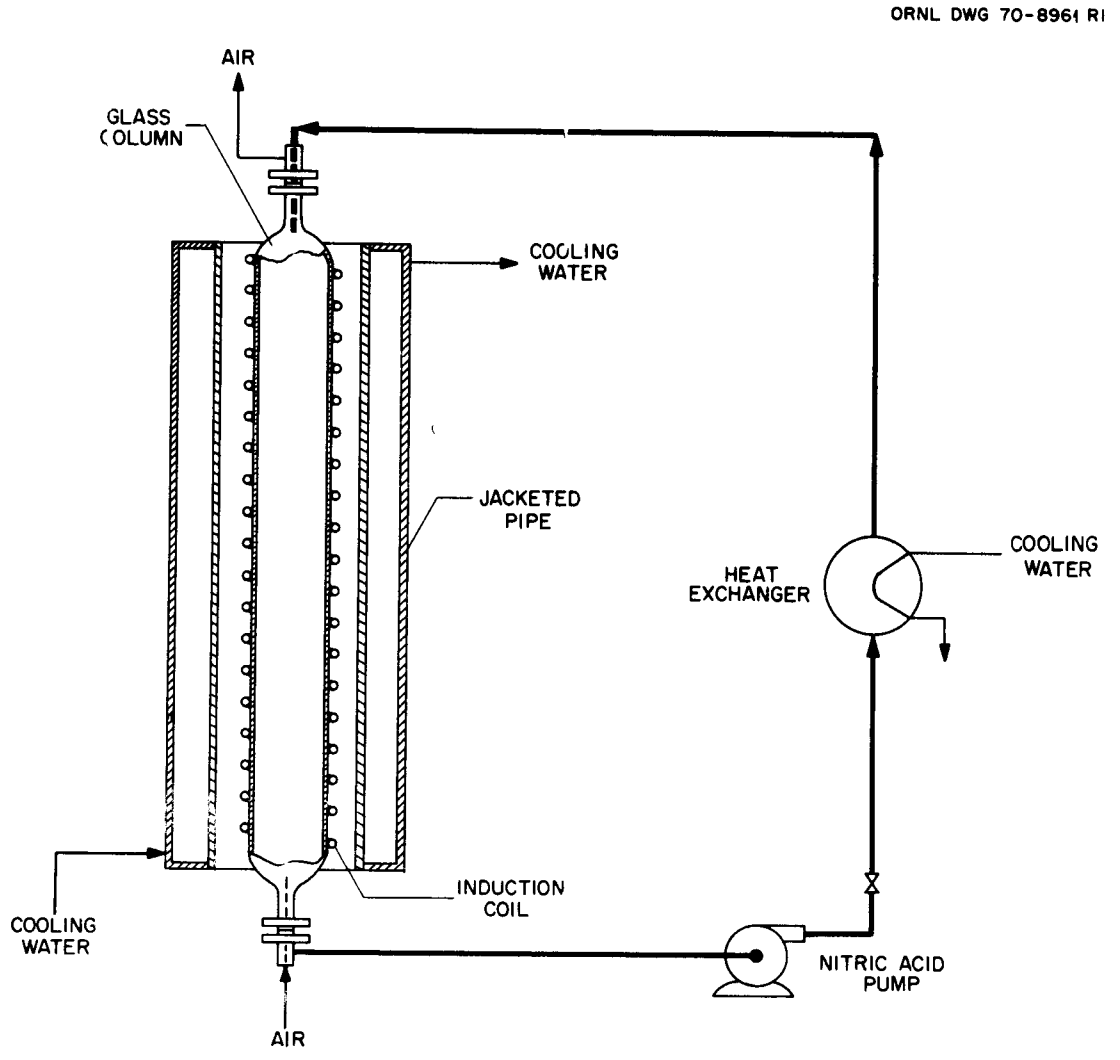

Fig. 12. Simplified Flow Diagram of a Fluorinator Simulation in Which Heat Is Generated by Induction Heating.

ORNL DWG 70-14719

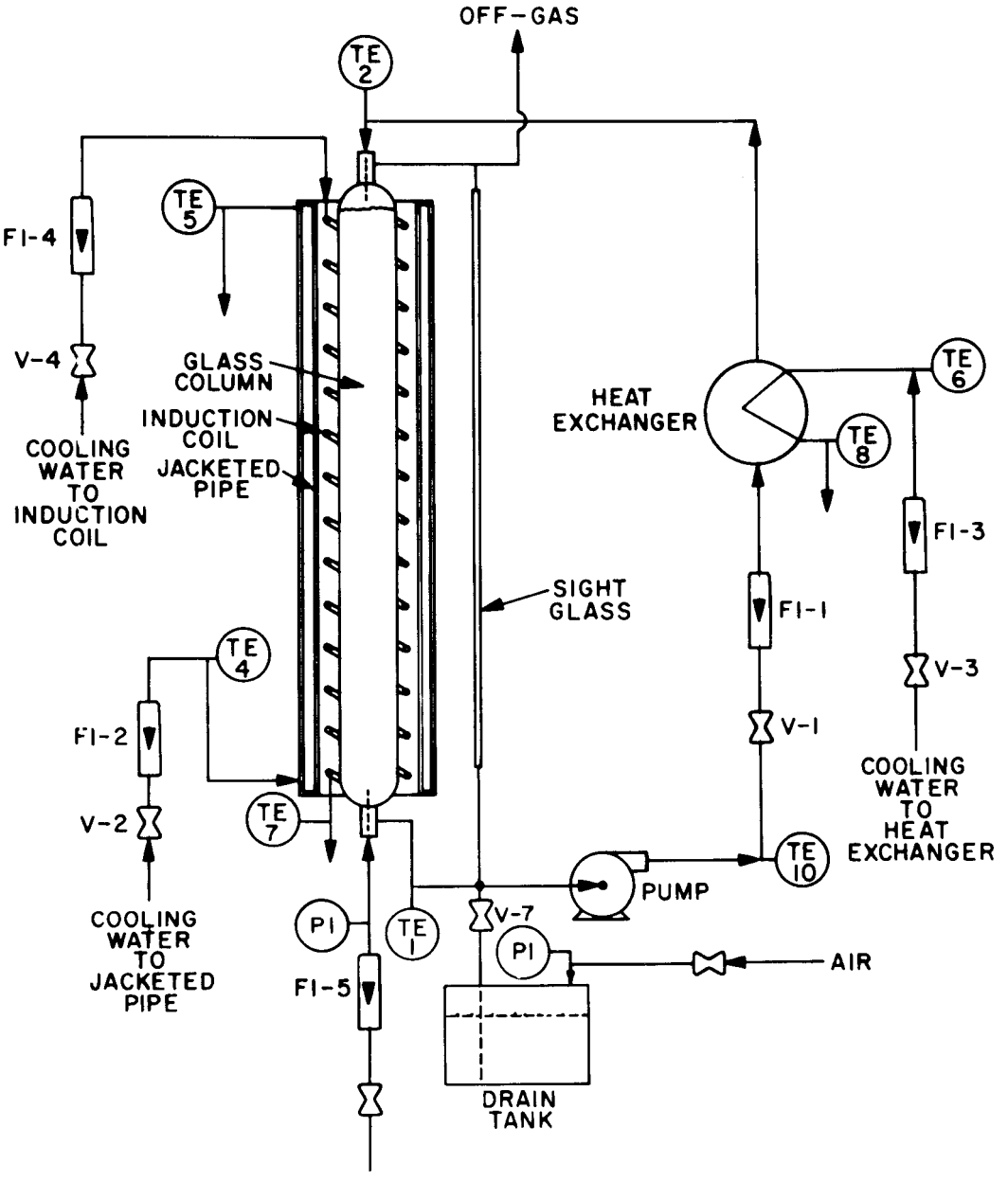

Fig. 13. Flow Diagram of Fluorinator Simulation and Nitric Acid Recirculation System.

values. The radio frequency (rf) generator was then started, and the current to the induction coil was adjusted to a value between 100 and 160 A (rms value). The flow rates and the coil current were maintained at constant levels by manual adjustment until the temperatures around the recirculation system became steady. Steady-state temperatures were usually achieved within 1 hr of operation with constant values for the flow rates and coil current. After steady-state conditions had been established, the run was completed by recording the operating conditions. The rf power and the acid recirculation pump were then turned off, and the acid was drained from the recirculation system by opening valve V-7.

6.2 Experimental Results

Eight runs have been carried out with the continuous fluorinator simulation to determine heat generation rates in the acid, in the pipe surrounding the acid column, and in the induction coil. Heat generation rates were calculated from the steady-state increase in the temperature of the acid as it passed through the column and in the temperature of the cooling water as it passed through the coil and the jacketed pipe. The experimental results for the first eight runs with the system are summarized in Table 1. During these runs, the induction coil consisted of 17 smaller coils arranged with alternate coils wound in opposite directions. Each coil section consisted of about 6.5 turns of 1/4-in.-diam Monel tubing that had been wound on a 5.6-in.-diam mandrel. The total length of the 17-section coil was 5 ft. The frequency of the rf current was 412 kHz during each of the runs.

The heat generation rates in acid in the 5-ft-long column section, in the pipe representing the fluorinator wall, and in the induction coil were proportional to the square of the total coil current as expected. The ratios of the heat generation rates (in watts) to the square of the coil current (rms value, in amperes) were designated as effective resistances that will be used subsequently in circuit calculations for design of the rf generator. The average effective resistance for the acid was 0.0161 Ω at average acid temperatures of 25 to 29°C and 0.0177 Ω for average acid temperatures of 46 to 51°C. The difference between these

Table 1. Summary of Results from Experiments on Induction Heating in a Simulated Continuous Fluorinator

Run No. (CFS-)	Total Coil Current (A)	Average Acid Temp. (°C)	Heat Generation Rate (W)			Equivalent Resistance (Ω)		
			Acid	Pipe	Coil	Acid	Pipe	Coil
1		24.1	242	140				
2	130	24.6	409	167		0.0242	0.0099	
3	150	26.5	316	279	1442	0.0140	0.0124	0.0641
4	100	25.6	141	116		0.0141	0.0116	
	150	28.1	378	263		0.0168	0.0117	
	150	29.1	383	309		0.0170	0.0137	
5	160	26.7	448	308		0.0175	0.0120	
6	150	46.5	393	282		0.0175	0.0125	
7	150	28.9	377	273	1356	0.0167	0.0121	0.0585
	120	26.6	235	178	870	0.0163	0.0126	0.060
8	150	51.4	402	275	1442	0.0178	0.0122	0.0641

values may be within experimental error. The effective resistance of the acid should have increased by about 25% as the temperature was increased from the lower to the higher value; however, the observed increase was only about 10%. The smaller variation in effective resistance with changes in temperature may be due to the use of short coil sections since the effective resistance of the acid should be proportional to the specific conductance for an infinitely long coil. The average effective resistance for the stainless steel pipe surrounding the acid was 0.0123 Ω; the average effective resistance of the induction coil was 0.0617 Ω.

The fraction of the total heat generation that occurred in the acid can be found by dividing the resistance of the acid by the sum of the resistances of the acid, pipe, and coil. About 19% of the total heat generation occurred in the acid during these runs. A 5-ft-long fluorinator having a 4.7-in.-diam molten zone would require generation of about 8.3 kW of heat in the molten salt.[11] If an efficiency of 19% were obtained for heating the molten salt, a 43.7-kW generator would be required.

The calculated values for the resistances of the acid and coil under the experimental conditions are 0.135 and 0.017 Ω respectively. The discrepancies between the calculated and measured values probably result from the use of a coil composed of a number of short sections and the use of equations that were derived for infinitely long coils.

We are presently evaluating alternative coil designs with a view toward improving the heating efficiency.

7. PREDICTED CORROSION RATES IN CONTINUOUS FLUORINATORS EMPLOYING FROZEN-WALL PROTECTION

J. R. Hightower, Jr.

Nickel is the preferred material of construction for fluorinators in MSBR processing plants since it exhibits greater resistance to attack by gaseous fluorine than other candidate materials. This resistance is due to the formation of a tightly adherent film of NiF_2 (a corrosion product) through which additional fluorine must diffuse in order to cause further corrosion of the nickel. The rate of attack is greatly reduced, although not to zero, once the protective film of NiF_2 is formed on the exposed nickel surface. In the proposed continuous fluorinators, a layer of frozen salt will be formed on the fluorinator wall in order to prevent the protective NiF_2 film from being dissolved by the molten salt. In the present analysis, no credit is taken for resistance to diffusion of fluorine which may be afforded by the layer of frozen salt. Since the protective NiF_2 film will likely be destroyed several times during operation of a fluorinator, an analysis has been carried out for estimating the corrosion rate under conditions such that the NiF_2 film is destroyed periodically.

7.1 Data on the Rate of Corrosion of Nickel in Gaseous Fluorine

Data relative to the corrosion of Ni-200 and Ni-201 in gaseous fluorine at a pressure of 1 atm were collected from the literature. A summary of this information is given in Tables 2 and 3. It has been shown[13] that the reaction of high-purity nickel with fluorine initially follows a parabolic rate law at temperatures of 300 to 600°C but that, after a period of time, the reaction rate decreases and follows a third- or higher-order rate law. The literature-derived corrosion-rate data were used to calculate rate constants for the reaction of fluorine with nickel in the temperature range of 360 to 700°C under the assumption that the reaction rate follows a parabolic rate law at all times. The assumption of a parabolic rate law correctly represents the initial reaction rate but should yield high estimates of the corrosion rate for long periods of exposure.

Table 2. Calculated Parabolic Reaction Rate Constants for Ni-200 Exposed to Gaseous Fluorine

Temp. (°C)	Depth of Penetration (mils)	Exposure Time (hr)	Calculated Parabolic Rate Constant (mils/hr$^{1/2}$)	Reference[a]	
362	0.0048	120	0.000438	[14]	(5)
400	0.00681	33.3	0.00118	[13]	
400	0.00701	50	0.000991	[15]	
475	0.0187	240	0.00242[b]	[16]	
475	0.0375	480	0.00342[b]	[16]	
475	0.0750	960	0.00484[b]	[16]	
500	0.0132	33.3	0.00229	[13]	
500	0.0144	5	0.00643	[17]	(27)
500	1.97	240	0.1272	[17]	(25)
500	0.0754	50	0.01066	[17]	(23)
500	0.0206	150	0.00168	[17]	(13)
500	0.043	150	0.00352	[17]	(13)
500	0.0243	9	0.0081	[14]	
535	0.181	120	0.0165	[17]	(18)
550	0.00299	6	0.00122	[14]	(2)
550	0.192	120	0.0175	[14]	(5)
600	0.0616	33.3	0.01067	[13]	
600	0.00684	5	0.00306	[17]	(27)
600	0.0657	96	0.00671	[17]	(20)
600	0.315	96	0.0322	[17]	(20)
600	0.00404	8	0.00143	[17]	(24)
600	0.0931	8	0.0329	[17]	(24)
600	0.753	50	0.1065	[17]	(23)
600	0.00887	13	0.00246	[18]	
600	0.0736	28	0.0139	[18]	
600	0.0417	28	0.00788	[18]	
600	0.0287	77	0.00327	[18]	
600	0.0171	77	0.00195	[18]	
600	0.134	93	0.0139	[18]	
600	0.0744	93	0.00772	[18]	
600	0.0416	124	0.00374	[18]	
600	0.0307	124	0.00276	[18]	
600	0.162	132	0.0141	[18]	
600	0.0936	132	0.00815	[18]	
600	0.0690	195	0.00494	[18]	
600	0.0628	195	0.0045	[18]	
600	0.104	243	0.00666	[18]	
700	0.103	8	0.0364	[17]	(24)
700	0.0274	8	0.00969	[17]	(24)
700	3.28	240	0.212	[17]	(25)
700	0.727	5	0.325	[17]	(27)

[a]The numbers shown in brackets are primary references; the numbers shown in parentheses are reference numbers in the primary references.

[b]Measured in F_2-N_2 (50-50%) mixture; rate constant corrected to 100% F_2.

Table 3. Calculated Parabolic Corrosion Rate Constants for Ni-201 Exposed to Gaseous Fluorine

Temp. (°C)	Depth of Penetration (mils)	Exposure Time (hr)	Calculated Parabolic Rate Constant (mils/hr$^{1/2}$)	Reference[a]
380	0.00085	5	0.000380	[14] (5)
500	0.00959	5	0.00429	[17] (27)
500	0.00899	6	0.00367	[14]
550	0.0115	5	0.00514	[14] (5)
600	0.00259	5	0.00116	[17] (5)
600	0.0471	28	0.00891	[18]
600	0.0283	28	0.00534	[18]
600	0.0936	77	0.01067	[18]
600	0.235	77	0.0268	[18]
600	0.109	93	0.0113	[18]
600	0.111	93	0.0115	[18]
600	0.142	132	0.0124	[18]
600	0.160	132	0.0139	[18]
700	0.0595	5	0.0266	[17] (27)

[a]The numbers shown in brackets are primary references; the numbers shown in parentheses are reference numbers in the primary references.

For the assumption of a parabolic rate law, the extent of corrosion of nickel exposed to gaseous fluorine is described by the following relation:

$$d = k\sqrt{t} \quad , \tag{20}$$

where

d = depth of nickel attacked by F_2, mils,

t = time of exposure of nickel metal to fluorine after a zero film thickness, hr,

k = parabolic rate constant, mil $hr^{-1/2}$.

The rate constant values calculated from the literature data are shown in Tables 2 and 3, along with information on the length of exposure of the nickel specimens to fluorine, the extent of attack on the specimens, and the references from which data were obtained.

It was assumed that the temperature dependence of the parabolic rate constants would be of the Arrhenius type; thus the calculated values were fitted to the following equation:

$$\ln k = B + A/T \ , \tag{21}$$

where

T = temperature, °K,

A, B = constants,

with the criterion that the best fit occurred when the quantity

$$\sum \left[\ln k - \ln k_{obs}\right]^2$$

was minimized. This criterion places more importance on reaction rate constant values resulting from low corrosion rates than does the usual criterion that the quantity

$$\sum (k - k_{obs})^2$$

have a minimum value. This procedure was used since it was believed that experimental errors were likely to yield corrosion rates that were too high rather than rates that were too low.

The resulting equations for the variation of the parabolic rate constants for Ni-200 and Ni-201 are as follows:

$$\ln k = 0.3773 - 3961/T \ , \tag{22}$$

and

$$\ln k = 4.3083 - 7836/T \ , \tag{23}$$

where

k = parabolic rate constant, mil $hr^{-1/2}$,

T = temperature, °K.

The variation of these constants with temperature is shown in Figs. 14 and 15.

7.2 Predicted Corrosion Rates

If it is assumed that the protective NiF_2 film is removed n times per year at equal time intervals, the extent of corrosion experienced during a 1-year period is given by the expression:

$$d = n\,k\sqrt{8760/n}\ , \qquad (24)$$

where

d = corrosion rate, mils/year,

n = number of times NiF_2 film is destroyed annually.

Figure 16 shows the variation of the average corrosion rate with frequency of destruction of the NiF_2 film at 450°C, the approximate wall temperature that will be used in a frozen-wall fluorinator. If the NiF_2 film were destroyed 52 times annually, the average corrosion rates at this temperature would be 2.9 mils/year and 0.97 mil/year for Ni-200 and Ni-201 respectively. It appears that Ni-201 is more resistant to corrosion by fluorine than Ni-200. However, either of these materials will show satisfactory corrosion resistance if the NiF_2 film is destroyed less frequently than once per week.

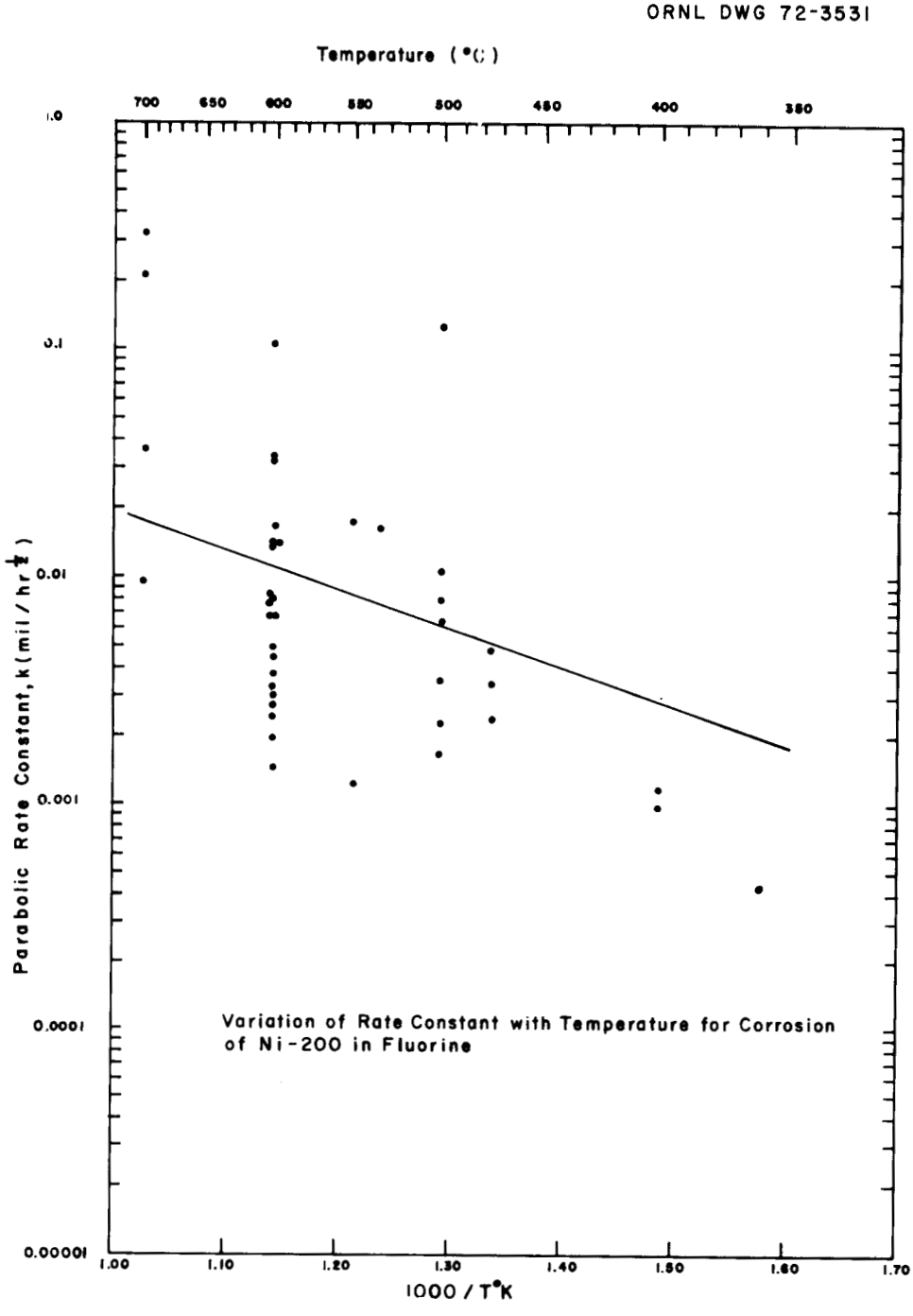

Fig. 14. Corrosion Rate Constant for Ni-200 as a Function of Temperature.

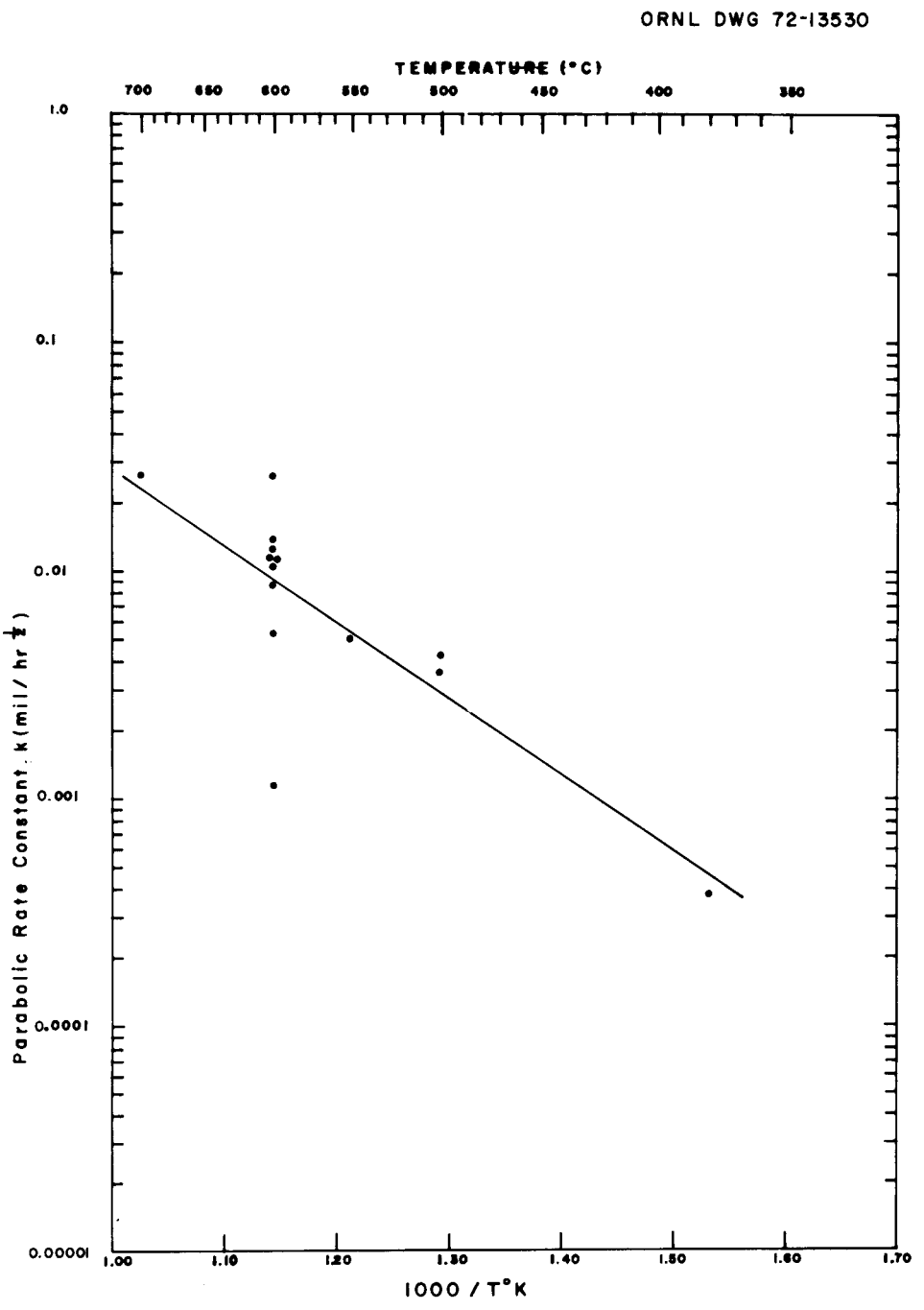

Fig. 15. Corrosion Rate Constant for Ni-201 as a Function of Temperature.

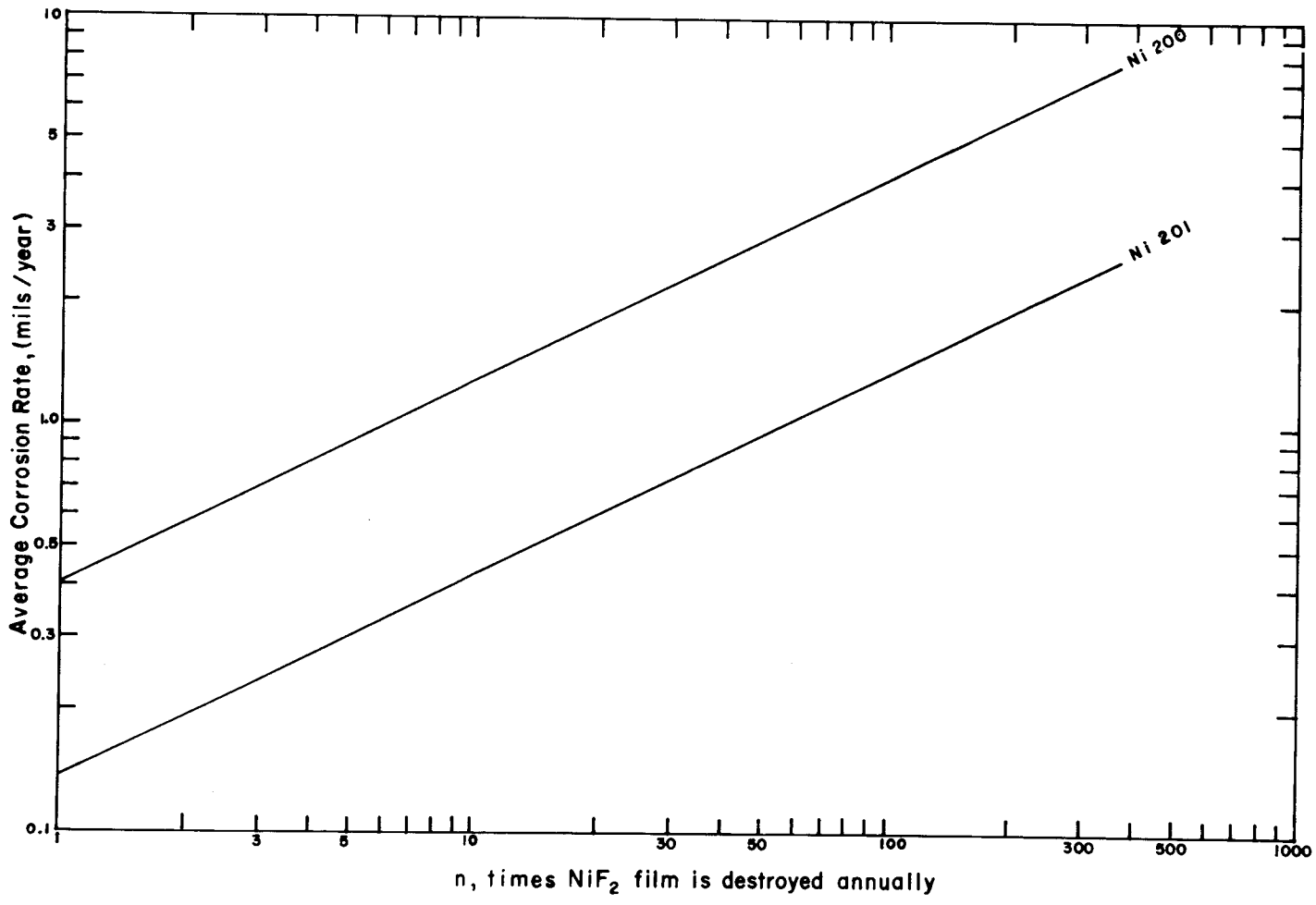

Fig. 16. Effect of Frequency of Destruction of NiF_2 Film on the Corrosion Rates of Ni-200 and Ni-201 at 450°C.

8. PREDICTED PERFORMANCE OF CONTINUOUS FLUORINATORS

L. E. McNeese J. S. Watson
T. O. Rogers

Most of the flowsheets[19-22] considered to date for processing MSBR fuel salt require fluorination of molten salt for removal of uranium at one or more points. These applications include:

(1) removal of trace quantities of uranium from relatively small salt streams prior to discard,

(2) removal of uranium from a captive salt volume in which ^{233}Pa is accumulated and held for decay to ^{233}U,

(3) removal of most of the uranium from relatively large fuel salt streams prior to isolation of protactinium and removal of rare earths, and

(4) nearly quantitative removal of uranium from a salt stream containing ^{233}Pa in order to produce isotopically pure ^{233}U.

Not all of these applications require continuous fluorinators; in fact, the use of batch fluorinators results in definite advantages in certain cases. However, as the quantities of salt and uranium to be handled increase, the use of continuous fluorinators becomes mandatory in order to avoid undesirably large inventory charges on uranium and molten salt as well as the detrimental increase in reactor doubling time that is associated with an increased fissile inventory.

We previously estimated[23] the performance of continuous fluorinators by assuming that the rate of removal of uranium from the salt is first order with respect to the concentration of uranium in the salt. If the transfer of uranium in the salt by axial dispersion and by convection is taken into account, the concentration of uranium in the salt is defined by the following relation:

$$D \frac{d^2C}{dX^2} - V \frac{dC}{dX} - kC = 0 \quad , \tag{25}$$

where

D = axial dispersion coefficient, cm^2/sec,

C = concentration of uranium in salt, $moles/cm^3$,

X = position in column measured from top of column, cm,

V = superficial salt velocity, cm/sec,

k = reaction rate constant, sec^{-1}.

The terms in Eq. (25) represent the transfer of uranium in the salt by axial dispersion, the transfer of uranium in the salt by convection, and the removal of uranium from the salt by reaction with fluorine respectively. The assumption of the first-order reaction does not imply a particular rate-limiting reaction mechanism; however, it is consistent with the assumption that the rate-limiting step is diffusion of uranium in the salt to the gas-liquid interface. In this case, the first-order expression would imply that the concentration of uranium in the salt at the interface is negligible in comparison with the uranium concentration in the salt at points a short distance from the interface.

The boundary conditions chosen for use with Eq. (25) assume that the diffusive flux across the fluorinator boundaries is negligible: at X = 0 (top of fluorinator),

$$\left.\frac{dC}{dX}\right|_{X=0+} = -\frac{V}{D}\left[C_{feed} - C_{0+}\right] \quad , \tag{26}$$

and at X = L (bottom of fluorinator),

$$\left.\frac{dC}{dX}\right|_{X=L} = 0 \quad , \tag{27}$$

where

C_{feed} = concentration of uranium in salt fed to the fluorinator,

C_{0+} = concentration of uranium in salt at top of the fluorinator.

Note that C_{0+} is not equal to C_{feed} since there is a discontinuity in uranium concentration in the salt at the top of the fluorinator where the salt enters.

Solution of Eq. (25) with the stated boundary conditions yields the following expression for the ratio of the uranium concentration in salt leaving the fluorinator to the concentration in the feed salt:

$$\frac{C(L)}{C_{feed}} =$$

$$\frac{1}{\left\{\frac{1/2 + \eta}{\sqrt{1 + 4\eta}} + 1/2\right\} e^{\xi\left[\sqrt{1/4 + \eta} - 1/2\right]} - \left\{\frac{1/2 + \eta}{\sqrt{1 + 4\eta}} - 1/2\right\} e^{-\xi\left[1/2 + \sqrt{1/4 + \eta}\right]}}, \quad (28)$$

where

$C(L)$ = concentration of uranium in salt leaving fluorinator,

$\eta = \frac{kD}{V^2}$,

$\xi = \frac{VL}{D}$,

L = length of fluorinator, cm.

Application of Eq. (28) to the design and evaluation of continuous fluorinators requires values for the rate constant k and the axial dispersion coefficient D. When we made the earlier estimates of fluorinator performance,[20] only limited data were available for the axial dispersion coefficient; these data resulted from studies with air and water in 1.5-, 2-, and 3-in.-ID columns. At that time it was assumed that the axial dispersion coefficient was represented by the following relation:

$$D = 5.22\sqrt{G}, \quad (29)$$

where

D = axial dispersion coefficient, cm^2/sec,

G = gas flow rate at top of fluorinator, cm^3/sec.

The rate constant, k, was evaluated from experimental data obtained with a 1-in.-diam open-column, continuous fluorinator.[20] In correcting the data for the effect of axial dispersion, results obtained with the 1.5-in.-diam column were used and no correction was made for the differences in the physical properties of molten salt and water. Since that time, additional data on axial dispersion in open bubble columns have been

obtained in 1-, 1.5-, 2-, 3-, and 6-in.-diam columns using widely varying gas flow rates and aqueous solutions having a range of physical properties. One method for correlating the data yields the following relations: for low gas flow rates (bubble flow),

$$N_{Pe} = 18.0\, N_{Re}^{0.88}\, N_{Ar}^{-0.435}\, N_{Su}^{-0.075}\, n^{-0.0475} , \qquad (30)$$

and at high gas flow rates (slug flow),

$$N_{Pe} = 0.46\, N_{Re}^{0.4}\, N_{Ar}^{0.11}\, N_{Su}^{-0.38} , \qquad (31)$$

where

$N_{Pe} = \frac{dV}{D}$ = Peclet number,

$N_{Re} = \frac{\rho dV}{\mu}$ = Reynolds number,

$N_{Ar} = \frac{d^3 \rho^2 g}{\mu^2}$ = Archimedes number,

$N_{Su} = \frac{d\rho\sigma}{\mu^2}$ = Suratman number,

d = column diameter,

V = superficial gas velocity,

ρ = density of liquid,

μ = viscosity of liquid,

σ = surface tension of liquid,

g = acceleration of gravity,

n = number of gas inlets in disperser.

The transition from bubble to slug flow occurs at the point represented by the following relation:

$$N_{Re} = 4.81 \times 10^{-4}\, N_{Ar}^{1.14}\, N_{Su}^{-0.635}\, n^{0.099} . \qquad (32)$$

These relations for the axial dispersion coefficient differ somewhat from those developed most recently (see Sect. 9); however, the axial dispersion coefficient values predicted by the two sets of relations are in good

agreement. It is not believed that the use of Eqs. (30)-(32) introduces significant error in the calculated performance data for continuous fluorinators given later in this section.

The reaction rate constant, k, was reevaluated from data from a 1-in.-diam continuous fluorinator operated at 525°C with an inlet uranium concentration of 0.35 mole $\%^{23}$ by using the mathematical model represented by Eqs. (25)-(27) and the data on axial dispersion represented by Eqs. (30)-(32). The results, summarized in Table 4, show no trend with salt or fluorine flow rate; that is, the values for k are seen to be reasonably constant.

Table 4. Summary of Data for Evaluation of Fluorination Reaction Rate Constant from Data Obtained at 525°C in a 1-in.-diam Continuous Fluorinator

Salt Superficial Velocity (cm/sec)	$\frac{C(L)}{C_{feed}}$	F_2 Flow Rate (cm^3/sec)	D (cm^2/sec)	k (sec^{-1})
0.0625	0.0257	6.8	17.6	0.00805
0.0445	0.0096	5.0	14.6	0.01033
0.0225	0.00457	3.82	10.6	0.00886
			Avg	0.00908

The performance of large open-column, continuous fluorinators (6, 8, 10, and 12 in. in diameter) was estimated from Eq. (28) using the previously discussed estimate of k and the correlations for predicting the axial dispersion coefficient, D. The required fluorinator heights are shown in Figs. 17-20 for fractional uranium removal values of 0.9, 0.95, 0.99, and 0.999. The uranium concentration in the inlet salt was assumed to be 0.0033 mole fraction in each case, and the fluorine flow rate was assumed to be 150% of the stoichiometric requirement. These results are encouraging since they suggest that single fluorination vessels of moderate size will suffice for removing uranium from MSBR fuel salt prior to the

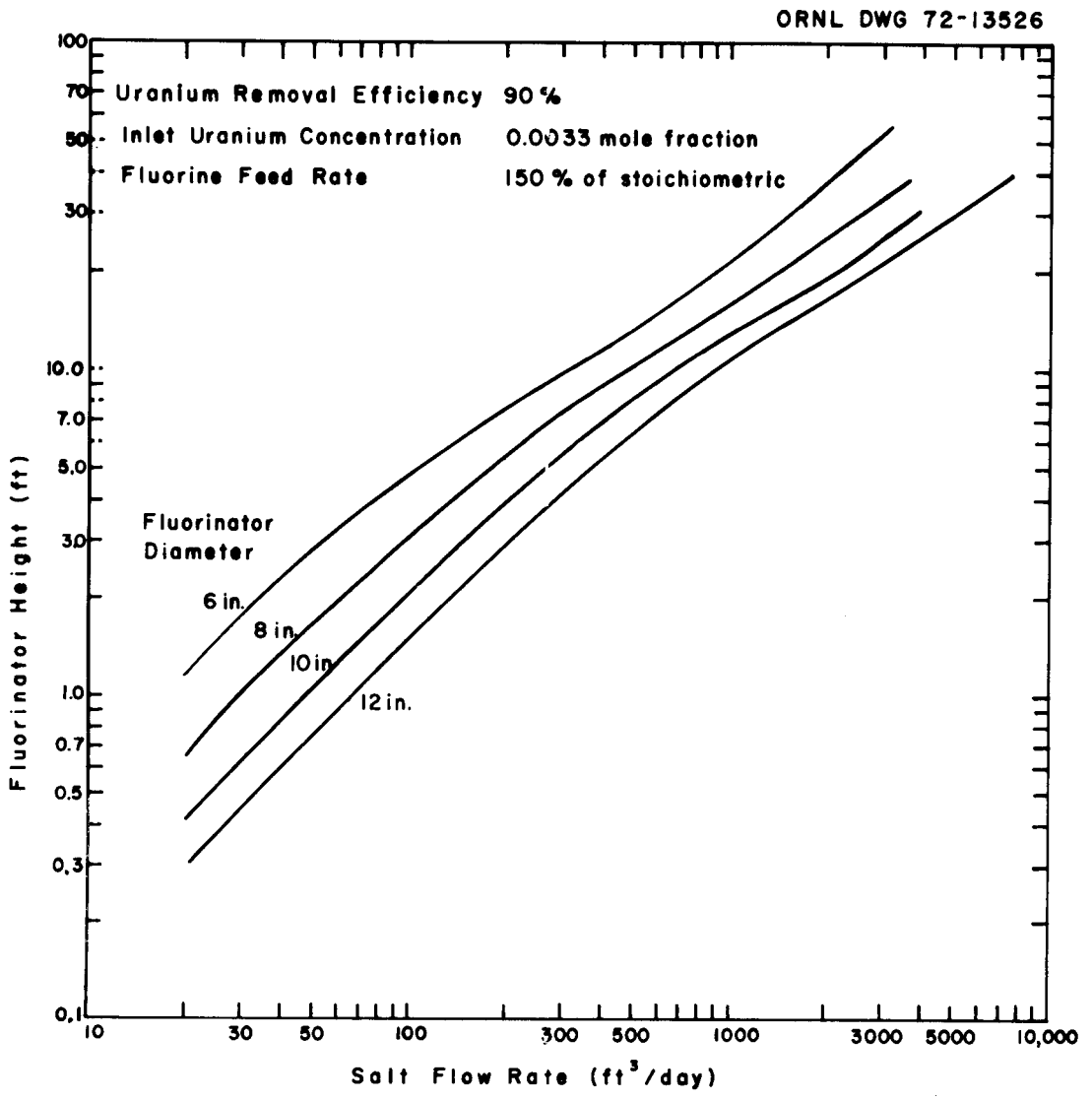

Fig. 17. Variation of Calculated Fluorinator Height with Salt Flow Rate and Fluorinator Diameter for a Uranium Removal Efficiency of 90%.

ORNL DWG 71-10788

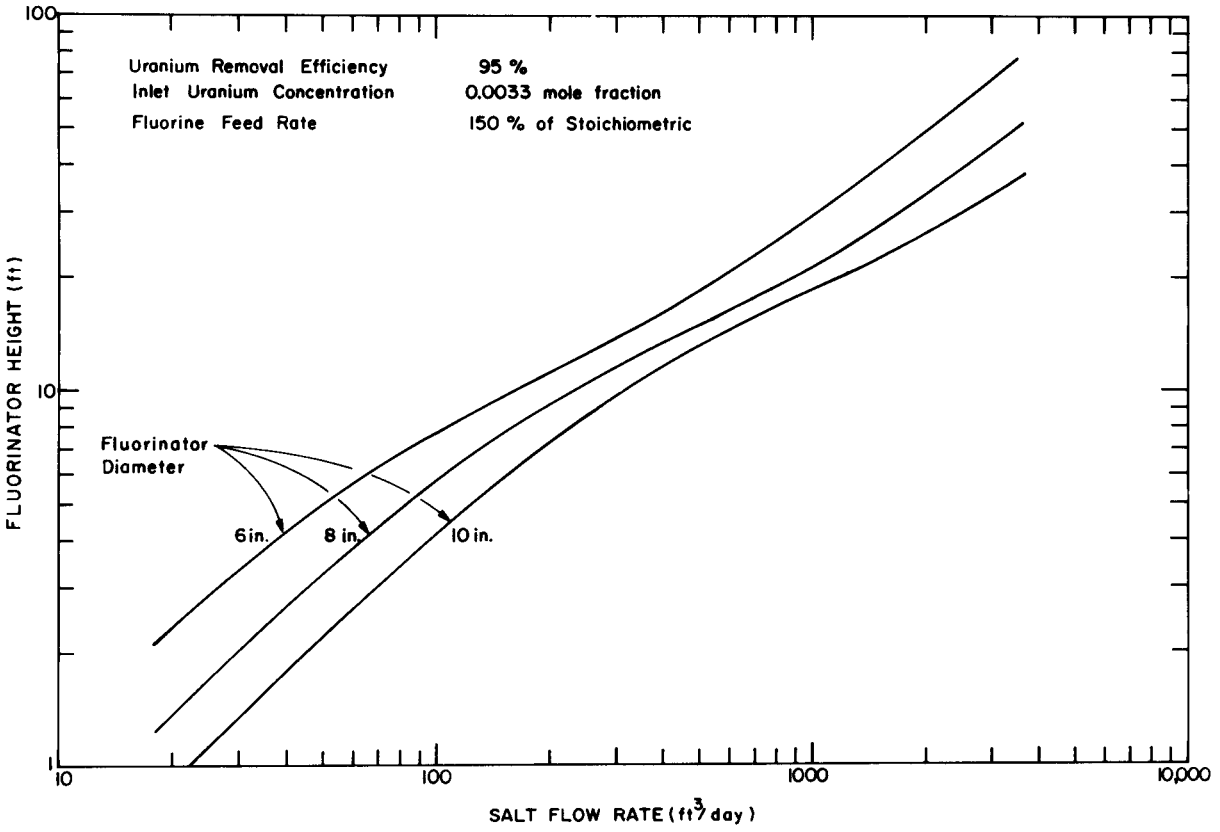

Fig. 18. Variation of Calculated Fluorinator Height with Salt Flow Rate and Fluorinator Diameter for a Uranium Removal Efficiency of 95%.

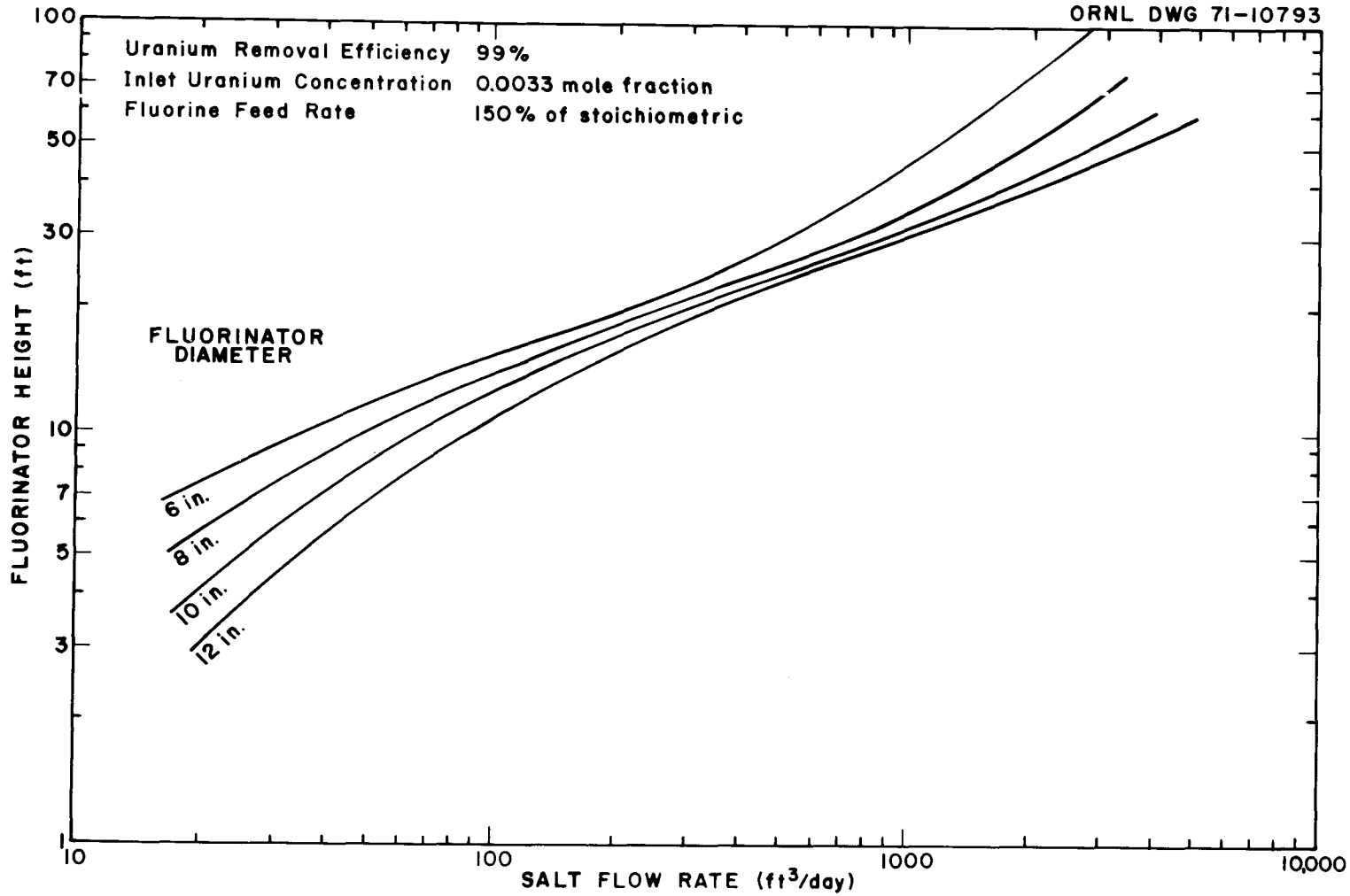

Fig. 19. Variation of Calculated Fluorinator Height with Salt Flow Rate and Fluorinator Diameter for a Uranium Removal Efficiency of 99%.

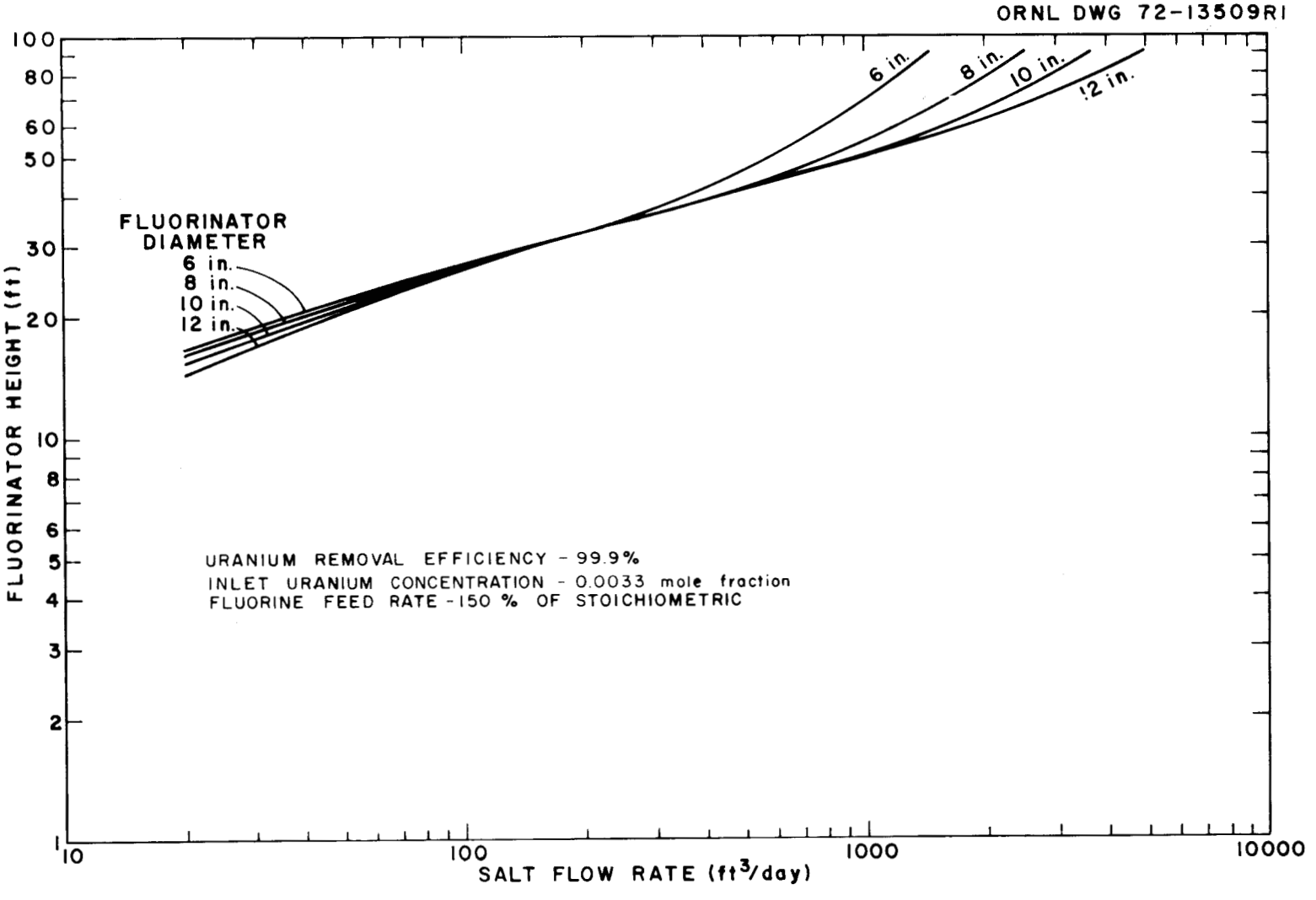

Fig. 20. Variation of Calculated Fluorinator Height with Salt Flow Rate and Fluorinator Diameter for a Uranium Removal Efficiency of 99.9%.

isolation of protactinium by reductive extraction. The reference flow-sheet for isolating protactinium by fluorination--reductive extraction[24] requires fluorination of fuel salt at the rate of 170 ft^3/day, which is equivalent to a 10-day processing cycle. A 6-in.-diam fluorination having a height of 10.2 ft will be required for a uranium removal efficiency of 95%; an 8-in.-diam fluorinator having a height of 17.8 ft will be required for a uranium removal efficiency of 99%.

Fluorinators having a high uranium removal efficiency are required in the production of high-purity ^{233}U because incomplete removal of uranium from a salt stream containing ^{233}Pa would result in contamination of the ^{233}U with other uranium isotopes. Therefore, fluorination of salt streams having flow rates of 550 to 1700 ft^3/day with uranium removal efficiencies as high as 99.9% may be required. As shown in Fig. 20, a column diameter of 10 in. and heights of 42.5 to 60 ft would be required if a single, open-column, continuous fluorinator were used. In this case, the fluorinator would be divided into several open-column fluorinators operating in series. If two columns were used, the required heights of each column would be less than half the height required for a single column since there would be no axial dispersion across the fluorinator inlets and outlets. The required uranium removal efficiency for each column would be 96.8%; and, as shown in Fig. 21, column heights of 17 to 28.3 ft would be required for a 10-in.-diam fluorinator. The use of three columns, each with a 90% uranium removal efficiency, would reduce the total column height even further. Column heights of 7.8 to 17.2 ft would be required for a 10-in.-diam fluorinator in this case.

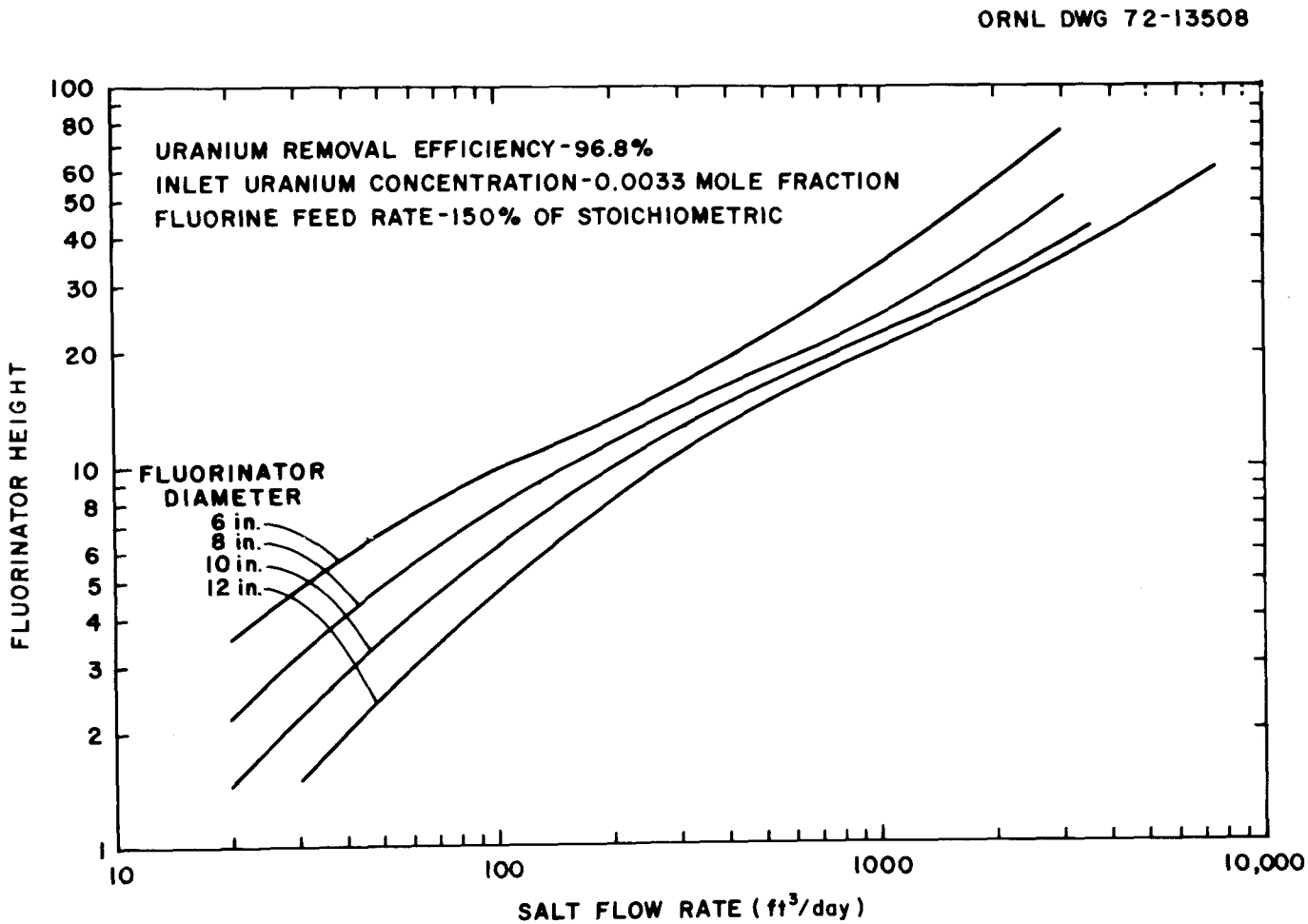

Fig. 21. Variation of Calculated Fluorinator Height with Salt Flow Rate and Fluorinator Diameter for a Uranium Removal Efficiency of 96.8%.

9. MEASUREMENT OF AXIAL DISPERSION COEFFICIENTS AND GAS HOLDUP IN OPEN BUBBLE COLUMNS

J. S. Watson L. E. McNeese

Axial dispersion is important in the design and performance of continuous fluorinators to be used in processing MSBR fuel salt. Since molten salt saturated with fluorine is corrosive, the fluorinators will be simple, open vessels having a protective layer of frozen salt on all exposed metal surfaces. In such systems the rising gas bubbles may cause appreciable axial dispersion throughout the salt. For the past few years, we have been involved in a program for measuring axial dispersion resulting from the flow of air through liquids in open bubble columns. The objectives of this program are to evaluate the effect of axial dispersion on fluorinator performance and to account for this effect in the design of fluorinators.

9.1 Previous Studies on Axial Dispersion

Initial studies on axial dispersion in open bubble columns were carried out by Bautista and McNeese,[25] who studied axial dispersion during the countercurrent flow of air and water in a 2-in.-ID, 72-in.-long column. Two regions of operation were observed. The first of these consisted of a "bubble flow" region at low gas flow rates in which the air moved up the column as individual bubbles and coalescence was minimal. The second consisted of a "slug flow" region at higher gas flow rates in which the air coalesced rapidly into bubbles having diameters equal to the column diameter. A plot of the logarithm of the dispersion coefficient vs the logarithm of the gas flow rate was linear in both regions. However, the slope of the line representing data in the slug flow region was higher than that for data in the bubble flow region. The transition between the two regions was well defined.

The same column and equipment were used by A. M. Sheikh and J. D. Dearth,[26] of the MIT Practice School, for investigating the effects of the viscosity and surface tension of the liquid. The dispersion coefficient was found to decrease in the bubble flow region as the viscosity

of the liquid was increased from 1 cP to 15 cP by the addition of glycerol to the water; little effect was noted in the slug flow region. An increase in the dispersion coefficient was observed as the surface tension of the liquid was decreased by the addition of n-butanol to the water.

The equipment was also used by A. A. Jeje and C. R. Bozzuto,[27] of the MIT Practice School, who investigated the effects of gas inlet diameter and column diameter on axial dispersion and obtained data on gas holdup in bubble columns. In the slug flow region, the dispersion coefficient appeared to be proportional to the square root of the volumetric gas flow rate, but was independent of column diameter. In the bubble flow region, the dispersion coefficient was dependent only on the volumetric gas flow rate in the case of columns having diameters of 2 in. or larger. Dispersion coefficient data obtained with a 1.5-in.-diam column deviated from this condition. At low gas flow rates, the gas holdup was linearly dependent on the superficial gas velocity but independent of column diameter. At superficial velocities above the transition from bubble to slug flow, the gas holdup data for the various column diameters diverged; the holdup was greatest for the smallest column diameter.

All of the dispersion coefficient data obtained by the above investigators resulted from measurements of the steady-state axial distribution of a cupric nitrate tracer that was continuously injected into the bottom of the column near the water exit. The studies indicated that the axial dispersion coefficient is independent of both axial position in the column and water superficial velocity in the range of interest. The steady-state experimental technique had two principal disadvantages: (1) the measurements were time-consuming since about 2 hr was required for the column to attain steady state; and (2) at high gas flow rates, air was entrained with water withdrawn from the column for determination of the tracer concentration, and the resulting error in the dispersion coefficient data was unacceptably high. In order to circumvent these problems, Bautista[28] developed a transient technique for obtaining data on axial dispersion. In this

technique there was no net flow of water through the column; however, data obtained with the steady-state technique indicated that the water flow rate did not affect the axial dispersion coefficient at the water flow rates of interest. A small amount of electrolyte tracer (KCl) was quickly injected into the top of the column and the concentration of the tracer was measured continuously at a point near the bottom of the column by use of a conductivity probe. The resulting data were in agreement with earlier data obtained with the steady-state technique; on the other hand, data obtained with the transient technique showed minimal scatter even at high gas flow rates and could be obtained in less than 10% of the time required for the steady-state technique. During this report period, additional studies were carried out using the transient technique in order to determine the effects of changes in column diameter, gas inlet design, and physical properties of the liquid phase on axial dispersion and gas holdup.

9.2 Equipment and Experimental Procedure

The equipment and experimental procedure used in the present studies have been described previously.[28] The equipment consisted of an open bubble column, a means for injecting KCl tracer solution at the top of the column, a conductivity probe located at an intermediate axial point along the column for determining the KCl concentration in the aqueous solution at the point, an electronics system and a recorder for recording the output from the conductivity probe, an air supply and metering system for feeding air at a known flow rate to a gas disperser located in the base of the column, and a manometer for obtaining data on gas holdup in the column. Eight-foot-long Plexiglas columns with inside diameters of 1.0, 1.5, 2, 3, and 6 in. were used. Gas distributor plates having different numbers and sizes of orifice openings were installed at the bottom of the column in order to determine the effect of gas inlet design on axial dispersion and gas holdup. The air flow rate was measured at the top of the column. A soap bubble buret was employed for flow rates below 15 cm^3/sec; a wet-test meter was used for higher flow rates. The solutions used in the study consisted of demineralized water or mixtures of demineralized water and glycerin or

n-butanol. The aqueous solutions were prepared in a tank and pumped to the column. Demineralized water could be introduced at the top of the column to facilitate cleaning of the column between runs.

After the column had been filled with liquid having the desired physical properties, a sufficient volume of 2.4 N KCl tracer solution (5 to 15 cm^3, depending on column size) was added to the liquid in the column in order to obtain a recordable reading from the conductivity probe. The air flow rate was then adjusted to the desired value, and a second volume of tracer was quickly injected at the top of the column. Subsequently, the response of the conductivity probe was recorded until the tracer was uniformly dispersed throughout the column. The height of the gas-liquid mixture in the column and the height of the liquid with no gas flow were measured. Samples of the liquid were then taken for surface tension and viscosity measurements. The viscosity of the liquid was determined with a Ubbelohde viscometer, while surface tension measurements were made using the capillary rise method. Visual observations of the gas and liquid in the column were made during the course of the experiments.

9.3 Experimental Data on Axial Dispersion

Experimental data on axial dispersion in open bubble columns were obtained during this report period in a series of four separate studies. The first study, made by a group of students at the University of Tennessee, was carried out with a 1-in.-ID, 8-ft-long column. The gas disperser at the bottom of the column consisted of a single inlet having an inside diameter of 4.3 mm. The studies were carried out with demineralized water, and the superficial gas velocity was varied from 0.156 to 76.6 cm/sec. The data obtained during this study are summarized in Table 5. The axial dispersion coefficient values obtained in the 1-in.-diam column fall below the values obtained previously at the same superficial gas velocity in columns having diameters of 1.5 and 2 in.

The second study was carried out by J. C. Bronfenbrenner, L. J. Marquez, and J. F. Mayer, of the MIT Practice School, who determined the effects on axial dispersion caused by changes in column diameter,

Table 5. Summary of Data on Axial Dispersion Obtained in a 1.0-in.-ID Open Bubble Column Containing Demineralized Water at 25°C

Tracer injection volume: ~ 5 cm^3

Relative probe position[a]: 0.825

Gas inlet: one orifice, 4.3 mm in diameter

Run No.	Gas Flow Rate[b] (cm/sec)	Superficial Gas Velocity (cm/sec)	Dispersion Coefficient (cm^2/sec)
1	94.6	18.7	82.3
2	387.9	76.6	319.0
3	387.9	76.6	261.8
4	331.1	65.4	255.2
5	378.4	74.7	182.3
6	283.8	56.0	319.0
7	189.2	37.3	170.2
8	94.6	18.7	63.8
9	141.9	28.0	170.2
10	236.5	46.1	232.0
11	52.0	10.3	52.0
12	94.6	18.7	92.8
13	146.6	28.9	128.3
14	118.2	23.3	102.6
15	70.9	14.0	61.1
16	165.6	32.7	146.6
17	189.2	37.3	213.8
18	236.5	46.7	185.5
19	321.7	63.5	285.1
20	227.0	44.8	181.1
21	5.91	1.166	20.8
22	5.51	1.088	18.3
23	5.12	1.011	17.1
24	4.73	0.933	22.5
25	4.33	0.855	17.1
26	3.94	0.778	15.5
27	3.55	0.700	14.1
28	0.79	0.156	5.84
29	6.33	1.25	14.8
30	5.17	1.02	24.6
31	3.95	0.78	19.7
32	2.37	0.468	14.8
33	0.79	0.156	7.04
34	6.74	1.33	22.4
35	5.12	1.01	17.8
36	3.56	0.702	14.5
37	1.98	0.390	10.7
38	0.79	0.156	6.42

[a] Ratio of distance of probe from surface of gas-liquid mixture to total height of gas-liquid mixture.

[b] Measured under conditions at top of column.

viscosity of the liquid phase, and superficial gas velocity. The columns used in this study consisted of 1.5-, 2-, and 6-in.-ID Lucite tubes, each having a length of 8 ft. A conductivity cell was inserted in the columns at a height of 70.5 cm from the bottom of the column. The liquid in the column consisted of mixtures of distilled water and glycerin in which the glycerin concentrations were 0, 25, and 65 wt %. The physical properties of these solutions are summarized in Table 6. Air entered the column through a single orifice at the bottom of the column; the orifice ID was 0.04 in. for the two smaller columns and 0.4 in. for the 6-in.-diam column. The superficial gas velocity was varied from 0.26 to 40 cm/sec in the smaller columns and 0.27 to 9.5 cm/sec in the 6-in.-diam column. Data on axial dispersion obtained during the second study are summarized in Tables 7-9. The results obtained with water in a 1.5-in.-diam column are in good agreement with those obtained previously;[28] the axial dispersion coefficient shows little change as the viscosity of the liquid is increased from 0.9 cP to 1.8 cP. Similarly, there is little difference in the axial dispersion coefficient values obtained in a 2-in.-diam column with a liquid having a viscosity of 0.9 cP and those obtained with a liquid having a viscosity of 1.8 cP. Dispersion coefficient values obtained with a liquid having a viscosity of 12.1 cP are about 50 to 70% of those obtained with liquids having viscosities of 0.9 and 1.8 cP. Essentially no difference was observed in the axial dispersion coefficient values obtained in a 6-in.-diam column for liquids having viscosities of 0.9, 1.8, and 12.1 cP.

Table 6. Physical Properties of Water-Glycerin Solutions Used During Second Study of Axial Dispersion and Gas Holdup in Bubble Columns

Glycerin Concentration (wt %)	Viscosity (cP)	Density (g/cm^3)	Surface Tension (dynes/cm)
0	0.89	0.997	73
25	1.8	1.05	72
65	12.1	1.16	67.9

Table 7. Summary of Data on Axial Dispersion Obtained in a 1.5-in.-ID Column During Second Study

Relative probe position[a]: 0.69

Gas inlet: one orifice, 1.0 mm in diameter

Run No.	Gas Flow Rate[b] (cm^3/sec)	Superficial Gas Velocity (cm/sec)	Glycerin Conc. (wt %)	Axial Dispersion Coefficient (cm^2/sec)
1	187.0	16.4	0	138.5
2	97.8	8.58	0	85.6
3	140.2	12.3	0	114.8
4	112.8	9.89	0	93.4
5	19.6	1.72	0	31.6
6	403.6	35.4	0	482.2
7	7.87	0.69	0	20.8
8	403.6	35.4	0	380.5
9	34.1	2.99	0	39.0
10	58.2	5.11	0	65.0
11	10.4	0.912	0	24.8
12	255.4	22.4	0	177.0
13	118.6	10.4	0	149.0
14	191.5	16.8	0	136.0
15	155.0	13.6	0	95.2
16	118.6	10.4	25	88.9
17	18.9	1.66	25	24.9
18	372.8	32.7	25	813.9
19	566.6	49.7	25	655.9
20	372.8	32.7	25	155.1
21	46.3	4.06	25	44.6
22	118.6	10.4	25	88.9
23	249.7	21.9	25	115.3
24	149.4	13.1	25	131.4
25	118.6	10.4	25	56.2
26	75.5	6.62	25	62.2

[a] Ratio of distance of probe from surface of gas-liquid mixture to total height of gas-liquid mixture.

[b] Measured under conditions at top of column.

Table 8. Summary of Data on Axial Dispersion Obtained in a 2.0-in.-ID Column During Second Study

Relative probe position[a]: 0.69
Gas inlet: one orifice, 1.0 mm in diameter

Run No.	Gas Flow Rate (cm^3/sec)	Superficial Gas Velocity (cm/sec)	Glycerin Conc. (wt %)	Axial Dispersion Coefficient (cm^2/sec)
1	81.1	4.0	0	51.0
2	411.4	20.3	0	206.0
3	482.4	23.8	0	172.7
4	291.9	14.4	0	144.9
5	11.4	0.56	0	22.3
6	78.6	3.88	0	58.7
7	120.8	5.96	0	67.5
8	117.2	5.78	25	72.2
9	177.3	8.75	25	97.8
10	210.8	10.4	25	119.7
11	377.0	18.6	25	178.3
12	553.3	27.3	25	427.0
13	56.5	2.79	25	45.3
14	81.3	4.01	25	52.1
15	10.7	0.53	25	26.5
16	8.31	0.41	25	26.5
17	15.2	0.75	25	31.2
18	24.5	1.21	25	34.5
19	44.8	2.21	25	48.2
20	18.4	0.91	65	27.6
21	9.93	0.49	65	21.4
22	6.28	0.31	65	18.9
23	25.1	1.24	65	27.8
24	47.6	2.35	65	34.1
25	60.8	3.0	65	37.2
26	83.3	4.11	65	44.4
27	116.9	5.77	65	51.0
28	184.4	9.1	65	75.3
29	208.8	10.3	65	79.2
30	326.3	16.1	65	105.3
31	504.7	24.9	65	144.2
32	758.0	37.4	65	213.6

[a]Ratio of distance of probe from surface of gas-liquid mixture to total height of gas-liquid mixture.

[b]Measured under conditions at top of column.

Table 9. Summary of Data on Axial Dispersion Obtained in a 6.0-in.-ID Column During Second Study

Relative probe position[a]: 0.69
Gas inlet: one orifice, 10 mm in diameter

Run No.	Gas Flow Rate (cm^3/sec)	Superficial Gas Velocity (cm/sec)	Glycerin Conc. (wt %)	Axial Dispersion Coefficient (cm^2/sec)
1	1530	8.39	0	207.0
2	561.8	3.08	0	178.8
3	145.9	0.8	0	152.1
4	94.8	0.52	0	156.6
5	94.8	0.52	0	160.7
6	271.8	1.49	0	183.2
7	394.0	2.16	0	161.3
8	1299	7.12	0	370.8
9	113.1	0.62	0	173.4
10	698.6	3.83	0	156.9
11	195.2	1.07	0	123.1
12	60.2	0.33	0	146.0
13	286.4	1.57	0	146.2
14	1665	9.13	0	280.6
15	899.3	4.93	0	245.8
16	479.8	2.63	0	141.0
17	1372	7.52	25	231.5
18	1757	9.63	25	265.9
19	1757	9.63	25	303.0
20	474.3	2.6	25	169.5
21	923.0	5.06	25	262.0
22	1572	8.62	25	229.3
23	58.4	0.32	25	124.7
24	372.1	2.04	25	187.7
25	217.1	1.19	25	180.5
26	543.6	2.98	25	184.0
27	707.8	3.88	25	210.8
28	543.6	2.98	25	181.1
29	1094	6.0	25	215.9
30	220.7	1.21	65	152.8
31	295.5	1.62	65	148.6
32	49.2	0.27	65	161.8
33	727.8	3.99	65	181.1
34	521.7	2.86	65	179.6
35	361.2	1.98	65	145.6
36	1096	6.01	65	215.6

Table 9. (continued)

Relative probe position[a]: 0.69
Gas inlet: one orifice, 10 mm in diameter

Run No.	Gas Flow Rate (cm^3/sec)	Superficial Gas Velocity (cm/sec)	Glycerin Conc. (wt %)	Axial Dispersion Coefficient (cm^2/sec)
37	1532	8.4	65	254.2
38	93.0	0.51	65	157.2
39	136.8	0.75	65	172.6

[a]Ratio of distance of probe from surface of gas-liquid mixture to total height of gas-liquid mixture.

[b]Measured under conditions at top of column.

The third study carried out during this period was made by A. K. Padia, G. T. Marion, and R. H. McCue, of the MIT Practice School, who studied the effects of changes in the number and size of gas inlet orifices, column diameter, superficial air velocity, and viscosity and surface tension of the liquid phase on the axial dispersion coefficient and gas holdup. The ranges of the independent parameters that were varied in this study are summarized in Table 10. Column diameters of 1.5, 2, and 3 in. were used with both single and multiple orifices ranging in size from 0.4 to 6.4 mm. The viscosity of the liquid phase was varied from 0.9 to 11.3 cP, and the surface tension of the liquid was varied from 27 to 70 dynes/cm. The superficial gas velocity was varied from 0.0318 to 20 cm/sec in 12 to 17 increments for each value of column diameter, gas distributor design, and property of the liquid phase. Data obtained during the third study are summarized in Tables

Table 10. Ranges of Parameters During Third Study of Axial Dispersion in Open Bubble Columns

Parameter	Values Used
Column Diameter, in.	1.5, 2, 3
Number of Orifices in Gas Inlet	1, 5, 19, 37
Gas Inlet Orifice Diameter, mm	0.4, 1, 2, 4, 6.4
Surface Tension of Liquid, dynes/cm	27, 45, 70
Viscosity of Liquid, cP	0.9, 2.05, 10.7, 11.3
Superficial Gas Velocity, cm/sec	0.0318 to 20

11-19. The variation of the axial dispersion coefficient with changes in the superficial gas velocity and orifice diameter for a 2-in.-ID column for which the gas distributor consisted of five orifices is in general agreement with that obtained previously for a 2-in.-diam column operated with a single gas inlet. The variation in the dispersion coefficient in the slug flow region with changes in the diameter of the gas inlet orifices is not believed to be significant. However, the differences observed in the bubble flow region are probably meaningful. Data of the same type, obtained with a gas disperser consisting of 37 orifices, show even less deviation from previous values obtained with a single gas inlet. For a column diameter of 2 in. and gas distributor orifice diameters of 1 mm, only slight differences in the dispersion coefficient are noted in the slug flow region; however, in the bubble flow region, a progressive increase in axial dispersion coefficient is observed as the number of orifices is increased. The variation of the axial dispersion coefficient with changes in the viscosity of the liquid phase and the superficial gas velocity for column diameters of 1.5 and

Table 11. Summary of Data on Axial Dispersion Obtained in a 1.5-in.-ID Column Containing Water During Third Study

Tracer injection volume: ~ 5 cm^3

Relative probe position[a]: 0.79

Gas inlet: one orifice, 1 mm ID

Run No.	Gas Flow Rate[b] (cm^3/sec)	Superficial Gas Velocity (cm/sec)	Axial Dispersion Coefficient (cm^2/sec)
1	11.9	1.045	25.8
2	2.42	0.212	12.9
3	5.14	0.451	18.9
4	8.20	0.719	24.4
5	15.2	1.33	32.9
6	19.2	1.68	31.6
7	25.2	2.21	39.5
8	44.0	3.86	50.0
9	74.6	6.54	69.4
10	101.8	8.93	85.9
11	242.8	21.3	242.0

[a]Ratio of distance of probe from surface of gas-liquid mixture to total height of gas-liquid mixture.

[b]Measured under conditions at top of column.

Table 12. Summary of Data on Axial Dispersion in a 1.5-in.-ID Column Containing Aqueous Isopropanol During Third Study

Tracer injection volume: ~ 5 cm^3

Relative probe position[a]: 0.79

Surface tension of liquid: 45.3 dynes/cm

Gas inlet: one orifice, 0.638 cm ID

Run No.	Gas Flow Rate[b] (cm^3/sec)	Superficial Gas Velocity (cm/sec)	Axial Dispersion Coefficient (cm^2/sec)
1	11.9	1.045	20.9
2	8.09	0.710	23.3
3	6.10	0.535	20.5
4	2.87	0.252	17.3
5	1.06	0.0930	14.6
6	16.6	1.456	23.1
7	17.7	1.55	26.7
8	29.4	2.58	33.7
9	49.1	4.31	40.6
10	66.0	5.79	50.0
11	84.9	7.45	58.0

[a]Ratio of distance of probe from surface of gas-liquid mixture to total height of gas-liquid mixture.

[b]Measured under conditions at top of column.

Table 13. Summary of Data on Axial Dispersion in a 1.5-in.-ID Column Containing Aqueous Isobutanol During Third Study

Tracer injection volume: ~ 5 cm^3

Relative probe position[a]: 0.79

Surface tension of liquid: 27.3 dynes/cm

Gas inlet: one orifice, 0.638 cm ID

Run No.	Gas Flow Rate[b] (cm^3/sec)	Superficial Gas Velocity (cm/sec)	Axial Dispersion Coefficient (cm^2/sec)
1	11.6	1.02	21.9
2	1.52	0.133	15.0
3	0.804	0.0705	11.9
4	2.44	0.214	15.8
5	5.63	0.494	20.6
6	8.70	0.763	22.2
7	15.6	1.37	22.3
8	23.6	2.07	27.9
9	40.6	3.56	36.2
10	73.0	6.4	51.5
11	98.0	8.6	65.7

[a]Ratio of distance of probe from surface of gas-liquid mixture to total height of gas-liquid mixture.

[b]Measured under conditions at top of column.

Table 14. Summary of Data on Axial Dispersion Obtained in a 1.5-in.-ID Column Containing a Water-Glycerin Mixture During Third Study

Tracer injection volume: ~ 5 cm^3

Relative probe position[a]: 0.79

Gas inlet: one orifice, 0.638 cm ID

Run No.	Gas Flow Rate[b] (cm^3/sec)	Superficial Gas Velocity (cm/sec)	Glycerin Conc. (wt %)	Axial Dispersion Coefficient (cm^2/sec)
1	0.727	0.0638	25	7.65
2	2.13	0.187	25	12.5
3	3.80	0.333	25	24.6
4	6.02	0.528	25	26.4
5	10.2	0.895	25	28.4
6	14.2	1.25	25	36.4
7	18.5	1.625	25	36.4
8	29.8	2.61	25	43.5
9	65.9	5.78	25	60.6
10	92.0	8.07	25	81.0
11	2.44	0.214	65	10.6
12	1.01	0.0888	65	7.45
13	3.57	0.313	65	12.3
14	5.13	0.45	65	15.2
15	7.42	0.651	65	21.3
16	11.4	1.0	65	21.8
17	15.7	1.38	65	27.3
18	19.8	1.74	65	27.7
19	33.1	2.9	65	34.7
20	66.0	5.79	65	55.6

[a]Ratio of distance of probe from surface of gas-liquid mixture to total height of gas-liquid mixture.

[b]Measured under conditions at top of column.

Table 15. Summary of Data on Axial Dispersion Obtained in a 2.0-in.-ID Column Containing Water During Third Study

Tracer injection volume: ~ 5 cm^3

Relative probe position[a]: 0.79

Gas inlet: one orifice, 1 mm ID

Run No.	Gas Flow Rate[b] (cm^3/sec)	Superficial Gas Velocity (cm/sec)	Axial Dispersion Coefficient (cm^2/sec)
1	0.896	0.0442	19.6
2	0.255	0.0126	28.1
3	4.24	0.209	28.9
4	5.98	0.295	31.1
5	8.21	0.405	37.6
6	10.4	0.515	40.5
7	12.5	0.618	43.4
8	16.2	0.798	45.5
9	19.2	0.95	48.2
10	30.8	1.52	52.7
11	59.2	2.92	60.8
12	92.8	4.58	72.6
13	145.9	7.2	81.5

[a]Ratio of distance of probe from surface of gas-liquid mixture to total height of gas-liquid mixture.

[b]Measured under conditions at top of column.

Table 16. Summary of Data on Axial Dispersion Obtained in a 4-in.-ID Column Containing Water During Third Study

Number of orifices: 5
Tracer injection volume: ~5 cm^3
Relative probe position[a]: Runs 1-12 – 0.767
Runs 13-68 – 0.790

Run No.	Gas Flow Rate[b] (cm^3/sec)	Superficial Gas Velocity (cm/sec)	Gas Inlet Orifice ID (mm)	Axial Dispersion Coefficient (cm^2/sec)	Run No.	Gas Flow Rate[b] (cm^3/sec)	Superficial Gas Velocity (cm/sec)	Gas Inlet Orifice ID (mm)	Axial Dispersion Coefficient (cm^2/sec)
1	7.80	0.385	0.4	40.6	35	4.76	0.235	2.0	35.8
2	0.926	0.0457	0.4	15.4	36	10.2	0.503	2.0	30.0
3	2.50	0.1235	0.4	16.4	37	20.3	1.0	2.0	44.0
4	4.90	0.242	0.4	22.8	38	5.13	0.253	4.0	27.1
5	10.9	0.537	0.4	33.1	39	10.3	0.509	4.0	41.2
6	15.2	0.749	0.4	35.4	40	31.2	1.54	4.0	41.8
7	19.4	0.96	0.4	36.5	41	84.5	4.17	4.0	65.5
8	34.4	1.7	0.4	41.5	42	1.90	0.0938	4.0	30.8
9	65.3	3.22	0.4	57.8	43	10.4	0.512	4.0	38.3
10	97.1	4.79	0.4	60.8	44	45.8	2.26	4.0	54.0
11	141.9	7.00	0.4	72.6	45	111.5	5.5	4.0	69.5
12	171.5	8.46	0.4	83.6	46	450	22.2	4.0	326.0
13	13.9	0.688	1.0	37.2	47	282	13.9	4.0	129.0
14	1.55	0.0767	1.0	31.7	48	19.7	0.97	4.0	33.7
15	3.20	0.158	1.0	31.5	49	2.45	0.121	4.0	26.4
16	5.27	0.26	1.0	44.8	50	26.3	1.3	4.0	41.8
17	7.03	0.347	1.0	47.0	51	14.6	0.72	4.0	36.8
18	9.30	0.459	1.0	37.9	52	7.56	0.373	4.0	32.5
19	11.9	0.589	1.0	35.5	53	1.54	0.076	4.0	25.5
20	18.6	0.92	1.0	39.0	54	1.04	0.0512	2.0	20.8
21	30.8	1.52	1.0	55.1	55	2.53	0.125	2.0	41.0
22	59.8	2.95	1.0	57.5	56	4.09	0.202	2.0	45.6
23	86.5	4.27	1.0	63.5	57	6.16	0.304	2.0	37.0
24	113.3	5.59	1.0	92.4	58	8.21	0.405	2.0	36.5
25	147.8	7.29	1.0	111.1	59	10.6	0.525	2.0	49.2
26	280	13.8	1.0	137.0	60	13.2	0.65	2.0	57.0
27	88.2	4.35	2.0	71.6	61	15.4	0.76	2.0	62.7
28	5.37	0.265	2.0	35.8	62	18.7	0.923	2.0	52.2
29	16.2	0.80	2.0	23.8	63	30.9	1.525	2.0	46.8
30	50.7	2.5	2.0	57.4	64	63.8	3.15	2.0	59.5
31	185.4	9.15	2.0	139.0	65	89.2	4.4	2.0	69.5
32	438	21.6	2.0	200.0	66	117.8	5.81	2.0	75.2
33	2.23	0.11	2.0	29.8	67	144.5	7.13	2.0	96.5
34	4.01	0.198	2.0	30.5	68	330	16.3	2.0	87.2

[a]Ratio of distance of probe from surface of gas-liquid mixture to total height of gas-liquid mixture.

[b]Measured under conditions at top of column.

Table 17. Summary of Data on Axial Dispersion Obtained in a 2.0-in.-ID Column Containing Water During Third Study

Gas inlet: 19 orifices, 1 mm ID

Tracer injection volume: ~ 5 cm^3

Relative probe position[a]: 0.808

Run No.	Gas Flow Rate[b] (cm^3/sec)	Superficial Gas Velocity (cm/sec)	Axial Dispersion Coefficient (cm^2/sec)
1	1.02	0.0505	26.4
2	2.31	0.114	36.7
3	4.22	0.208	38.5
4	6.10	0.301	39.7
5	8.19	0.404	40.1
6	10.8	0.535	44.5
7	12.8	0.632	46.5
8	14.7	0.726	47.0
9	18.6	0.919	44.9
10	30.0	1.48	42.8
11	61.2	3.02	54.4
12	85.9	4.24	62.5
13	115.7	5.71	80.4
14	149.6	7.38	124.0
15	280.0	13.8	155.0

[a]Ratio of distance of probe from surface of gas-liquid mixture to total height of gas-liquid mixture.

[b]Measured under conditions at top of column.

Table 18. Summary of Data on Axial Dispersion Obtained in a 2.0-in.-ID Column Containing Water During Third Study

Gas inlet: 37 orifices

Tracer injection volume: ~ 5 cm^3

Relative probe position[a]: 0.738

Run No.	Gas Flow Rate[b] (cm^3/sec)	Superficial Gas Velocity (cm/sec)	Gas Inlet Orifice ID (mm)	Axial Dispersion Coefficient (cm^2/sec)
1	1.06	0.0525	1.0	27.3
2	2.41	0.119	1.0	33.3
3	3.46	0.171	1.0	40.4
4	5.86	0.289	1.0	37.8
5	7.96	0.393	1.0	33.7
6	10.7	0.529	1.0	34.2
7	13.9	0.687	1.0	45.0
8	15.8	0.78	1.0	48.0
9	19.2	0.945	1.0	48.0
10	30.8	1.52	1.0	44.4
11	60.2	2.97	1.0	58.2
12	88.4	4.36	1.0	121.0
13	113.5	5.6	1.0	95.0
14	149.0	7.35	1.0	101.0
15	259	12.8	1.0	136.0
16	503	24.8	1.0	214.0
17	746	36.8	1.0	228.0
18	2.27	0.112	2.0	36.7
19	7.62	0.376	2.0	34.7
20	13.6	0.67	2.0	39.3
21	1.42	0.0703	2.0	20.5
22	5.31	0.262	2.0	35.5
23	9.69	0.478	2.0	33.2
24	17.7	0.875	2.0	38.0
25	27.8	1.37	2.0	49.5
26	44.8	2.21	2.0	61.0
27	101	5.0	2.0	91.8
28	72.6	3.58	2.0	80.8
29	3.69	0.182	2.0	33.9
30	148	7.28	2.0	100.0
31	590	29.12	2.0	269.0
32	14.9	0.737	4.0	33.4
33	1.25	0.0618	4.0	28.2
34	3.00	0.148	4.0	33.1
35	5.09	0.251	4.0	31.9
36	6.71	0.331	4.0	30.0
37	8.17	0.403	4.0	33.7
38	11.8	0.585	4.0	32.4
39	20.5	1.01	4.0	51.3
40	30.2	1.49	4.0	50.0
41	53.9	2.66	4.0	59.7
42	73.4	3.62	4.0	61.0
43	94.4	4.66	4.0	72.2
44	118	5.8	4.0	79.5
45	150	7.43	4.0	77.5
46	537	26.5	4.0	164.0

[a]Ratio of distance of probe from surface of gas-liquid mixture to total height of gas-liquid mixture.

[b]Measured under conditions at top of column.

Table 19. Summary of Data on Axial Dispersion Obtained in a 3.0-in.-ID Column Containing a Water-Glycerin Mixture During Third Study

Gas Inlet: one orifice, 0.638 cm ID

Tracer injection volume: Runs 1-14, ~ 4.5 cm^3
Runs 15-27, ~ 1.5 cm^3

Relative probe position[a]: 0.79

Run No.	Gas Flow Rate[b] (cm^3/sec)	Superficial Gas Velocity (cm/sec)	Glycerin Concentration (wt %)	Axial Dispersion Coefficient (cm^2/sec)
1	36.9	0.81	25	50.0
2	1.60	0.0352	25	28.1
3	3.50	0.0768	25	43.2
4	5.56	0.122	25	38.2
5	8.94	0.196	25	48.9
6	13.0	0.285	25	51.8
7	19.4	0.425	25	45.0
8	25.2	0.553	25	48.7
9	46.7	1.025	25	46.2
10	84.8	1.86	25	64.0
11	130.0	2.85	25	66.4
12	258	5.66	25	89.1
13	377	8.26	25	92.2
14	1.47	0.0323	25	30.2
15	1.45	0.0318	65	27.0
16	3.51	0.0769	65	29.1
17	4.92	0.108	65	42.4
18	7.07	0.155	65	56.0
19	10.6	0.232	65	41.4
20	15.4	0.338	65	47.4
21	19.3	0.424	65	45.0
22	30.8	0.675	65	52.8
23	76.2	1.67	65	47.4
24	57.0	1.25	65	56.3
25	104	2.28	65	57.2
26	135	2.96	65	64.3
27	245	5.37	65	86.7

[a]Ratio of distance of probe from surface of gas-liquid mixture to total height of gas-liquid mixture.

[b]Measured under conditions at top of column.

3 in. shows that axial dispersion coefficient values obtained with the 3-in. column are higher than those obtained with the 1.5-in. column at a given superficial gas velocity, particularly in the case of bubble flow. In general, there is a progressive decrease in the value of the axial dispersion coefficient as the viscosity of the liquid is increased. The axial dispersion coefficient is observed to decrease as the surface tension is decreased in a 1.5-in.-diam column.

The final study carried out during this report period was made to determine the effect of using a side gas inlet, which consisted of a 1-in.-ID tube attached to the side of the column at an angle of 45° with respect to the column axis. This type of gas inlet is envisioned for use in continuous fluorinators having frozen-wall corrosion protection as a means for also protecting the inlet gas nozzle from corrosion.[29] Demineralized water was used during the study, which was carried out with a 3-in.-ID column. Data on axial dispersion obtained during this study are summarized in Table 20. Comparison of the data with other data on axial dispersion in a 3-in.-diam column for which the gas distributor consisted of a single, 0.432-cm-diam orifice shows very little difference between the two sets of data.

9.4 Experimental Data on Gas Holdup

Experimental data on gas holdup in open bubble columns were obtained during this report period in the first, second, and third studies. The ranges of operating parameters used during these two studies are summarized in Table 21. Column diameters of 1.0, 1.5, 2, 3, and 6 in. were used with gas inlet dispersers that consisted of both single and multiple orifices having diameters that ranged from 0.4 to 6.4 mm. The viscosity of the liquid phase was varied from 0.9 to 12.1 cP, and the surface tension of the liquid was varied from 27 to 73 dynes/cm. The superficial gas velocity was varied from 0.013 to 50 cm/sec. Data obtained during the studies are summarized in Tables 22-34.

Table 20. Summary of Data on Axial Dispersion Obtained in a 3-in.-ID Column Having a 1-in.-ID Side Inlet Joined to the Column at an Angle of 45° with Respect to the Column Axis

Tracer injection volume: ~ 5 cm^3

Relative probe position[a]: 0.79

Run No.	Gas Flow Rate[b] (cm^3/sec)	Superficial Gas Velocity (cm/sec)	Dispersion Coefficient (cm^2/sec)
1	852.8	18.7	111.9
2	706.8	15.5	159.2
3	579.2	12.7	137.2
4	483.4	10.6	132.6
5	367.6	8.06	114.9
6	277.7	6.09	91.1
7	118.8	4.14	67.3
8	98.0	2.15	74.3
9	192.0	4.21	70.7
10	162.3	3.56	74.4
11	141.8	3.11	65.0
12	124.0	2.72	68.4
13	94.4	2.07	53.7
14	89.4	1.96	58.0
15	72.0	1.58	49.0
16	67.9	1.49	59.1
17	40.4	0.887	56.8
18	20.0	0.438	47.3
19	26.2	0.574	67.8
20	18.0	0.395	37.6
21	13.5	0.296	39.9
22	9.62	0.211	47.1
23	5.88	0.129	31.8
24	2.79	0.0612	28.1
25	97.1	2.13	60.7
26	141.8	3.11	65.3
27	91.2	2.00	54.9
28	21.9	0.481	42.0
29	218.9	4.80	71.8
30	5.65	0.124	29.5

[a]Ratio of distance of probe from surface of gas-liquid mixture to total height of gas-liquid mixture.

[b]Measured under conditions at top of column.

Table 21. Ranges of Parameters During Studies of Gas Holdup in Open Bubble Columns

Parameter	Values Used
Column Diameter, in.	1.0, 1.5, 2, 3, 6
Number of Orifices in Gas Inlet	1, 5, 19, 37
Gas Inlet Orifice Diameter, mm	0.4, 1, 2, 4, 6.4
Surface Tension of Liquid, dynes/cm	27, 45, 70, 73
Viscosity of Liquid, cP	0.9, 1.8, 2.05, 10.7, 11.3, 12.1
Gas Superficial Velocity, cm/sec	0.013 to 49.7

9.5 Correlation of Data on Gas Holdup

The data on gas holdup obtained in the second and third studies of this report period and in studies by Bautista[28] were correlated by the method of least squares. These data, a total of 349 holdup determinations, cover column diameters from 1.5 to 6 in. and include a range of values for the superficial gas velocity and physical properties of the liquid. The results obtained for the 1-in.-diam column in the first study were not used in developing the correlation since these values are believed to be of a lower quality than the remaining ones. It was found that gas holdup could be represented by the relation

$$h = \frac{V_g}{1.468\, V_g + 0.4071\sqrt{g d_c}}, \qquad (33)$$

where

h = fraction of column volume occupied by gas,

V_g = superficial gas velocity, cm/sec,

g = acceleration of gravity, cm/sec^2,

d_c = column diameter, cm.

Table 22. Summary of Data on Gas Holdup Obtained in a 1.0-in.-ID Open Bubble Column Containing Demineralized Water at 25°C

Gas inlet: one orifice, 4.3 mm in diameter

Run No.	Gas Flow Rate[a] (cm^3/sec)	Superficial Gas Velocity (cm/sec)	Gas Holdup	Bubble Rise Velocity (cm/sec)
1	94.6	18.7	0.492	38.0
2	387.9	76.6	0.719	106.5
3	387.9	76.6	0.719	106.5
4	331.1	65.4	0.707	92.5
5	378.4	74.7	0.719	103.9
6	283.8	56.0	0.713	78.5
7	189.2	37.3	0.641	58.2
8	94.6	18.7	0.513	36.5
9	141.9	28.0	0.6	46.7
10	236.5	46.1	0.686	67.2
11	52.0	10.3	0.309	33.3
12	94.6	18.7	0.450	41.6
13	146.6	28.9	0.529	54.6
14	118.2	23.3	0.492	47.4
15	70.9	14.0	0.372	37.6
16	165.6	32.7	0.568	57.6
17	189.2	37.3	0.575	64.9
18	236.5	46.7	0.587	79.6
19	321.7	63.5	0.642	98.9
20	227.0	44.8	0.584	76.7
21	5.91	1.166	0.0658	17.7
22	5.51	1.088	0.0598	18.2
23	5.12	1.011	0.0523	19.3
24	4.73	0.933	0.0516	18.1
25	4.33	0.855	0.0486	17.6
26	3.94	0.778	0.0412	18.9
27	3.55	0.700	0.0387	18.1
28	0.79	0.156	0.0098	15.9
29	6.33	1.25	0.0645	19.4
30	5.17	1.02	0.0387	26.4
31	3.95	0.78	0.0451	17.3
32	2.37	0.468	0.0254	18.4
33	0.79	0.156	0.00645	24.2
34	6.74	1.33	0.068	19.6
35	5.12	1.01	0.056	18.0
36	3.56	0.702	0.045	15.6
37	1.98	0.390	0.023	17.0
38	0.79	0.156	0.015	10.4

[a]Measured under conditions at top of column.

Table 23. Summary of Data on Gas Holdup Obtained in a 1.5-in.-ID Column During Second Study

Run No.	Gas Flow Rate[a] (cm^3/sec)	Superficial Gas Velocity (cm/sec)	Glycerin Concentration (wt %)	Gas Holdup	Bubble Rise Velocity (cm/sec)
1	187.0	16.4	0	0.328	50.0
2	97.8	8.58	0	0.211	40.7
3	140.2	12.3	0	0.272	45.2
4	112.8	9.89	0	0.233	42.4
5	19.6	1.72	0	0.052	33.1
6	403.6	35.4	0	0.516	68.6
7	7.87	0.69	0	0.022	31.4
8	403.6	35.4	0	0.523	67.7
9	34.1	2.99	0	0.09	33.2
10	58.2	5.11	0	0.14	36.5
11	10.4	0.912	0	0.03	30.4
12	255.4	22.4	0	0.394	56.9
13	118.6	10.4	0	0.242	43.0
14	191.5	16.8	0	0.333	50.5
15	155.0	13.6	0	0.291	46.7
16	118.6	10.4	25	0.307	33.9
17	18.9	1.66	25	0.056	29.6
18	372.8	32.7	25	0.598	54.7
19	566.6	49.7	25	0.675	73.6
20	372.8	32.7	25	0.598	54.7
21	46.3	4.06	25	0.149	27.2
22	118.6	10.4	25	0.307	33.9
23	249.7	21.9	25	0.514	42.6
24	149.4	13.1	25	0.281	46.6
25	118.6	10.4	25	0.262	39.7
26	75.5	6.62	25	0.161	41.1

[a]Measured under conditions at top of column.

Table 24. Summary of Data on Gas Holdup Obtained in a 2.0-in.-ID Column During Second Study

Run No.	Gas Flow Rate[a] (cm^3/sec)	Superficial Gas Velocity (cm/sec)	Glycerin Conc. (wt %)	Gas Holdup	Bubble Rise Velocity (cm/sec)
1	81.1	4.0	0	0.108	37.0
2	411.4	20.3	0	0.359	56.5
3	482.4	23.8	0	0.378	63.0
4	291.9	14.4	0	0.239	60.3
5	11.4	0.56	0	0.012	46.7
6	78.6	3.88	0	0.098	39.6
7	120.8	5.96	0	0.136	43.8
8	117.2	5.78	25	0.159	36.4
9	177.3	8.75	25	0.207	42.3
10	210.8	10.4	25	0.233	44.6
11	377.0	18.6	25	0.35	53.1
12	553.3	27.3	25	0.466	58.6
13	56.5	2.79	25	0.075	37.2
14	81.3	4.01	25	0.106	37.8
15	10.7	0.53	25	0.009	58.9
16	8.31	0.41	25	0.009	45.6
17	15.2	0.75	25	0.02	37.5
18	24.5	1.21	25	0.035	34.6
19	44.8	2.21	25	0.063	35.1
20	18.4	0.91	65	0.021	43.3
21	9.93	0.49	65	0.012	40.8
22	6.28	0.31	65	0.009	34.4
23	25.1	1.24	65	0.035	35.4
24	47.6	2.35	65	0.054	43.5
25	60.8	3.0	65	0.073	41.1
26	83.3	4.11	65	0.095	43.3
27	116.9	5.77	65	0.124	46.5
28	184.4	9.1	65	0.18	50.6
29	208.8	10.3	65	0.199	51.8
30	326.3	16.1	65	0.254	63.4
31	504.7	24.9	65	0.325	76.6
32	758.0	37.4	65	0.4	93.5

[a]Measured under conditions at top of column.

Table 25. Summary of Data on Gas Holdup Obtained in a 6.0-in.-ID Column During Second Study

Run No.	Gas Flow Rate[a] (cm^3/sec)	Superficial Gas Velocity (cm/sec)	Glycerin Concentration (wt %)	Gas Holdup	Bubble Rise Velocity (cm/sec)
1	1530	8.39	0	0.146	57.5
2	561.8	3.08	0	0.071	43.4
3	145.9	0.8	0	0.021	38.1
4	94.8	0.52	0	0.016	32.5
5	94.8	0.52	0	0.016	32.5
6	271.8	1.49	0	0.036	41.4
7	394.0	2.16	0	0.054	40.0
8	1299	7.12	0	0.128	55.6
9	113.1	0.62	0	0.016	38.8
10	698.6	3.83	0	0.081	47.3
11	195.2	1.07	0	0.028	38.2
12	60.2	0.33	0	0.009	36.7
13	286.4	1.57	0	0.034	46.2
14	1665	9.13	0	0.156	58.5
15	899.3	4.93	0	0.089	55.4
16	479.8	2.63	25	0.056	47.0
17	1372	7.52	25	0.16	47.0
18	1757	9.63	25	0.217	44.4
19	1757	9.63	25	0.217	44.4
20	474.3	2.6	25	0.076	34.2
21	923.0	5.06	25	0.126	40.2
22	1572	8.62	25	0.196	44.0
23	58.4	0.32	25	0.008	40.0
24	372.1	2.04	25	0.06	34.0
25	217.1	1.19	25	0.032	37.2
26	543.6	2.98	25	0.074	40.3
27	707.8	3.88	25	0.09	43.1
28	543.6	2.98	25	0.074	40.3
29	1094	6.0	25	0.118	50.8
30	220.7	1.21	65	0.028	43.2
31	295.5	1.62	65	0.038	42.6
32	727.8	3.99	65	0.081	49.3
33	521.7	2.86	65	0.066	43.3
34	361.2	1.98	65	0.052	38.1
35	1096	6.01	65	0.105	57.2
36	1532	8.4	65	0.13	64.6
37	93.0	0.51	65	0.013	39.2
38	136.8	0.75	65	0.017	44.1

[a]Measured under conditions at top of column.

Table 26. Summary of Data on Gas Holdup Obtained in a 1.5-in.-ID Column Containing Water During Third Study

Gas inlet: one orifice, 1 mm ID

Run No.	Gas Flow Rate[a] (cm^3/sec)	Superficial Gas Velocity (cm/sec)	Gas Holdup	Bubble Rise Velocity (cm/sec)
1	2.42	0.212	0.00862	24.6
2	8.20	0.719	0.0308	23.3
3	15.2	1.33	0.0424	31.4
4	19.2	1.68	0.0531	31.6
5	25.2	2.21	0.0675	32.7
6	44.0	3.86	0.121	31.9
7	74.6	6.54	0.183	35.7
8	101.8	8.93	0.250	35.7
9	242.8	21.3	0.427	49.9

[a]Measured under conditions at top of column.

Table 27. Summary of Data on Gas Holdup in a 1.5-in.-ID Column Containing Aqueous Isopropanol During Third Study

Surface tension of liquid: 45.3 dynes/cm

Gas inlet: one orifice, 0.638 cm ID

Run No.	Gas Flow Rate[a] (cm^3/sec)	Superficial Gas Velocity (cm/sec)	Gas Holdup	Bubble Rise Velocity (cm/sec)
1	11.9	1.045	0.0344	30.4
2	8.09	0.710	0.0247	28.7
3	6.10	0.535	0.019	28.2
4	2.87	0.252	0.00976	25.8
5	1.06	0.0930	0.00423	22.0
6	16.6	1.456	0.0487	29.9
7	17.7	1.55	0.0567	27.3
8	29.4	2.58	0.089	29.0
9	49.1	4.31	0.149	28.9
10	66.0	5.79	0.183	31.6
11	84.9	7.45	0.167	44.6

[a]Measured under conditions at top of column.

Table 28. Summary of Data on Gas Holdup in a 1.5-in.-ID Column Containing Aqueous Isobutanol During Third Study

Surface tension of liquid: 27.3 dynes/cm

Gas inlet: one orifice, 0.638 cm ID

Run No.	Gas Flow Rate[a] (cm^3/sec)	Superficial Gas Velocity (cm/sec)	Gas Holdup	Bubble Rise Velocity (cm/sec)
1	11.6	1.02	0.0328	31.1
2	1.52	0.133	0.00463	28.7
3	0.804	0.0705	0.00278	25.4
4	2.44	0.214	0.0088	24.3
5	5.63	0.494	0.0174	28.4
6	8.70	0.763	0.0276	27.6
7	15.6	1.37	0.052	26.3
8	23.6	2.07	0.081	25.6
9	40.6	3.56	0.141	25.2
10	73.0	6.4	0.247	25.9
11	98.0	8.6	0.38	22.6

[a]Measured under conditions at top of column.

Table 29. Summary of Data on Gas Holdup Obtained in a 1.5-in.-ID Column Containing a Water-Glycerin Mixture During Third Study

Gas inlet: one orifice, 0.638 cm ID

Run No.	Gas Flow Rate[a] (cm^3/sec)	Superficial Gas Velocity (cm/sec)	Glycerin Conc. (wt %)	Gas Holdup	Bubble Rise Velocity (cm/sec)
1	2.13	0.187	25	0.00793	23.6
2	3.80	0.333	25	0.0126	26.4
3	6.02	0.528	25	0.0194	27.2
4	10.2	0.895	25	0.0298	30.0
5	14.2	1.25	25	0.0387	32.3
6	18.5	1.625	25	0.052	31.3
7	29.8	2.61	25	0.0732	35.7
8	65.9	5.78	25	0.171	33.8
9	92.0	8.07	25	0.204	39.6
10	3.57	0.313	65	0.0101	31.0
11	5.13	0.45	65	0.016	28.1
12	7.42	0.651	65	0.0216	30.1
13	11.4	1.0	65	0.0335	29.9
14	15.7	1.38	65	0.0435	31.7
15	19.8	1.74	65	0.0554	31.4
16	33.1	2.9	65	0.0925	31.4
17	66.0	5.79	65	0.227	25.5

[a]Measured under conditions at top of column.

Table 30. Summary of Data on Gas Holdup Obtained in a 2.0-in.-ID Column Containing Water During Third Study

Gas inlet: one orifice, 1 mm ID

Run No.	Gas Flow Rate[a] (cm^3/sec)	Superficial Gas Velocity (cm/sec)	Gas Holdup	Bubble Rise Velocity (cm/sec)
1	0.896	0.0442	0.00225	19.6
2	2.55	0.126	0.0045	28.0
3	4.24	0.209	0.00625	33.4
4	5.98	0.295	0.00936	31.5
5	8.21	0.405	0.012	33.8
6	10.4	0.515	0.0146	35.3
7	12.5	0.618	0.0186	33.2
8	16.2	0.798	0.0216	36.9
9	19.2	0.95	0.0252	37.7
10	30.8	1.52	0.0437	34.8
11	59.2	2.92	0.07	41.7
12	92.8	4.58	0.107	42.8
13	145.9	7.2	0.152	47.4

[a]Measured under conditions at top of column.

Table 31. Summary of Data on Gas Holdup Obtained in a 2-in.-ID Column Containing Water During Third Study

Number of orifices: 5

Run No.	Gas Flow Rate[a] (cm^3/sec)	Superficial Gas Velocity (cm/sec)	Gas Inlet Orifice ID (mm)	Gas Holdup	Bubble Rise Velocity (cm/sec)	Run No.	Gas Flow Rate[a] (cm^3/sec)	Superficial Gas Velocity (cm/sec)	Gas Inlet Orifice ID (mm)	Gas Holdup	Bubble Rise Velocity (cm/sec)
1	7.80	0.389	0.4	0.0142	27.1	35	4.76	0.235	2.0	0.0129	18.2
2	0.926	0.0457	0.4	0.00283	16.1	36	10.2	0.503	2.0	0.0237	21.2
3	2.50	0.1235	0.4	0.00473	26.1	37	20.3	1.0	2.0	0.0302	33.1
4	4.90	0.242	0.4	0.00988	24.5	38	5.13	0.253	4.0	0.0075	33.7
5	10.9	0.537	0.4	0.0186	28.9	39	10.3	0.509	4.0	0.0219	23.2
6	15.2	0.749	0.4	0.0276	27.1	40	31.2	1.54	4.0	0.0376	41.0
7	19.4	0.96	0.4	0.0344	27.9	41	84.5	4.17	4.0	0.098	42.6
8	34.4	1.7	0.4	0.0632	26.9	42	1.90	0.0938	4.0	0.00335	28.0
9	65.3	3.22	0.4	0.101	31.9	43	10.4	0.512	4.0	0.0159	32.2
10	97.1	4.79	0.4	0.127	37.7	44	45.8	2.26	4.0	0.0713	39.7
11	141.9	7.00	0.4	0.157	44.6	45	111.5	5.5	4.0	0.125	44.0
12	171.5	8.46	0.4	0.176	48.1	46	450	22.2	4.0	0.339	65.5
13	13.9	0.688	1.0	0.0205	33.6	47	282	13.9	4.0	0.247	56.3
14	1.55	0.0767	1.0	0.00264	29.1	48	19.7	0.97	4.0	0.0263	36.9
15	3.20	0.158	1.0	0.00485	32.6	49	2.45	0.121	4.0	0.00418	28.9
16	5.27	0.26	1.0	0.00615	42.3	50	26.3	1.3	4.0	0.0346	37.6
17	7.03	0.347	1.0	0.00835	41.6	51	14.6	0.72	4.0	0.0188	38.3
18	9.30	0.459	1.0	0.0114	40.3	52	7.56	0.373	4.0	0.0368	10.1
19	11.9	0.589	1.0	0.014	42.1	53	1.04	0.0512	2.0	0.00176	29.1
20	18.6	0.92	1.0	0.0253	36.4	54	2.53	0.125	2.0	0.0044	28.4
21	30.8	1.52	1.0	0.0405	37.5	55	4.09	0.202	2.0	0.0057	35.4
22	59.8	2.95	1.0	0.0738	40.0	56	6.16	0.304	2.0	0.0105	28.9
23	86.5	4.27	1.0	0.10	42.7	57	8.21	0.405	2.0	0.018	22.5
24	113.3	5.59	1.0	0.124	45.1	58	10.6	0.525	2.0	0.0219	24.0
25	147.8	7.29	1.0	0.127	57.4	59	13.2	0.65	2.0	0.0175	37.1
26	280	13.8	1.0	0.228	60.5	60	15.4	0.76	2.0	0.0145	52.4
27	88.5	4.35	2.0	0.107	40.7	61	18.7	0.923	2.0	0.0247	37.4
28	5.37	0.265	2.0	0.0113	23.5	62	30.9	1.525	2.0	0.0413	36.9
29	16.2	0.80	2.0	0.0343	23.3	63	63.8	3.15	2.0	0.0745	42.3
30	50.7	2.5	2.0	0.061	41.0	64	89.2	4.4	2.0	0.0982	44.8
31	185.4	9.15	2.0	0.18	50.8	65	117.8	5.81	2.0	0.127	45.7
32	438	21.6	2.0	0.329	65.7	66	144.5	7.13	2.0	0.155	46.0
33	2.23	0.11	2.0	0.0052	21.2	67	330	16.3	2.0	0.26	62.7
34	4.01	0.198	2.0	0.0082	24.1						

[a]Measured under conditions at top of column.

Table 32. Summary of Data on Gas Holdup Obtained in a 2.0-in.-ID Column During Third Study

Gas inlet: 19 orifices, 1 mm ID

Run No.	Gas Flow Rate[a] (cm^3/sec)	Superficial Gas Velocity (cm/sec)	Gas Holdup	Bubble Rise Velocity (cm/sec)
1	1.02	0.0505	0.00219	23.1
2	2.31	0.114	0.00392	29.1
3	4.22	0.208	0.0061	34.1
4	6.10	0.301	0.0087	34.6
5	8.19	0.404	0.0117	34.5
6	10.8	0.535	0.0156	34.3
7	12.8	0.632	0.0173	36.5
8	14.7	0.726	0.021	34.6
9	18.6	0.919	0.0253	36.3
10	30.0	1.48	0.0353	41.9
11	61.2	3.02	0.0748	40.4
12	85.9	4.24	0.11	38.5
13	115.7	5.71	0.133	42.9
14	149.6	7.38	0.158	46.7
15	280	13.8	0.249	55.4

[a]Measured under conditions at top of column.

Table 33. Summary of Data on Gas Holdup Obtained in a 2.0-in.-ID Column Containing Water During Third Study

Gas inlet: 37 orifices

Run No.	Gas Flow Rate[a] (cm^3/sec)	Superficial Gas Velocity (cm/sec)	Gas Inlet Orifice ID (mm)	Gas Holdup	Bubble Rise Velocity (cm/sec)
1	1.06	0.0525	1.0	0.00307	17.1
2	2.41	0.119	1.0	0.00438	27.2
3	3.46	0.171	1.0	0.00788	21.7
4	5.86	0.289	1.0	0.00918	31.5
5	7.96	0.393	1.0	0.0118	33.3
6	10.7	0.529	1.0	0.0144	36.7
7	13.9	0.687	1.0	0.0195	35.2
8	15.8	0.78	1.0	0.0282	27.7
9	19.2	0.945	1.0	0.0288	32.8
10	30.8	1.52	1.0	0.0474	32.1
11	60.2	2.97	1.0	0.0895	33.2
12	88.4	4.36	1.0	0.097	44.9
13	113.5	5.6	1.0	0.144	38.9
14	149.0	7.35	1.0	0.174	42.2
15	259	12.8	1.0	0.233	54.9
16	503	24.8	1.0	0.325	76.3
17	746	36.8	1.0	0.395	93.2
18	2.27	0.112	2.0	0.0039	28.7
19	7.62	0.376	2.0	0.0112	33.6
20	13.6	0.67	2.0	0.0185	36.2
21	1.42	0.0703	2.0	0.00175	40.2
22	5.31	0.262	2.0	0.00825	31.8
23	9.69	0.478	2.0	0.0148	32.3
24	17.7	0.875	2.0	0.024	36.5
25	27.8	1.37	2.0	0.0372	36.8
26	44.8	2.21	2.0	0.0592	37.3
27	101	5.0	2.0	0.12	41.7
28	72.6	3.58	2.0	0.0895	40.0
29	3.69	0.182	2.0	0.0065	28.0
30	148	7.28	2.0	0.16	45.5
31	590	29.12	2.0	0.385	75.6
32	14.9	0.737	4.0	0.0218	33.8
33	1.25	0.0618	4.0	0.0026	23.8
34	3.00	0.148	4.0	0.00488	30.3
35	5.09	0.251	4.0	0.00574	43.7
36	6.71	0.331	4.0	0.00795	41.6
37	8.17	0.403	4.0	0.015	26.9
38	11.8	0.585	4.0	0.0185	31.6
39	20.5	1.01	4.0	0.0282	35.8
40	30.2	1.49	4.0	0.0424	35.1
41	53.9	2.66	4.0	0.071	37.5
42	73.4	3.62	4.0	0.0876	41.3
43	94.4	4.66	4.0	0.109	42.8
44	118	5.8	4.0	0.131	44.3
45	150	7.43	4.0	0.155	47.9
46	537	26.5	4.0	0.34	77.9

[a]Measured under conditions at top of column.

Table 34. Summary of Data on Gas Holdup Obtained in a 3.0-in.-ID Column Containing a Water-Glycerin Mixture During Third Study

Gas inlet: one orifice, 0.638 cm ID

Run No.	Gas Flow Rate[a] (cm^3/sec)	Superficial Gas Velocity (cm/sec)	Glycerin Concentration (wt %)	Gas Holdup	Bubble Rise Velocity (cm/sec)
1	36.9	0.81	25	0.0252	32.1
2	1.60	0.0352	25	0.000928	37.9
3	3.50	0.0768	25	0.0045	17.1
4	5.56	0.122	25	0.004	30.5
5	8.94	0.196	25	0.0056	35.0
6	13.0	0.285	25	0.01	28.5
7	19.4	0.425	25	0.0107	39.7
8	25.2	0.553	25	0.0162	34.1
9	46.7	1.025	25	0.0295	34.7
10	84.8	1.86	25	0.0492	37.8
11	130.0	2.85	25	0.0765	37.3
12	258	5.66	25	0.113	50.1
13	377	8.26	25	0.171	48.3
14	1.47	0.0323	25	0.00141	22.9
15	3.51	0.0769	65	0.00188	40.9
16	4.92	0.108	65	0.00327	33.0
17	7.07	0.155	65	0.00468	33.1
18	10.6	0.232	65	0.00658	35.3
19	15.4	0.338	65	0.00889	38.0
20	19.3	0.424	65	0.0117	36.2
21	30.8	0.675	65	0.0199	33.9
22	76.2	1.67	65	0.043	38.8
23	57.0	1.25	65	0.0316	39.6
24	104	2.28	65	0.0628	36.3
25	135	2.96	65	0.0701	42.2
26	245	5.37	65	0.114	47.1

[a]Measured under conditions at top of column.

A comparison of the experimental data with values predicted by the correlation is shown in Fig. 22. Equation (33) predicts that gas holdup should be essentially proportional to superficial gas velocity at low gas flow rates and that the dependence should decrease as the gas flow rate is increased. A limiting value for gas holdup of about 0.68 is predicted.

The following expression for the bubble rise velocity, V_g/h, can be obtained from Eq. (33):

$$\frac{V_g}{h} = 1.468\, V_g + 0.4071\sqrt{gd_c} \quad . \qquad (34)$$

This relation predicts that the bubble rise velocity should be essentially constant at low gas flow rates and should depend on the square root of the column diameter. The bubble rise velocity should increase at a rate that is essentially proportional to the superficial gas velocity at high gas flow rates and should show little dependence on the column diameter. The physical properties of the liquid are of negligible importance in determining either gas holdup or bubble rise velocity.

Comparisons of the predicted and experimentally determined values for gas holdup and bubble rise velocity are shown in Figs. 23-40. The measured and the predicted values are seen to be in good agreement. Most of the predicted values lie within 15% of the measured values. Figures 23-32 show the variations of gas holdup and bubble rise velocity resulting from changes in the viscosity of the liquid phase and the superficial gas velocity for columns having diameters of 1.0, 1.5, 2, 3, and 6 in. In the bubble flow regime, the bubble rise velocity is essentially constant at about 25 to 40 cm/sec, and the gas holdup increases almost linearly as the superficial gas velocity is increased. Increases in the column diameter result in small increases in the bubble rise velocity and small decreases in the gas holdup. In the slug flow regime, the bubble rise velocity increases with increases in the superficial gas velocity and the gas holdup is not linearly dependent on the superficial gas velocity.

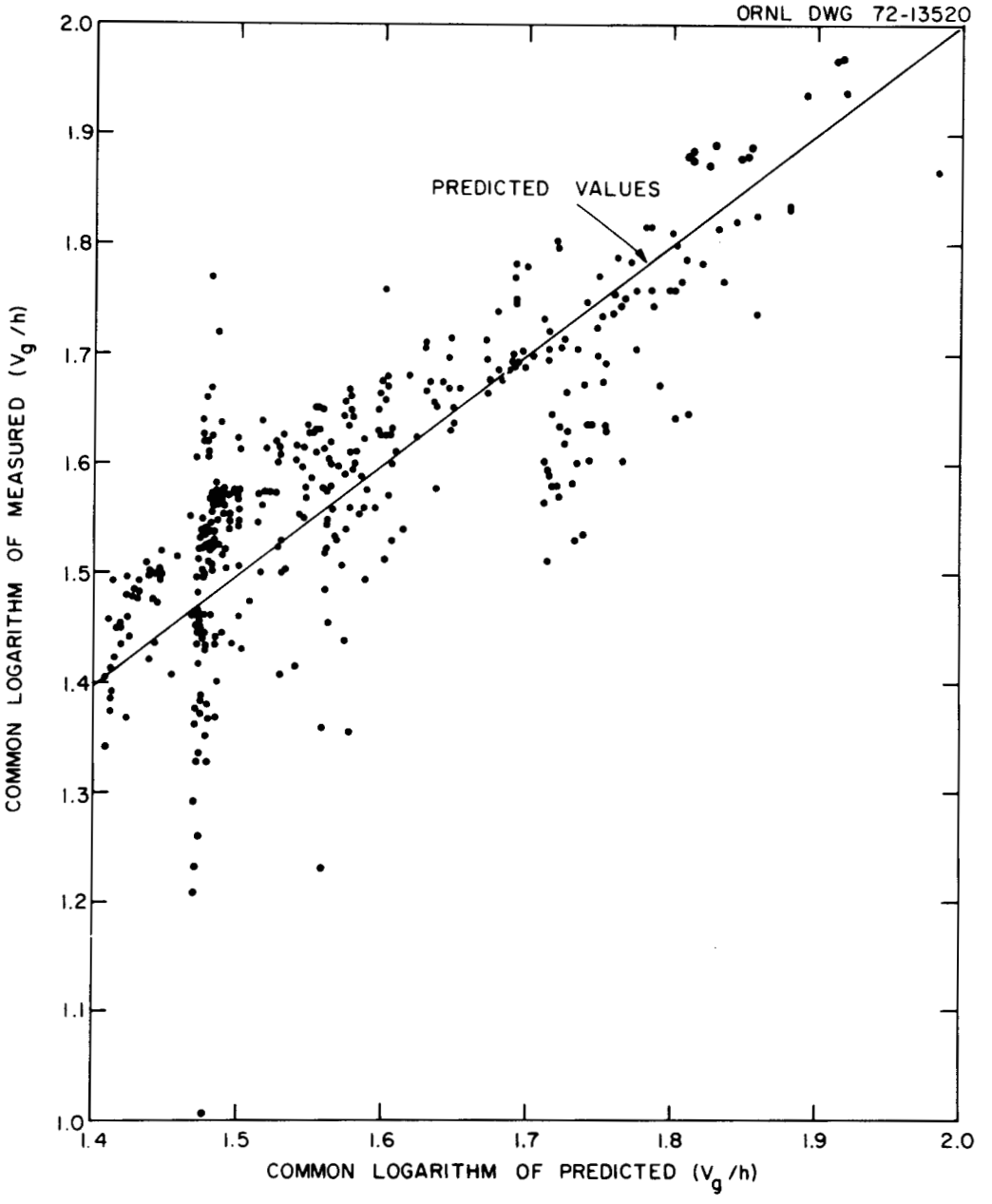

Fig. 22. Comparison of Experimentally-Determined and Calculated Data on Gas Holdup in Open Bubble Columns Having Diameters Ranging from 1.5 to 6 in.

ORNL DWG 72-11742

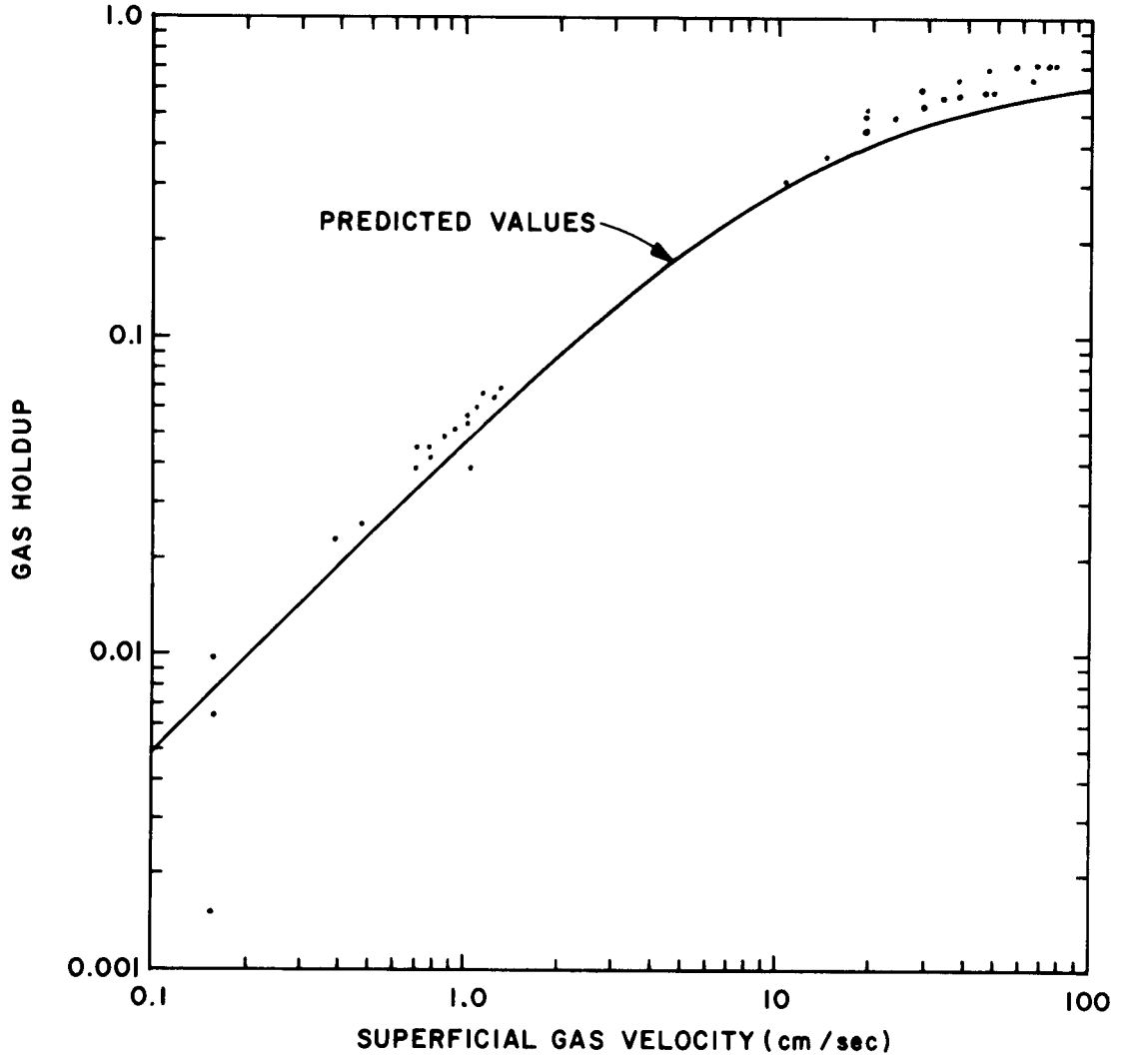

Fig. 23. Variation of Gas Holdup with Changes in Superficial Gas Velocity in a 1.0-in.-ID Bubble Column.

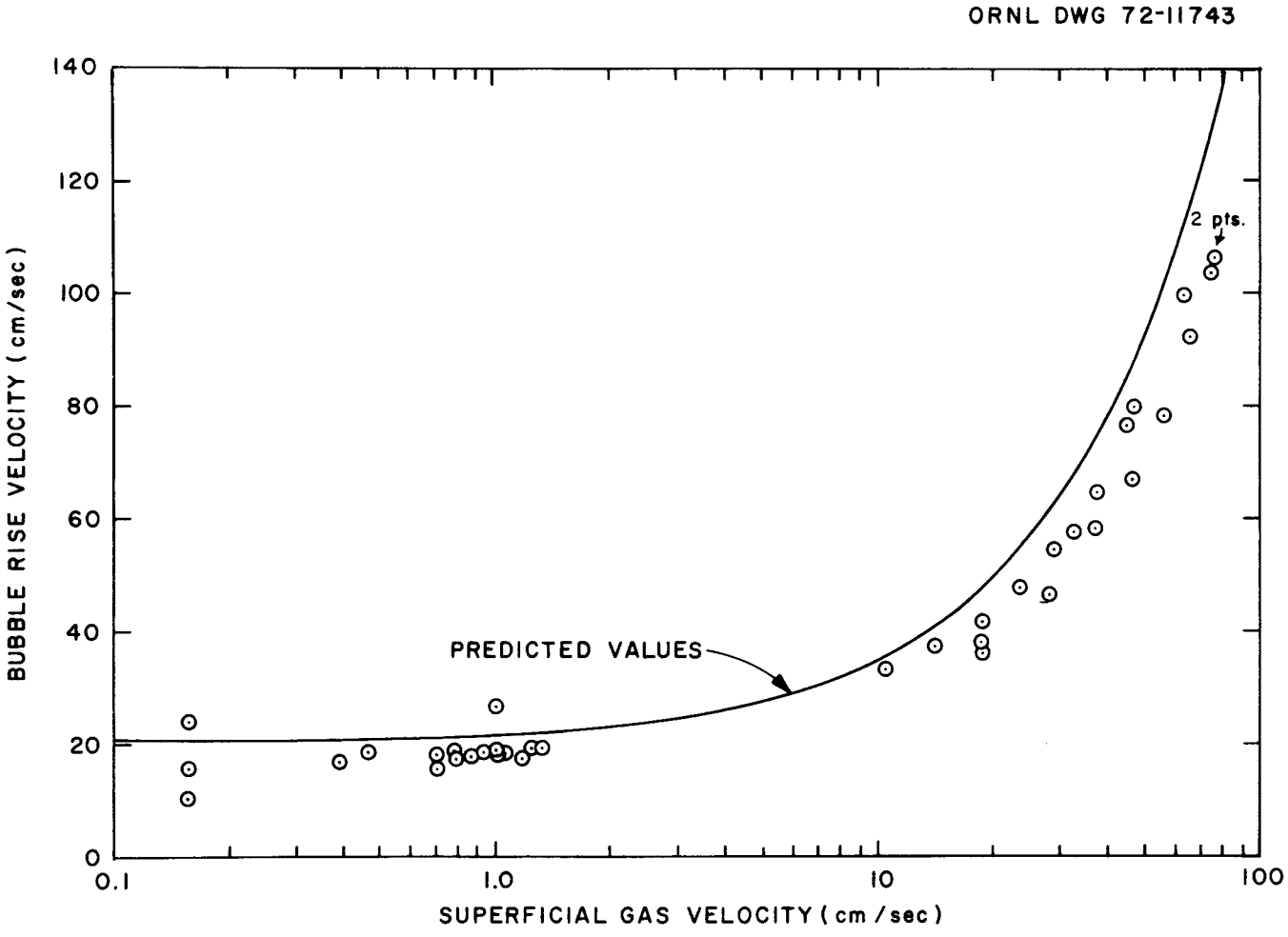

Fig. 24. Variation of Bubble Rise Velocity with Changes in Superficial Gas Velocity in a 1.0-in.-ID Bubble Column.

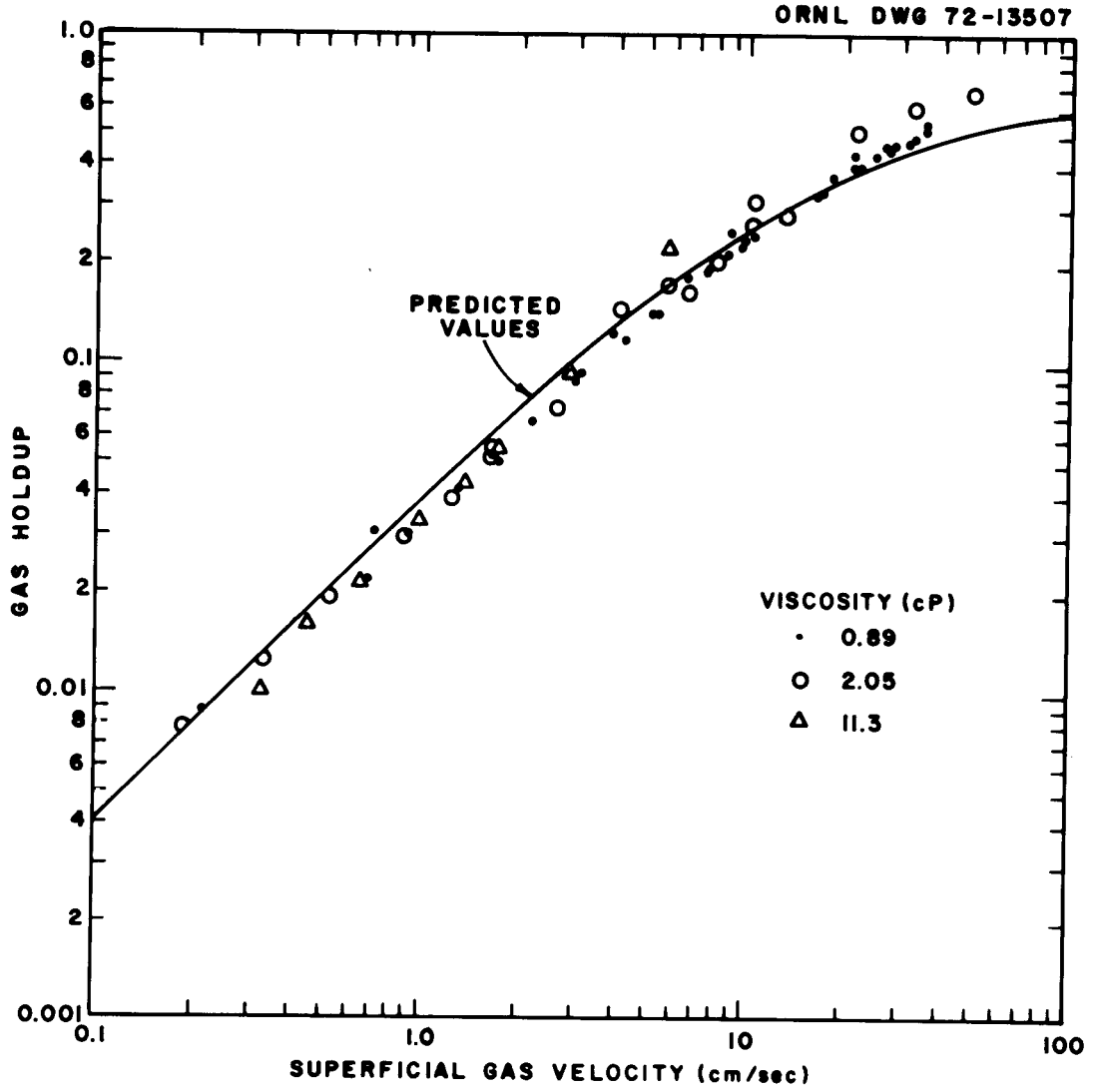

Fig. 25. Variation of Gas Holdup with Changes in Superficial Gas Velocity and Viscosity of Liquid in a 1.5-in.-ID Bubble Column.

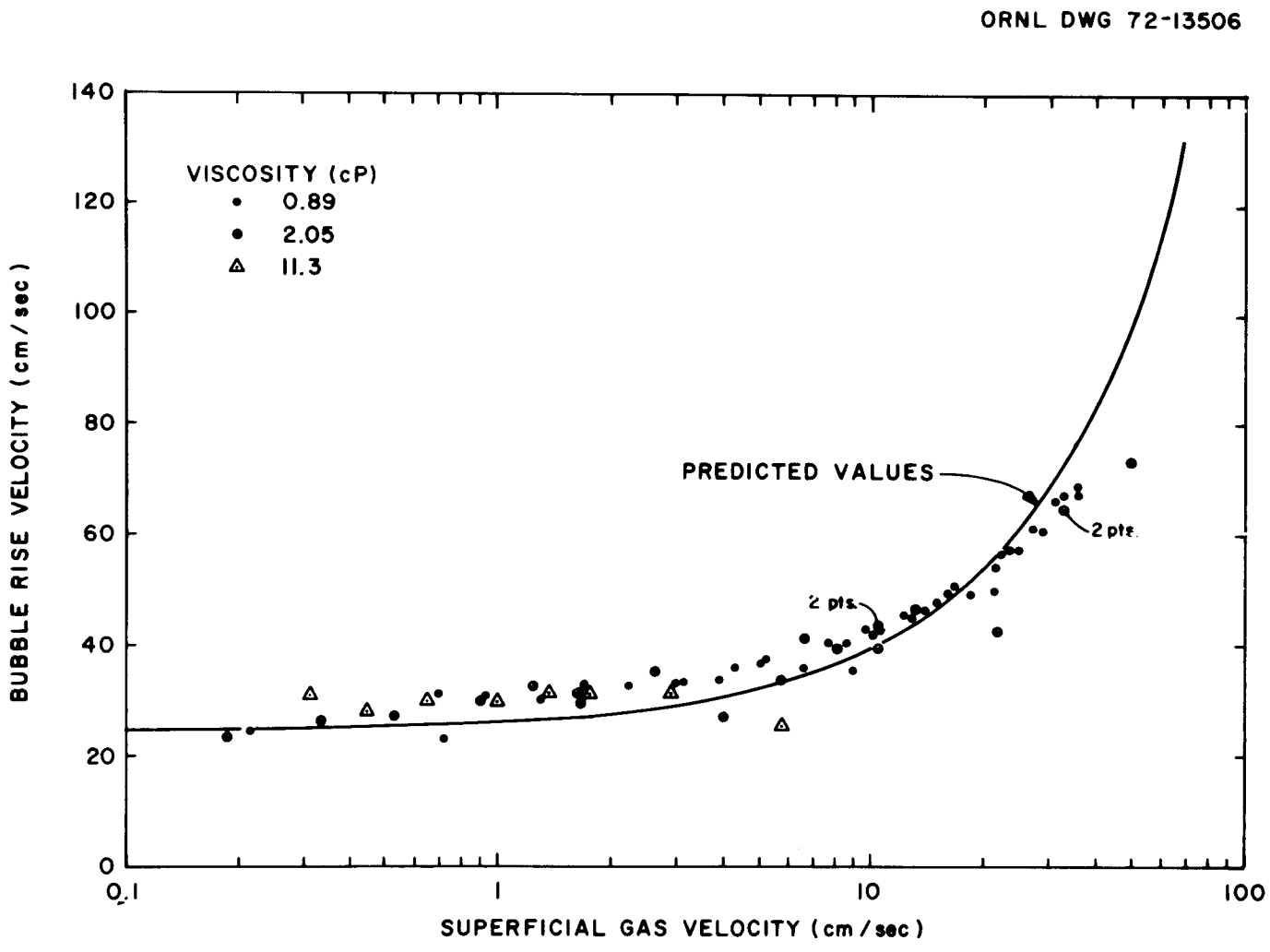

Fig. 26. Variation of Bubble Rise Velocity with Changes in Superficial Gas Velocity and Viscosity of Liquid in a 1.5-in.-ID Bubble Column.

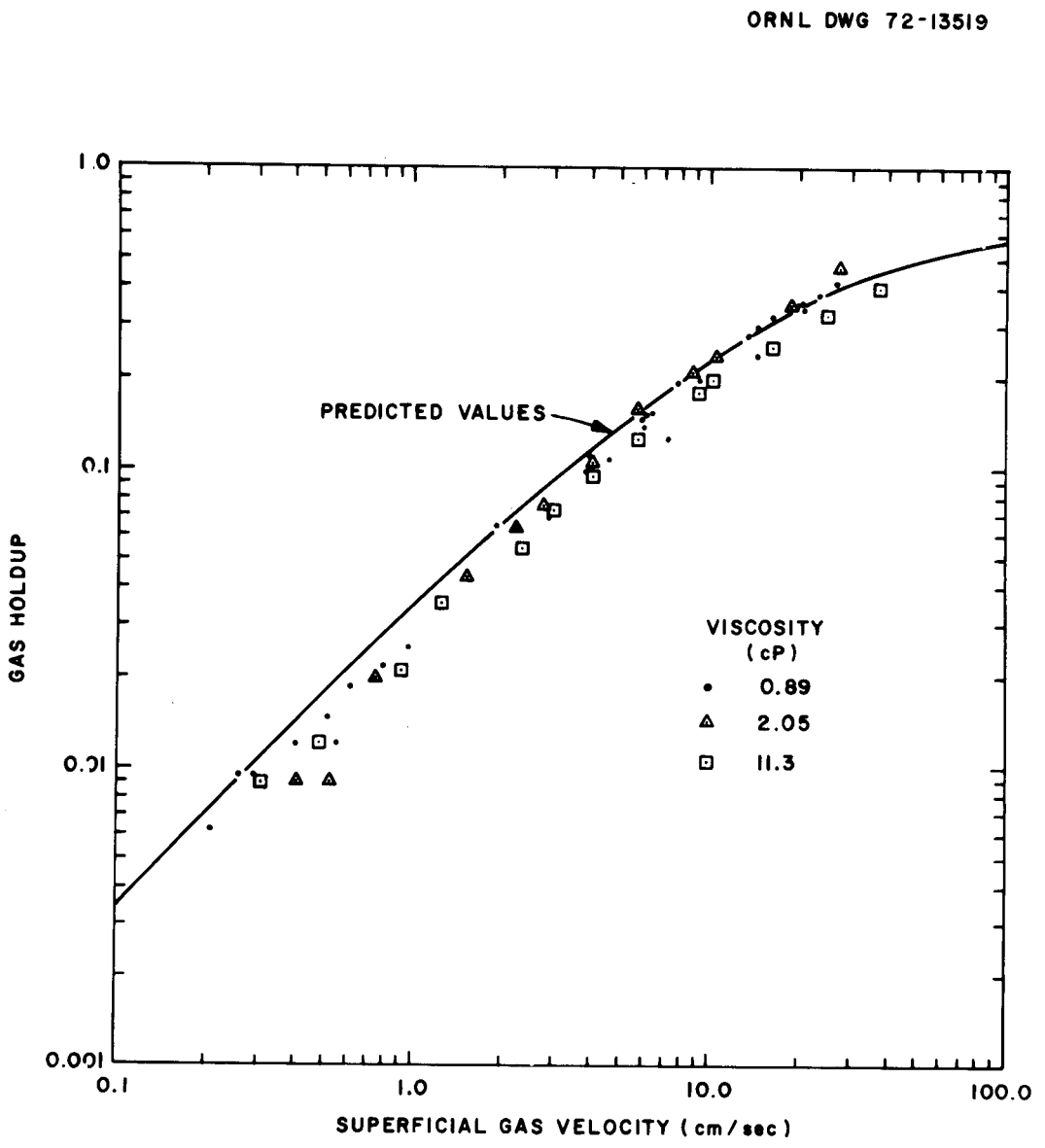

Fig. 27. Variation of Gas Holdup with Changes in Superficial Gas Velocity and Viscosity of Liquid in a 2.0-in.-ID Bubble Column.

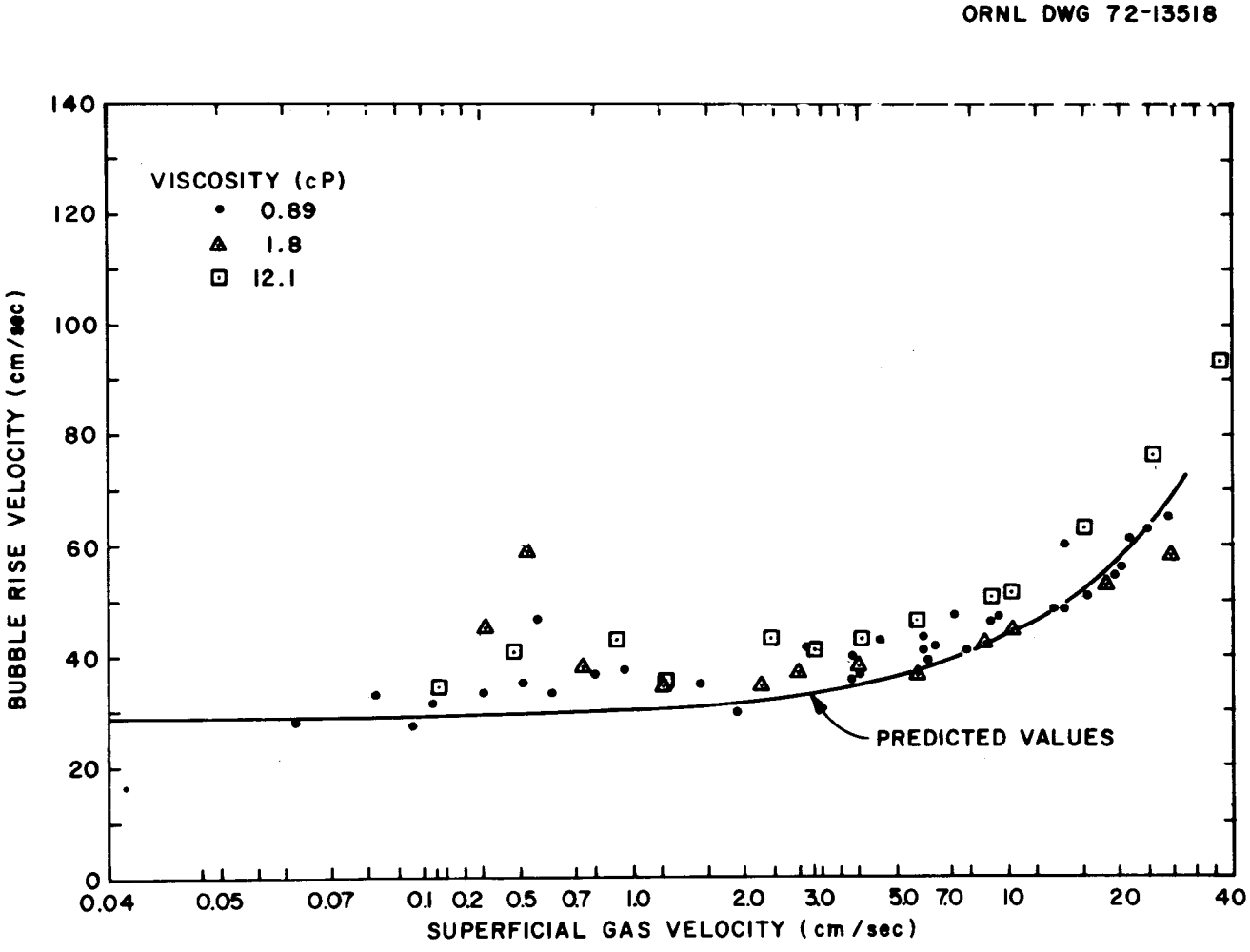

Fig. 28. Variation of Bubble Rise Velocity with Changes in Superficial Gas Velocity and Viscosity of the Liquid in a 2.0-in.-ID Bubble Column.

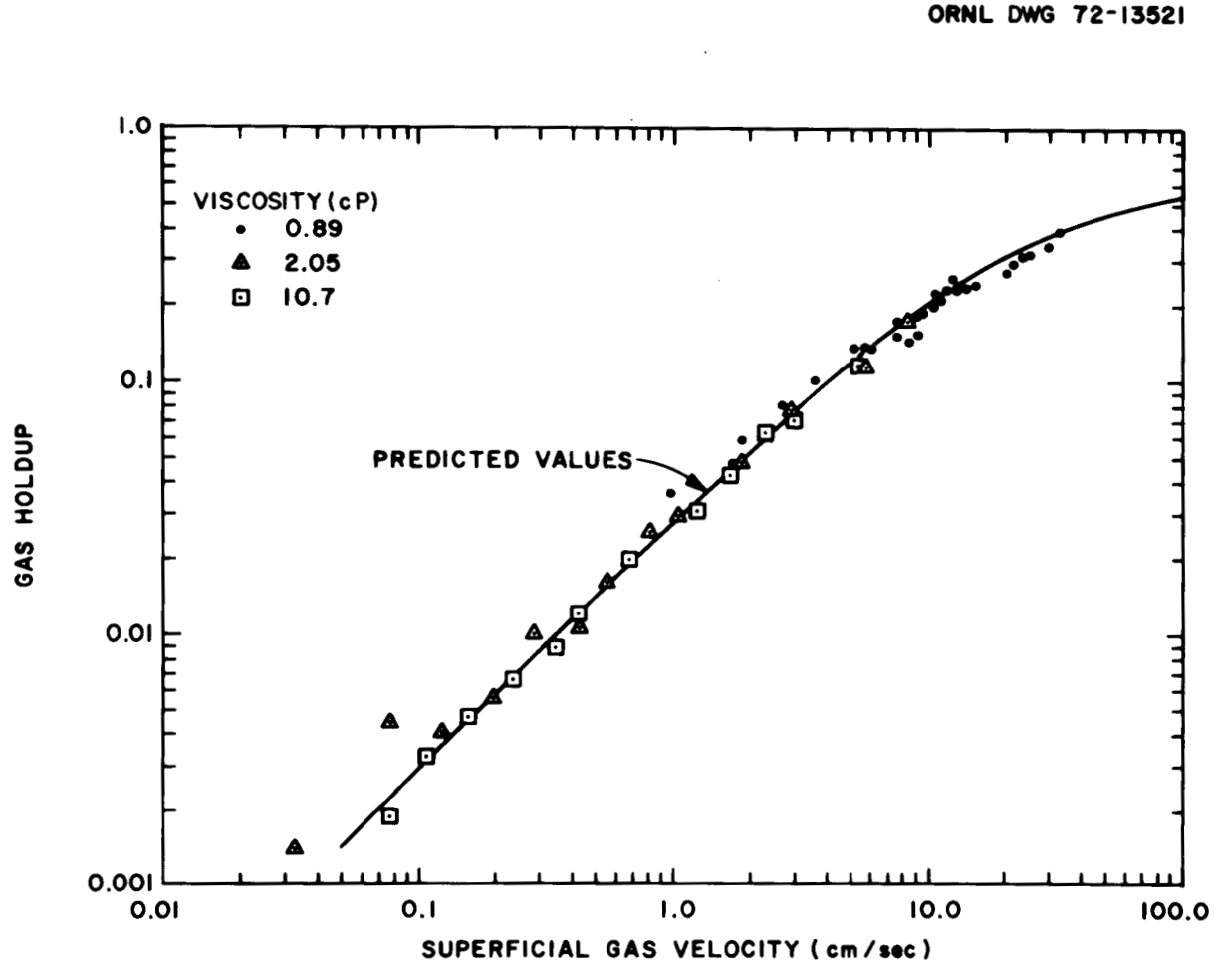

Fig. 29. Variation of Gas Holdup with Changes in Superficial Gas Velocity and Viscosity of Liquid in a 3.0-in.-ID Bubble Column.

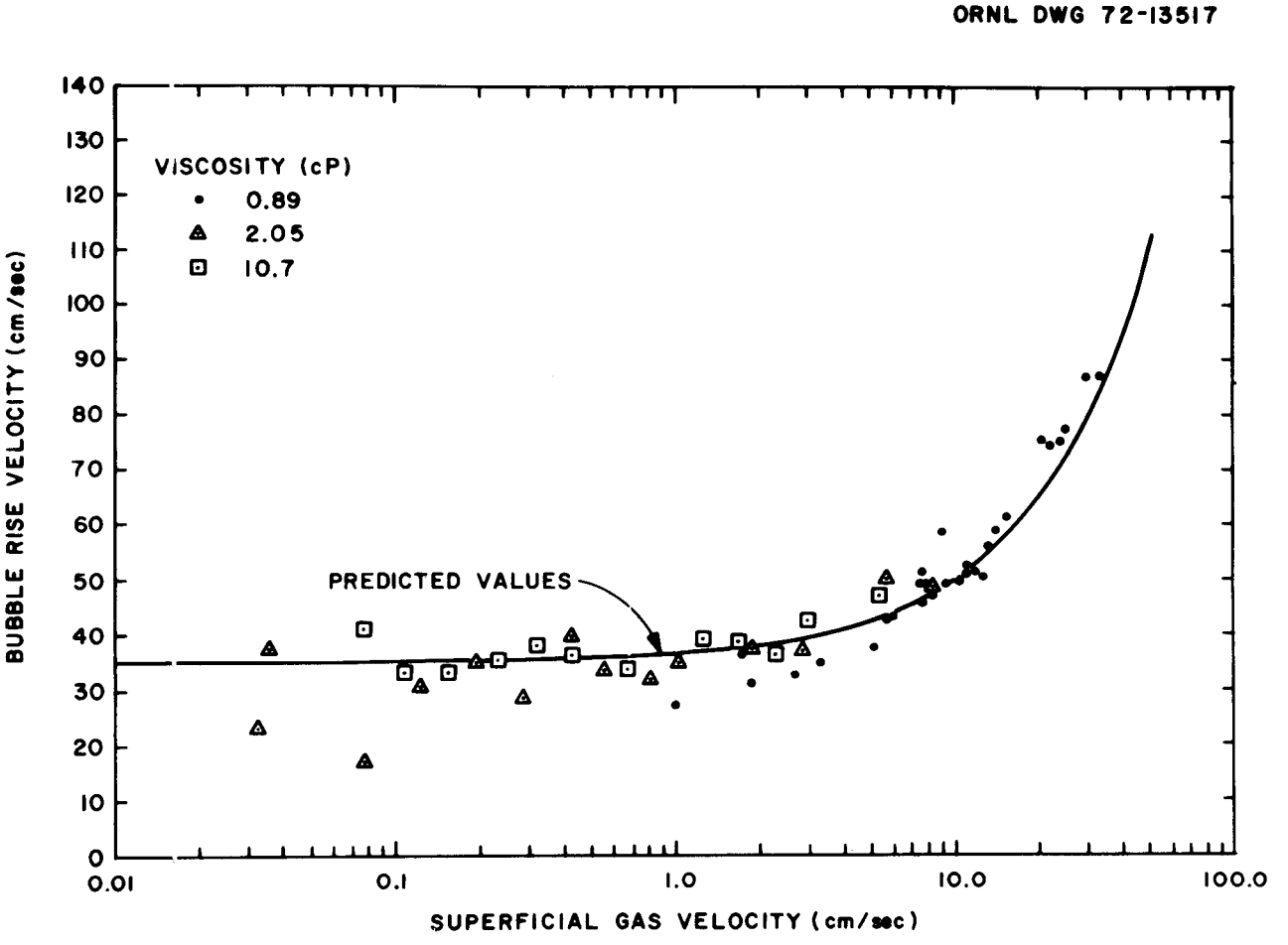

Fig. 30. Variation of Bubble Rise Velocity with Changes in Superficial Gas Velocity and Viscosity of Liquid in a 3.0-in.-ID Bubble Column.

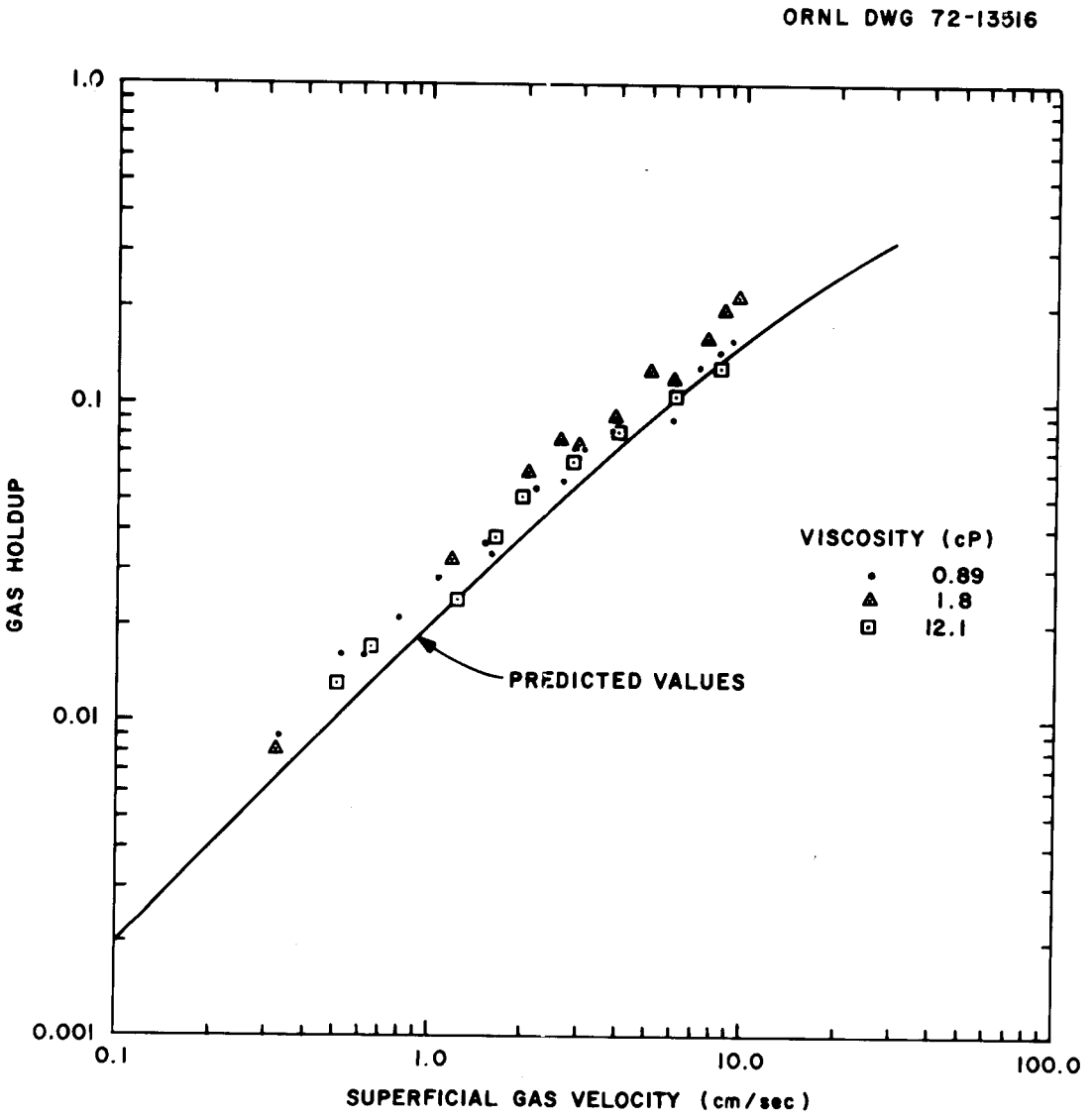

Fig. 31. Variation of Gas Holdup with Changes in Superficial Gas Velocity and Viscosity of Liquid in a 6.0-in.-ID Bubble Column.

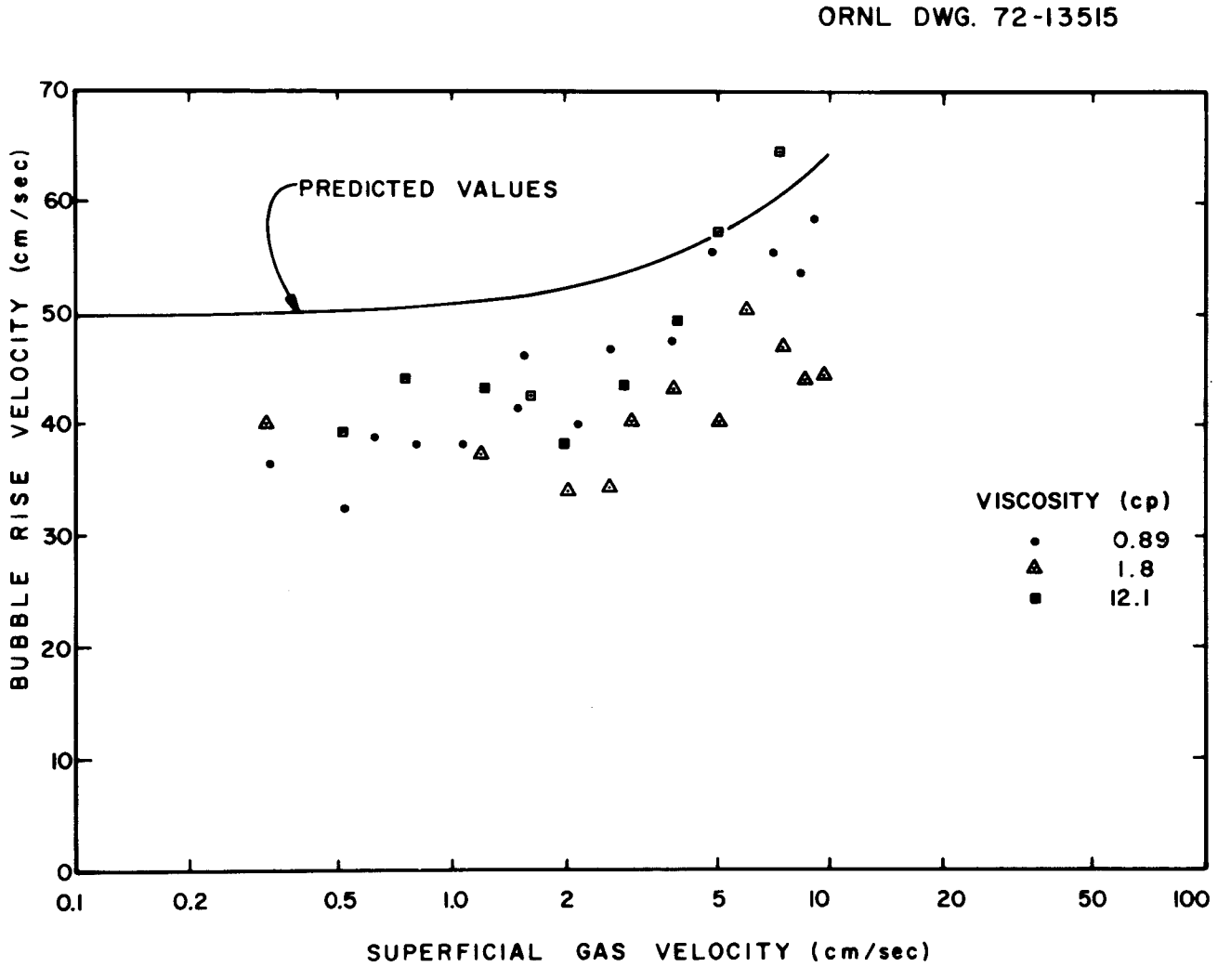

Fig. 32. Variation of Bubble Rise Velocity with Changes in Superficial Gas Velocity and Viscosity of Liquid in a 6.0-in.-ID Bubble Column.

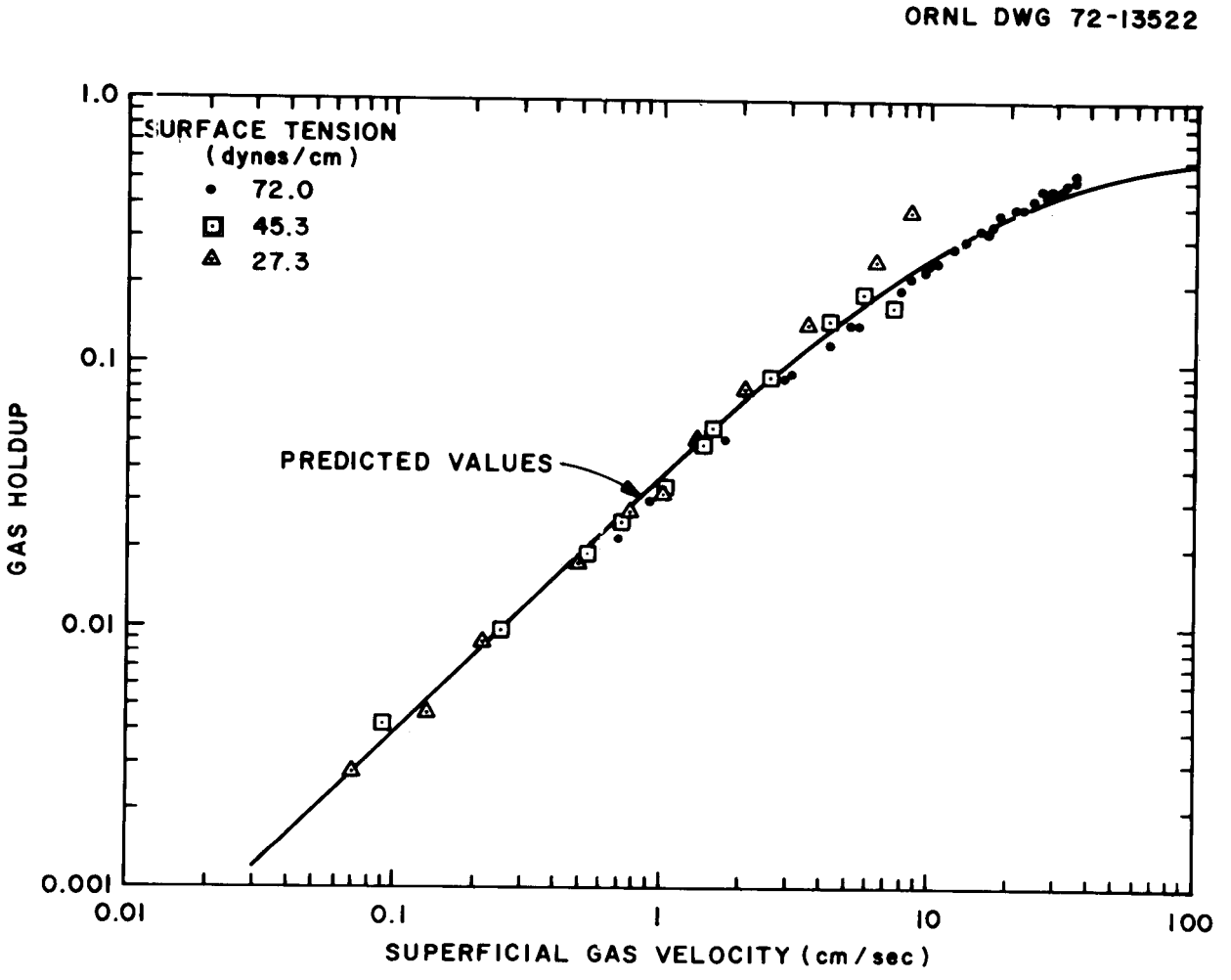

Fig. 33. Variation of Gas Holdup with Changes in Superficial Gas Velocity and Surface Tension of Liquid in a 1.5-in.-ID Bubble Column.

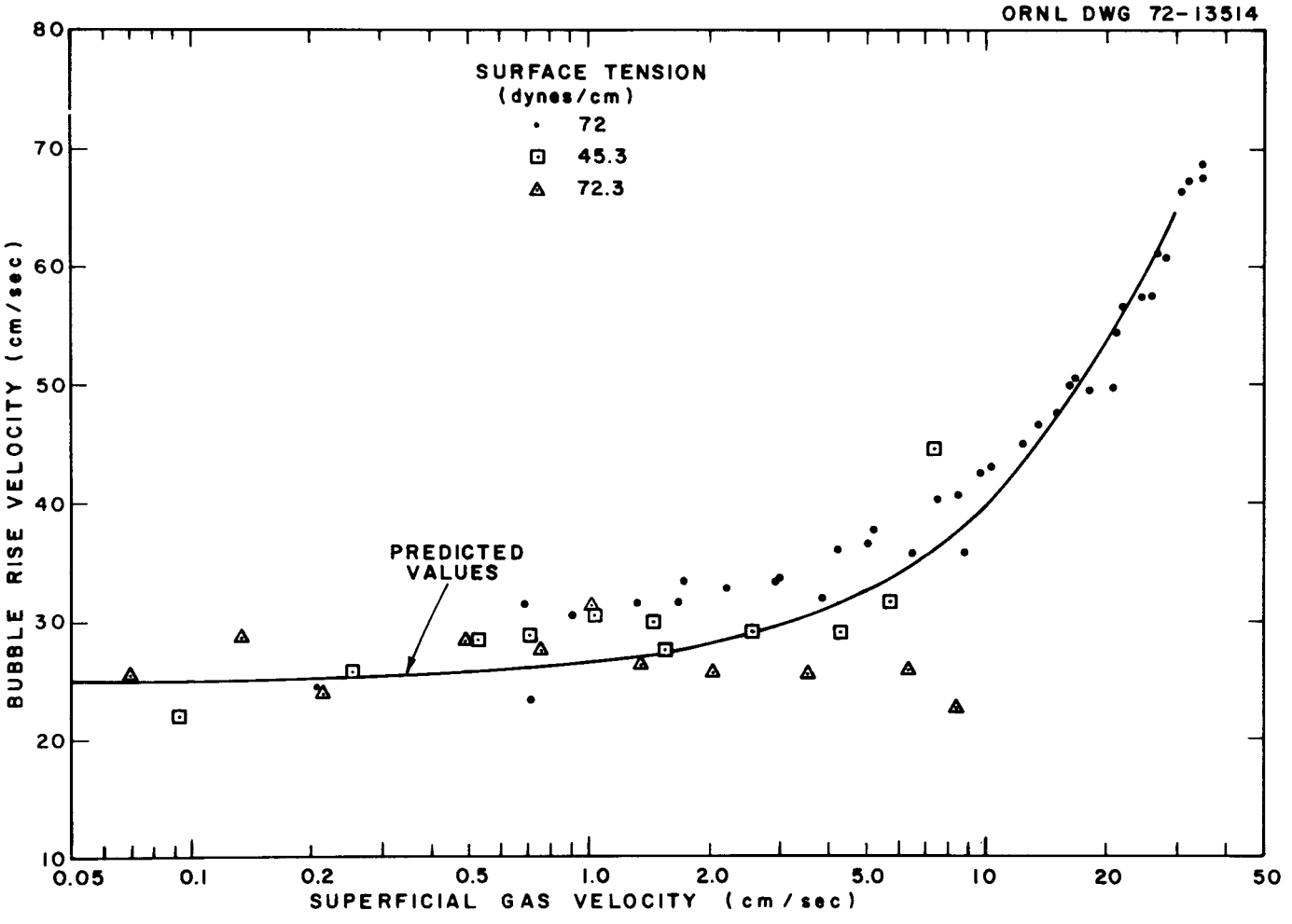

Fig. 34. Variation of Bubble Rise Velocity with Changes in Superficial Gas Velocity and Surface Tension of Liquid in a 1.5-in.-ID Bubble Column.

ORNL DWG 72-13523RI

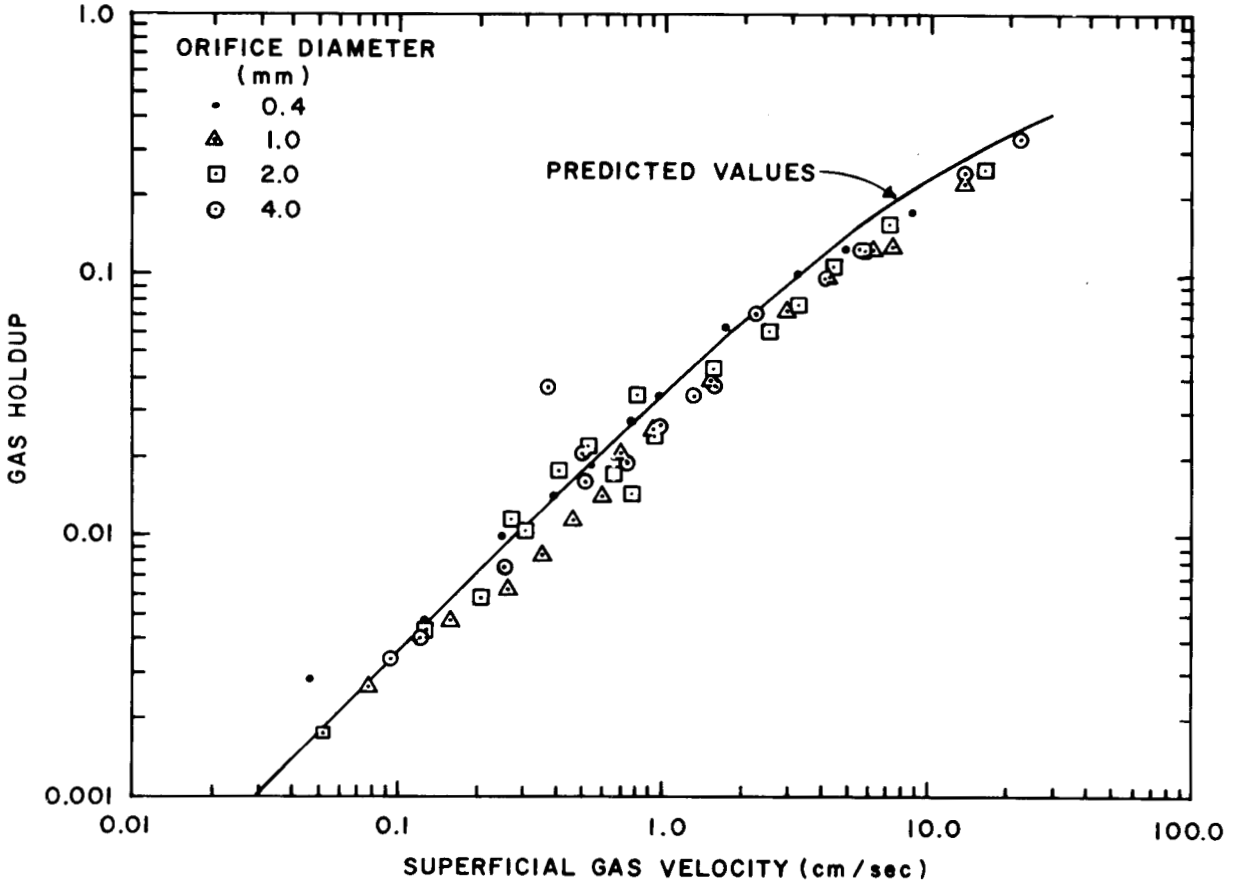

Fig. 35. Variation of Gas Holdup with Changes in Superficial Gas Velocity and Diameter of Orifices in Gas Distributor in a 2.0-in.-ID Bubble Column Filled with Water. The gas distributor consisted of five orifices of the diameter indicated.

ORNL DWG. 72-13513

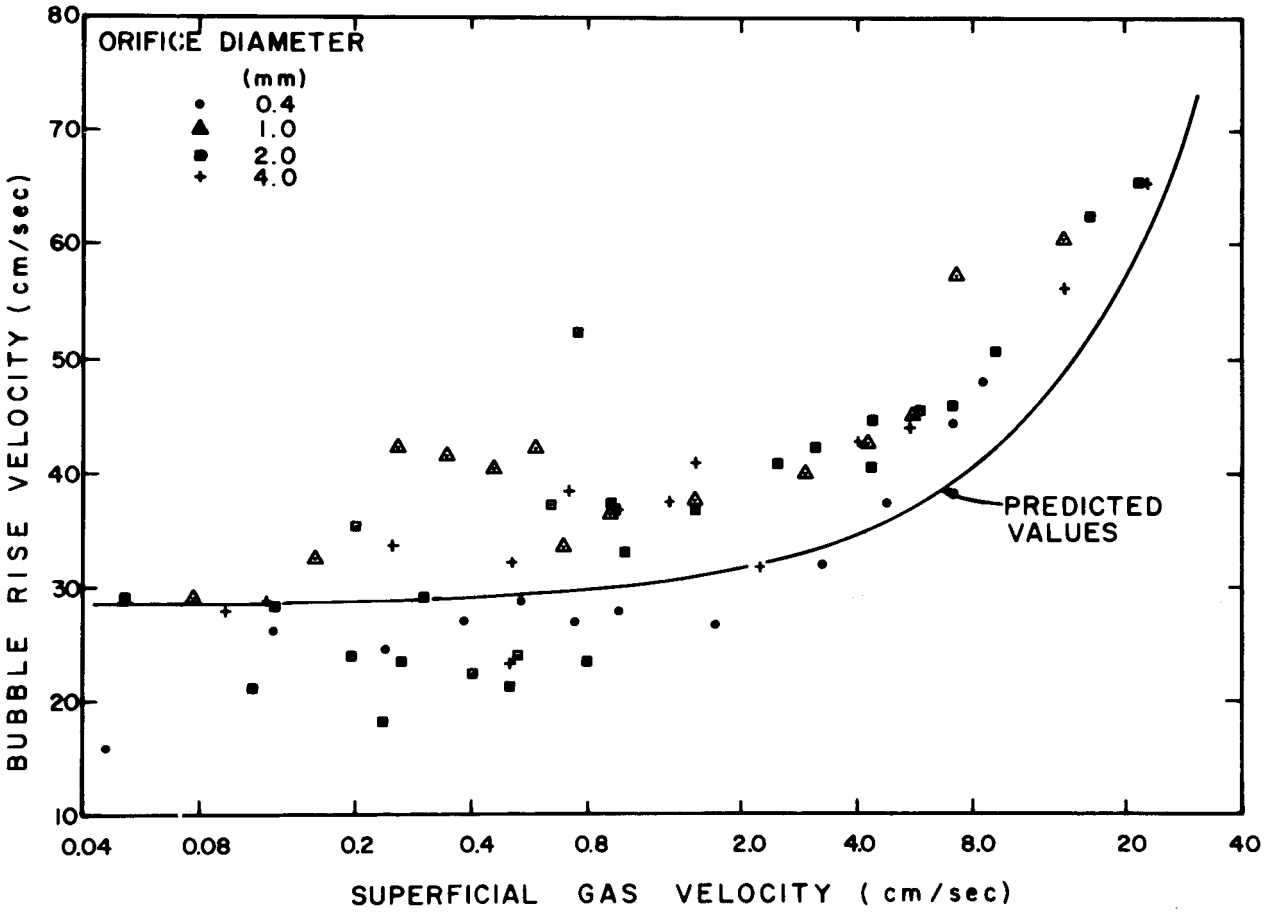

Fig. 36. Variation of Bubble Rise Velocity with Changes in Superficial Gas Velocity and Diameter of Crifices in Gas Distributor in a 2.0-in.-ID Bubble Column Filled with Water. The gas distributor consisted of five orifices of the diameter indicated.

ORNL DWG 72-13512RI

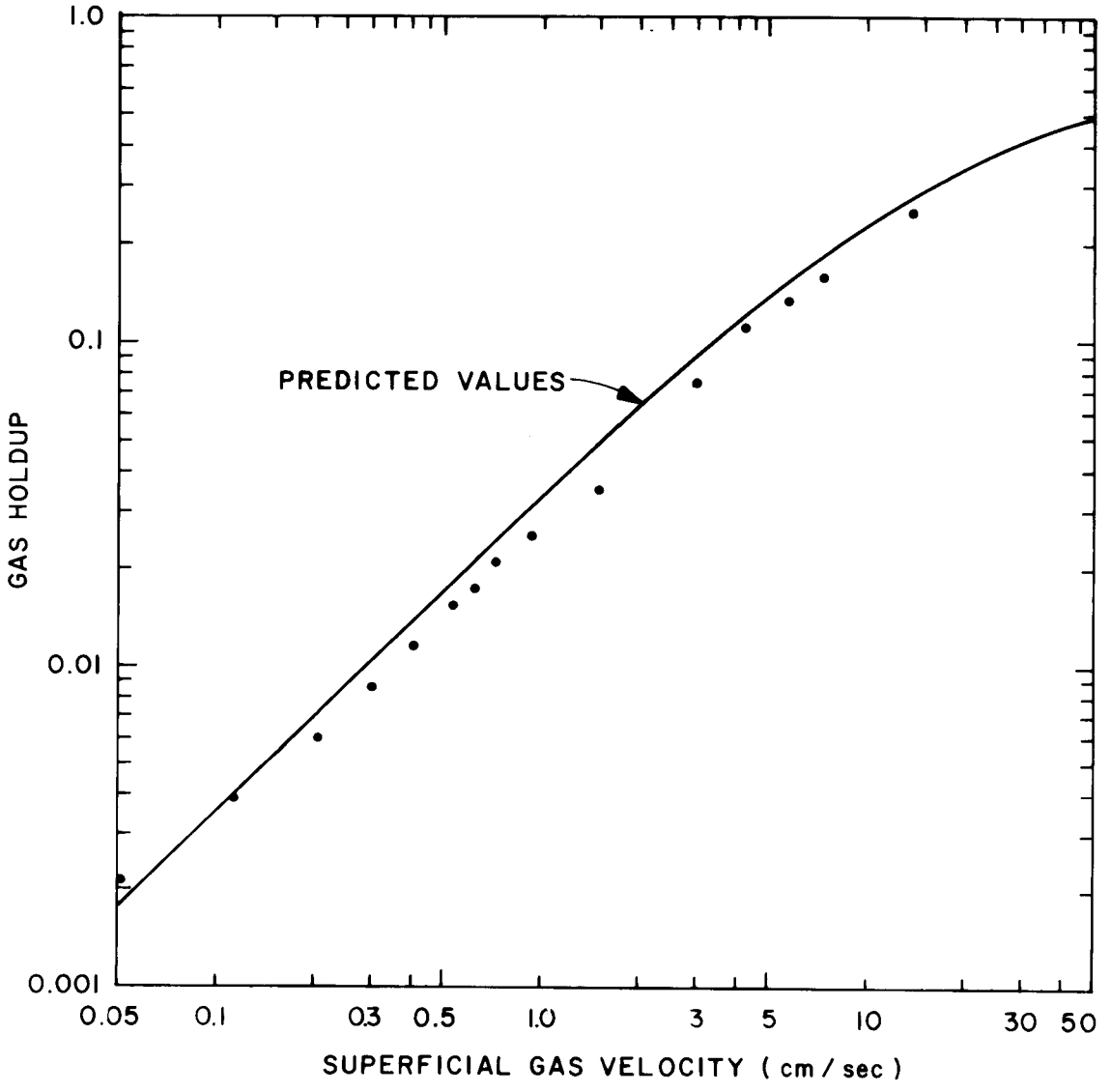

Fig. 37. Variation of Gas Holdup with Superficial Gas Velocity in a 2.0-in.-ID Bubble Column Filled with Water. The gas distributor consisted of 19 orifices, each having a diameter of 1.0 mm.

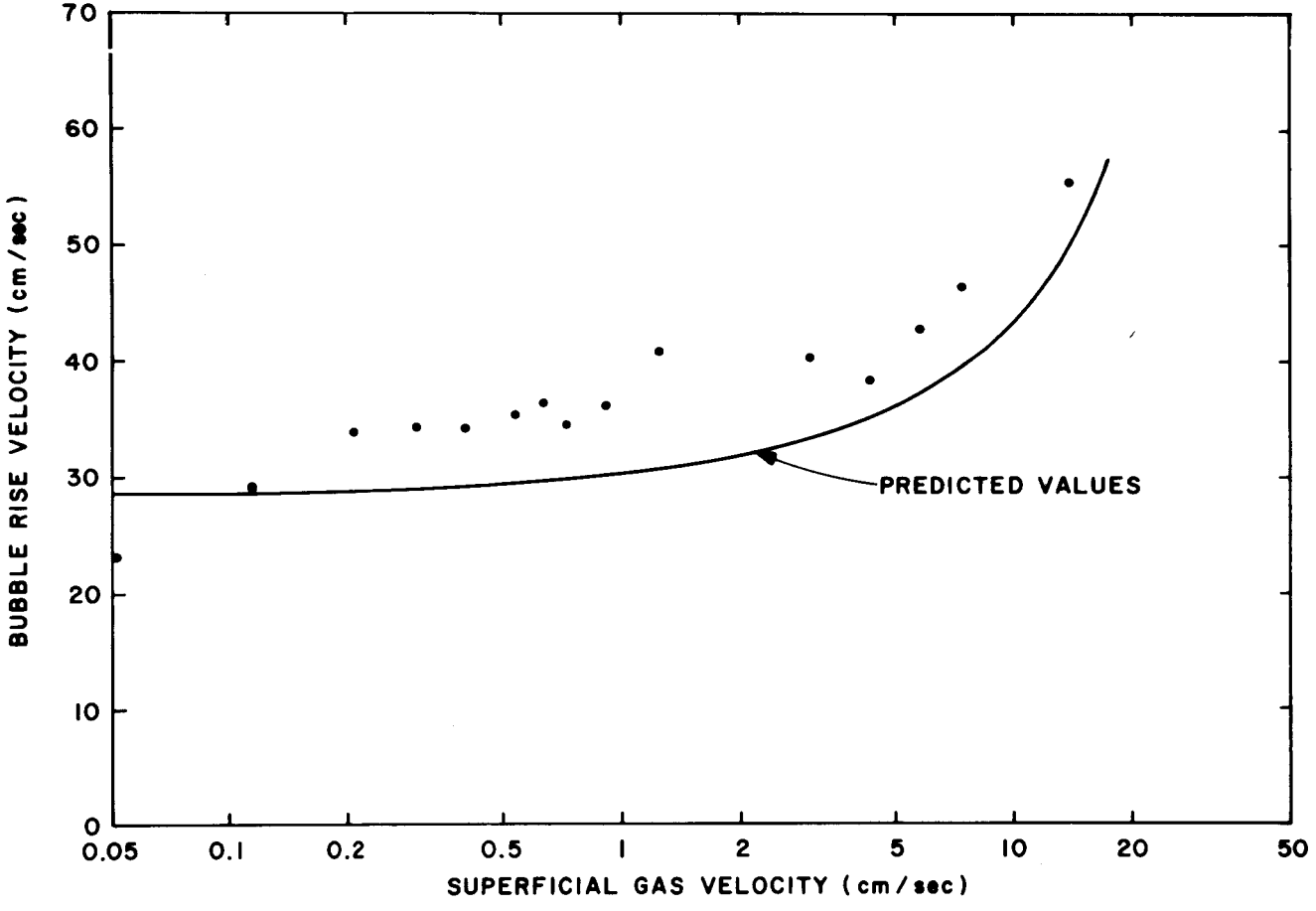

Fig. 38. Variation of Bubble Rise Velocity with Superficial Gas Velocity in a 2.0-in.-ID Bubble Column Filled with Water. The gas distributor consisted of 19 orifices, each having a diameter of 1.0 mm.

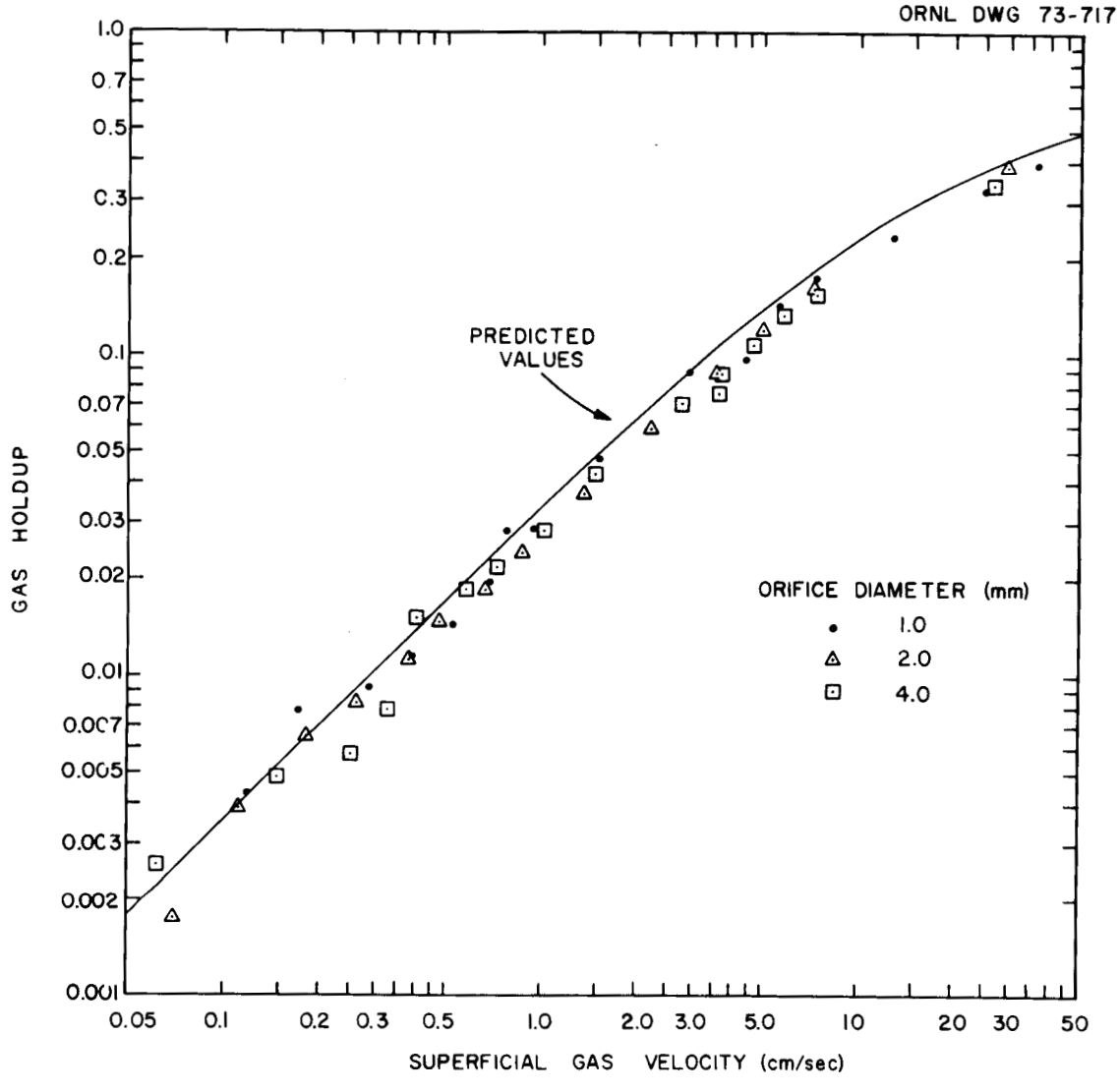

Fig. 39. Variation of Gas Holdup with Changes in Superficial Gas Velocity and Diameter of Orifices in Gas Distributor in a 2.0-in.-ID Bubble Column. The gas distributor consisted of 37 orifices of the diameter indicated.

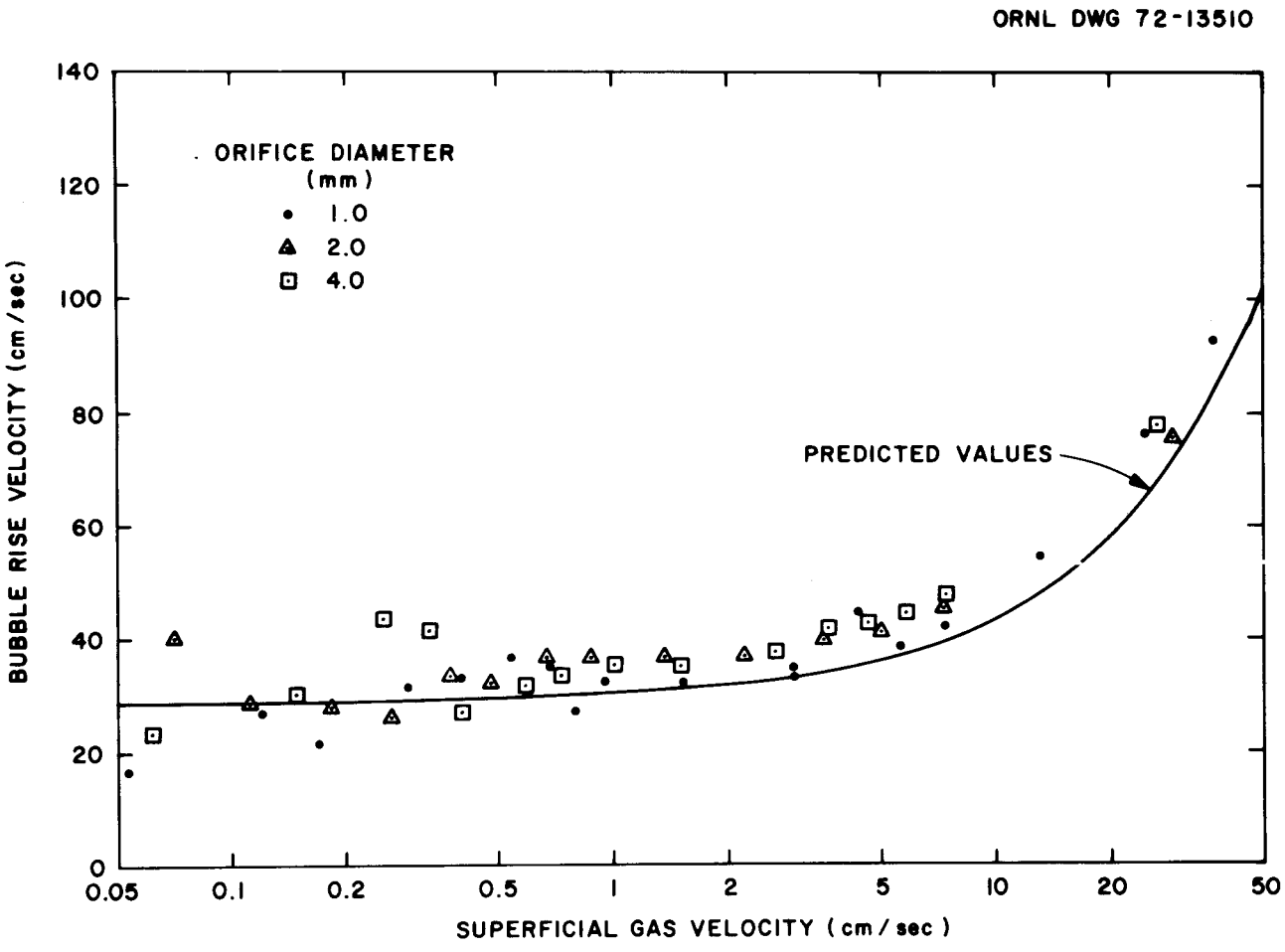

Fig. 40. Variation of Bubble Rise Velocity with Changes in Superficial Gas Velocity and Diameter of Orifices in Gas Distributor in a 2.0-in.-ID Bubble Column. The gas distributor consisted of 37 orifices having the indicated diameter.

The variations of gas holdup and bubble rise velocity with changes in the surface tension of the liquid and the superficial gas velocity are shown in Figs. 33 and 34 for a column diameter of 1.5 in. Decreases in the surface tension tend to increase the gas holdup, to decrease the bubble rise velocity, and to cause the transition from bubble flow to slug flow to occur at higher superficial gas velocities; on the other hand, the importance of changes in these parameters is very slight.

Data on gas holdup and bubble rise velocity obtained in a 2-in.-diam column with multiple gas inlets having diameters of 0.4, 1.0, 2.0, and 4.0 mm are shown in Figs. 35-40. Within the accuracy of the data, there is no dependence of gas holdup or bubble rise velocity on the number or diameter of the orifices in the gas distributor except in the case of the smallest orifice diameter studied (0.4 mm). The bubble rise velocity observed with the 0.4-mm-diam orifice is appreciably lower, and the gas holdup is higher, than for the larger orifice diameters.

9.6 Compilation of Data on Axial Mixing

A compilation was made of the axial dispersion data that have been accumulated in experiments made thus far. This was done in preparation for developing a general correlation for predicting axial dispersion in open bubble columns. The information, which consists of about 420 measurements of the axial dispersion coefficient in columns with diameters ranging from 1.0 to 6.0 in., was divided into 34 data sets (as shown in Table 35). The results obtained in the individual runs with column diameters of 1.0, 1.5, 2.0, 3.0, and 6.0 in. are summarized in Tables 36, 37, 38, 39, and 40, respectively.

9.7 Correlation of Data on Axial Dispersion

The axial dispersion data were analyzed using dimensional analysis and were fitted by the method of least squares to the resulting power-law expression. The power-law expression is of the form

Table 35. Description of Data Sets for Data on Axial Dispersion in Open Bubble Columns

Data Set No.	Column Diameter (in.)	Orifice Diameter (cm)	Number of Orifices	Fluid Viscosity (cP)	Surface Tension (dynes/cm)	Density (g/cm^3)	Number of Data Points	Reference
1	1.5	0.432	1	0.894	73.0	0.997	15	a
2	2.0	0.432	1	0.894	73.0	0.997	7	a
3	6.0	0.432	1	0.894	73.0	0.997	16	a
4	2.0	0.1	1	0.894	73.0	0.997	13	b
5	2.0	0.04	5	0.894	73.0	0.997	12	b
6	2.0	0.1	5	0.894	73.0	0.997	14	b
7	2.0	0.2	5	0.894	73.0	0.997	26	b
8	2.0	0.4	5	0.894	73.0	0.997	16	b
9	2.0	0.1	19	0.894	73.0	0.997	15	b
10	2.0	0.1	37	0.894	73.0	0.997	17	b
11	2.0	0.2	37	0.894	73.0	0.997	14	b
12	2.0	0.4	37	0.894	73.0	0.997	15	b
13	1.5	0.432	1	0.894	73.0	0.997	11	b
14	1.5	0.432	1	1.07	45.3	0.995	11	b
15	1.5	0.432	1	1.09	27.3	0.996	11	b
16	1.5	0.432	1	2.05	71.5	1.04	10	b
17	1.5	0.432	1	11.3	70.0	1.15	10	b
18	3.0	0.432	1	2.05	71.5	1.04	14	b
19	3.0	0.432	1	10.7	70.0	1.15	13	b
20	2.0	0.432	1	1.8	71.8	1.05	12	a
21	2.0	0.432	1	12.1	67.9	1.16	13	a
22	1.5	0.432	1	1.8	71.8	1.05	11	a
23	6.0	0.432	1	1.8	71.8	1.05	13	a
24	6.0	0.432	1	12.1	67.9	1.16	10	a
25	2.0	0.102	1	0.894	37.6	0.997	6	23
26	2.0	0.102	1	0.894	53.2	0.997	4	23
27	2.0	0.102	1	0.894	73.0	0.997	5	23
28	2.0	0.102	1	15.0	65.2	1.15	5	23
29	2.0	0.102	1	0.894	67.4	0.997	1	23
30	2.0	0.102	1	0.894	73.0	0.997	21	22
31	1.5	0.432	1	0.894	73.0	0.997	7	25
32	2.0	0.432	1	0.894	73.0	0.997	13	25
33	3.0	0.432	1	0.894	73.0	0.997	9	25
34	1.0	0.432	1	0.894	73.0	0.997	38	c

[a] Data obtained during second study.

[b] Data obtained during third study.

[c] Data obtained during first study.

Table 36. Experimentally Determined Values[a] for the Axial Dispersion Coefficient in a 1.0-in.-ID Open Bubble Column Filled with Water

Data set No. 34

Run No.	Superficial Gas Velocity (cm/sec)	Axial Dispersion Coefficient (cm^2/sec)	Run No.	Superficial Gas Velocity (cm/sec)	Axial Dispersion Coefficient (cm^2/sec)
1	18.7	82.3	20	44.8	181.1
2	76.6	319.0	21	1.166	20.8
3	76.6	261.8	22	1.088	18.3
4	65.4	255.2	23	1.011	17.1
5	74.7	182.3	24	0.933	22.5
6	56.0	319.0	25	0.855	17.1
7	37.3	170.2	26	0.778	15.5
8	18.7	63.8	27	0.700	14.1
9	28.0	170.2	28	0.156	5.84
10	46.1	232.0	29	1.25	14.8
11	10.3	52.0	30	1.02	24.6
12	18.7	92.8	31	0.78	19.7
13	28.9	128.3	32	0.468	14.8
14	23.3	102.6	33	0.156	7.04
15	14.0	61.1	34	1.33	22.4
16	32.7	146.6	35	1.01	17.8
17	37.3	213.8	36	0.702	14.5
18	46.7	185.5	37	0.390	10.7
19	63.5	285.1	38	0.156	6.42

[a]Data obtained during first study.

Table 37. Experimentally Determined Values for the Axial Dispersion Coefficient in a 1.5-in.-ID Open Bubble Column

Data Set No.	Run No.	Superficial Gas Velocity (cm/sec)	Gas Disperser Diameter[a] (cm)	Properties of Liquid			Axial Dispersion Coefficient (cm^2/sec)	Ref.
				Density (g/cm^3)	Viscosity (cP)	Surface Tension (dynes/cm)		
1	1	16.4	0.635	0.997	0.894	73.0	138.5	b
1	2	8.58	0.635	0.997	0.894	73.0	85.6	b
1	3	12.3	0.635	0.997	0.894	73.0	114.8	b
1	4	9.89	0.635	0.997	0.894	73.0	93.4	b
1	5	1.72	0.635	0.997	0.894	73.0	31.6	b
1	6	35.4	0.635	0.997	0.894	73.0	482.2	b
1	7	0.69	0.635	0.997	0.894	73.0	20.8	b
1	8	35.4	0.635	0.997	0.894	73.0	380.5	b
1	9	2.99	0.635	0.997	0.894	73.0	39.0	b
1	10	5.11	0.635	0.997	0.894	73.0	65.0	b
1	11	0.912	0.635	0.997	0.894	73.0	24.8	b
1	12	22.4	0.635	0.997	0.894	73.0	177.0	b
1	13	10.4	0.635	0.997	0.894	73.0	149.0	b
1	14	16.8	0.635	0.997	0.894	73.0	136.0	b
1	15	13.6	0.635	0.997	0.894	73.0	95.2	b
13	1	1.045	0.635	0.997	0.89	72.0	25.8	c
13	2	0.212	0.635	0.997	0.89	72.0	12.9	c
13	3	0.451	0.635	0.997	0.89	72.0	18.9	c
13	4	0.719	0.635	0.997	0.89	72.0	24.4	c
13	5	1.33	0.635	0.997	0.89	72.0	32.9	c
13	6	1.68	0.635	0.997	0.89	72.0	31.6	c
13	7	2.21	0.635	0.997	0.89	72.0	39.5	c
13	8	3.86	0.635	0.997	0.89	72.0	50.0	c
13	9	6.54	0.635	0.997	0.89	72.0	69.4	c
13	10	8.93	0.635	0.997	0.89	72.0	85.9	c

Table 37 (continued)

Data Set No.	Run No.	Superficial Gas Velocity (cm/sec)	Gas Disperser Diameter[a] (cm)	Properties of Liquid			Axial Dispersion Coefficient (cm^2/sec)	Ref.
				Density (g/cm^3)	Viscosity (cP)	Surface Tension (dynes/cm)		
13	11	21.3	0.635	0.997	0.89	72.0	242	c
14	1	1.045	0.635	0.995	1.07	45.3	20.9	c
14	2	0.710	0.635	0.995	1.07	45.3	23.3	c
14	3	0.535	0.635	0.995	1.07	45.3	20.5	c
14	4	0.252	0.635	0.995	1.07	45.3	17.3	c
14	5	0.0930	0.635	0.995	1.07	45.3	14.6	c
14	6	1.456	0.635	0.995	1.07	45.3	23.1	c
14	7	1.55	0.635	0.995	1.07	45.3	26.7	c
14	8	2.58	0.635	0.995	1.07	45.3	33.7	c
14	9	4.31	0.635	0.995	1.07	45.3	40.6	c
14	10	5.79	0.635	0.995	1.07	45.3	50.0	c
14	11	7.45	0.635	0.995	1.07	45.3	58.0	c
15	1	1.02	0.635	0.996	1.09	27.3	21.9	c
15	2	0.133	0.635	0.996	1.09	27.3	15.0	c
15	3	0.0705	0.635	0.996	1.09	27.3	11.9	c
15	4	0.214	0.635	0.996	1.09	27.3	15.8	c
15	5	0.494	0.635	0.996	1.09	27.3	20.6	c
15	6	0.763	0.635	0.996	1.09	27.3	22.2	c
15	7	1.37	0.635	0.996	1.09	27.3	22.3	c
15	8	2.07	0.635	0.996	1.09	27.3	27.9	c
15	9	3.56	0.635	0.996	1.09	27.3	36.2	c
15	10	6.4	0.635	0.996	1.09	27.3	51.5	c
15	11	8.6	0.635	0.996	1.09	27.3	65.7	c
16	1	0.0638	0.635	1.04	2.05	71.5	7.65	c
16	2	0.187	0.635	1.04	2.05	71.5	12.5	c
16	3	0.333	0.635	1.04	2.05	71.5	24.6	c

Table 37 (continued)

Data Set No.	Run No.	Superficial Gas Velocity (cm/sec)	Gas Disperser Diameter[a] (cm)	Properties of Liquid			Axial Dispersion Coefficient (cm^2/sec)	Ref.
				Density (g/cm^3)	Viscosity (cP)	Surface Tension (dynes/cm)		
16	4	0.528	0.635	1.04	2.05	71.5	26.4	c
16	5	0.895	0.635	1.04	2.05	71.5	28.4	c
16	6	1.25	0.635	1.04	2.05	71.5	36.4	c
16	7	1.625	0.635	1.04	2.05	71.5	36.4	c
16	8	2.61	0.635	1.04	2.05	71.5	43.5	c
16	9	5.78	0.635	1.04	2.05	71.5	60.6	c
16	10	8.07	0.635	1.04	2.05	71.5	81.0	c
17	1	0.214	0.635	1.15	11.3	70.0	10.6	c
17	2	0.0888	0.635	1.15	11.3	70.0	7.45	c
17	3	0.313	0.635	1.15	11.3	70.0	12.3	c
17	4	0.45	0.635	1.15	11.3	70.0	15.2	c
17	5	0.651	0.635	1.15	11.3	70.0	21.3	c
17	6	1.0	0.635	1.15	11.3	70.0	21.8	c
17	7	1.38	0.635	1.15	11.3	70.0	27.3	c
17	8	1.74	0.635	1.15	11.3	70.0	27.7	c
17	9	2.9	0.635	1.15	11.3	70.0	34.7	c
17	10	5.79	0.635	1.15	11.3	70.0	55.6	c
22	1	10.4	0.635	1.05	1.8	71.8	88.9	b
22	2	1.66	0.635	1.05	1.8	71.8	24.9	b
22	3	32.7	0.635	1.05	1.8	71.8	814	b
22	4	49.7	0.635	1.05	1.8	71.8	656	b
22	5	32.7	0.635	1.05	1.8	71.8	155	b
22	6	4.06	0.635	1.05	1.8	71.8	44.6	b
22	7	10.4	0.635	1.05	1.8	71.8	88.9	b
22	8	21.9	0.635	1.05	1.8	71.8	115	b
22	9	13.1	0.635	1.05	1.8	71.8	131	b

Table 37 (continued)

Data Set No.	Run No.	Superficial Gas Velocity (cm/sec)	Gas Disperser Diameter[a] (cm)	Properties of Liquid			Axial Dispersion Coefficient (cm^2/sec)	Ref.
				Density (g/cm^3)	Viscosity (cP)	Surface Tension (dynes/cm)		
22	10	10.4	0.635	1.05	1.8	71.8	56.2	b
22	11	6.62	0.635	1.05	1.8	71.8	62.2	b
31	1	0.631	0.102	0.997	0.89	73.0	18.3	25
31	2	7.88	0.102	0.997	0.89	73.0	74.2	25
31	3	3.11	0.102	0.997	0.89	73.0	39.4	25
31	4	25.3	0.102	0.997	0.89	73.0	194	25
31	5	20.7	0.102	0.997	0.89	73.0	154	25
31	6	13.3	0.102	0.997	0.89	73.0	100.3	25
31	7	11.2	0.102	0.997	0.89	73.0	97.6	25

[a]Gas disperser consisted of a single orifice having the indicated inside diameter.

[b]Data obtained during second study.

[c]Data obtained during third study.

Table 38. Experimentally Determined Values for the Axial Dispersion Coefficient in a 2.0-in.-ID Open Bubble Column

Data Set No.	Run No.	Superficial Gas Velocity (cm/sec)	Gas Disperser Design: Number of Inlets	Gas Disperser Design: Inlet Diameter (cm)	Properties of Liquid: Density (g/cm^3)	Properties of Liquid: Viscosity (cP)	Properties of Liquid: Surface Tension (dynes/cm)	Axial Dispersion Coefficient (cm^2/sec)	Ref.
2	1	4.0	1	0.432	0.997	0.894	73.0	51.0	a
2	2	20.3	1	0.432	0.997	0.894	73.0	206.0	a
2	3	23.8	1	0.432	0.997	0.894	73.0	172.7	a
2	4	14.4	1	0.432	0.997	0.894	73.0	144.9	a
2	5	0.56	1	0.432	0.997	0.894	73.0	22.3	a
2	6	3.88	1	0.432	0.997	0.894	73.0	58.7	a
2	7	5.96	1	0.432	0.997	0.894	73.0	67.5	a
4	1	0.0442	1	0.1	0.997	0.894	72.0	19.6	b
4	2	0.126	1	0.1	0.997	0.894	72.0	28.1	b
4	3	0.209	1	0.1	0.997	0.894	72.0	28.9	b
4	4	0.295	1	0.1	0.997	0.894	72.0	31.1	b
4	5	0.405	1	0.1	0.997	0.894	72.0	37.6	b
4	6	0.515	1	0.1	0.997	0.894	72.0	40.5	b
4	7	0.618	1	0.1	0.997	0.894	72.0	43.4	b
4	8	0.798	1	0.1	0.997	0.894	72.0	45.5	b
4	9	0.95	1	0.1	0.997	0.894	72.0	48.2	b
4	10	1.52	1	0.1	0.997	0.894	72.0	52.7	b
4	11	2.92	1	0.1	0.997	0.894	72.0	60.8	b
4	12	4.58	1	0.1	0.997	0.894	72.0	72.6	b
4	13	7.2	1	0.1	0.997	0.894	72.0	81.5	b
5	1	0.385	5	0.04	0.997	0.894	73.0	40.6	b
5	2	0.0457	5	0.04	0.997	0.894	73.0	15.4	b
5	3	0.124	5	0.04	0.997	0.894	73.0	16.4	b
5	4	0.242	5	0.04	0.997	0.894	73.0	22.8	b
5	5	0.537	5	0.04	0.997	0.894	73.0	33.1	b

Table 38 (continued)

Data Set No.	Run No.	Superficial Gas Velocity (cm/sec)	Gas Disperser Design: Number of Inlets	Gas Disperser Design: Inlet Diameter (cm)	Properties of Liquid: Density (g/cm^3)	Properties of Liquid: Viscosity (cP)	Properties of Liquid: Surface Tension (dynes/cm)	Axial Dispersion Coefficient (cm^2/sec)	Ref.
5	6	0.749	5	0.04	0.997	0.894	73.0	35.4	b
5	7	0.96	5	0.04	0.997	0.894	73.0	36.4	b
5	8	1.7	5	0.04	0.997	0.894	73.0	41.5	b
5	9	3.22	5	0.04	0.997	0.894	73.0	57.8	b
5	10	4.79	5	0.04	0.997	0.894	73.0	60.8	b
5	11	7.00	5	0.04	0.997	0.894	73.0	72.6	b
5	12	8.46	5	0.04	0.997	0.894	73.0	83.6	b
6	1	0.688	5	0.1	0.997	0.894	73.0	37.2	b
6	2	0.0767	5	0.1	0.997	0.894	73.0	31.7	b
6	3	0.158	5	0.1	0.997	0.894	73.0	31.5	b
6	4	0.26	5	0.1	0.997	0.894	73.0	44.8	b
6	5	0.347	5	0.1	0.997	0.894	73.0	47.0	b
6	6	0.459	5	0.1	0.997	0.894	73.0	37.9	b
6	7	0.589	5	0.1	0.997	0.894	73.0	35.5	b
6	8	0.92	5	0.1	0.997	0.894	73.0	39.0	b
6	9	1.52	5	0.1	0.997	0.894	73.0	55.1	b
6	10	2.95	5	0.1	0.997	0.894	73.0	57.5	b
6	11	4.27	5	0.1	0.997	0.894	73.0	63.5	b
6	12	5.59	5	0.1	0.997	0.894	73.0	92.4	b
6	13	7.29	5	0.1	0.997	0.894	73.0	111.1	b
6	14	13.8	5	0.1	0.997	0.894	73.0	137.0	b
7	1	4.35	5	0.2	0.997	0.894	73.0	71.6	b
7	2	0.265	5	0.2	0.997	0.894	73.0	35.8	b
7	3	0.80	5	0.2	0.997	0.894	73.0	23.8	b
7	4	2.5	5	0.2	0.997	0.894	73.0	57.4	b

Table 38 (continued)

Data Set No.	Run No.	Superficial Gas Velocity (cm/sec)	Gas Disperser Design: Number of Inlets	Gas Disperser Design: Inlet Diameter (cm)	Properties of Liquid: Density (g/cm^3)	Properties of Liquid: Viscosity (cP)	Properties of Liquid: Surface Tension (dynes/cm)	Axial Dispersion Coefficient (cm^2/sec)	Ref.
7	5	9.15	5	0.2	0.997	0.894	73.0	139.0	b
7	6	21.6	5	0.2	0.997	0.894	73.0	200.0	b
7	7	0.11	5	0.2	0.997	0.894	73.0	29.8	b
7	8	0.198	5	0.2	0.997	0.894	73.0	30.5	b
7	9	0.235	5	0.2	0.997	0.894	73.0	35.8	b
7	10	0.503	5	0.2	0.997	0.894	73.0	30.0	b
7	11	1.0	5	0.2	0.997	0.894	73.0	44.0	b
8	1	0.253	5	0.4	0.997	0.894	73.0	27.1	b
8	2	0.509	5	0.4	0.997	0.894	73.0	41.2	b
8	3	1.54	5	0.4	0.997	0.894	73.0	41.8	b
8	4	4.17	5	0.4	0.997	0.894	73.0	65.5	b
8	5	0.0938	5	0.4	0.997	0.894	73.0	30.8	b
8	6	0.512	5	0.4	0.997	0.894	73.0	38.3	b
8	7	2.26	5	0.4	0.997	0.894	73.0	54.0	b
8	8	5.5	5	0.4	0.997	0.894	73.0	69.5	b
8	9	22.2	5	0.4	0.997	0.894	73.0	326	b
8	10	13.9	5	0.4	0.997	0.894	73.0	129	b
8	11	0.97	5	0.4	0.997	0.894	73.0	33.7	b
8	12	0.121	5	0.4	0.997	0.894	73.0	26.4	b
8	13	1.3	5	0.4	0.997	0.894	73.0	41.8	b
8	14	0.72	5	0.4	0.997	0.894	73.0	36.8	b
8	15	0.373	5	0.4	0.997	0.894	73.0	32.5	b
8	16	0.076	5	0.4	0.997	0.894	73.0	25.5	b
7	12	0.0512	5	0.2	0.997	0.894	73.0	20.8	b
7	13	0.125	5	0.2	0.997	0.894	73.0	41.0	b
7	14	0.202	5	0.2	0.997	0.894	73.0	45.6	b

Table 38 (continued)

Data Set No.	Run No.	Superficial Gas Velocity (cm/sec)	Gas Disperser Design: Number of Inlets	Gas Disperser Design: Inlet Diameter (cm)	Properties of Liquid: Density (g/cm^3)	Properties of Liquid: Viscosity (cP)	Properties of Liquid: Surface Tension (dynes/cm)	Axial Dispersion Coefficient (cm^2/sec)	Ref.
7	15	0.304	5	0.2	0.997	0.894	73.0	37.0	b
7	16	0.405	5	0.2	0.997	0.894	73.0	36.5	b
7	17	0.525	5	0.2	0.997	0.894	73.0	49.2	b
7	18	0.65	5	0.2	0.997	0.894	73.0	56.0	b
7	19	0.76	5	0.2	0.997	0.894	73.0	62.7	b
7	20	0.923	5	0.2	0.997	0.894	73.0	52.2	b
7	21	1.525	5	0.2	0.997	0.894	73.0	46.8	b
7	22	3.15	5	0.2	0.997	0.894	73.0	59.5	b
7	23	4.4	5	0.2	0.997	0.894	73.0	69.5	b
7	24	5.81	5	0.2	0.997	0.894	73.0	75.2	b
7	25	7.13	5	0.2	0.997	0.894	73.0	96.5	b
7	26	16.3	5	0.2	0.997	0.894	73.0	87.2	b
9	1	0.0505	19	0.1	0.997	0.894	73.0	26.4	b
9	2	0.114	19	0.1	0.997	0.894	73.0	36.7	b
9	3	0.208	19	0.1	0.997	0.894	73.0	38.5	b
9	4	0.301	19	0.1	0.997	0.894	73.0	39.7	b
9	5	0.404	19	0.1	0.997	0.894	73.0	40.1	b
9	6	0.535	19	0.1	0.997	0.894	73.0	44.5	b
9	7	0.632	19	0.1	0.997	0.894	73.0	46.5	b
9	8	0.726	19	0.1	0.997	0.894	73.0	47.0	b
9	9	0.919	19	0.1	0.997	0.894	73.0	44.9	b
9	10	1.48	19	0.1	0.997	0.894	73.0	42.8	b
9	11	3.02	19	0.1	0.997	0.894	73.0	54.4	b
9	12	4.24	19	0.1	0.997	0.894	73.0	62.5	b
9	13	5.71	19	0.1	0.997	0.894	73.0	80.4	b
9	14	7.38	19	0.1	0.997	0.894	73.0	124	b
9	15	13.8	19	0.1	0.997	0.894	73.0	155	b

Table 38 (continued)

Data Set No.	Run No.	Superficial Gas Velocity (cm/sec)	Gas Dispersor Design: Number of Inlets	Gas Dispersor Design: Inlet Diameter (cm)	Properties of Liquid: Density (g/cm^3)	Properties of Liquid: Viscosity (cP)	Properties of Liquid: Surface Tension (dynes/cm)	Axial Dispersion Coefficient (cm^2/sec)	Ref.
10	1	0.0525	37	0.1	0.997	0.894	73.0	27.3	b
10	2	0.119	37	0.1	0.997	0.894	73.0	33.3	b
10	3	0.171	37	0.1	0.997	0.894	73.0	40.4	b
10	4	0.289	37	0.1	0.997	0.894	73.0	37.8	b
10	5	0.393	37	0.1	0.997	0.894	73.0	33.7	b
10	6	0.529	37	0.1	0.997	0.894	73.0	34.2	b
10	7	0.687	37	0.1	0.997	0.894	73.0	45.0	b
10	8	0.78	37	0.1	0.997	0.894	73.0	48.0	b
10	9	0.945	37	0.1	0.997	0.894	73.0	48.0	b
10	10	1.52	37	0.1	0.997	0.894	73.0	44.4	b
10	11	2.97	37	0.1	0.997	0.894	73.0	58.2	b
10	12	4.36	37	0.1	0.997	0.894	73.0	121	b
10	13	5.6	37	0.1	0.997	0.894	73.0	95.0	b
10	14	7.35	37	0.1	0.997	0.894	73.0	101	b
10	15	12.8	37	0.1	0.997	0.894	73.0	136	b
10	16	24.6	37	0.1	0.997	0.894	73.0	214	b
10	17	36.8	37	0.1	0.997	0.894	73.0	228	b
11	1	0.112	37	0.2	0.997	0.894	73.0	36.7	b
11	2	0.376	37	0.2	0.997	0.894	73.0	34.7	b
11	3	0.67	37	0.2	0.997	0.894	73.0	39.3	b
11	4	0.0703	37	0.2	0.997	0.894	73.0	20.5	b
11	5	0.262	37	0.2	0.997	0.894	73.0	35.5	b
11	6	0.478	37	0.2	0.997	0.894	73.0	33.2	b
11	7	0.875	37	0.2	0.997	0.894	73.0	38.0	b
11	8	1.37	37	0.2	0.997	0.894	73.0	49.5	b
11	9	2.21	37	0.2	0.997	0.894	73.0	61.0	b
11	10	5.0	37	0.2	0.997	0.894	73.0	91.8	b

Table 38 (continued)

Data Set No.	Run No.	Superficial Gas Velocity (cm/sec)	Gas Disperser Design: Number of Inlets	Gas Disperser Design: Inlet Diameter (cm)	Properties of Liquid: Density (g/cm^3)	Properties of Liquid: Viscosity (cP)	Properties of Liquid: Surface Tension (dynes/cm)	Axial Dispersion Coefficient (cm^2/sec)	Ref.
11	11	3.58	37	0.2	0.997	0.894	73.0	80.0	b
11	12	0.182	37	0.2	0.997	0.894	73.0	33.9	b
11	13	7.28	37	0.2	0.997	0.894	73.0	100	b
11	14	29.1	37	0.2	0.997	0.894	73.0	269	b
12	1	0.737	37	0.4	0.997	0.894	73.0	33.4	b
12	2	0.0618	37	0.4	0.997	0.894	73.0	28.2	b
12	3	0.148	37	0.4	0.997	0.894	73.0	33.1	b
12	4	0.251	37	0.4	0.997	0.894	73.0	31.9	b
12	5	0.331	37	0.4	0.997	0.894	73.0	30.0	b
12	6	0.403	37	0.4	0.997	0.894	73.0	33.7	b
12	7	0.585	37	0.4	0.997	0.894	73.0	32.4	b
12	8	1.01	37	0.4	0.997	0.894	73.0	51.3	b
12	9	1.49	37	0.4	0.997	0.894	73.0	50.0	b
12	10	2.66	37	0.4	0.997	0.894	73.0	59.7	b
12	11	3.62	37	0.4	0.997	0.894	73.0	61.0	b
12	12	4.66	37	0.4	0.997	0.894	73.0	72.2	b
12	13	5.8	37	0.4	0.997	0.894	73.0	79.5	b
12	14	7.43	37	0.4	0.997	0.894	73.0	77.5	b
12	15	26.5	37	0.4	0.997	0.894	73.0	164	b
20	1	5.78	1	0.432	1.047	1.8	71.8	72.2	a
20	2	8.75	1	0.432	1.047	1.8	71.8	97.8	a
20	3	10.4	1	0.432	1.047	1.8	71.8	120	a
20	4	18.6	1	0.432	1.047	1.8	71.8	178	a
20	5	27.3	1	0.432	1.047	1.8	71.8	427	a
20	6	2.79	1	0.432	1.047	1.8	71.8	45.3	a
20	7	4.01	1	0.432	1.047	1.8	71.8	52.1	a

Table 38 (continued)

Data Set No.	Run No.	Superficial Gas Velocity (cm/sec)	Gas Disperser Design: Number of Inlets	Gas Disperser Design: Inlet Diameter (cm)	Properties of Liquid: Density (g/cm^3)	Properties of Liquid: Viscosity (cP)	Properties of Liquid: Surface Tension (dynes/cm)	Axial Dispersion Coefficient (cm^2/sec)	Ref.
20	8	0.53	1	0.432	1.047	1.8	71.8	26.5	a
20	9	0.41	1	0.432	1.047	1.8	71.8	26.5	a
20	10	0.75	1	0.432	1.047	1.8	71.8	31.2	a
20	11	1.21	1	0.432	1.047	1.8	71.8	34.5	a
20	12	2.21	1	0.432	1.047	1.8	71.8	48.2	a
21	1	0.91	1	0.432	1.163	12.1	67.9	27.6	a
21	2	0.49	1	0.432	1.163	12.1	67.9	21.4	a
21	3	0.31	1	0.432	1.163	12.1	67.9	18.9	a
21	4	1.24	1	0.432	1.163	12.1	67.9	27.8	a
21	5	2.35	1	0.432	1.163	12.1	67.9	34.1	a
21	6	3.0	1	0.432	1.163	12.1	67.9	37.2	a
21	7	4.11	1	0.432	1.163	12.1	67.9	44.4	a
21	8	5.77	1	0.432	1.163	12.1	67.9	51.0	a
21	9	9.1	1	0.432	1.163	12.1	67.9	75.3	a
21	10	10.3	1	0.432	1.163	12.1	67.9	79.2	a
21	11	16.1	1	0.432	1.163	12.1	67.9	105	a
21	12	24.9	1	0.432	1.163	12.1	67.9	144	a
21	13	37.4	1	0.432	1.163	12.1	67.9	214	a
30	1	0.405	1	0.102	0.997	0.894	73.0	29.6	22
30	2	0.493	1	0.102	0.997	0.894	73.0	27.3	22
30	3	0.74	1	0.102	0.997	0.894	73.0	29	22
30	4	1.50	1	0.102	0.997	0.894	73.0	33.3	22
30	5	2.55	1	0.102	0.997	0.894	73.0	39.1	22
30	6	3.64	1	0.102	0.997	0.894	73.0	52.0	22
30	7	0.256	1	0.102	0.997	0.894	73.0	26.9	22
30	8	0.404	1	0.102	0.997	0.894	73.0	28.4	22
30	9	0.405	1	0.102	0.997	0.894	73.0	28.6	22

Table 38 (continued)

Data Set No.	Run No.	Superficial Gas Velocity (cm/sec)	Gas Disperser Design: Number of Inlets	Gas Disperser Design: Inlet Diameter (cm)	Properties of Liquid: Density (g/cm^3)	Properties of Liquid: Viscosity (cP)	Properties of Liquid: Surface Tension (dynes/cm)	Axial Dispersion Coefficient (cm^2/sec)	Ref.
30	10	0.47	1	0.102	0.997	0.894	73.0	26.4	22
30	11	0.582	1	0.102	0.997	0.894	73.0	31.4	22
30	12	0.671	1	0.102	0.997	0.894	73.0	28.9	22
30	13	0.784	1	0.102	0.997	0.894	73.0	29.6	22
30	14	0.918	1	0.102	0.997	0.894	73.0	28.9	22
30	15	1.159	1	0.102	0.997	0.894	73.0	32.1	22
30	16	1.50	1	0.102	0.997	0.894	73.0	32.6	22
30	17	1.55	1	0.102	0.997	0.894	73.0	35.6	22
30	18	2.26	1	0.102	0.997	0.894	73.0	35	22
30	19	2.91	1	0.102	0.997	0.894	73.0	43.6	22
30	20	3.69	1	0.102	0.997	0.894	73.0	48	22
30	21	5.28	1	0.102	0.997	0.894	73.0	68.7	22
27	1	0.432	1	0.102	0.997	0.894	73.0	28.5	23
27	2	3.31	1	0.102	0.997	0.894	73.0	49.7	23
27	3	3.31	1	0.102	0.997	0.894	73.0	61.7	23
27	4	18.7	1	0.102	0.997	0.894	73.0	67.7	23
27	5	10.9	1	0.102	0.997	0.894	73.0	76.8	23
28	1	0.432	1	0.102	1.15	15	65.2	19.1	23
28	2	3.31	1	0.102	1.15	15	65.2	49.7	23
28	3	2.28	1	0.102	1.15	15	65.2	42.7	23
28	4	1.77	1	0.102	1.15	15	65.2	28.2	23
28	5	1.25	1	0.102	1.15	15	65.2	23.6	23
25	1	0.432	1	0.102	0.997	0.894	37.6	38.8	23
25	2	1.25	1	0.102	0.997	0.894	37.6	44.6	23
25	3	2.28	1	0.102	0.997	0.894	37.6	45.6	23
25	4	3.31	1	0.102	0.997	0.894	37.6	57.1	23

Table 38 (continued)

Data Set No.	Run No.	Superficial Gas Velocity (cm/sec)	Gas Disperser Design: Number of Inlets	Gas Disperser Design: Inlet Diameter (cm)	Properties of Liquid: Density (g/cm^3)	Properties of Liquid: Viscosity (cP)	Properties of Liquid: Surface Tension (dynes/cm)	Axial Dispersion Coefficient (cm^2/sec)	Ref.
25	5	0.201	1	0.102	0.997	0.894	37.6	37.9	23
25	6	4.48	1	0.102	0.997	0.894	37.6	89.1	23
26	1	0.201	1	0.102	0.997	0.894	53.2	37.9	23
26	2	3.31	1	0.102	0.997	0.894	53.2	55.0	23
26	3	0.432	1	0.102	0.997	0.894	53.2	40.2	23
26	4	4.48	1	0.102	0.997	0.894	53.2	79.4	23
29	1	1.25	1	0.102	0.997	0.894	64.7	39.0	23
32	1	10.2	1	0.432	0.997	0.894	73.0	113	25
32	2	15.0	1	0.432	0.997	0.894	73.0	148	25
32	3	18.5	1	0.432	0.997	0.894	73.0	139	25
32	4	23.3	1	0.432	0.997	0.894	73.0	176	25
32	5	21.0	1	0.432	0.997	0.894	73.0	145	25
32	6	24.4	1	0.432	0.997	0.894	73.0	282	25
32	7	25.4	1	0.432	0.997	0.894	73.0	192	25
32	8	37.7	1	0.432	0.997	0.894	73.0	265	25
32	9	29.8	1	0.432	0.997	0.894	73.0	258	25
32	10	0.384	1	0.432	0.997	0.894	73.0	21.4	25
32	11	2.83	1	0.432	0.997	0.894	73.0	46.0	25
32	12	1.59	1	0.432	0.997	0.894	73.0	33.1	25
32	13	0.380	1	0.432	0.997	0.894	73.0	31.0	25

[a] Data obtained during second study.

[b] Data obtained during third study.

Table 39. Experimentally Determined Values for the Axial Dispersion Coefficient in a 3.0-in.-ID Open Bubble Column

Gas disperser: one orifice, 0.432 cm ID

Data Set No.	Run No.	Superficial Gas Velocity (cm/sec)	Properties of Liquid			Axial Dispersion Coefficient (cm^2/sec)	Reference
			Density (g/cm^3)	Viscosity (cP)	Surface Tension (dynes/cm)		
18	1	0.81	1.04	2.05	71.5	50.0	a
18	2	0.0352	1.04	2.05	71.5	28.1	a
18	3	0.0768	1.04	2.05	71.5	43.2	a
18	4	0.122	1.04	2.05	71.5	38.2	a
18	5	0.196	1.04	2.05	71.5	48.9	a
18	6	0.285	1.04	2.05	71.5	51.8	a
18	7	0.425	1.04	2.05	71.5	45.0	a
18	8	0.553	1.04	2.05	71.5	48.7	a
18	9	1.025	1.04	2.05	71.5	46.2	a
18	10	1.86	1.04	2.05	71.5	64.0	a
18	11	2.85	1.04	2.05	71.5	66.4	a
18	12	5.66	1.04	2.05	71.5	89.1	a
18	13	8.26	1.04	2.05	71.5	92.2	a
18	14	0.0323	1.04	2.05	71.5	30.2	a
19	1	0.0318	1.15	10.7	70.0	27.0	a
19	2	0.0769	1.15	10.7	70.0	29.1	a
19	3	0.108	1.15	10.7	70.0	42.4	a
19	4	0.155	1.15	10.7	70.0	56.0	a
19	5	0.232	1.15	10.7	70.0	41.4	a
19	6	0.338	1.15	10.7	70.0	47.4	a
19	7	0.424	1.15	10.7	70.0	45.0	a
19	8	0.675	1.15	10.7	70.0	52.8	a
19	9	1.67	1.15	10.7	70.0	47.4	a
19	10	1.25	1.15	10.7	70.0	56.3	a
19	11	2.28	1.15	10.7	70.0	57.2	a
19	12	2.96	1.15	10.7	70.0	64.3	a
19	13	5.37	1.15	10.7	70.0	86.7	a
33	1	10.7	0.997	0.894	73.0	124	25
33	2	18.3	0.997	0.894	73.0	164	25
33	3	19.3	0.997	0.894	73.0	207	25
33	4	3.70	0.997	0.894	73.0	74	25
33	5	7.32	0.997	0.894	73.0	94.2	25
33	6	0.700	0.997	0.894	73.0	43.0	25
33	7	4.78	0.997	0.894	73.0	78.9	25
33	8	11.6	0.997	0.894	73.0	132	25
33	9	11.1	0.997	0.894	73.0	119	25
33	10	26.5	0.997	0.894	73.0	239	25

[a]Data obtained during third study.

Table 40. Experimentally Determined Values[a] for the Axial Dispersion Coefficient in a 6.0-in.-ID Open Bubble Column

Gas disperser: one orifice, 0.432 cm ID

Data Set No.	Run No.	Superficial Gas Velocity (cm/sec)	Properties of Liquid			Axial Dispersion Coefficient (cm^2/sec)
			Density (g/cm^3)	Viscosity (cP)	Surface Tension (dynes/cm)	
3	1	8.39	0.997	0.894	73.0	207
3	2	3.08	0.997	0.894	73.0	179
3	3	0.8	0.997	0.894	73.0	152
3	4	0.52	0.997	0.894	73.0	157
3	5	0.52	0.997	0.894	73.0	161
3	6	1.49	0.997	0.894	73.0	183
3	7	2.16	0.997	0.894	73.0	161
3	8	7.12	0.997	0.894	73.0	371
3	9	0.62	0.997	0.894	73.0	173
3	10	3.83	0.997	0.894	73.0	157
3	11	1.07	0.997	0.894	73.0	123
3	12	0.33	0.997	0.894	73.0	146
3	13	1.57	0.997	0.894	73.0	146
3	14	9.13	0.997	0.894	73.0	281
3	15	4.93	0.997	0.894	73.0	246
3	16	2.63	0.997	0.894	73.0	141
23	1	7.52	1.047	1.8	71.8	232
23	2	9.63	1.047	1.8	71.8	266
23	3	9.63	1.047	1.8	71.8	303
23	4	2.6	1.047	1.8	71.8	169.5
23	5	5.06	1.047	1.8	71.8	262
23	6	8.62	1.047	1.8	71.8	229
23	7	0.32	1.047	1.8	71.8	125
23	8	2.04	1.047	1.8	71.8	188
23	9	1.19	1.047	1.8	71.8	180
23	10	2.98	1.047	1.8	71.8	184
23	11	3.88	1.047	1.8	71.8	211
23	12	2.98	1.047	1.8	71.8	181
23	13	6.0	1.047	1.8	71.8	216
24	1	1.21	1.16	12.1	67.9	153
24	2	1.62	1.16	12.1	67.9	149
24	3	0.27	1.16	12.1	67.9	162
24	4	3.99	1.16	12.1	67.9	181
24	5	2.86	1.16	12.1	67.9	180
24	6	1.98	1.16	12.1	67.9	146
24	7	6.01	1.16	12.1	67.9	216
24	8	8.4	1.16	12.1	67.9	254
24	9	0.51	1.16	12.1	67.9	157
24	10	0.75	1.16	12.1	67.9	173

[a]Data obtained during second study.

$$N_{Pe} = K\, N_{Re}^{\ a}\, N_{Su}^{\ b}\, N_{Ar}^{\ c}\, (\delta/d_c)^d\, n^e\, (1-h)^f\,, \qquad (35)$$

where

$$N_{Pe} = \text{Peclet number} = \frac{d_c V_g}{D}\,,$$

$$N_{Re} = \text{Reynolds number} = \frac{d_c V_g \rho_\ell}{\mu_\ell}\,,$$

$$N_{Su} = \text{Suratman number} = \frac{d_c \rho_\ell \sigma}{\mu_\ell^{\,2}}\,,$$

$$N_{Ar} = \text{Archimedes number} = \frac{d_c^{\,3} \rho_\ell^{\,2} g}{\mu_\ell^{\,2}}\,,$$

d_c = column diameter, cm,

V_g = superficial gas velocity, cm/sec,

D = axial dispersion coefficient, cm^2/sec,

ρ_ℓ = density of liquid, g/cm^3,

μ_ℓ = viscosity of liquid, g/cm·sec,

σ = surface tension of liquid, dynes/cm,

δ = gas distributor diameter, cm,

n = number of openings in gas distributor,

h = fraction of column volume occupied by gas, and

a, b, c, d, e, f, and K are constants to be determined by the method of least squares.

The quality of the data from the 1-in.-diam column was considered to be lower than that for the larger-diameter columns; hence only data obtained with column diameters of 1.5, 2, 3, and 6 in. were used in determining the final correlation. Because of the observed difference in behavior in the bubble- and slug-flow regions, the data were divided into two sets corresponding to the two flow regimes; each data set was then

correlated separately using the general power-law expression given by Eq. (35). The criterion for separating the data was that the manner of division should result in the best possible fit of the data to the two resulting power-law expressions. In determining the final expressions, all terms shown in Eq. (35) were considered; however, only those terms were retained for which the uncertainty in the value of the exponent was less than 30% of the value of the exponent, or which, when neglected, resulted in a poorer fit of the data as indicated by the F factor. The F factor is defined as:

$$F = \frac{\sum(\ln N_{Pe} - \overline{\ln N_{Pe}})^2}{\sum(\ln N_{Pe} - \ln N_{Pe}^c)^2} , \qquad (36)$$

where

$\ln N_{Pe}$ = natural logarithm of an experimentally determined value for the Peclet number,

$\overline{\ln N_{Pe}}$ = average of all values for the natural logarithm of the experimentally determined values of the Peclet number,

$\ln N_{Pe}^c$ = predicted value for the natural logarithm of the Peclet number,

and the indicated summations are over all data points considered. The values for the F factor for Eqs. (37) and (38) were 1200 and 125 respectively. Both of these values imply that the agreement between the experimentally determined values and the predicted values is very good. The final correlations resulting from the analysis are as follows:

for bubble flow,

$$N_{Pe} = 8.30\ N_{Re}^{0.82}\ N_{Ar}^{-0.44}\ n^{-0.094} ; \qquad (37)$$

for slug flow,

$$N_{Pe} = 0.70\ N_{Re}^{0.802}\ N_{Su}^{-0.422}\ (1 - h)^{3.10} . \qquad (38)$$

The expression for bubble flow is based on 190 data points; a comparison of the experimental and calculated values is shown in Fig. 41. The expression for slug flow is based on 122 data points; a comparison of the experimental and calculated values is shown in Fig. 42. Seven data points in the transition region between the bubble and slug flow regions were excluded from consideration in order to facilitate fitting of the data.

Comparisons of the predicted and experimentally determined values for the axial dispersion coefficient are shown in Figs. 43-54 for columns having diameters of 1, 1.5, 2, 3, and 6 in. In general, good agreement is observed. The predicted values for the 1-in.-diam column are about twice the experimentally determined values (which were not used in developing the correlation) and show the greatest divergence from the experimentally determined values. The points at which the transition from bubble flow to slug flow occurs are indicated in the figures. These points are in good agreement with visual observations on the changes in flow mode.

9.8 Discussion of Data on Axial Mixing and Gas Holdup

The following observations can be made with regard to the general flow behavior in open bubble columns and to the effects on axial dispersion and gas holdup caused by variations in column diameter, viscosity and surface tension of the liquid, gas inlet orifice diameter, and number of orifices in the gas inlet.

9.8.1 Flow Regimes and Effect of Gas Superficial Velocity

Three different flow regimes can be identified by visual observation of the mixing patterns in open bubble columns and by examination of the associated data on axial mixing and gas holdup. These regimes — bubble flow, transition flow, and slug flow — are observed successively as the superficial gas velocity is increased from low to high values.

For superficial gas velocities below about 1 cm/sec, the bubbles rise as discrete entities and do not occupy the entire cross section of the column. The gas holdup increases linearly with increases in the

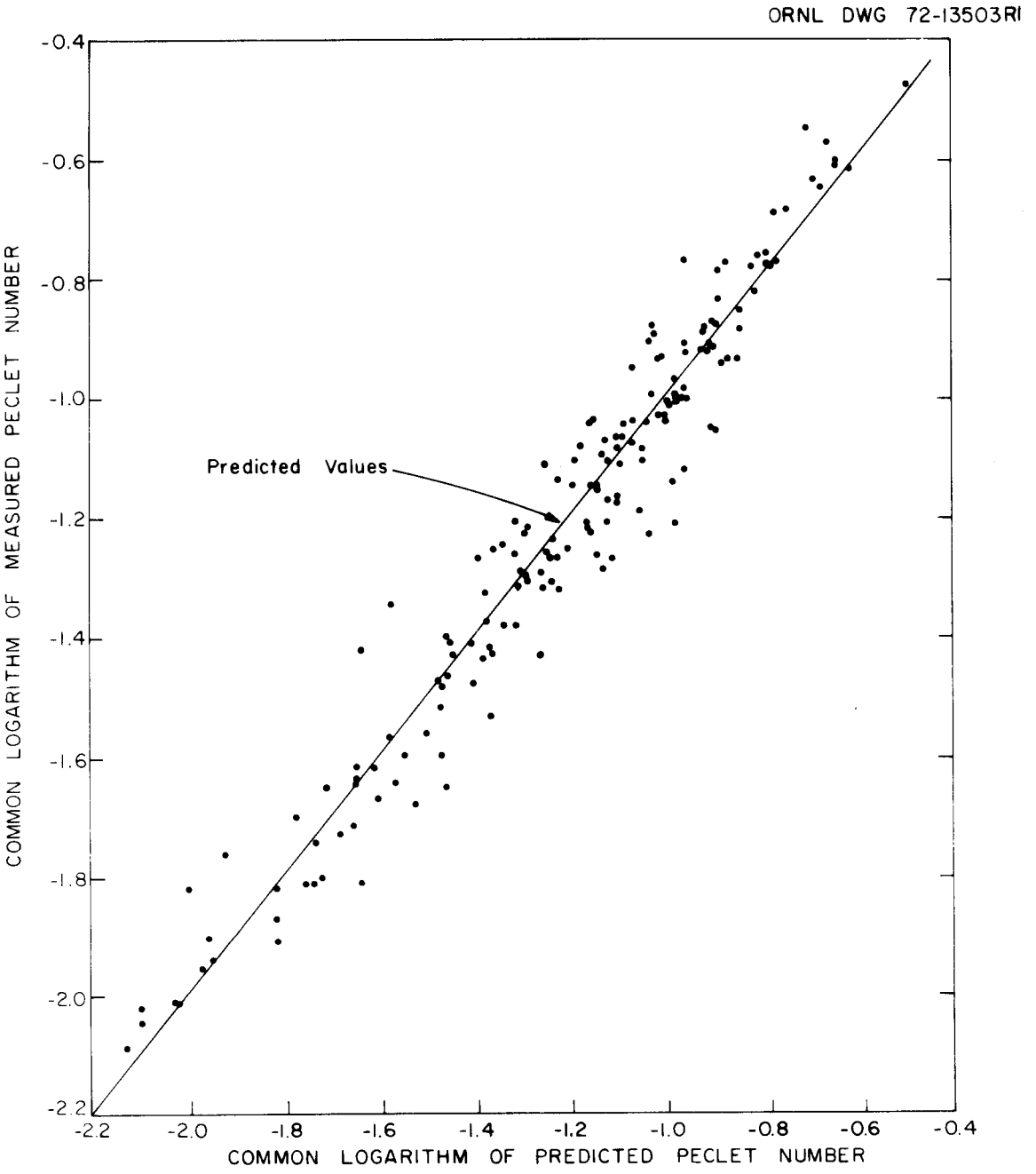

Fig. 41. Comparison of Predicted and Experimentally-Determined Values for the Peclet Number During Bubble Flow in Columns Having Diameters Ranging from 1.5 to 6 in.

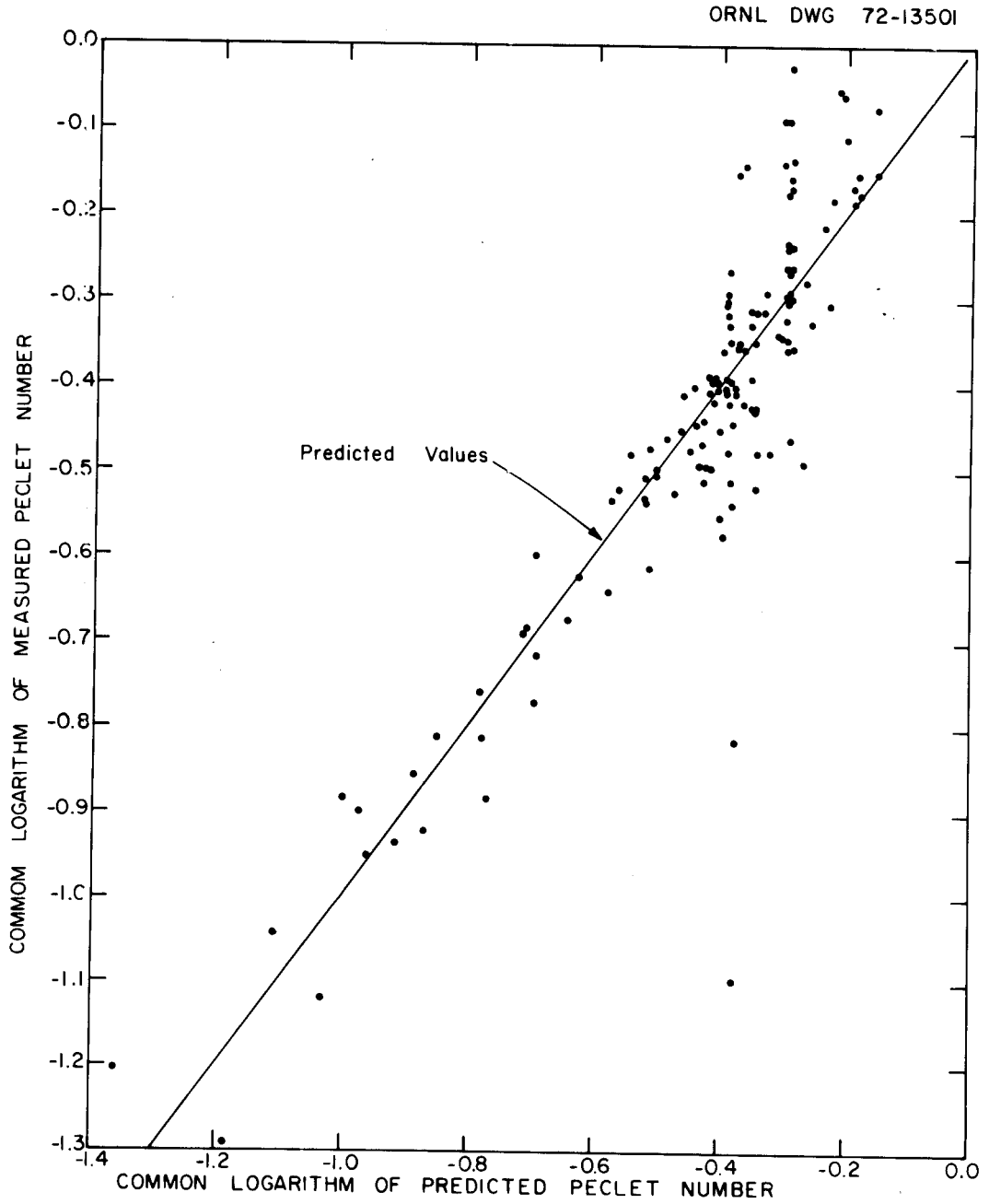

Fig. 42. Comparison of Predicted and Experimentally-Determined Values for the Peclet Number During Slug Flow in Columns Having Diameters Ranging from 1.5 to 6 in.

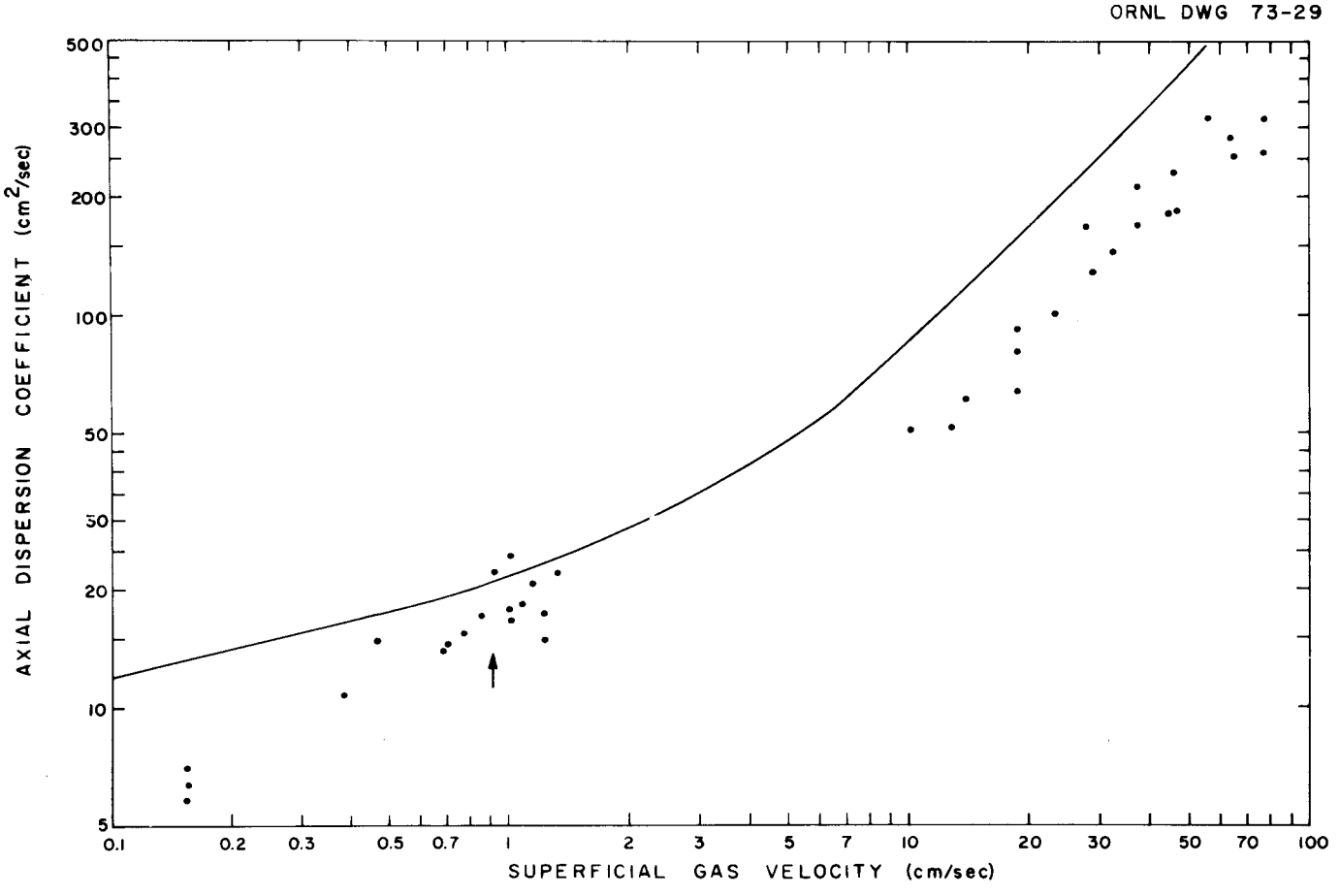

Fig. 43. Variation of Axial Dispersion Coefficient with Changes in Superficial Gas Velocity in a 1.0-in.-ID Bubble Column Filled with Water. The transition point between the bubble- and slug-flow regimes is denoted by a vertical arrow.

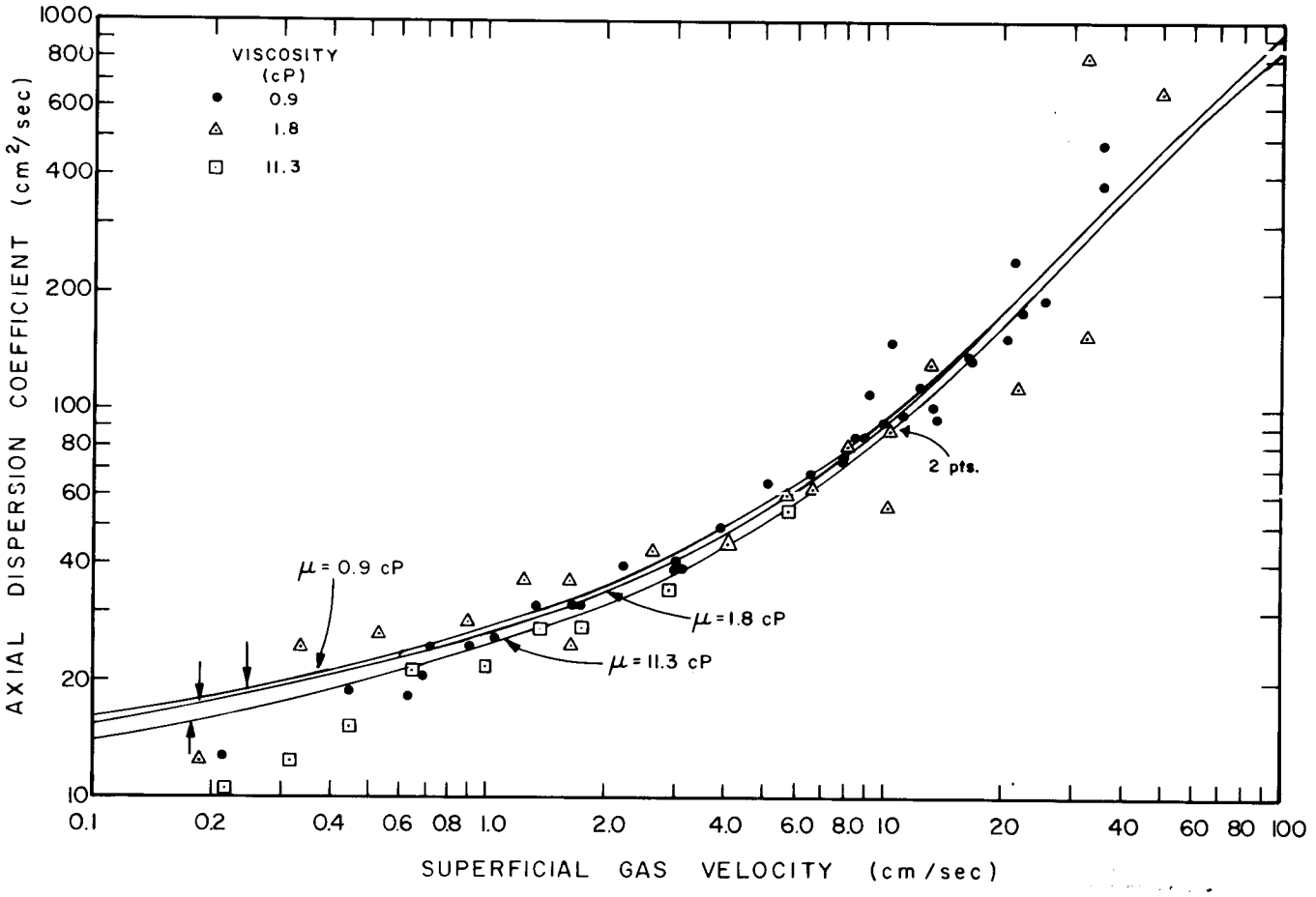

Fig. 44. Variation of Axial Dispersion Coefficient with Changes in Superficial Gas Velocity and Viscosity of Liquid in a 1.5-in.-ID Bubble Column. The transition between the bubble- and slug-flow regimes is denoted by vertical arrows for the three viscosity values considered.

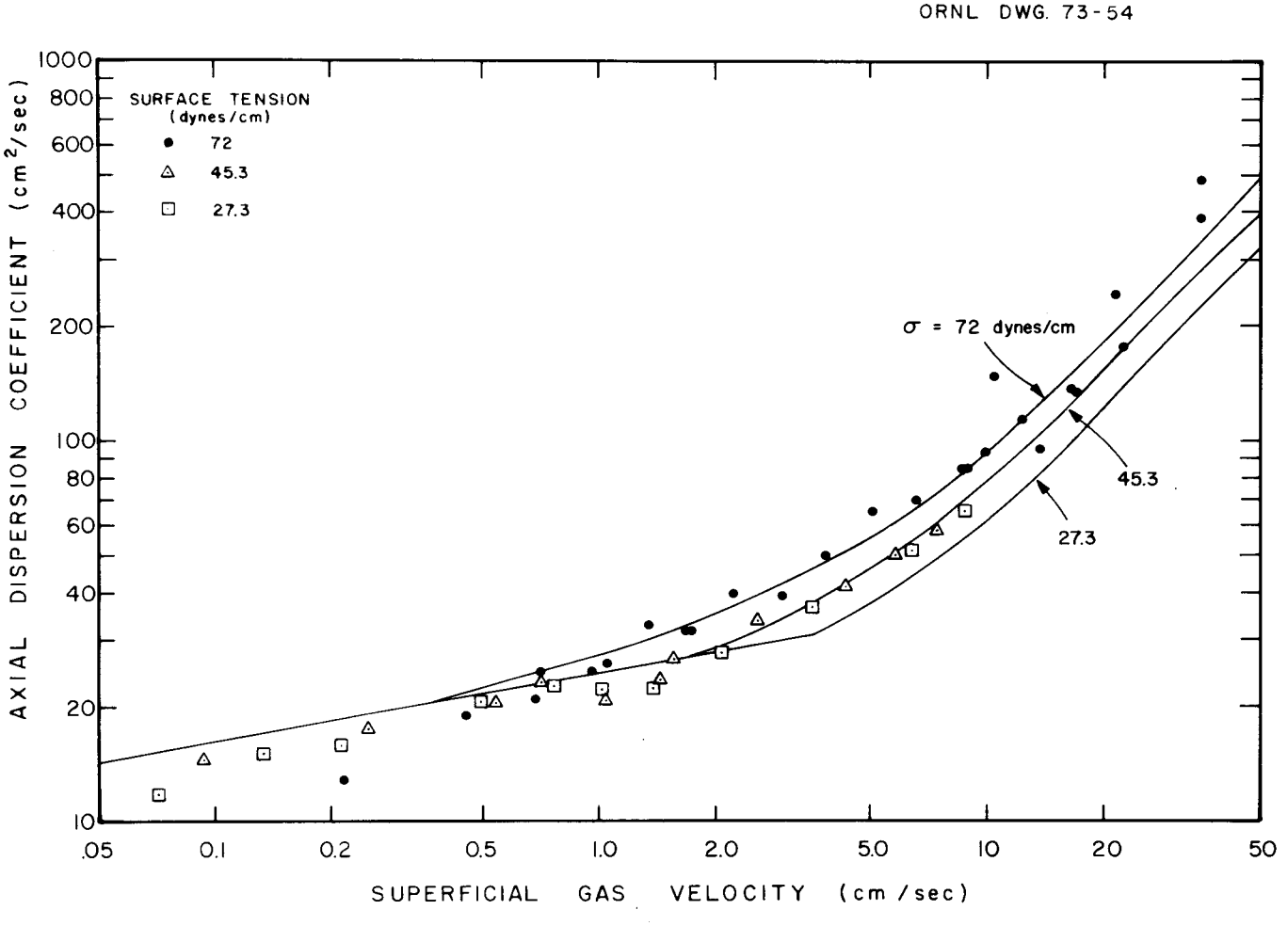

Fig. 45. Variation of Axial Dispersion Coefficient with Changes in Superficial Gas Velocity and Surface Tension of Liquid in a 1.5-in.-ID Bubble Column Having a Single 0.432-cm-ID Gas Inlet.

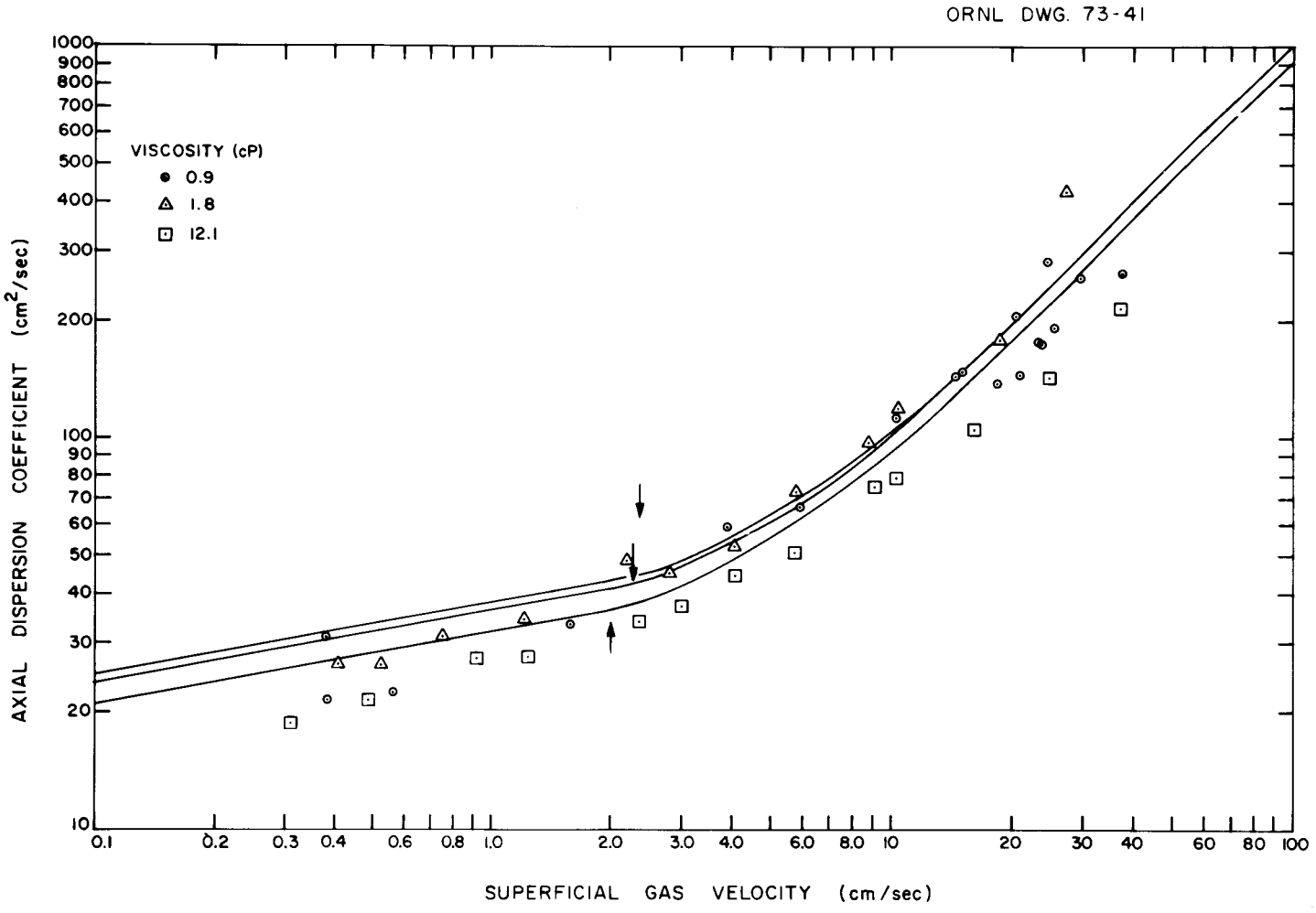

Fig. 46. Variation of Axial Dispersion Coefficient with Changes in Superficial Gas Velocity and Viscosity of Liquid in a 2.0-in.-ID Bubble Column. The transition points between bubble- and slug-flow regimes are denoted by vertical arrows.

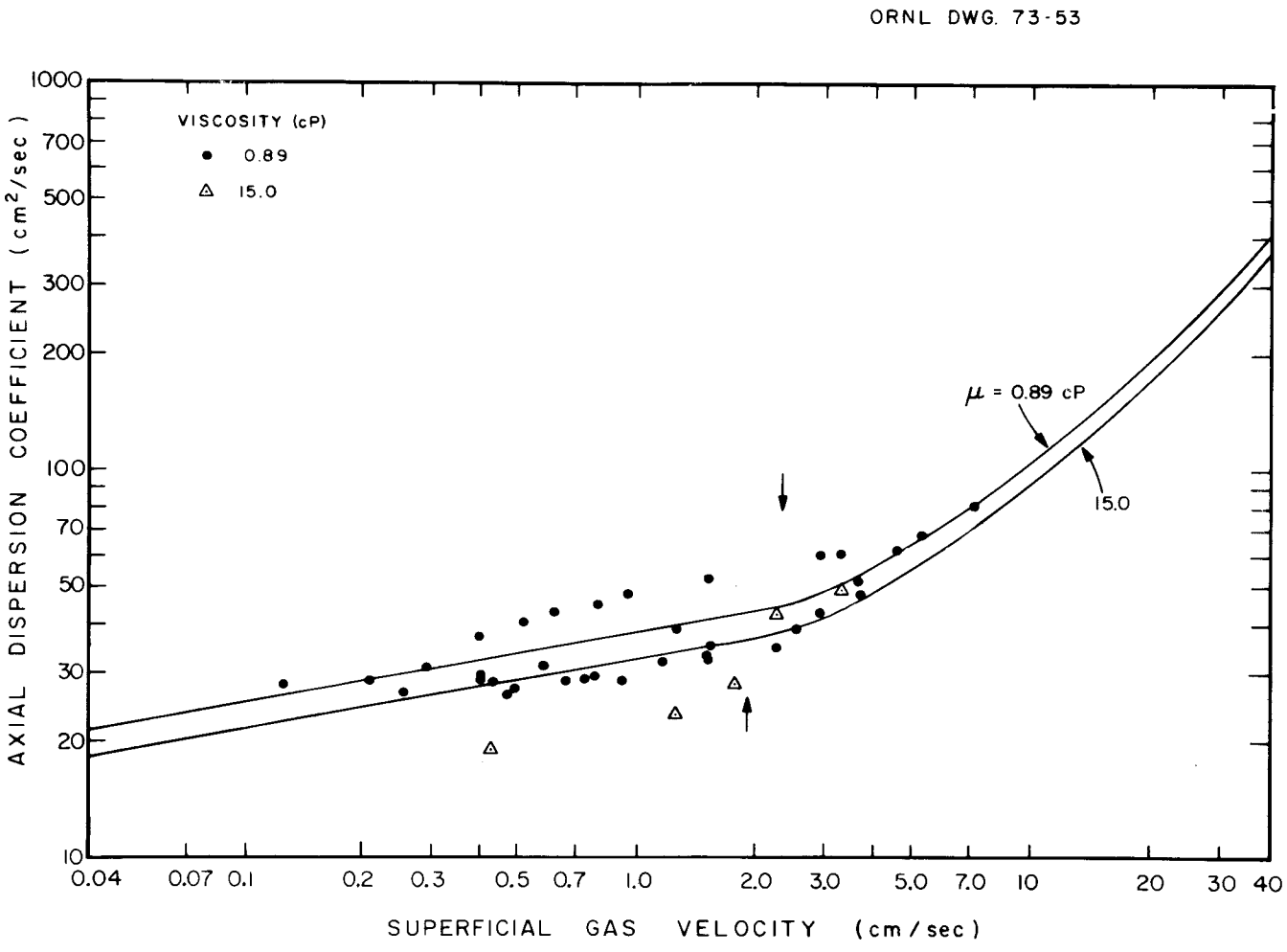

Fig. 47. Variation of Axial Dispersion Coefficient with Changes in Superficial Gas Velocity and Viscosity of Liquid in a 2.0-in.-ID Bubble Column. The transition points between bubble- and slug-flow regimes are denoted by vertical arrows.

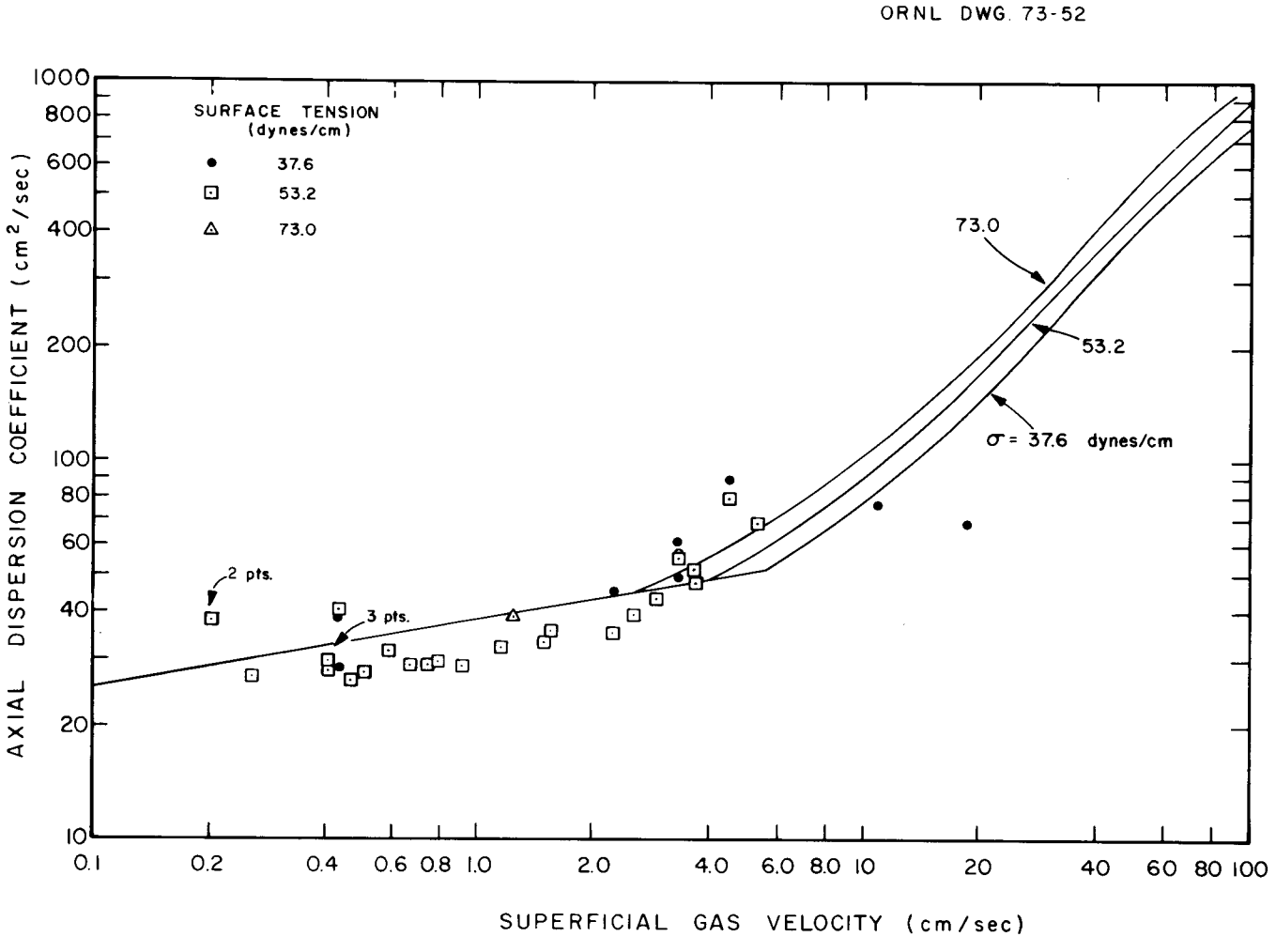

Fig. 48. Variation of Axial Dispersion Coefficient with Changes in Superficial Gas Velocity and Surface Tension of Liquid in a 2-in.-ID Bubble Column.

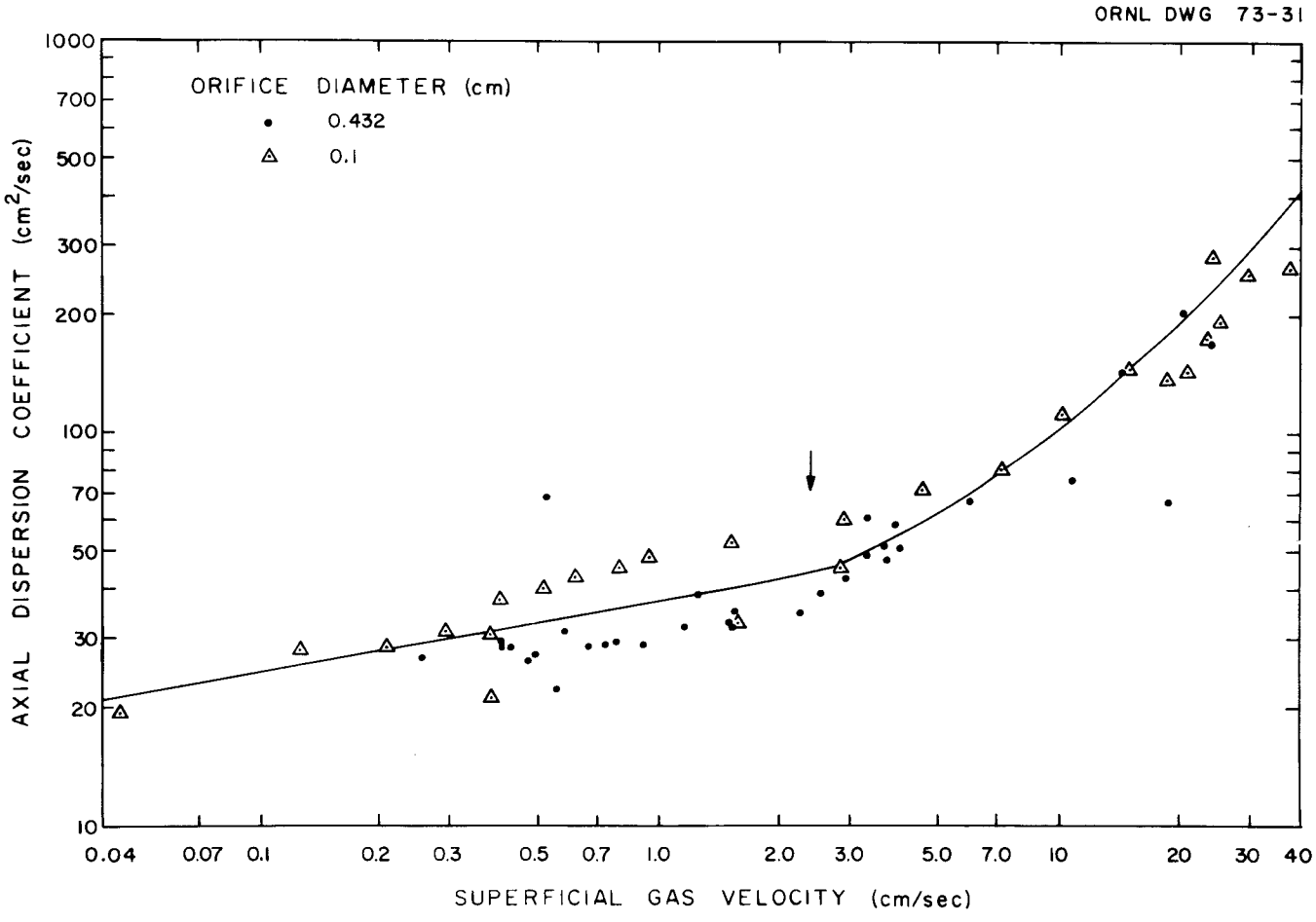

Fig. 49. Variation of Axial Dispersion Coefficient with Changes in Superficial Gas Velocity and Gas Inlet Diameter in a 2.0-in.-ID Bubble Column. The transition point between the bubble- and slug-flow regimes is denoted by a vertical arrow.

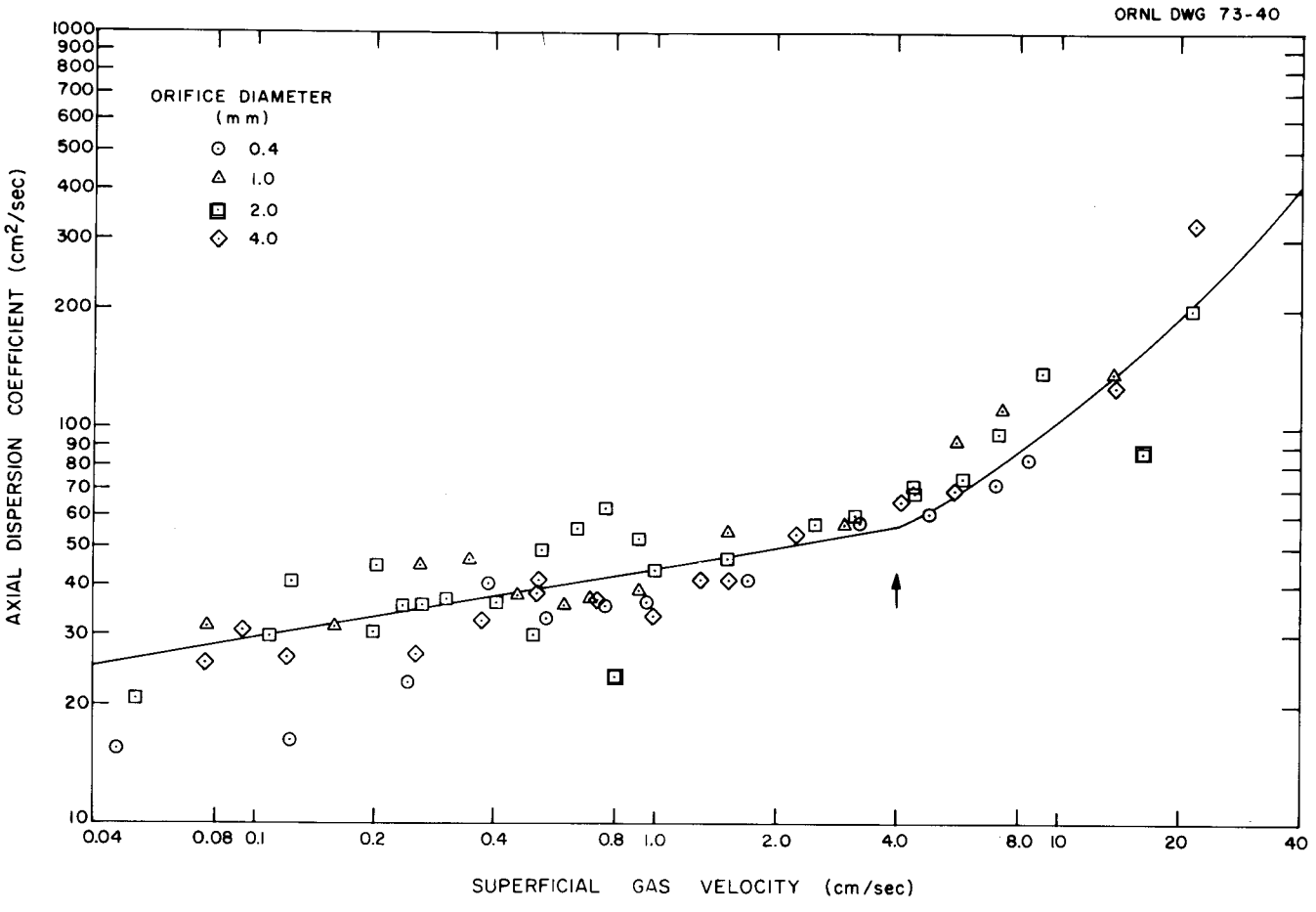

Fig. 50. Variation of Axial Dispersion Coefficient with Changes in Superficial Gas Velocity and Gas Inlet Diameter for a Column Diameter of 2 in. The gas distributor consisted of five orifices of the indicated diameter. The transition point between the bubble- and slug-flow regimes is denoted by a vertical arrow.

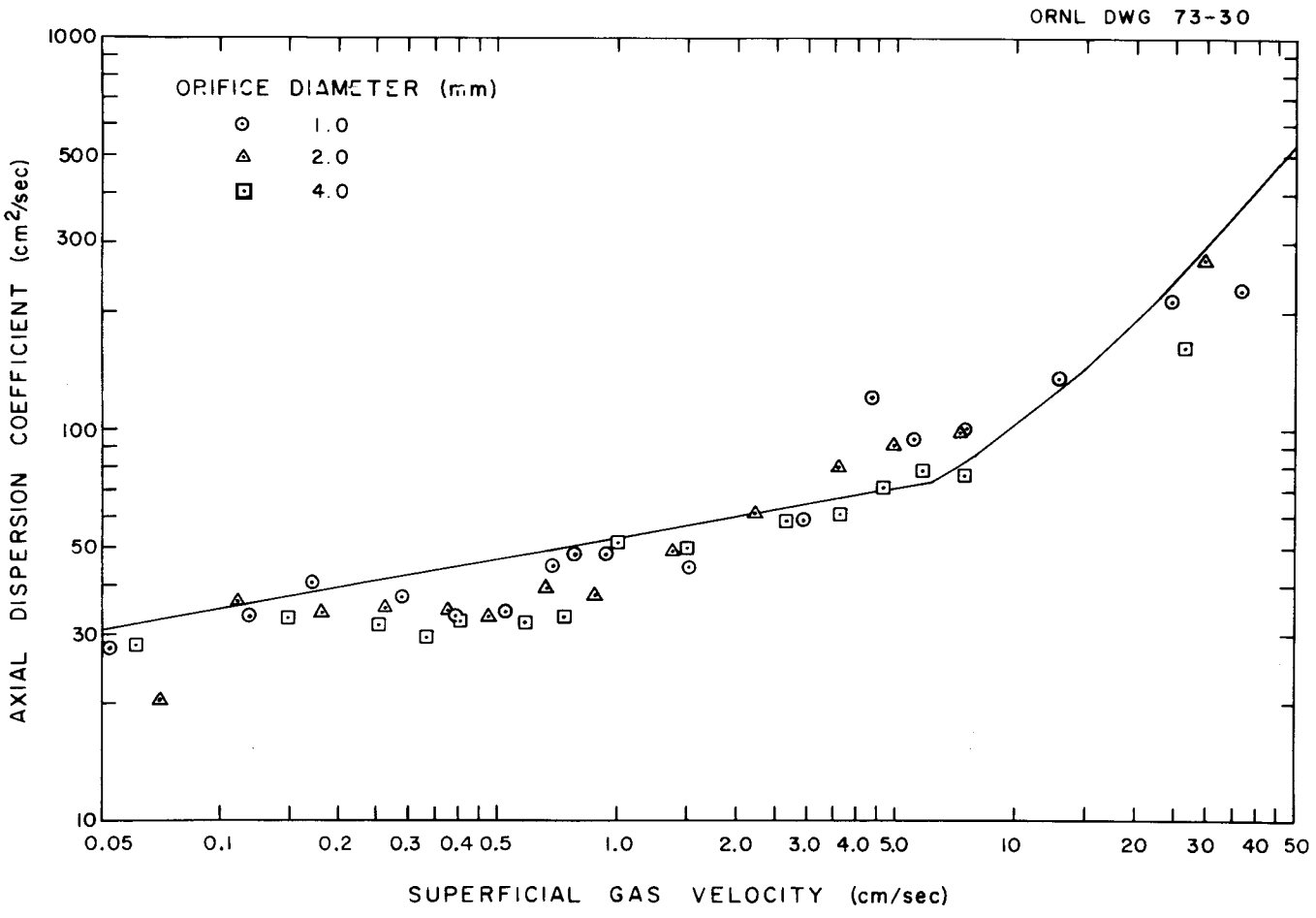

Fig. 51. Variation of Axial Dispersion Coefficient with Changes in Superficial Gas Velocity and Gas Inlet Orifice Diameter for a Column Diameter of 2 in. The gas inlet consisted of 37 orifices of the indicated diameter.

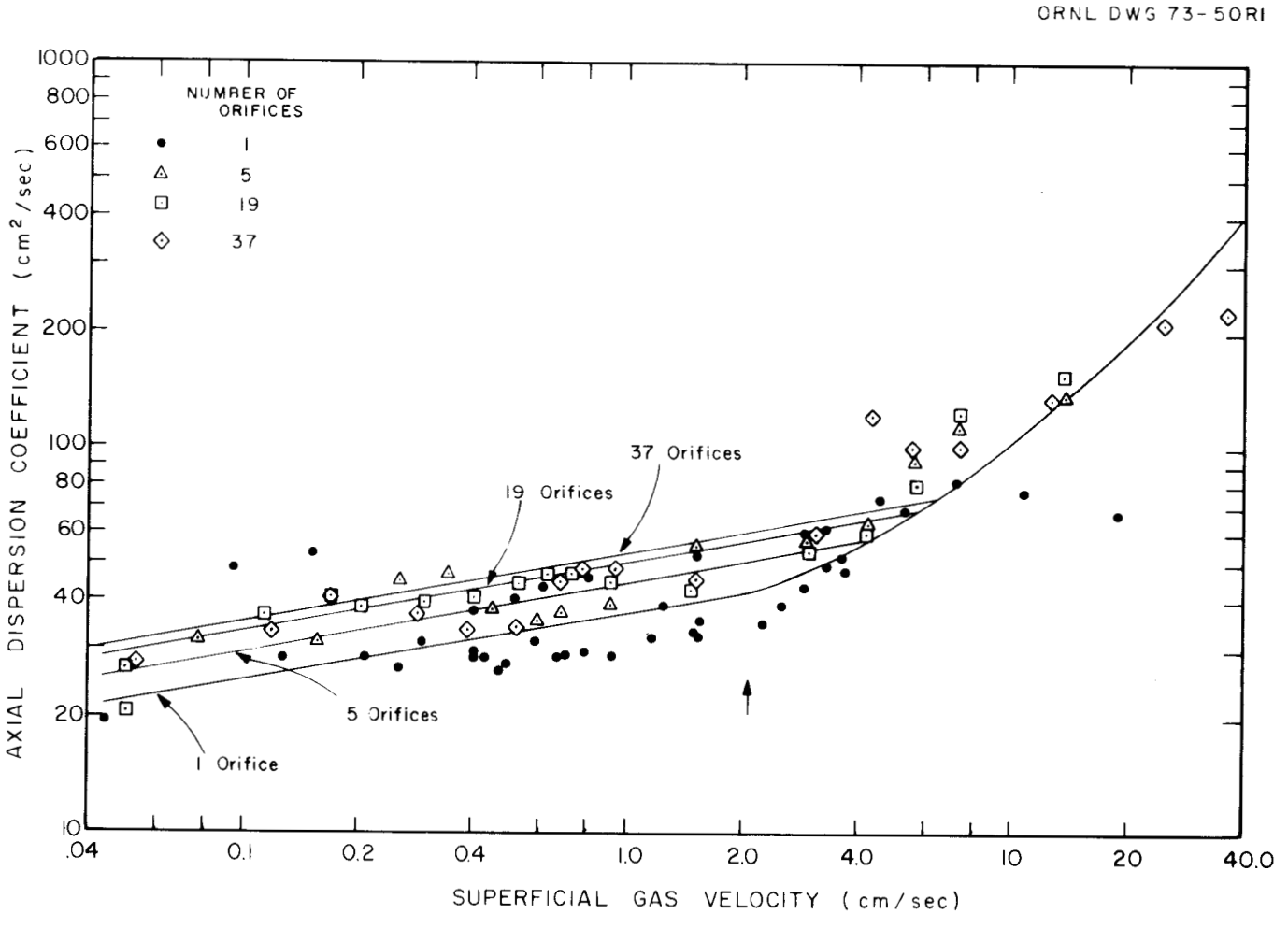

Fig. 52. Variation of Axial Dispersion Coefficient with Changes in Superficial Gas Velocity and Number of Orifices in Gas Distributor in a 2-in.-ID Column Filled with Water. The gas inlet orifices had a diameter of 1 mm. The transition between the bubble- and slug-flow regimes for the case of a single orifice is denoted by a vertical arrow.

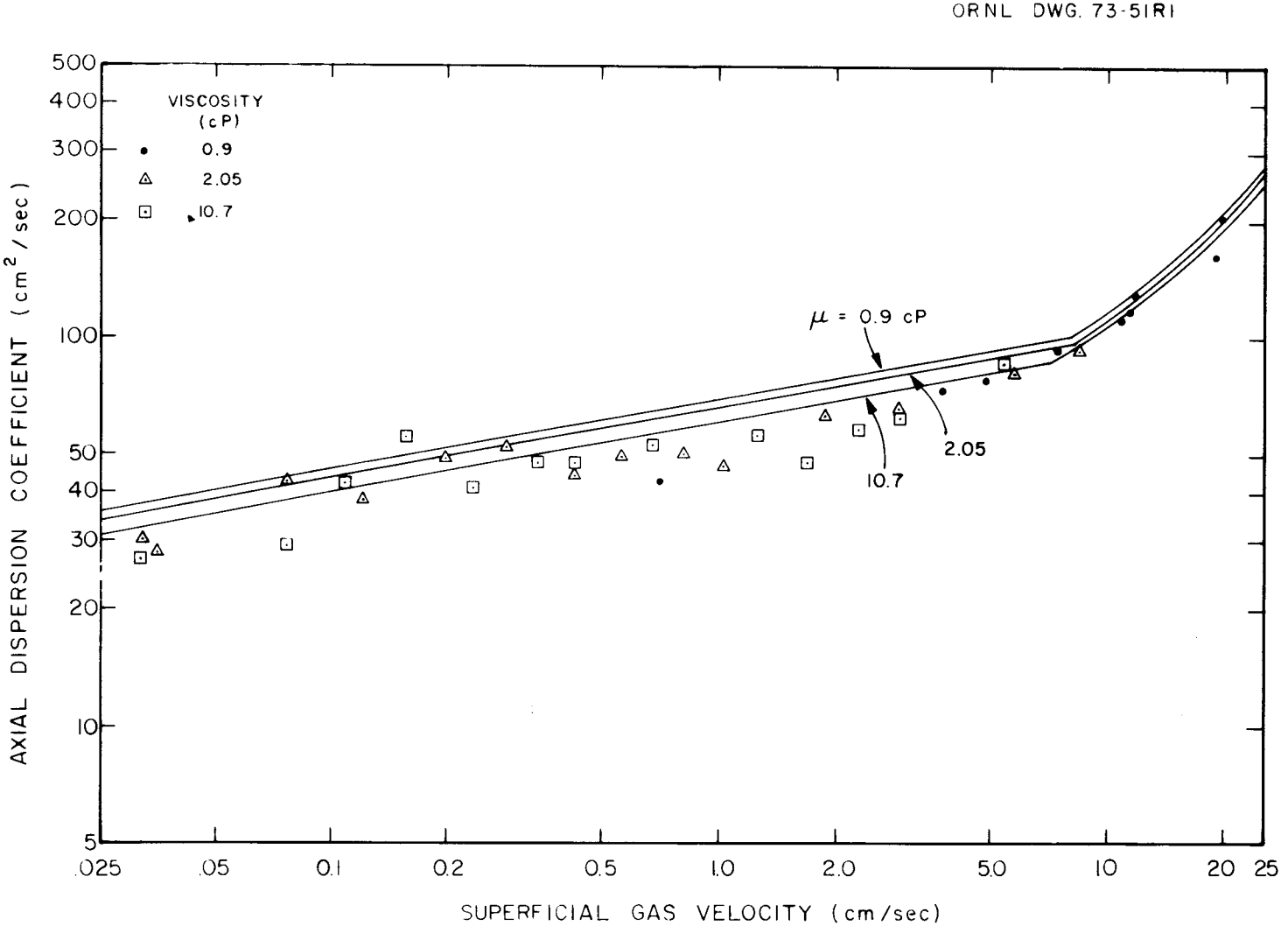

Fig. 53. Variation of Axial Dispersion Coefficient with Changes in Superficial Gas Velocity and Viscosity of Liquid in a Column Having a Diameter of 3 in.

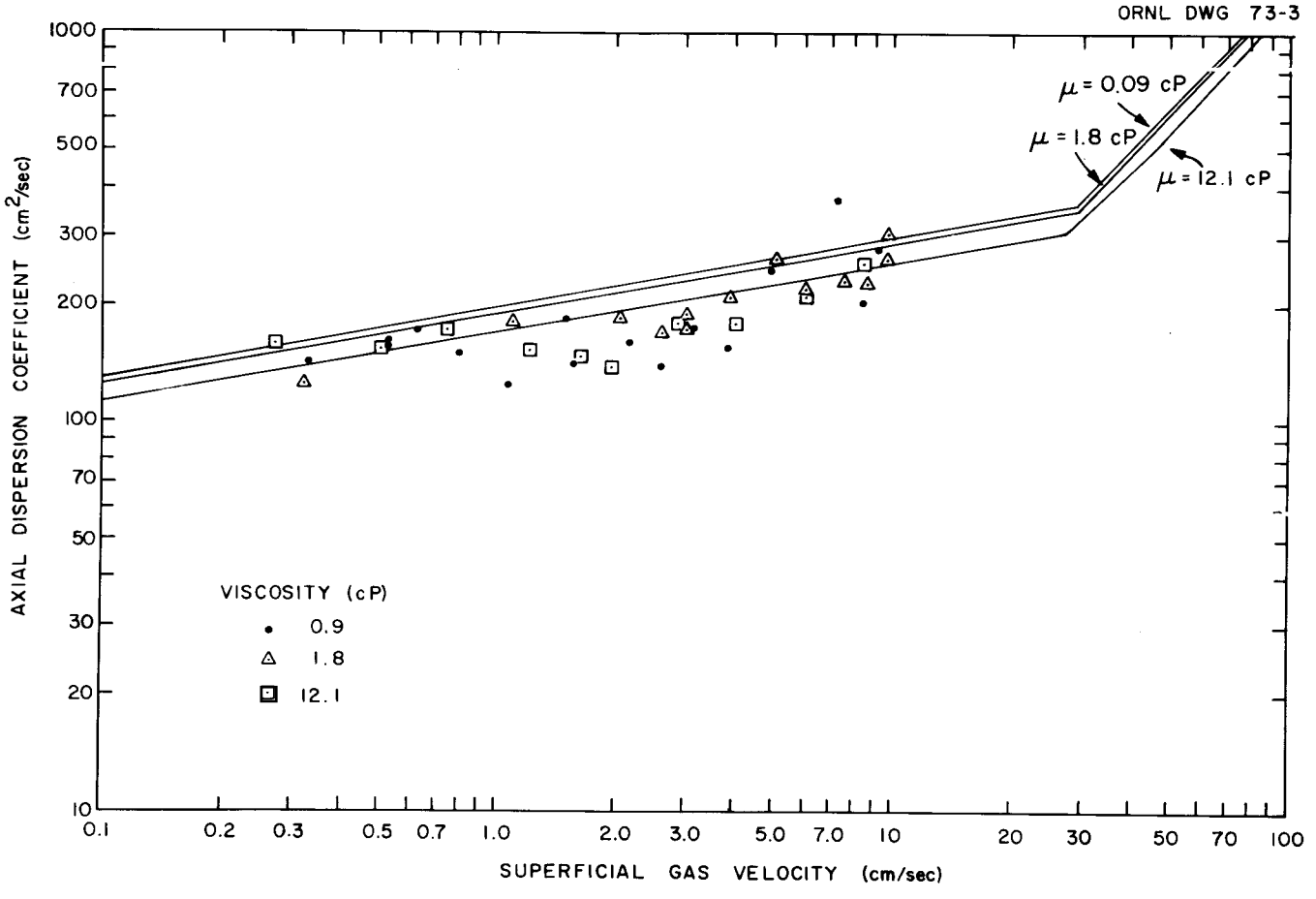

Fig. 54. Variation of Axial Dispersion Coefficient with Changes in Superficial Gas Velocity and Viscosity of Liquid in a 6-in.-ID Bubble Column.

superficial gas velocity. The bubble rise velocity (for the case of a negligible liquid superficial velocity) is determined by the ratio of the superficial gas velocity to the gas holdup and remains essentially constant at a value in the range of about 25 to 40 cm/sec. This flow regime is designated as bubble flow. Bubble size and bubble size distribution in this flow regime are a complex function of gas inlet orifice diameter, gas flow rate, and properties of the liquid phase. For air-water systems, bubble rise velocities of 25 to 30 cm/sec have been reported in the literature as approximate values.[30,31]

As the superficial gas velocity is increased, bubble-bubble interactions become important and some coalescence is observed at the top of the column, resulting in the formation of larger bubbles. This marks the onset of transition flow, and further increases in the superficial gas velocity lead to greater coalescence and the formation of bubble platelets having a size in the horizontal direction equal to about 90% of the column diameter and lengths of about 1 to 2 cm. Further increases in the superficial gas velocity result in still greater coalescence and the formation of bullet-like bubbles whose diameters are almost equal to the column diameter. These large-diameter bubbles, or "slugs", are initially formed near the top of the column; however, the point of slug formation gradually moves downward with increases in the superficial gas velocity. Thus, in the transition region, part of the column may be characterized by bubble flow and part by slug flow, and the axial dispersion coefficient begins to increase at a higher rate with increases in the superficial gas velocity.

In the slug flow regime, bubbles that have a smooth, spherical cap and a flat trailing edge are present throughout the column. The bubbles or slugs are usually 2 to 7 cm in length, although even greater lengths are observed at very high gas velocities. In this flow regime, acceleration of the liquid near the column wall occurs since the liquid must pass through a narrow, annular channel between the gas-liquid interface and the column wall. Vigorous mixing is produced at the rear of each slug, and the axial dispersion coefficient increases rapidly with increases in the superficial gas velocity. In slug flow, the dependence

of gas holdup on superficial gas velocity diverges from the linear relationship observed at low superficial gas velocities.

The mixing patterns observed in a 6-in.-diam bubble column for superficial gas velocities greater than 6 cm/sec were different from those observed for smaller columns. No pronounced transition to slug flow was observed; instead, very turbulent circulation and mixing patterns were seen. Three types of bubble motion were noted: small bubble swirls that circulated downward along the column wall; long, extended bubbles that spiraled up the column across the entire cross-section; and a core of bubbles that ascended up the center of the column. Similar circulation patterns have been observed by Towell et al.[32] in large-diameter bubble columns.

The variation of the axial dispersion coefficient with changes in the superficial gas velocity is shown in Fig. 55 for water-filled columns having diameters of 1, 1.5, 2, 3, and 6 in. The axial dispersion coefficient was found to depend on the superficial gas velocity to the 0.12 and 0.63 powers in bubble and slug flow, respectively, regardless of the column diameter.

9.8.2 Effect of Column Diameter

The variation of the axial dispersion coefficient with changes in column diameter is shown in Fig. 56 for superficial gas velocities of 0.5 cm/sec (bubble flow) and 25 cm/sec (slug flow). In each of the two flow regimes, the axial dispersion coefficient increases rapidly with increases in the column diameter. In bubble flow, the axial dispersion coefficient shows a 1.5 power dependence on column diameter. Aoyama[33] and Imafuku[34] also reported a 1.5 power dependence of the axial dispersion coefficient on column diameter. Ohki[35] derived semi-empirical relations which suggest that the dispersion coefficient is dependent on the column diameter to the 2.0 power in bubble flow. The power dependence of the dispersion coefficient on column diameter, as predicted by Eqs. (33) and (38), is not constant but has a value of about 0.64. The semiempirical relations derived by Ohki[35] suggest a power dependence of 1.0.

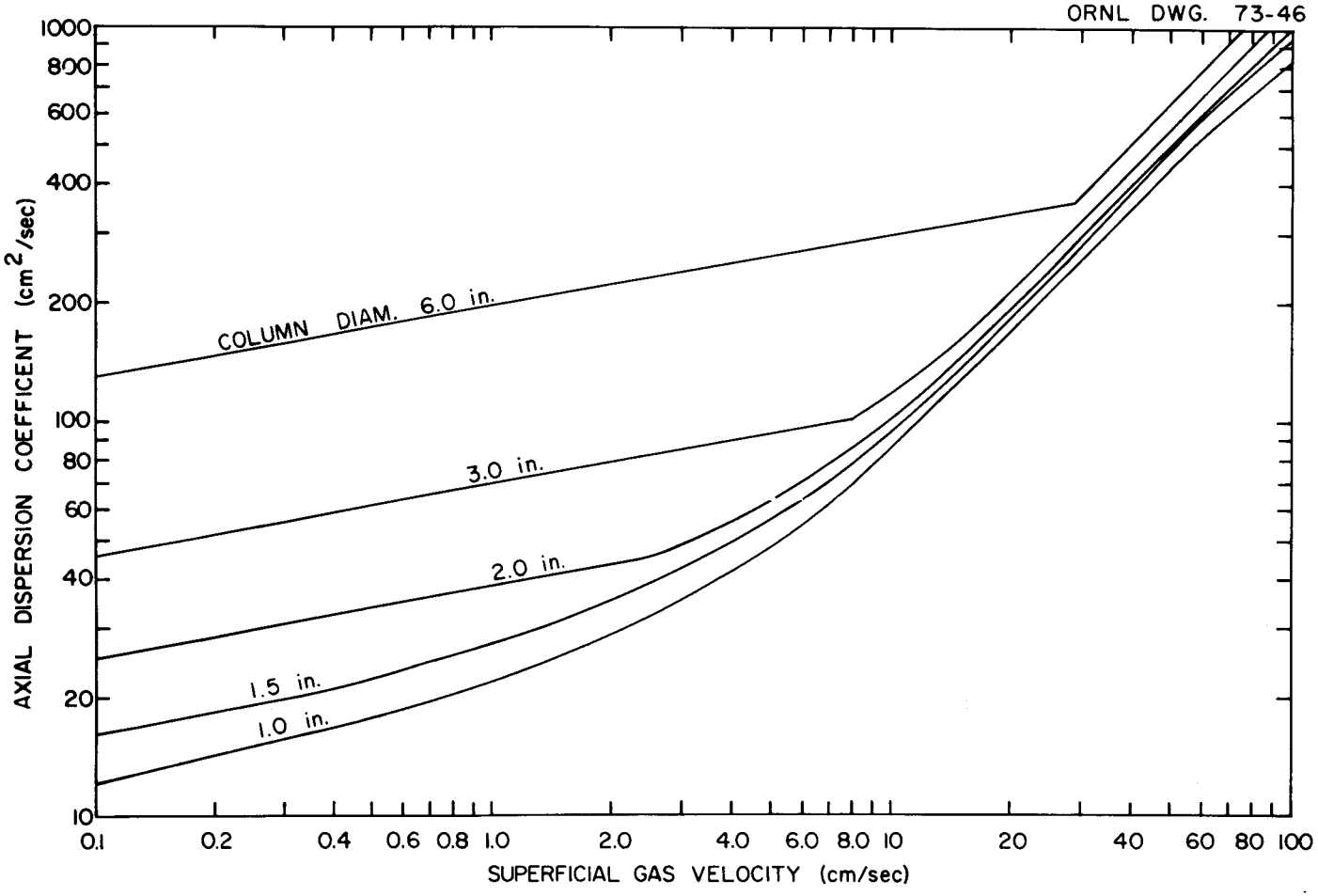

Fig. 55. Variation of Axial Dispersion Coefficient with Changes in Superficial Gas Velocity and Column Diameter.

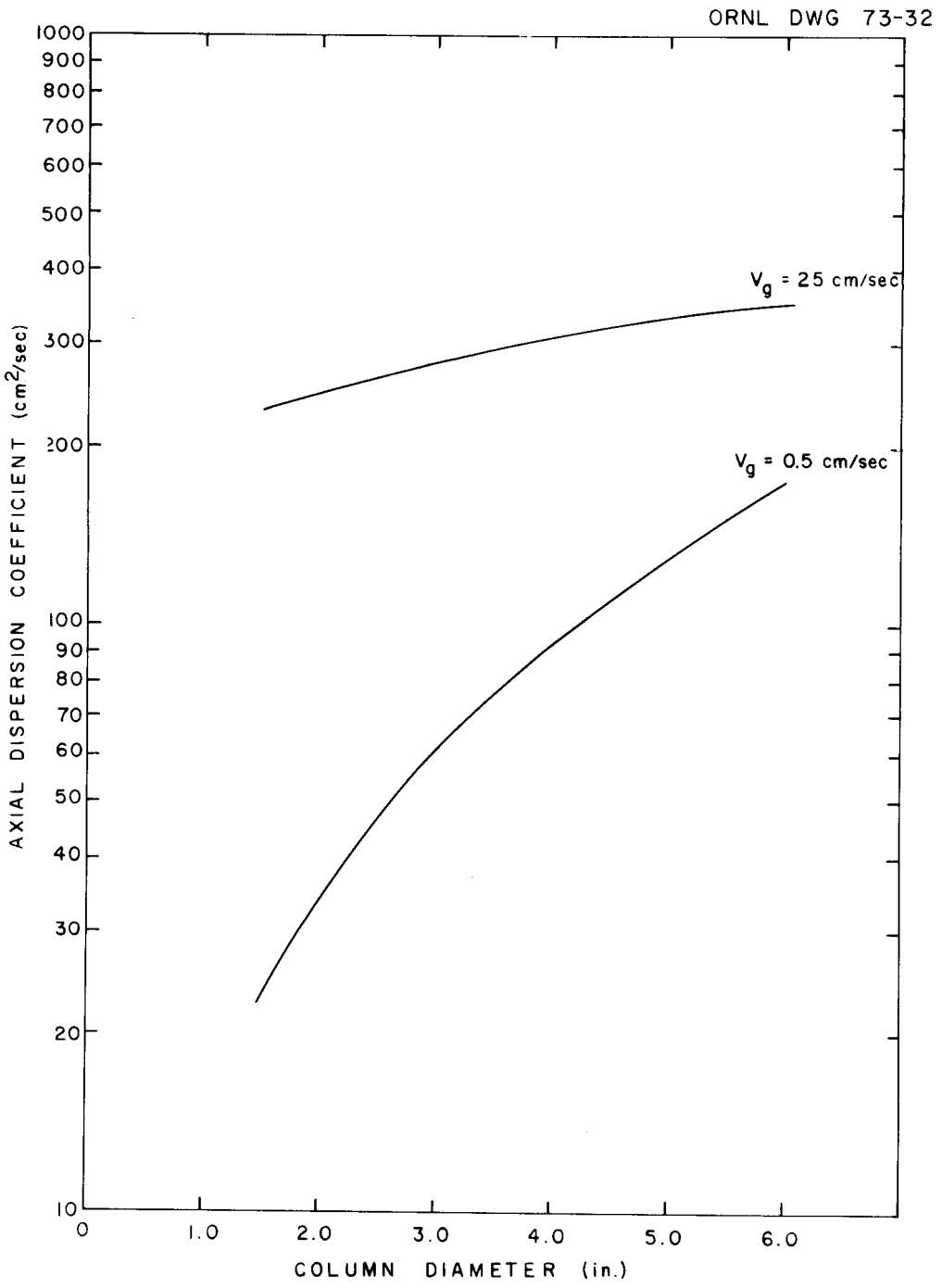

Fig. 56. Variation of Axial Dispersion Coefficient with Changes in Column Diameter and Superficial Gas Velocity.

Although the transition from bubble to slug flow in the present studies did not occur at a single value of the superficial gas velocity, certain qualitative conclusions can be inferred. As the column diameter is increased, the superficial gas velocity at which slug flow is obtained increases rapidly. Slug flow was obtained in the 1.5-, 2-, and 3-in. columns at superficial gas velocities of 0.005, 1.14, and 5.54 cm/sec, respectively, for bubble columns filled with water; however, slug flow was not obtained in the 6-in.-diam column at velocities as high as 9.5 cm/sec.

9.8.3 Effect of Viscosity of the Liquid Phase

The variation of the axial dispersion coefficient with changes in the viscosity of the liquid and the superficial gas velocity is shown in Figs. 44, 46, 47, 53, and 54 for columns having diameters of 1.5, 2, 3, and 6 in. In each case, no observable change was noted in the axial dispersion coefficient as the viscosity of the liquid was increased from 0.9 cP to about 2 cP. A further increase in viscosity to about 11 cP resulted in a decrease of about 20% in the axial dispersion coefficient for the smaller columns (1.5 and 2 in. in diameter), while the effect was less pronounced for the 3-in.-diam column. However, increasing the viscosity of the liquid by as much as a factor of 12 produced no observable change in the dispersion coefficient for the 6-in.-diam column. Although the axial dispersion coefficient values for the more viscous solutions were lower, the observed dependence of the axial dispersion coefficient on the superficial gas velocity was the same as that observed for columns filled with water. These observations are in agreement with the correlations shown in Eqs. (37) and (38), which predict that the dispersion coefficient depends on the viscosity of the liquid phase to the -0.057 and -0.072 powers for bubble and slug flow respectively.

The variation of gas holdup and bubble rise velocity with changes in the viscosity of the liquid is shown in Figs. 25-32 for 1.5-, 2-, 3-, and 6-in.-diam columns. An increase in the viscosity of the liquid results in a slight increase in the gas holdup for the smaller-diameter

columns. However, the gas holdup values for the larger columns appear to be unaffected by changes in viscosity. The relation used for correlating the holdup data [Eq. (33)] shows no dependence of holdup on viscosity of the liquid phase.

9.8.4 Effect of Surface Tension of the Liquid Phase

The effects of changes in the surface tension of the liquid on the axial dispersion coefficient and the gas holdup in a 1.5-in.-diam column are shown in Figs. 45 and 33 respectively. A decrease in the surface tension of the liquid from about 72 dynes/cm to about 27 dynes/cm resulted in a 25% decrease in the dispersion coefficient during slug flow; however, essentially no change was observed during bubble flow. A slight increase in the gas holdup was noted as the surface tension was decreased for a given value of the superficial gas velocity. The correlations for the axial dispersion data indicate no dependence of dispersion coefficient on surface tension during bubble flow and a 0.43-power dependence during slug flow. The correlation for gas holdup indicates that holdup is not affected by changes in surface tension. Decreases in the surface tension of the liquid delayed the change from transition flow to slug flow; that is, the change in flow regime occurred at progressively higher values of the superficial gas velocity as the surface tension of the liquid was decreased.

9.8.5 Effect of Gas Inlet Orifice Diameter

The variation of the axial dispersion coefficient with a change in the gas inlet diameter is shown in Fig. 49 for a 2-in.-diam column filled with water. The gas distributor consisted of a single orifice having a diameter of either 0.1 or 0.432 cm. Only a minor effect at low superficial gas velocities was noted.

The effect of the diameter of the gas inlet orifice on the axial dispersion coefficient in a 2-in.-diam column employing a gas distributor consisting of five orifices is shown in Fig. 50. The gas inlet orifice diameter was varied from 0.4 to 4 mm, which corresponds to a range of 13 to 127 for the column diameter/orifice diameter ratio. For gas

distributors containing multiple orifices, the axial dispersion coefficient values in the transition flow regime exhibit an anomalous behavior, which is probably due to complex bubble-bubble interaction effects. A similar behavior was observed by two other investigators,[36,37] who considered it to be a hindered mixing effect caused by bubble coalescence.

In the slug flow regime, the axial dispersion coefficient values show no dependence on gas inlet orifice diameter. This is to be expected since the large bubbles or slugs formed by coalescence of smaller bubbles are independent of the initial bubble population. In the bubble flow regime, however, the smallest orifice diameter (0.4 mm) produced axial dispersion coefficient values that were significantly lower than those produced by the other, larger orifices. The axial dispersion coefficient values for the larger orifices were essentially the same (within the accuracy of the data). The gas holdup values for the 1.0-, 2.0-, and 4.0-mm-diam orifices were identical, while the values obtained by using a 0.4-mm-diam orifice were higher. The higher values imply a lower bubble rise velocity. Thus, except in the case of very small orifice diameters, the dispersion coefficient is independent of orifice diameter, as is assumed by the dispersion coefficient correlations.

Data were also obtained with gas distributor plates containing 37 orifices. No effect on axial dispersion coefficient was observed (within the accuracy of the data) when the orifice diameter was varied from 1 to 4 mm, as shown in Fig. 51. Reith[38] found no effect of orifice diameter on axial dispersion during slug flow; during bubble flow, the axial dispersion appeared to be marginally affected, although no quantitative dependence was reported. For column-to-orifice diameter ratios less than 80, Ohki[35] observed a very small influence of orifice diameter on axial dispersion. However, for higher values of this ratio, a marked decrease in the dispersion coefficient was observed.

9.8.6 Effect of Number of Orifices in Gas Distributor

The effect of the number of orifices in the gas distributor on the axial dispersion coefficient is shown in Fig. 52 for a 2-in.-diam bubble column filled with water. The orifice diameter was 1 mm in each case. In the bubble flow regime, the axial dispersion coefficient increased as the number of orifices in the gas distributor was increased from 1 to 37. In the transition flow regime, no clear dependence on number of orifices is apparent. In the slug flow regime, the axial dispersion coefficient values are essentially independent of the number of orifices in the gas distributor. This is to be expected since, for a given superficial gas velocity, the number of orifices will only alter the initial size and number of bubbles, and the effects of these quantities are eliminated by coalescence and slug formation. The correlations of the dispersion coefficient data indicate that the dispersion coefficient is weakly dependent (0.098 power) on the number of orifices in the gas distributor during bubble flow and independent of the number of orifices during slug flow.

9.9 Future Work

It is believed that sufficient experimental data on gas holdup and axial dispersion have been obtained; hence no further experimental work in this area is planned. In the future, efforts will be made to develop relations that correlate the data on gas holdup satisfactorily and also extrapolate well to known limiting cases, such as the rate of rise of individual bubbles in vessels having very large diameters. Attempts will also be made to correlate the dispersion data obtained during slug flow without including gas holdup dependence since such a correlation would probably be much simpler.

10. SEMICONTINUOUS REDUCTIVE EXTRACTION EXPERIMENTS IN A MILD-STEEL FACILITY

B. A. Hannaford C. W. Kee
L. E. McNeese

We have continued operation of a facility in which semicontinuous reductive extraction experiments can be carried out in a mild-steel system.[39] Initial work with the facility was directed toward obtaining data on the hydrodynamics of the countercurrent flow of molten salt and bismuth in a 0.82-in.-ID, 24-in.-long column packed with 1/4-in. molybdenum Raschig rings. We have been able to show that flooding data obtained with this column are in agreement with predictions from a correlation[40] based on studies of the countercurrent flow of mercury and aqueous solutions in packed columns. We have carried out several experiments for determining the mass transfer performance of the packed column in which a salt stream containing UF_4 was countercurrently contacted with bismuth containing reductant over a range of operating conditions. During the second uranium mass transfer run (UTR-2), 95% of the uranium was extracted from the salt during a 40-min period in which the bismuth and salt were countercurrently contacted at flow rates of 247 and 52 cm^3/min respectively.[41] Two additional uranium mass transfer runs (UTR-3 and -4) were carried out under conditions such that the uranium extraction factor remained high throughout the column. The fraction of uranium extracted from the salt phase increased from 0.63 to 0.91 as the metal-to-salt flow rate ratio was varied from 0.75 to 2.05. It was found that the rate at which uranium transferred to the bismuth was controlled by the diffusive resistance in the salt film, and that the extraction data could be correlated in terms of the height of an overall transfer unit based on the salt phase. The HTU values ranged from 0.77 to 2.1 ft as the bismuth-to-salt flow rate ratio was decreased from 2.05 to 0.75.[42] In order to measure mass transfer rates in the column under more closely controlled conditions and under conditions where the controlling resistance is not necessarily in the salt phase, preparations were begun for experiments in which the rate of exchange of zirconium isotopes will be measured between salt and bismuth

phases otherwise at chemical equilibrium. In preparation for these experiments, reductant was removed from most of the bismuth by hydrofluorination of the salt and bismuth with a 70-30 mole % H_2-HF mixture. After hydrofluorination, the salt and bismuth were transferred through the system (during run UTR-5) in order to obtain uniform concentrations in the salt and bismuth phases throughout the system. There was a surprisingly large variation (±35%) in the reported concentrations of uranium in salt samples removed from the column effluent during the run.[43]

10.1 Run UTR-6

The objectives of run UTR-6 were: (1) to obtain additional information relative to the variation in the reported uranium concentrations in samples taken from the salt stream leaving the extraction column, because of the large variation (±35%) in these values during run UTR-5; and (2) to obtain additional hydrodynamic data on the countercurrent flow of salt and bismuth in the packed column by operating under conditions where flooding was predicted by the correlation based on countercurrent flow of mercury and water in packed columns. Following run UTR-5, the salt and bismuth were returned to the treatment vessel, from which the salt and bismuth phases were transferred to their respective feed tanks. After the transfers, the bismuth feed tank contained about 17 liters of bismuth in which the thorium concentration was about 6 ppm. The salt feed tank contained about 15 liters of salt having a uranium concentration (as UF_4) of about 3100 ppm. Essentially no extraction of uranium from the salt during the run would be expected because of the negligible concentration of reductant in the bismuth. As shown in Fig. 57 the run was initiated by starting a salt flow through the column; then, a few minutes later, a bismuth flow was begun. Constant salt and bismuth flow rates of 125 and 117 cm^3/min, respectively, were attained after a short time, and seven pairs of bismuth and salt samples were withdrawn from the salt and bismuth streams leaving the column. Subsequently, the flows of salt and bismuth to the column were stopped, and the freeze valve below the specific gravity pot was closed by cooling the line to a temperature below the salt liquidus temperature. The run was then

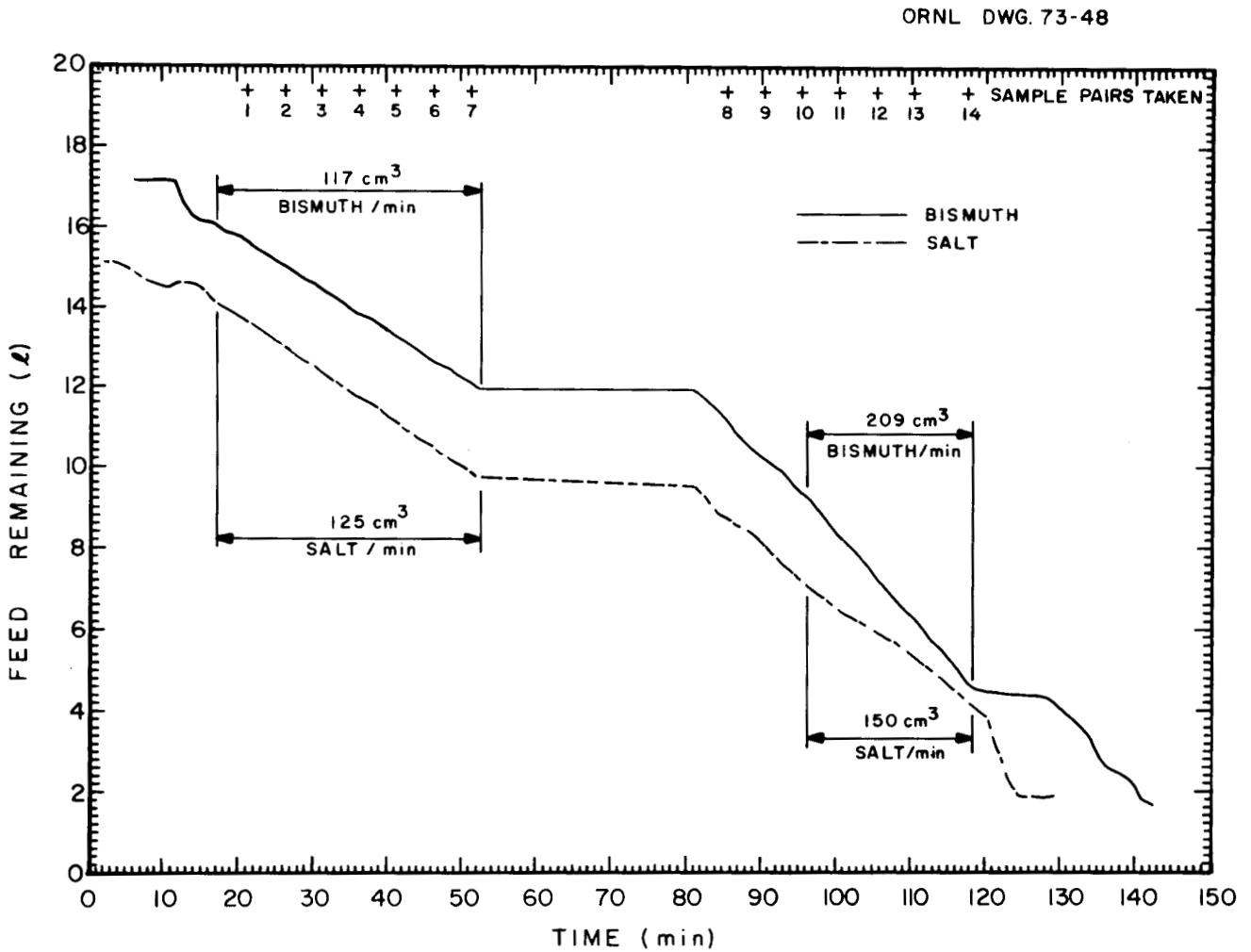

Fig. 57. Volume of Bismuth and Salt Remaining in Feed Tanks vs Run Time, Run UTR-6. Volumetric flow rate (ml/min) for each indicated interval was inferred from the slope.

resumed with salt and bismuth flow rates of 150 and 209 cm^3/min. This combination of salt and bismuth flow rates was selected in order to further test the prediction of flooding by the correlation based on countercurrent flow of mercury and aqueous solutions in packed columns (see Sect. 14). Seven additional salt samples were taken during the remainder of the run for bismuth analyses. Shortly after the salt and bismuth flows were resumed, the apparent dispersed-phase holdup (as indicated by column pressure drop) stabilized at 30%. The salt flow rate was then increased slightly (to 151 cm^3/min). This caused the apparent dispersed-phase holdup to increase until it reached a value of about 60%, at which point the specific gravity pot began to fill with bismuth (which clearly indicated that the column was flooded). The conditions under which the column flooded agree reasonably well with the values predicted from the correlation since the ratio of the observed column throughput to the predicted throughput at flooding was 1.13.

Results of the analyses of the salt and bismuth samples taken during the first part of the run are shown in Table 41. Little significance is attached to the analyses of the bismuth phase; the indicated increase in the concentration of reduced metals is probably the result of slight contamination of the samples with salt or may simply represent analytical errors. The uranium concentration in the salt samples should have remained constant at a value of 3100 ppm; nevertheless, the data show considerable scatter. The average of the uranium concentrations in the flowing salt samples is only 2714 ppm; however, the uranium content of the salt sample removed from the receiver tank is in agreement with the expected value. The variation of uranium concentrations in samples removed from the salt stream during this run is similar to that observed during run UTR-5; on the other hand, a much smaller variation in reported uranium concentrations was observed during an earlier, similar run (UTR-1).[41]

Bismuth concentrations in the salt samples taken during the second half of run UTR-6 are given in Table 42. These concentrations are relatively low, ranging from 0.8 to 15 ppm. It should be noted that

Table 41. Summary of Results for Samples Taken During Run UTR-6

Sample Source	Materials in Bismuth Samples (ppm)			Uranium Conc. in Salt (ppm)
	Li	Th	U	
Feed tanks	0.052	<2	<1	3100
	0.42	6	1	3200
Flowing stream				
1	0.060	9	2.45	2700
2	0.046	15	<1	3200
3	0.046	5	<1	2400
4	0.055	14	<1	3100
5	0.042	4	<1	2300
6	0.035	6	<1	2500
7	0.063	53	<1	2800
Avg.				2714
Receiver tanks	0.043	<2	<8	3100

Table 42. Tests for Bismuth Entrainment in Flowing Salt Samples[a] Taken in Run UTR-6

Flow rates: 150 ml/min salt, 209 ml/min bismuth

Sample (FS-)	Bismuth Concentration (ppm)	Equivalent Bismuth Entrainment[b] (vol %)
8	0.8	--
9	6.4	0.00015
10	6.9	0.00017
11	9.4	0.00026
12	15	0.00046
13	11	0.00032
14	8	0.00021

[a] A 0.042-in.-diam hole drilled in the side of a standard fritted sample capsule permitted collection of unfiltered samples.

[b] Corrected for the average concentration of bismuth reported for blank sample (2.0 ppm).

some of the bismuth entrained in salt leaving the column may have been separated from the salt in the specific gravity pot before the salt stream entered the sampler.

10.2 Preparation for Run UTR-7; Installation of Molybdenum Draft Tube in Treatment Vessel

After run UTR-6, the salt and bismuth phases were transferred to the treatment vessel so that reductant could be added to the bismuth phase and produce the desired uranium and zirconium distribution coefficient values in preparation for the zirconium mass transfer experiments. It was desired that about half of the uranium and zirconium be reduced into the bismuth phase in order to give a distribution coefficient of about 1 for the zirconium. A perforated mild-steel basket (shown in Fig. 58) containing 95.3 g of thorium metal was lowered into the bismuth in the treatment vessel, which was held at a temperature of

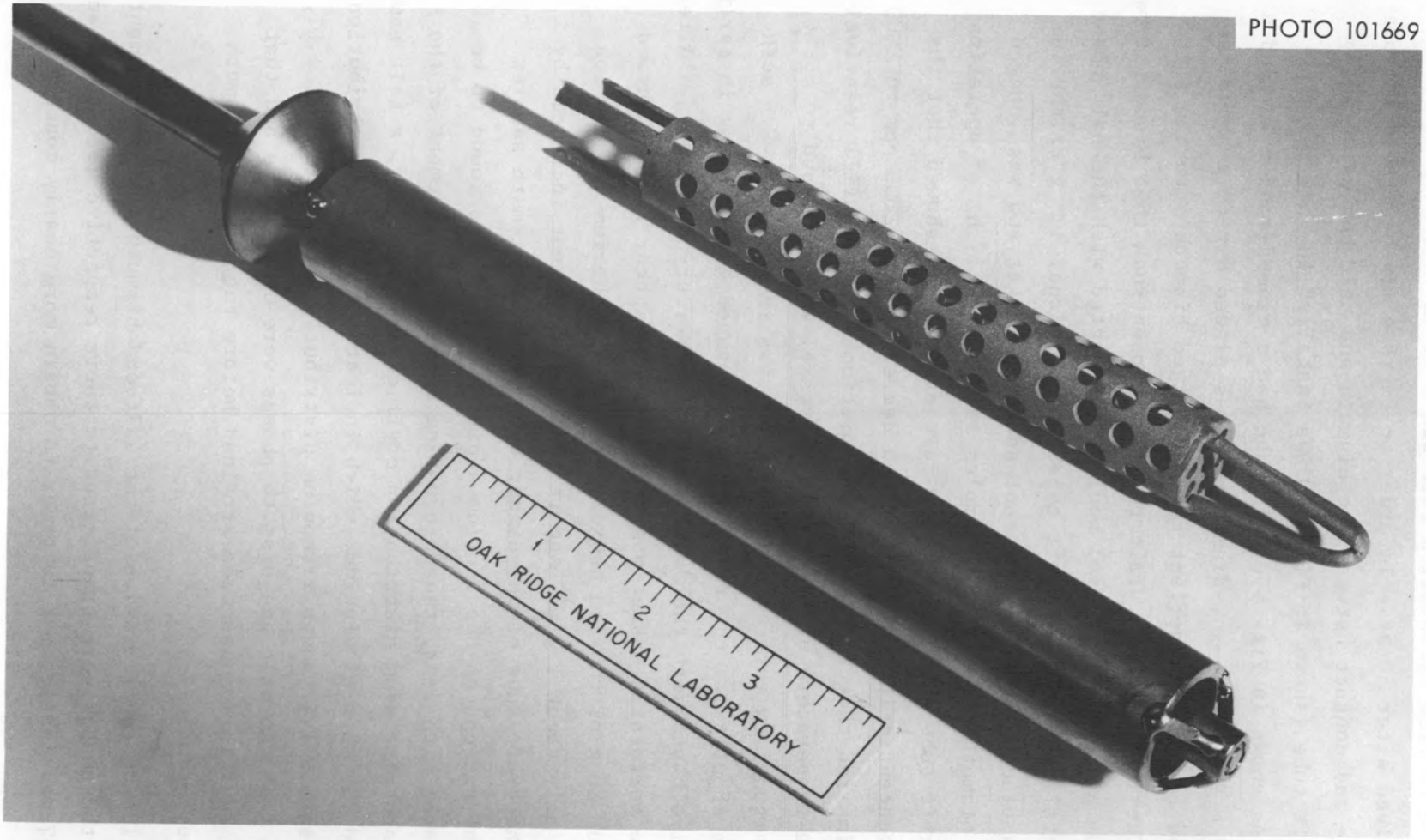

Fig. 58. Molybdenum Draft Tube Used for Agitating Bismuth and Salt Phases, and Perforated Steel Basket Used for Adding Thorium Metal to the Bismuth Phase in the Treatment Vessel.

600°C. The thorium dissolution rate was low; only 70 g of the metal had dissolved after 50 hr. In order to improve mixing within the bismuth phase and contact between the bismuth and salt phases, a molybdenum draft tube (shown in Fig. 58) was installed in the treatment vessel. As shown in Fig. 59, this tube had a diameter of 1 in. and a length of 8 in. A 1.5-in.-diam baffle was placed directly above the draft tube in order to deflect the discharged bismuth into the salt phase. The length of the draft tube was chosen such that bismuth from the bottom of the bismuth pool would be contacted with the salt phase. After installation of the draft tube, an additional 105 g of thorium metal was placed in a new reductant addition basket and was lowered into the bismuth phase. Salt samples taken after 17 hr of operation of the draft tube at an argon flow rate of 1.5 scfh showed that the uranium concentration in the salt had decreased from 2800 ppm to 2000 ppm and implied that the thorium dissolution rate was still relatively low. The temperature of the treatment vessel was increased to 650°C, and the argon flow rate to the draft tube was increased to 2.5 scfh (which is about twice the rate that had produced good pumping in earlier qualitative tests with the draft tube using mercury and water). After 90 hr the perforated basket was removed and weighed; results showed that about 86 g of thorium had dissolved. The thorium dissolution rate was only about 1 g/hr, and it apparently was not increased by use of the draft tube or the higher temperature. Bismuth samples removed at the end of the thorium addition period were found to be contaminated with salt, thus preventing a direct measurement of the uranium and zirconium distribution coefficients. However, a salt sample contained 1580 ppm of uranium, which indicates a uranium distribution coefficient of 1.11 and a zirconium distribution coefficient of 1.01, assuming that the salt and bismuth phases were homogeneous and that chemical equilibrium had been attained before the salt and bismuth phases were sampled.

Following equilibration of the salt and bismuth in the treatment vessel, the phases were transferred to their respective feed tanks and run UTR-7 was carried out in order to obtain more nearly constant

ORNL DWG 73-39

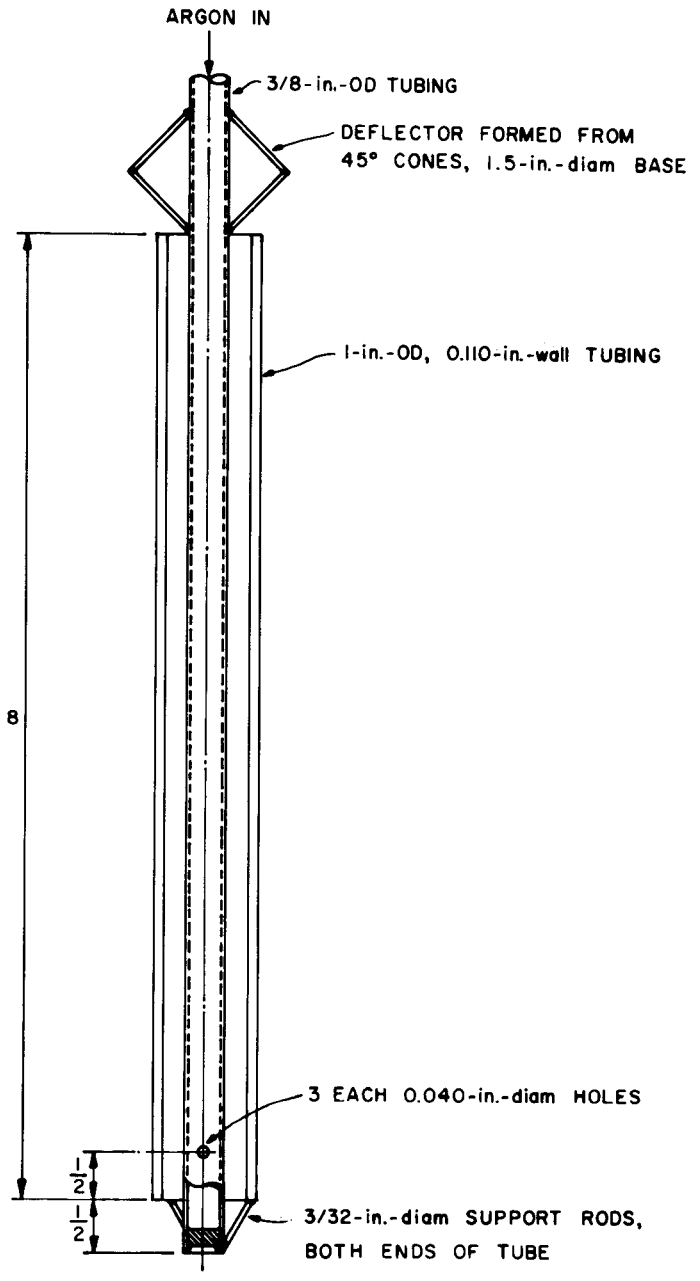

Fig. 59. All-Molybdenum Draft Tube for Circulating Molten Bismuth from a Pool Approximately 7 in. Deep.

concentrations of materials in the salt and bismuth throughout the system. During the run, the pressure drop through the column was erratic and an abnormally high pressure was required in the salt jackleg. No hydrodynamic data were obtained during the run because of variations in the flow conditions. Post-run examination of the system indicated that the bismuth return line between the column and the bismuth catch tank was slightly restricted and that a small rupture had occurred, causing the release of about 20 g of bismuth.

10.3 Preparation for Mass Transfer Run ZTR-1; Production of ^{97}Zr by Irradiation of ^{96}Zr

Plans have been made to carry out a series of mass transfer experiments in which the rate of exchange of zirconium isotopes between salt and bismuth phases containing natural zirconium will be measured. The results that are obtained will permit the mass transfer performance of the packed column to be evaluated. Zirconium-97, which has a 16.8-hr half-life, is thought to be the best zirconium isotope for these experiments since its use would not result in the successive buildup of radioactivity in the experimental facility. In our initial attempt at producing the tracer, 20 mg of $^{96}ZrO_2$ was sealed in a quartz ampul (Super Seal), which was then irradiated for 5 hr at a thermal flux of 2×10^{14} neutrons cm^{-2} sec^{-1} in the Oak Ridge Research Reactor. The ZrO_2 had the following isotopic analysis: ^{96}Zr, 85.25%; ^{94}Zr, 3.85%; ^{92}Zr, 2.24%; ^{91}Zr, 1.41%; and ^{90}Zr, 7.25%. After the irradiation period, the resulting ^{97}Zr activity was about four times the calculated value. The discrepancy was traced to the use of an outdated value[43] for the thermal-neutron cross section of ^{96}Zr (0.05 barn) as compared with a more recent value[44] of 0.2 barn. After a period of 20 days the $^{96}ZrO_2$ was reirradiated for a period of 2 hr in order to produce a calculated ^{97}Zr activity of 6.9 mCi. The measured activity after irradiation was about 100% higher than expected but was well within the limits required for safe handling after an 18-hr decay period, during which the activity of ^{31}Si (half-life, 2.62 hr) resulting from activation of the quartz ampul was allowed to decrease to a low level. The activity of 65-day ^{95}Zr produced during irradiation of the ZrO_2 was calculated to be about

0.1% of that observed initially for ^{97}Zr; therefore, the cumulative ^{95}Zr activity that will result from several tracer experiments is expected to be negligible.

The irradiated ZrO_2 powder was transferred from the quartz ampul to a 3/4-in.-diam carbon-steel capsule, which was used for adding the ZrO_2 to the salt feed tank. The design of the capsule is shown schematically in Fig. 58. After the capsule had been lowered into the salt feed tank, argon was fed through the capsule at the rate of ~ 1 scfh in order to dissolve the ZrO_2 in the molten salt. Samples of the salt were taken periodically following the addition of tracer and were counted for ^{97}Zr activity. These measurements indicated that addition of the tracer to the 15-liter salt volume was 75% complete within a 2-hr period. The ^{97}Zr counting rate in a sample taken 10 hr after the addition of tracer to the salt feed tank was about 200,000 counts/min, which indicates that the counting precision in the planned tracer experiments should be satisfactory.

When the salt feed tank was pressurized prior to starting experiment ZTR-1, salt did not begin transferring from the feed tank at the expected tank pressure. After a salt flow was established, it soon became apparent that a leak existed in the salt exit line at a point near the tank. Therefore, the experiment was canceled and an attempt was made to transfer the salt to the salt receiver tank via a bypass; however, this resulted in a second salt leak, which caused the Calrod heaters on the salt feed-and-catch tank to fail. Results of examination of the tank, along with details on equipment maintenance, are given in the following section.

10.4 Inspection of Salt Feed-and-Catch Tank, and Equipment Maintenance

Inspection of the salt feed-and-catch tank, after cooling to room temperature, showed that the failures in the transfer lines leaving the tank were identical, although they had occurred in different lines. In each case, the 3/8-in.-diam mild-steel tubing (initial wall thickness, 0.59 in.) had failed due to severe air oxidation in a narrow band on

the exterior of the tubing adjacent to a compression fitting; of course, thinning of the tubing caused by the ferrules in the compression fitting may have also contributed to the failures.

Damage to the protective coating of nickel aluminide on the vessel exterior and to the Calrod heaters made salvage of the vessel impractical. (The outside of the vessel was coated initially with 15 to 20 mils of nickel aluminide in order to decrease the rate of external air oxidation.) The protective coating appeared to be intact over a significant area of the tank, but it was either nonadherent or had completely spalled from the surface in a number of areas where extensive air oxidation had occurred. A 1.5-in.-diam metal specimen that was removed from the tank wall with a hole saw was examined by the Metals and Ceramics Division.[45] The vessel had operated for about 16,000 hr in the temperature range of 600 to 700°C and had been cooled to room temperature three or four times. The wall of the vessel had been constructed from 12-in.-diam, 3/8-in.-wall-thickness, seamless ASTM-A106 Grade B Steel [Fe--0.3% C (max)--0.29 to 1.06% Mn--0.048% P (max)--0.58% S (max)--0.1% Si (min)].

A cross section of the specimen from the vessel wall was mounted so that the inside and outside surfaces could be observed. Figure 60 presents photomicrographs of the inside surface. Intergranular voids that extend 2 to 3 mils into the metal are apparent in Fig. 60(a). The marks near the surface in Fig. 60(b) are directional polishing marks and have no significance. The inside of the vessel appeared to be in good condition, with little evidence of corrosion. Figure 61 presents photomicrographs of the external surface of the vessel. The nickel aluminide coating and most of the oxide corrosion product spalled from the specimen during its preparation. The predominant feature noted in the photomicrographs is the absence of fine black precipitates to a depth of about 10 mils. These precipitates are probably small graphite flakes, and their absence near the surface is indicative of decarburization, which would be expected under the highly oxidizing environment in which the vessel had operated.

It was of particular interest to determine whether the steel had graphitized. Steels normally contain carbon in the form of Fe_3C; however,

PHOTO 1632-73

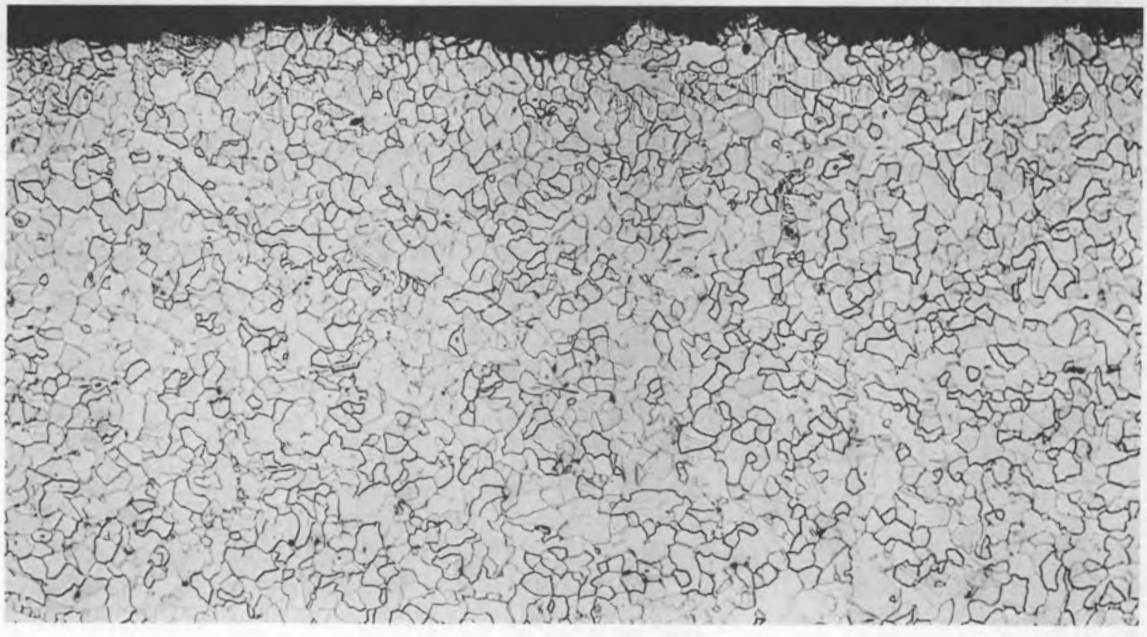

(a)

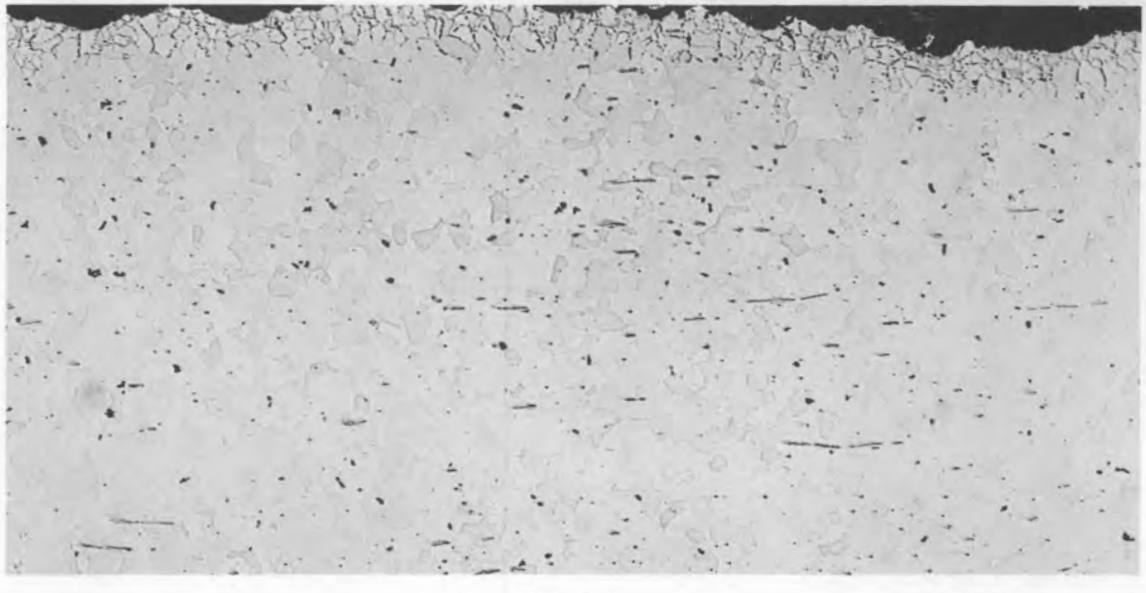

(b)

Fig. 60. Photomicrographs of the Inner Surface of the Salt Feed-and-Catch Tank in the (a) As Polished and (b) Etched Condition After Exposure to Salt at 600 to 700°C for 16,000 hr. Magnification, 100X. Etchant, 2% Nital.

PHOTO 1631-73

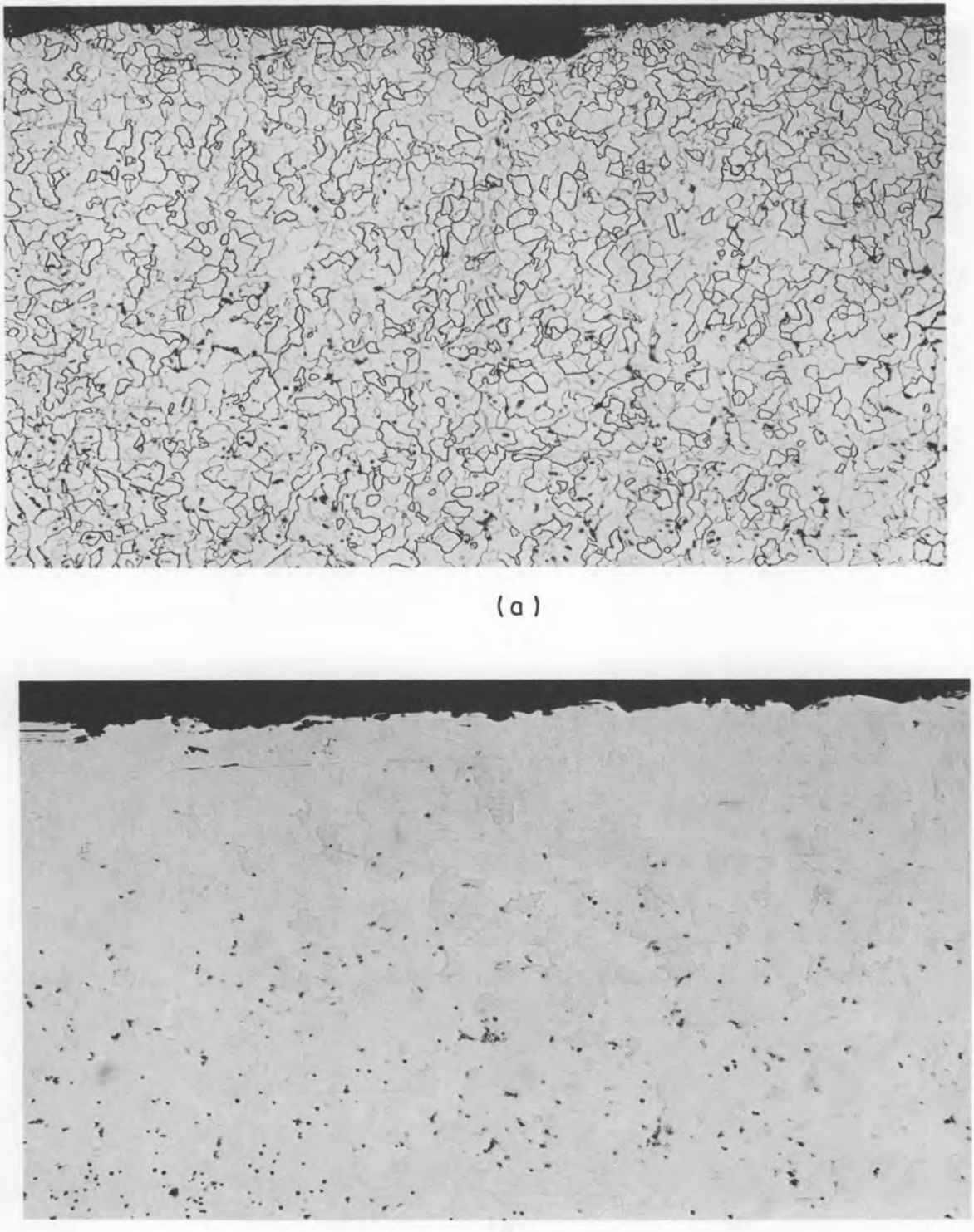

Fig. 61. Photomicrographs of the Outer Surface of the Salt Feed-and-Catch Tanks in the (a) As Polished and (b) Etched Condition After Exposure to Air at 600 to 700°C for 16,000 hr. Magnification, 100X. Etchant, 2% Nital.

this carbide will often decompose during prolonged exposure at elevated temperatures to iron and graphite. Decomposition is influenced strongly by the chemical composition of the steel, with the presence of Ni, Si, and C favoring the formation of graphite, Fe and S (if not present as a sulfide) favoring the stability of Fe_3C, and Mn having little effect on the stability of the carbide if present in concentrations below 1%. Only the nominal composition of the specimen is known. The most influential elements are carbon and silicon, and both would encourage graphite formation.

Examination of the microstructure shown in Fig. 62 indicates that two types of precipitate are present. The long stringers, which are gray, are typical of Fe_3C. The black precipitate is in the form of flakes that are typical of the appearance of graphite. The photomicrographs in Figs. 60(a) and 61(a) show that the mixed carbide-graphite structure is typical of most of the cross section. The graphite flakes may have been present before the vessel was put into service, or they may have formed during its operation.

The important effects of graphite formation are reductions in strength and ductility of the steel. The specimen was not of sufficient size for strength measurements; however, a test that would indicate the ductility of the material was made. A small piece (about 1.5 in. long, 3/8 in. thick, and 5/16 in. wide) of the specimen was bent 180° in a vise without formation of cracks, as shown in Fig. 63. Thus, no evidence for embrittlement of the material is apparent.

Dimensional measurements by the Inspection Engineering Division on the salt feed-and-catch tank and on the bismuth feed-and-catch tank were inconclusive, partly as a result of air oxidation of the reference points on the vessels and partly because of inaccessibility of the points. The observed strain, based on comparison with measurements made on the tanks after an initial stress relief, showed a variation of approximately $\pm$ 1%, with the mean value being near zero.

A new salt feed-and-catch tank of the initial design was fabricated and installed in the system. Thermal insulation was removed from all

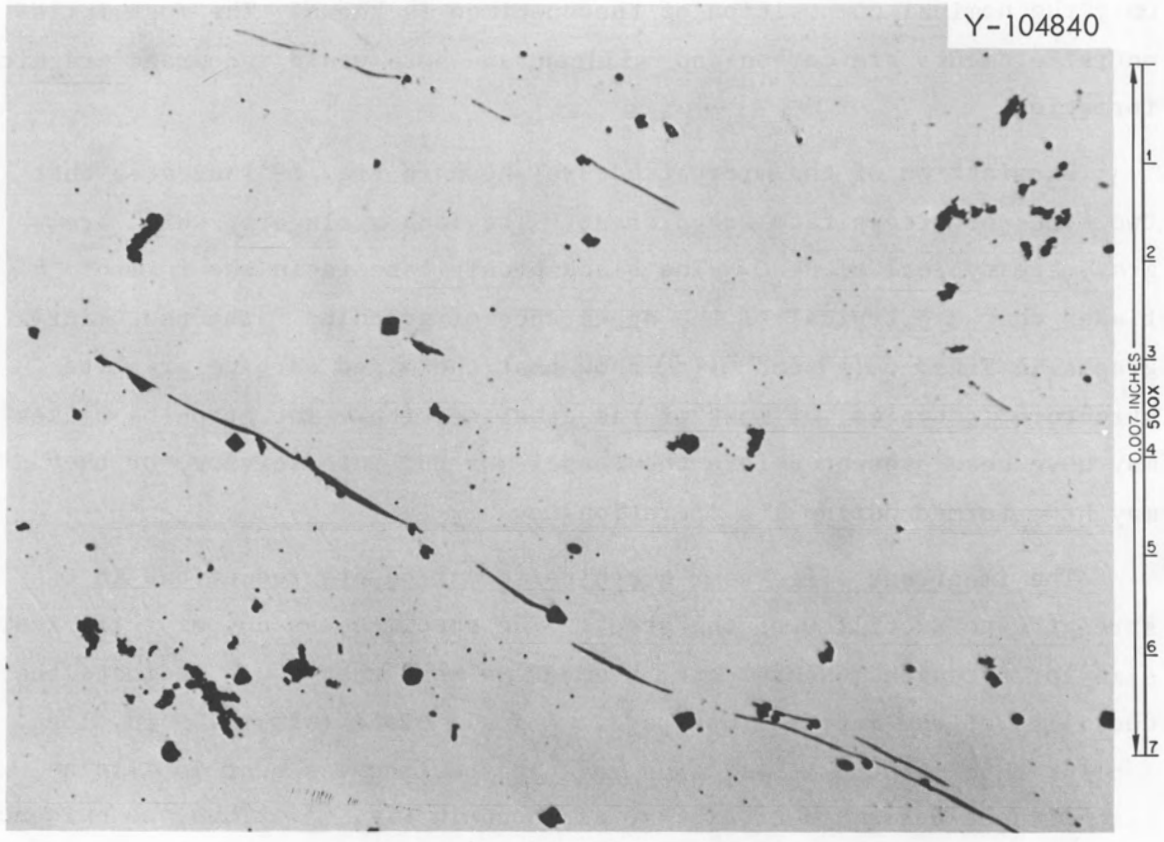

Fig. 62. Photomicrograph Showing Microstructure of Steel from Salt Feed-and-Catch Tank in the As-Polished Condition After Operation at 600 to 700°C for 16,000 hr. Magnification, 500X.

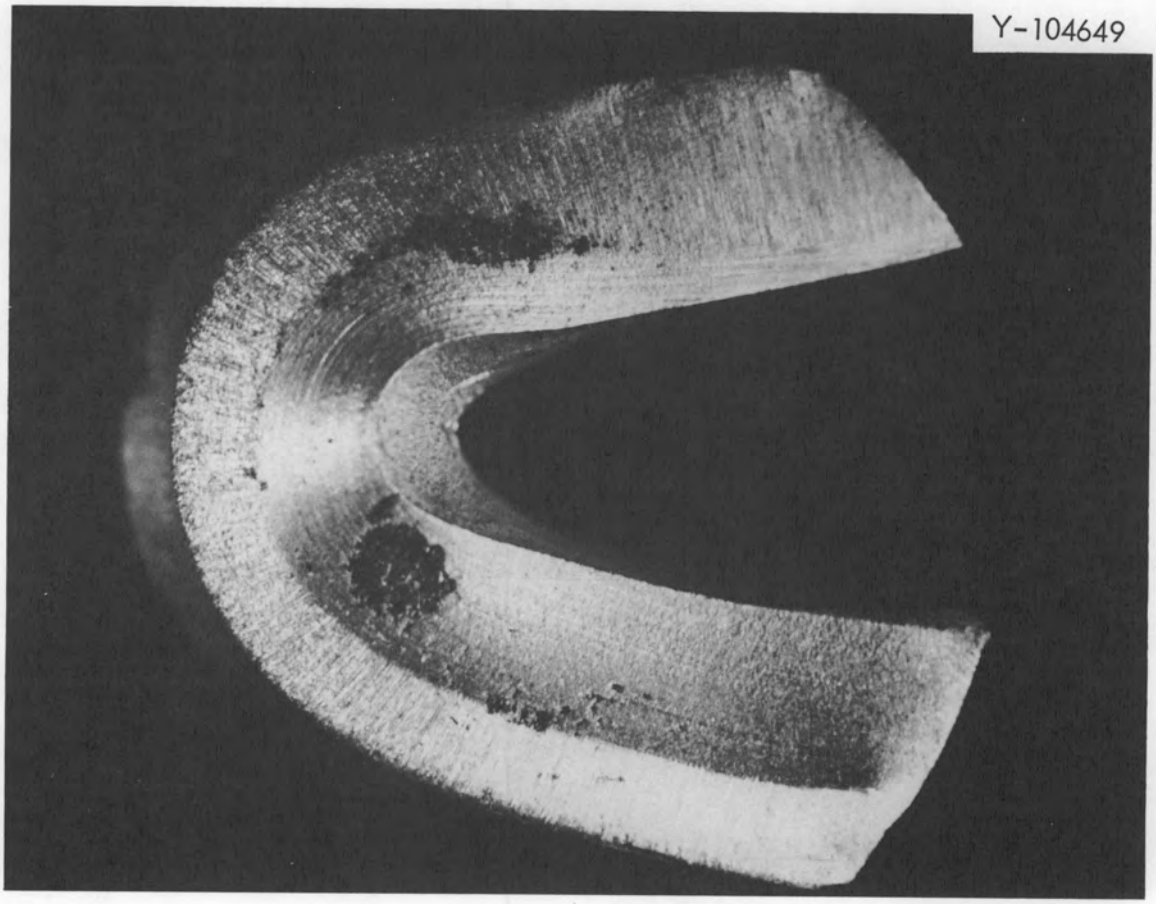

Fig. 63. Photograph of a Sample of Steel from the Salt Feed-and-Catch Tank After Being Bent 180° at Room Temperature. The dark spots are remnants of the original surface oxide. The tank was operated at 600 to 700°C for 16,000 hr. No evidence for embrittlement of the steel is apparent.

transfer lines to allow inspection of the lines, and lines that were more than moderately oxidized were replaced. The salt transfer line from the feed tank to the salt jackleg was rerouted to a point 11 in. higher than in the original design in order to improve control of the salt feed rate and to prevent backflow of bismuth into the salt feed tank during column upsets.

11. DEVELOPMENT OF THE METAL TRANSFER PROCESS: OPERATION OF EXPERIMENT MTE-2

E. L. Youngblood L. E. McNeese

It has been found that rare earths distribute selectively into molten LiCl from bismuth solutions containing rare earths and thorium, and an improved rare-earth removal process based on this observation has been devised. Work that will demonstrate all phases of the improved rare-earth removal method, which is known as the metal transfer process, is presently under way.

We previously[46] carried out an engineering experiment (MTE-1) for studying the removal of rare earths from single-fluid MSBR fuel salt by this process. During this experiment, approximately 50% of the lanthanum and 25% of the neodymium originally present in the fluoride salt were removed at about the expected rate. Surprisingly, however, the lanthanum and neodymium removed from the fluoride salt did not accumulate in the Li-Bi solution used for removing these materials from LiCl. It is believed that reaction of impurities in the system with the rare earths caused this unexpected behavior.

A second engineering experiment (MTE-2) was designed and put into operation previously.[47] This experiment, completed during this report period, was carried out in a vessel, made of 6-in.-diam carbon-steel pipe, which was divided into two compartments by a partition that extended to within 1/2 in. of the bottom of the vessel. The compartments were interconnected by a 2-in.-deep pool of molten bismuth, saturated with thorium, which formed a seal between the two compartments. One compartment contained MSBR fuel carrier salt (72-16-12 mole % LiF-BeF_2-ThF_4) to which were added 7 mCi of ^{147}Nd and sufficient LaF_3 to produce a lanthanum concentration of 0.3 mole %. The other compartment contained LiCl, a cup containing a Li-Bi solution, and a pump for recirculating the LiCl through the cup at the rate of about 25 cm^3/min. The concentration of reductant (35 at. % lithium) in the Li-Bi solution was sufficiently high that essentially all of the lanthanum and neodymium would be extracted from LiCl in equilibrium with the Li-Bi solution. In order to obtain mixing in the main bismuth pool, about

10% of the metal volume was forced to flow back and forth through the 1/2-in. slot below the partition between the fluoride and chloride compartments every 7 min. Gas-lift sparge tubes were used to disperse droplets of bismuth in the salt phase to improve contact between the salt and bismuth phases in each compartment. Provisions were made for obtaining filtered samples of the salt and bismuth phases in the experiment.

The remainder of this section describes the experimental procedure followed in the experiment, gives a mathematical analysis of factors affecting the rate of transfer of the rare earths, and presents the results of the experiment.

11.1 Experimental Procedure

After the materials[47] had been charged to the experiment, the system was allowed to stand for 76 hr at operating temperature (650°C) before circulation of the LiCl was initiated. The sequence of operations pursued during the experiment consisted in pumping the LiCl through the Li-Bi container for a 3-hr period at the rate of 25 cm^3/min. Circulation of the LiCl was then stopped, and the salt and bismuth phases were allowed to approach chemical equilibrium during a 4-hr period before filtered samples were taken of the salt and bismuth. This sequence was repeated on a three-shift-per-day basis during the first week and a two-shift-per-day basis during the second week. For the remainder of the three-month operating period, the LiCl was circulated for about 7 hr during the day shift and the salt and bismuth were allowed to approach chemical equilibrium during the off-shifts and on week-ends. During the pumping periods, the Th-Bi phase was forced back and forth between the fluoride and LiCl compartments at the rate of 10% of the metal volume every 7 min to promote mixing of the bismuth phase. The gas-lift sparges were kept in operation almost continuously except when samples were being withdrawn.

Eight days before the end of the experiment, 1 vol % of fluoride salt (72-16-12 mole % $LiF-BeF_2-ThF_4$) was added to the LiCl compartment in order to determine the effect of entrainment of small amounts of fluoride salt into the LiCl via circulation of the bismuth.

The filtered samples taken during the experiment were prepared for analysis by cutting off the filter section with tubing cutters and cleaning the external surfaces with emery cloth. The ^{147}Nd activity in a sample was determined by direct counting of the 0.53-MeV gamma radiation emitted by the sample. The lanthanum concentration in a sample was determined by neutron activation. The ^{228}Ra activity in the samples was determined by counting the 0.9-MeV gamma radiation emitted by the ^{228}Ac after a delay of about 24 hr to ensure that the ^{228}Ac was in secular equilibrium with the ^{228}Ra.

11.2 Mathematical Analysis of Transfer Rate

A mathematical analysis was carried out to determine the removal rate for a fluoride salt contaminant which could transfer between the salt and bismuth phases in experiment MTE-2. In making the analysis, it was assumed that equilibrium was maintained between the three phases present in the system: the fluoride salt, bismuth that is saturated with thorium, and the portion of the LiCl that is in contact with the Th-Bi phase. Under these conditions, the concentrations of the transferring material in these phases are related by the following distribution ratios:

$$D_F = \frac{X_{BT}}{X_{FS}}, \tag{39}$$

$$D_C = \frac{X_{BT}}{X_{CS}}, \tag{40}$$

where

D_F = distribution coefficient for the material transferring between the fluoride salt and the bismuth,

D_C = distribution coefficient for the material transferring between the chloride salt and the bismuth,

X_{BT} = concentration of the transferring material in the main bismuth pool, mole fraction,

X_{FS} = concentration of the transferring material in the fluoride salt, mole fraction,

X_{CS} = concentration of the transferring material in the LiCl, mole fraction.

If it is assumed that a portion of the transferring material is removed from the LiCl during its passage through the cup containing the Li-Bi solution and that an additional portion is removed from the system by radioactive decay, a material balance on the transferring material contained within the three phases that are assumed to be in equilibrium yields the following relation:

$$\frac{dI}{dt} = -\lambda I - F_{CS} f X_{CS} , \qquad (41)$$

where

I = inventory of the transferring material in the three phases that are assumed to be in equilibrium, moles,

t = time, sec,

λ = decay constant for the transferring material, sec^{-1},

F_{CS} = rate at which LiCl is circulated through the cup containing the Li-Bi solution, moles/sec,

f = fraction of the transferring material that is removed from the LiCl during its contact with the Li-Bi solution,

X_{CS} = concentration of the transferring material in LiCl that is in equilibrium with the Bi-Th solution, mole fraction.

The inventory of the transferring material in the three phases that are assumed to be in equilibrium is given by the following relation:

$$I = M_{FS}X_{FS} + M_{BT}X_{BT} + M_{CS}X_{CS} , \qquad (42)$$

where

M_{FS} = quantity of fluoride salt, moles,

M_{BT} = quantity of Bi-Th solution, moles,

M_{CS} = quantity of LiCl that is in equilibrium with Bi-Th solution, moles.

Substitution of Eqs. (39), (40), and (42) into Eq. (41) yields the following relation:

$$\frac{dX_{FS}}{dt} = -\left[\lambda + \frac{F_{CS} f \frac{D_F}{D_C}}{M_{FS} + M_{BT} D_F + M_{CS} \frac{D_F}{D_C}}\right] X_{FS} \cdot \qquad (43)$$

Integration of Eq. (43) between the limits indicated in Eq. (44),

$$\int_{X_{FS,i}}^{X_{FS,p}} \frac{dX_{FS}}{X_{FS}} = -\left[\lambda + \frac{F_{CS} f \frac{D_F}{D_C}}{M_{FS} + M_{BT} D_F + M_{CS} \frac{D_F}{D_C}}\right] \int_0^{t_p} dt \ , \qquad (44)$$

where

$X_{FS,i}$ = concentration of the transferring material in the fluoride salt at time t = 0, when contact of the LiCl with the Li-Bi solution is initiated, mole fraction,

$X_{FS,p}$ = concentration of the transferring material in the fluoride salt at time t_p, when contact of the LiCl with the Li-Bi solution is stopped, mole fraction,

t_p = length of time that the LiCl is circulated, sec,

yields the following relation for the concentration of the transferring material in the fluoride salt after the LiCl has been contacted with the Li-Bi solution for the indicated time period:

$$\frac{X_{FS,p}}{X_{FS,i}} = \exp\left\{-\left[\lambda + \frac{F_{CS} f \frac{D_F}{D_C}}{M_{FS} + M_{BT} D_F + M_{CS} \frac{D_F}{D_C}}\right]\right\} . \qquad (45)$$

During experiment MTE-2, several cycles of operation were carried out in which the LiCl was contacted with the Li-Bi solution for a certain period of time. On conclusion of this contacting period, no circulation of the LiCl was allowed to occur. The relative concentration of the transferring material in the fluoride salt after a period in which the LiCl was circulated is given by Eq. (45), and the relative concentration of the transferring material after a period during which no circulation occurred is given by the relation:

$$\frac{X_{FS,s}}{X_{FS,p}} = \exp\left(-\lambda t_s\right), \tag{46}$$

where

$X_{FS,s}$ = concentration of the transferring material in the fluoride salt at time t_s, mole fraction,

t_s = length of time during which no LiCl circulation occurs, sec.

Combination of Eqs. (45) and (46) yields the following relation for the concentration of the transferring material in the fluoride salt after one cycle of operation in which the LiCl is circulated for part of the time period and no circulation occurs during the remainder of the period:

$$\frac{X_{FS,s}}{X_{FS,i}} = \exp\left[-\lambda(t_s + t_p)\right] \exp\left(-Kt_p\right), \tag{47}$$

where

$$K = \frac{F_{CS} f \frac{D_F}{D_C}}{M_{FS} + M_{BT} D_F + M_{CS} \frac{D_F}{D_C}} .$$

Similarly, the relative concentration of the transferable material in the fluoride salt after n cycles in which both pumping and equilibration occur is given by the following expression:

$$\frac{X_{FS,sn}}{X_{FS,i}} = \exp\left[-\lambda \sum_{j=1}^{n} (t_{sj} + t_{pj})\right] \exp\left(-K \sum_{j=1}^{n} t_{pj}\right), \qquad (48)$$

where

$X_{FS,sn}$ = concentration of the transferable material in the fluoride salt after n cycles in which LiCl circulation and equilibration occur, mole fraction,

t_{sj} = length of time during which no LiCl is circulated during cycle j, sec,

t_{pj} = length of time during which LiCl is circulated during cycle j, sec.

It should be noted, however, that the two time summations in Eq. (48) have the following meanings:

$$t_n = \sum_{j=1}^{n} (t_{sj} + t_{pj}), \qquad (49)$$

$$t_{pn} = \sum_{j=1}^{n} t_{pj}, \qquad (50)$$

where

t_n = length of time between the beginning of the experiment and the end of the nth cycle, sec,

t_{pn} = length of time that LiCl circulation has occurred between the beginning of the experiment and the end of the nth cycle, sec.

Substitution of Eqs. (49) and (50) in Eq. (48) yields the following relation for the relative concentration of the transferable material in the fluoride salt at the end of the nth cycle:

$$\frac{X_{FS,sn}}{X_{FS,i}} = \exp(-\lambda t_n) \exp(-Kt_{pn}). \qquad (51)$$

This relation indicates that a plot of the quantity $\frac{X_{FS,sn}}{X_{FS,i}} \exp(\lambda t_n)$ vs the length of time that the LiCl has been circulated should yield a straight line having a slope of -K. The quantity f can be calculated after the value of K has been determined from a plot of this type.

11.3 Experimental Results

11.3.1 Rates of Transfer of Neodymium and Lanthanum

During the experiment, the lanthanum and ^{147}Nd that were added to the fluoride salt initially behaved as expected. The rates of accumulation of these two rare earths in the Li-Bi solution during the experiment are summarized in Table 43 and shown in Fig. 64. There was essentially no accumulation of either of the rare earths in the solution prior to operation of a gas-lift sparge tube in the cup (about 50 liters of LiCl was circulated through the Li-Bi compartment before operation of the sparge tube was initiated). After 400 liters of LiCl had been circulated (about two-thirds through the run), approximately 50% of the lanthanum and approximately 30% of the neodymium originally in fluoride salt were found to be in the Li-Bi solution. During the last one-third of the run the rare earths continued to accumulate in the Li-Bi solution, but the rate of accumulation could not be determined accurately because of a leak that developed in the lithium-bismuth cup. This leak allowed about 30% of the solution to flow into the area between the cup and the holder.

The extent of removal of lanthanum and neodymium from the fluoride salt is summarized in Tables 44 and 45 and shown in Figs. 65 and 66. As seen in the figures, more than 85% of the lanthanum and more than 50% of the neodymium had been removed from the fluoride salt at the end of the experiment. After about 50 liters of LiCl had been circulated through the cup containing the Li-Bi solution, the concentrations of lanthanum and neodymium decreased in the manner suggested by Eq. (51). There is some uncertainty in the f values that correspond to the lines shown in the figures because of uncertainty in the values for the distribution coefficients, as will be discussed later. The concentration of thorium in the Li-Bi solution in which the rare earths were accumulated remained below the limit of detection throughout the experiment (< 10 ppm).

Data on the distribution of lanthanum and neodymium between the fluoride salt, the thorium-saturated bismuth, and the LiCl are summarized in Tables 46 and 47. The distribution coefficient data were generally

Table 43. Rate of Accumulation of La and Nd in the Li-Bi Solution During Metal Transfer Experiment MTE-2

Pumping Time (hr)	Volume of LiCl Circulated (liters)	La Concentration (mg/g)	Nd Concentration[a] (dpm/g) x 10^7	Pumping Time (hr)	Volume of LiCl Circulated (liters)	La Concentration (mg/g)	Nd Concentration[a] (dpm/g) x 10^7
0	0	0.0	0.0	108.2	173.8	--	0.149
6	9.6	0.005	0.0	124.2	195.3	4.46	0.180
12	19.6	0.023	0.001	137.6	211.2	4.91	0.200
18	29.1	0.058	0.003	150.1	226.5	4.80	0.199
24	39.0	0.092	--	156.1	233.4	5.42	0.214
27	44.0	--	0.003	169.1	250.7	6.05	0.202
30	48.8	0.11	0.004	185.3	273.9	5.97	0.225
36	59.0	0.82	0.037	212.6	319.6	6.25	--
44.5	73.2	1.40	0.050	219.2	330.5	6.75	--
47.5	77.9	1.66	0.067	250.5	384.3	7.17	0.290
53.5	87.6	2.26	0.083	273.5	421.0	--	0.345
59.5	97.1	2.70	0.089	302.7	471.2	--	0.568
65.5	107.0	2.67	0.106	309.7	482.8	10.53	0.584
94.2	153.2	3.74	0.131	343.9	538.8	10.31	--
101.3	164.0	4.27	0.129	358.1	563.2	11.17	--

[a]Corrected for radioactive decay during the run.

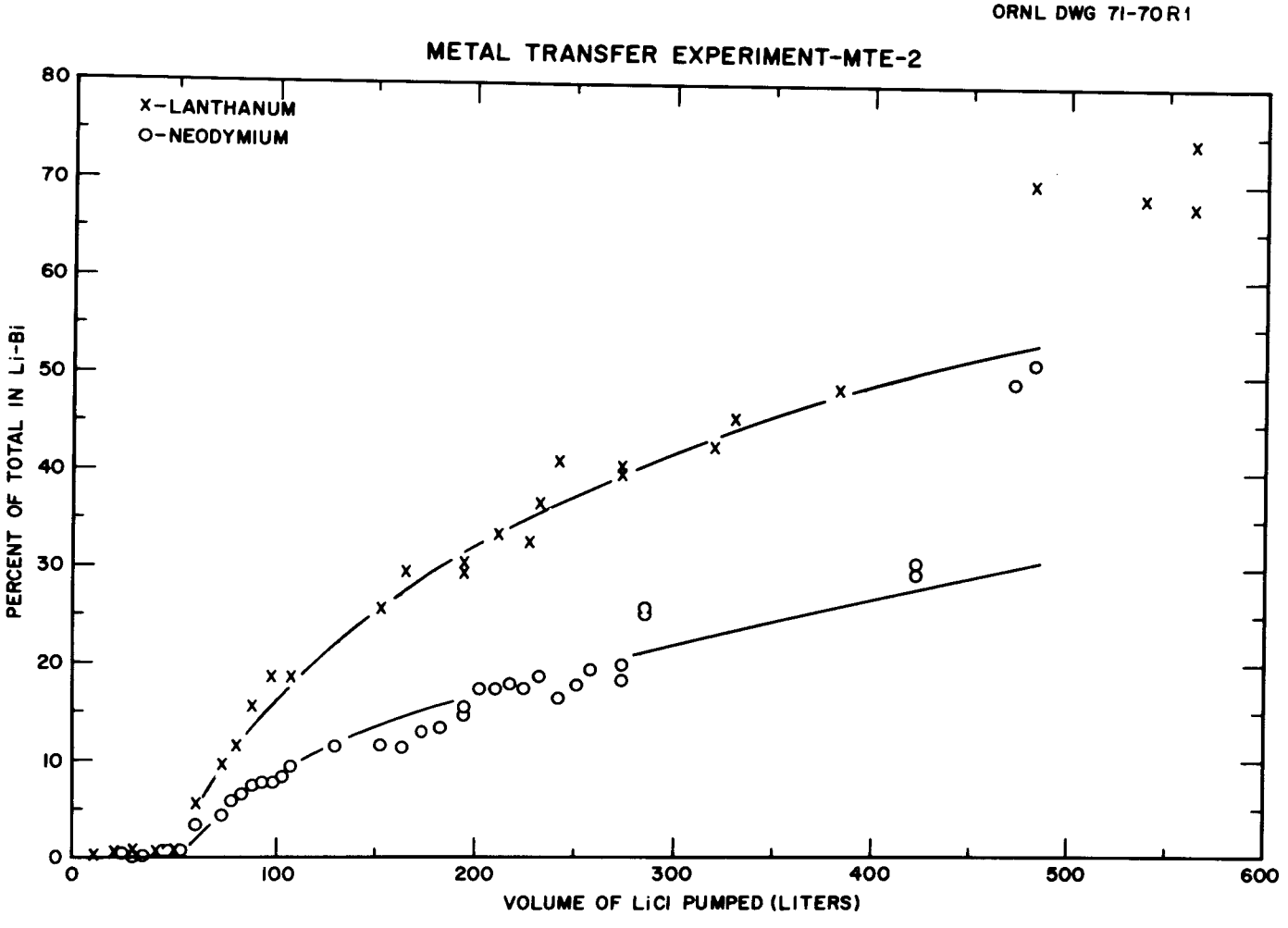

Fig. 64. Rates of Accumulation of Lanthanum and Neodymium in the Li-Bi Solution During Metal Transfer Experiment MTE-2.

Table 44. Concentration of Lanthanum in Fluoride Salt During Metal Transfer Experiment MTE-2

Pumping Time (hr)	Volume of LiCl Circulated (liters)	La Concentration in Fluoride Salt (mg/g)	Pumping Time (hr)	Volume of LiCl Circulated (liters)	La Concentration in Fluoride Salt (mg/g)
0	0	6.54	124.2	195.3	4.14
6	9.6	6.15	137.6	211.2	3.70
12	19.6	5.78	150.1	226.5	3.93
18	29.1	6.26	156.1	233.4	2.96
27	44.0	6.33	169.1	250.7	3.40
30	48.8	6.20	185.3	273.9	3.09
36	59.0	6.72	212.6	319.6	2.04
44.5	73.2	5.54	219.2	330.5	1.94
47.5	77.9	5.63	250.5	384.3	1.42
53.5	87.6	5.75	273.5	421.0	1.38
59.5	97.1	5.65	309.7	482.8	1.17
65.5	107.0	5.30	343.9	538.8	1.10
94.2	153.2	4.31	358.1	563.2	0.86
101.3	164.0	4.84			

Table 45. Concentration of Neodymium in Fluoride Salt During Metal Transfer Experiment MTE-2

Pumping Time (hr)	Volume of LiCl Circulated (liters)	Nd Concentration[a] in Fluoride Salt (dpm/g) x 10^7	Pumping Time (hr)	Volume of LiCl Circulated (liters)	Nd Concentration[a] in Fluoride Salt (dpm/g) x 10^7
0	0	0.508	80.0	130.4	0.422
3	4.7	0.545	94.2	153.2	0.390
6	9.6	0.487	101.3	164.0	0.387
9	14.7	0.531	108.2	173.8	0.383
12	19.6	0.474	114.9	183.5	0.358
15	24.5	0.473	124.2	195.3	0.397
18	29.1	0.458	130.7	202.3	0.329
21	33.9	0.458	137.6	211.2	0.313
27	44.0	0.492	143.5	218.2	0.323
30	48.8	0.463	150.1	226.5	0.347
33	54.1	0.450	156.1	233.4	0.289
36	59.0	0.517	162.6	241.2	0.310
44.5	73.2	0.493	169.1	250.7	0.268
47.5	77.9	0.477	175.9	258.5	0.300
50.5	82.7	0.471	185.3	273.9	0.315
53.5	87.6	0.478	250.5	384.3	0.278
56.5	92.3	0.458	273.5	421.0	0.251
59.5	97.1	0.441	302.7	471.2	0.114
62.5	102.1	0.469	309.7	482.8	0.138
65.5	107.0	0.434			

[a] Corrected for radioactive decay during the run.

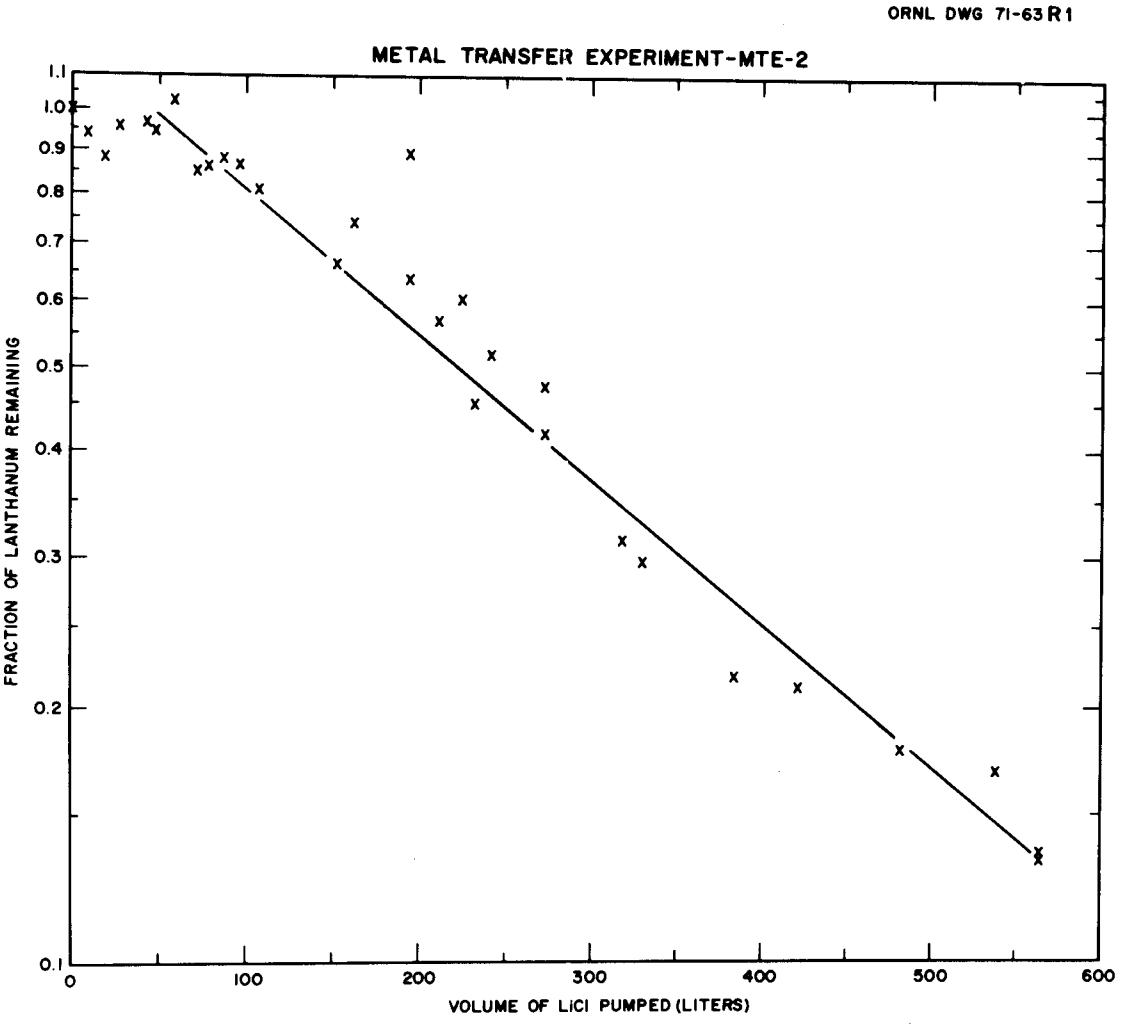

Fig. 65. Variation of Lanthanum Inventory in the Fluoride Salt Surge Tank with Time During Metal Transfer Experiment MTE-2.

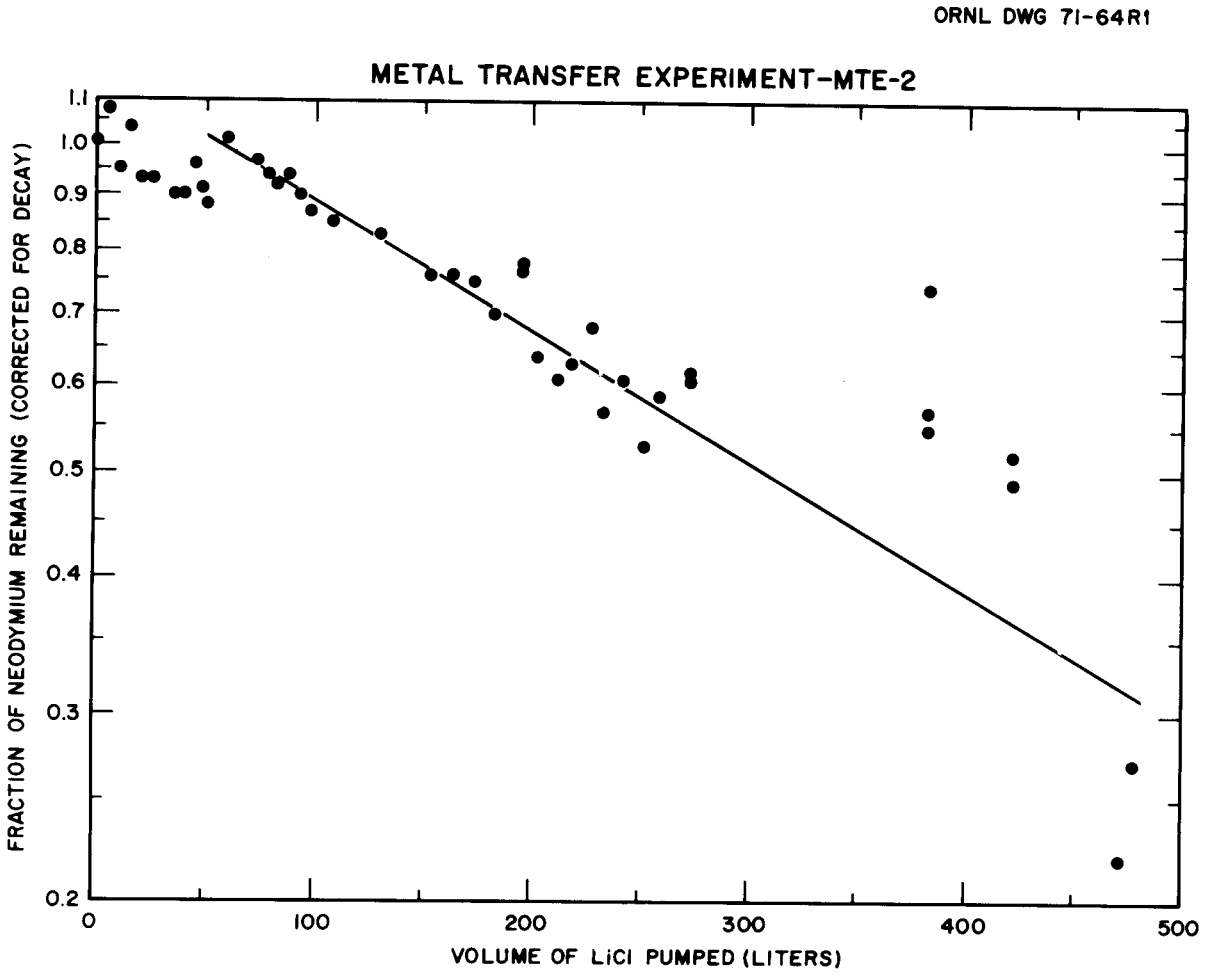

Fig. 66. Variation of the Neodymium Inventory in the Fluoride Salt Surge Tank with Time During Metal Transfer Experiment MTE-2.

Table 46. Variation of Lanthanum Distribution Coefficient with Time During Metal Transfer Experiment MTE-2

Pumping Time (hr)	Volume of LiCl Circulated (liters)	Distribution Coefficient at Fluoride Salt--Bi-Th Interface	Distribution Coefficient at LiCl--Bi-Th Interface
0	0	0.045	4.54
6	9.6	0.046	2.78
12	19.6	0.042	5.97
18	29.1	0.043	2.04
27	44.0	0.052	--
30	48.8	0.039	3.67
36	59.0	0.034	4.49
44.5	73.2	0.044	9.28
47.5	77.9	0.038	2.18
53.5	87.6	0.039	1.84
59.5	97.1	0.023	1.17
65.5	107.0	0.034	0.93
94.2	153.2	0.056	2.07
124.2	195.3	0.055	4.17
124.2	195.3	0.078	3.51
137.6	211.2	0.045	1.88
150.1	226.5	0.045	2.00
156.1	233.4	0.055	2.45
169.1	250.7	0.055	0.93
185.3	273.9	0.054	--
212.6	319.6	0.071	7.54
219.2	330.5	0.083	--
250.5	384.3	0.058	3.14
273.5	421.0	0.056	2.69
309.7	482.8	0.046	2.24
343.9	538.8	0.036	2.32
358.1	563.2	0.048	2.27
358.1	563.2	0.051	3.56

Table 47. Variation of Neodymium Distribution Coefficient with Time During Metal Transfer Experiment MTE-2

Pumping Time (hr)	Volume of LiCl Circulated (liters)	Distribution Coefficient at Fluoride Salt--Bi-Th Interface	Distribution Coefficient at LiCl--Bi-Th Interface
0	0	0.066	2.88
3	4.7	0.055	6.98
6	9.6	0.064	4.94
9	14.7	0.062	4.56
12	19.6	0.062	4.54
15	24.5	0.064	4.83
18	29.1	0.067	4.12
21	33.9	0.078	5.10
27	44.0	0.051	3.02
30	48.8	0.062	3.39
33	54.1	0.063	2.60
36	59.0	0.063	3.72
44.5	73.2	0.052	6.00
47.5	77.9	0.058	5.73
50.5	82.7	0.056	10.59
53.5	87.6	0.059	6.50
56.5	92.3	0.058	4.85
59.5	97.1	0.057	4.17
62.5	102.1	0.054	4.89
65.5	107.0	0.058	3.49
80.0	130.4	0.069	5.96
94.2	153.2	0.063	--
101.3	164.0	0.060	--
108.2	173.8	0.071	4.52
114.9	183.5	0.071	4.42
124.2	195.3	0.063	5.76
130.7	202.3	0.083	--
137.6	211.2	0.093	--
143.5	218.2	0.085	--
150.1	226.5	0.048	--
156.1	233.4	0.076	--
162.1	241.2	0.082	--
169.1	250.7	0.092	--
175.9	258.5	0.070	--
185.3	273.9	0.058	--
185.3	273.9	0.069	--
250.5	384.3	0.052	--
250.5	384.3	0.038	--

obtained from samples taken after circulation of the LiCl had been stopped and the phases had been allowed to approach chemical equilibrium for four or more hours. The variation of the coefficient for the distribution of lanthanum between the fluoride salt and the Th-Bi phase during the experiment is shown in Fig. 67. Although there is some variation in the distribution coefficient values, the average value (0.05) is relatively close to the value of 0.06 that was calculated from previously reported equilibrium relations. The variation of the coefficient for the distribution of lanthanum between the LiCl and the thorium-saturated bismuth during the run is shown in Fig. 68. The average value (3.1) is somewhat higher than the value predicted by equilibrium relations reported earlier (i.e., 0.9). Data on the coefficient for the distribution of neodymium between the fluoride salt and the thorium-saturated bismuth during the run are shown in Fig. 69. The average value for the distribution coefficient (0.06) is in good agreement with the expected value (0.062). The variation of the coefficient for the distribution of neodymium between the LiCl and the thorium-saturated bismuth during the experiment is shown in Fig. 70. The average value for the distribution coefficient (4.8) is slightly higher than the expected value of 3.5. The uncertainties in the distribution coefficient values for lanthanum and neodymium during the experiment result in some uncertainties of the values for f, the fractions of the lanthanum or neodymium that are removed from the LiCl during its passage through the cup containing the Li-Bi solution. The values of f for lanthanum and neodymium are 0.27 and 0.21, respectively, based on the average values for the distribution coefficients, and 0.08 and 0.16 based on the predicted values for the distribution coefficients.

The variations of the neodymium and lanthanum inventories in the system during the experiment are shown in Fig. 71. From 70 to 100% of each of the rare earths initially charged to the system could be accounted for, based on filtered samples. This indicates that essentially all of the rare earths remained in solution during the experiment.

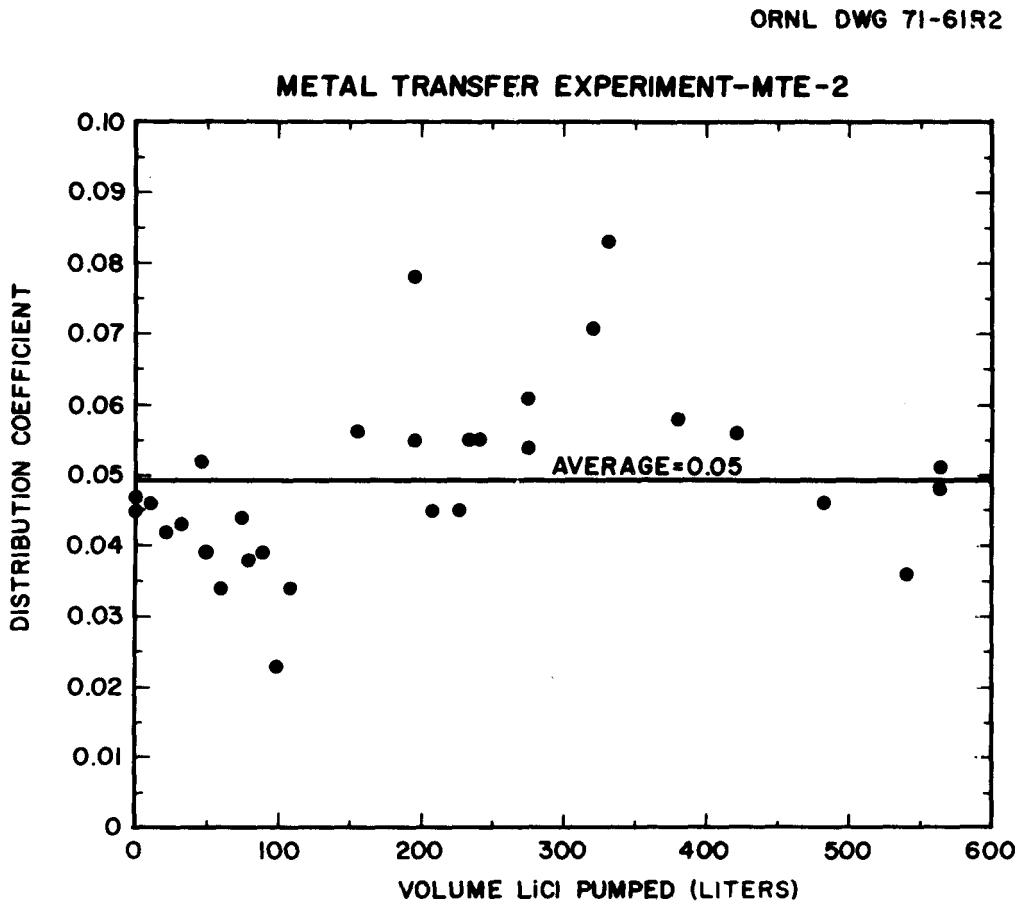

Fig. 67. Variation of the Coefficient for the Distribution of Lanthanum Between the Fluoride Salt and the Thorium-Saturated Bismuth During Metal Transfer Experiment MTE-2.

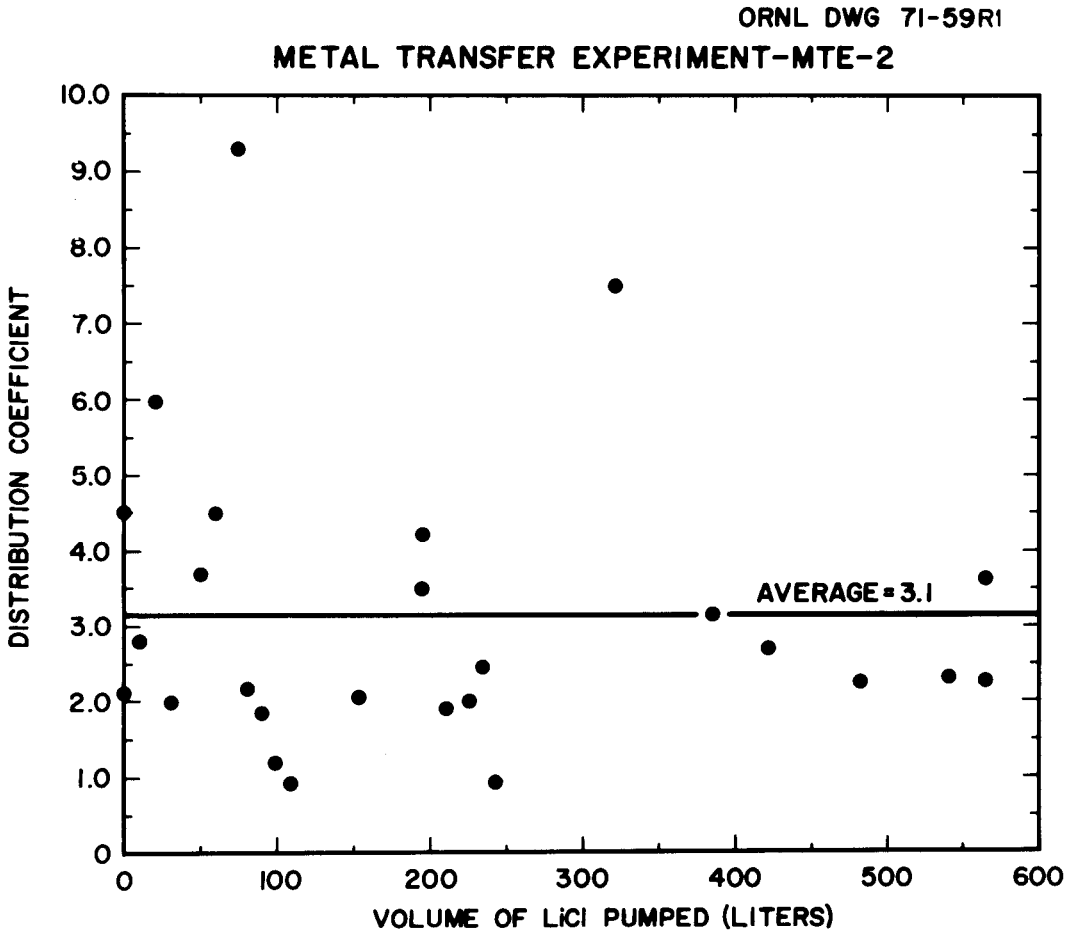

Fig. 68. Variation of the Coefficient for the Distribution of Lanthanum Between the LiCl and the Thorium-Saturated Bismuth During Metal Transfer Experiment MTE-2.

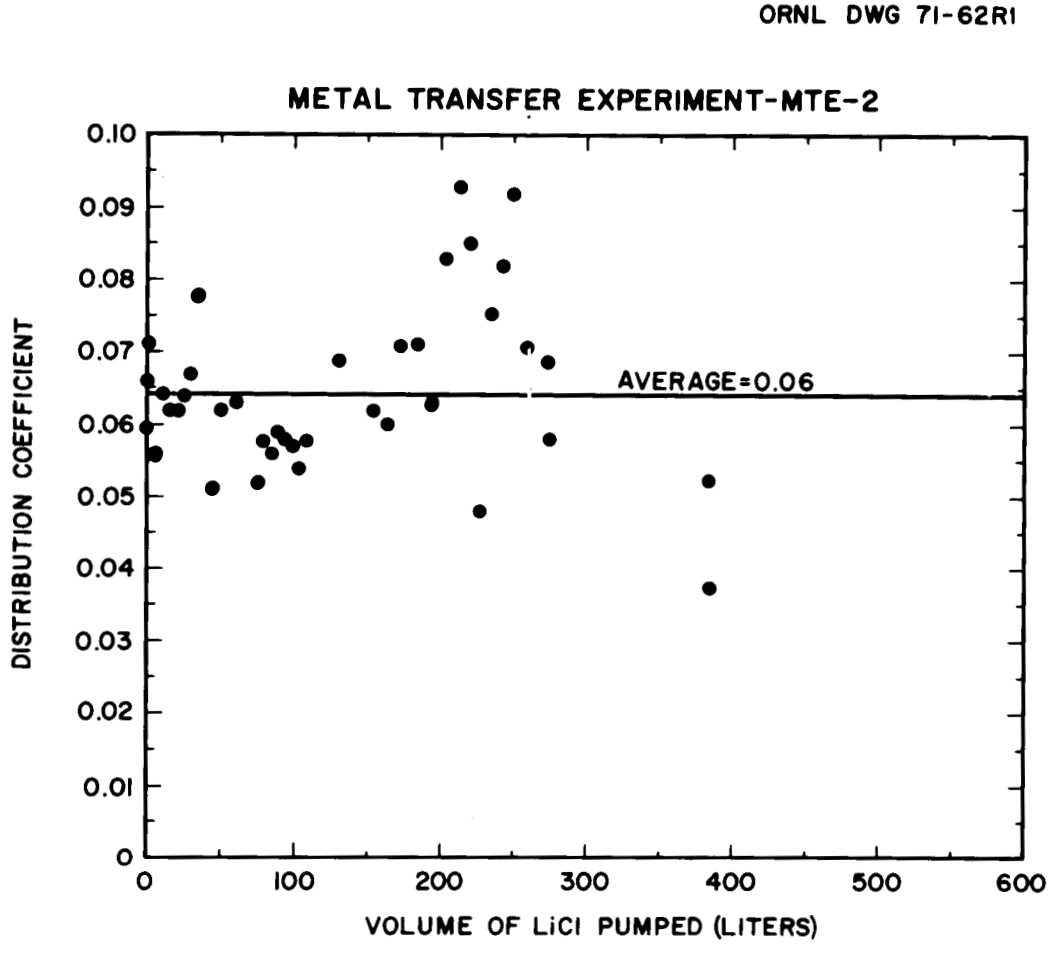

Fig. 69. Variation of the Coefficient for the Distribution of Neodymium Between the Fluoride Salt and the Thorium-Saturated Bismuth During Metal Transfer Experiment MTE-2.

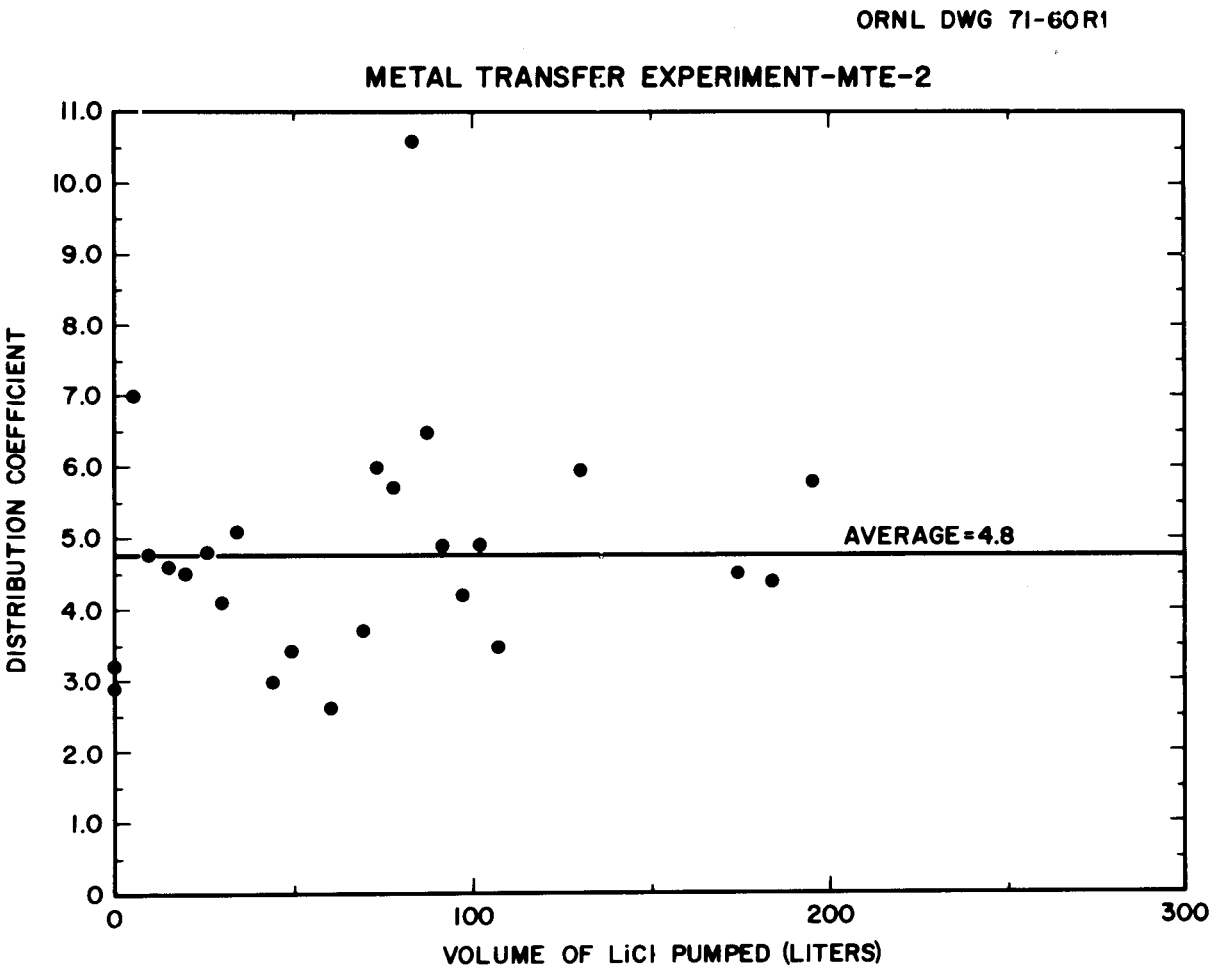

Fig. 70. Variation of the Coefficient for the Distribution of Neodymium Between the LiCl and the Thorium-Saturated Bismuth During Metal Transfer Experiment MTE-2.

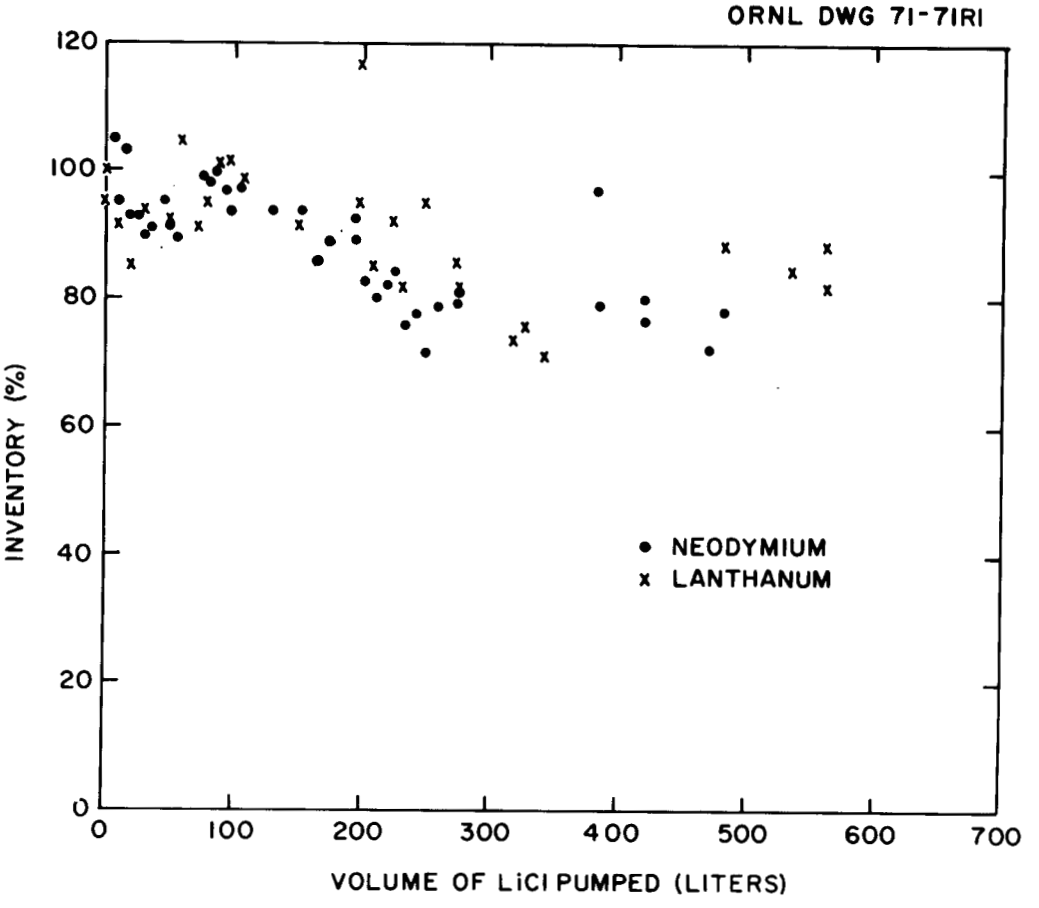

Fig. 71. Variation of the Inventories of Neodymium and Lanthanum During Metal Transfer Experiment MTE-2.

Decrease in Concentration of Lithium in the Li-Bi Solution. — During the experiment, the concentration of lithium in the Li-Bi solution decreased from an initial value of 1.8 wt % to 0.5 wt % (0.35 to 0.13 mole fraction), as summarized in Table 48 and shown in Fig. 72. A decrease of about 0.2 wt % in lithium concentration was expected as the result of extraction of the rare earths into the Li-Bi solution; however, the observed decrease was about six times this value. The reason for the decrease has not been determined at this time; it may have resulted from a slight solubility of lithium or a lithium-bismuth intermetallic in the LiCl or from transfer of lithium ions through the LiCl due to the difference in emf between the two bismuth phases in the system. The decrease in lithium concentration appears to have occurred only while LiCl was being circulated through the Li-Bi cup since no decrease was noted during long periods in which no circulation occurred (e.g., weekends).

Distribution of Radium Between the Salt and Metal Phases. — Radium was present in the system as a decay product of thorium, which was a constituent of the fluoride salt and of the bismuth phase (thorium-saturated). Data on the distribution of radium in the system during the experiment are summarized in Table 49 and shown in Fig. 73. At the end of the 76-hr equilibration period before circulation of the LiCl was begun, about 60% of the radium had transferred to the portion of the LiCl that was in contact with the thorium-saturated bismuth; the remaining 40% was present in the fluoride salt. No radium was present in the Li-Bi solution prior to circulation of the LiCl, and the radium concentration in the thorium-saturated bismuth remained below the limit of detection throughout the run. The radium slowly transferred into the Li-Bi solution as the LiCl was circulated through the Li-Bi cup. When operation of the gas-lift sparge tube in the Li-Bi cup was initiated (after about 50 liters of LiCl had been circulated), the concentration of ^{228}Ra in the Li-Bi solution increased abruptly and the concentration of radium in the LiCl decreased simultaneously. After a short period of time, the concentrations of radium throughout the system appeared to have reached equilibrium values, with about 40% of the radium in the Li-Bi solution, 40% in the LiCl, and 20% in the fluoride salt. During the remainder of the experiment, the radium slowly transferred out of the Li-Bi solution as the concentration of lithium in the solution decreased.

Table 48. Variation of Lithium Concentration in the Li-Bi Solution During Metal Transfer Experiment MTE-2

Pumping Time (hr)	Volume of LiCl Circulated (liters)	Lithium Conc. in Li-Bi (wt %)	Pumping Time (hr)	Volume of LiCl Circulated (liters)	Lithium Conc. in Li-Bi (wt %)
0	0	1.80	137.6	211.2	1.29
6	9.6	1.94	150.1	226.5	1.20
12	19.6	1.76	156.1	233.4	1.23
18	29.1	1.76	169.1	250.7	1.13
24	39.0	1.81	185.3	273.9	1.08
30	48.8	1.70	212.6	319.6	1.03
44.5	73.2	1.72	219.2	330.5	1.03
47.5	77.9	1.62	250.5	384.3	0.95
53.5	87.6	1.52	273.5	421.0	0.89
59.5	97.1	1.63	309.7	482.8	0.83
65.5	107.0	1.56	343.9	538.8	0.80
94.2	153.2	1.45	358.1	563.2	0.76
124.2	195.3	1.35	433.6	690.2	0.5

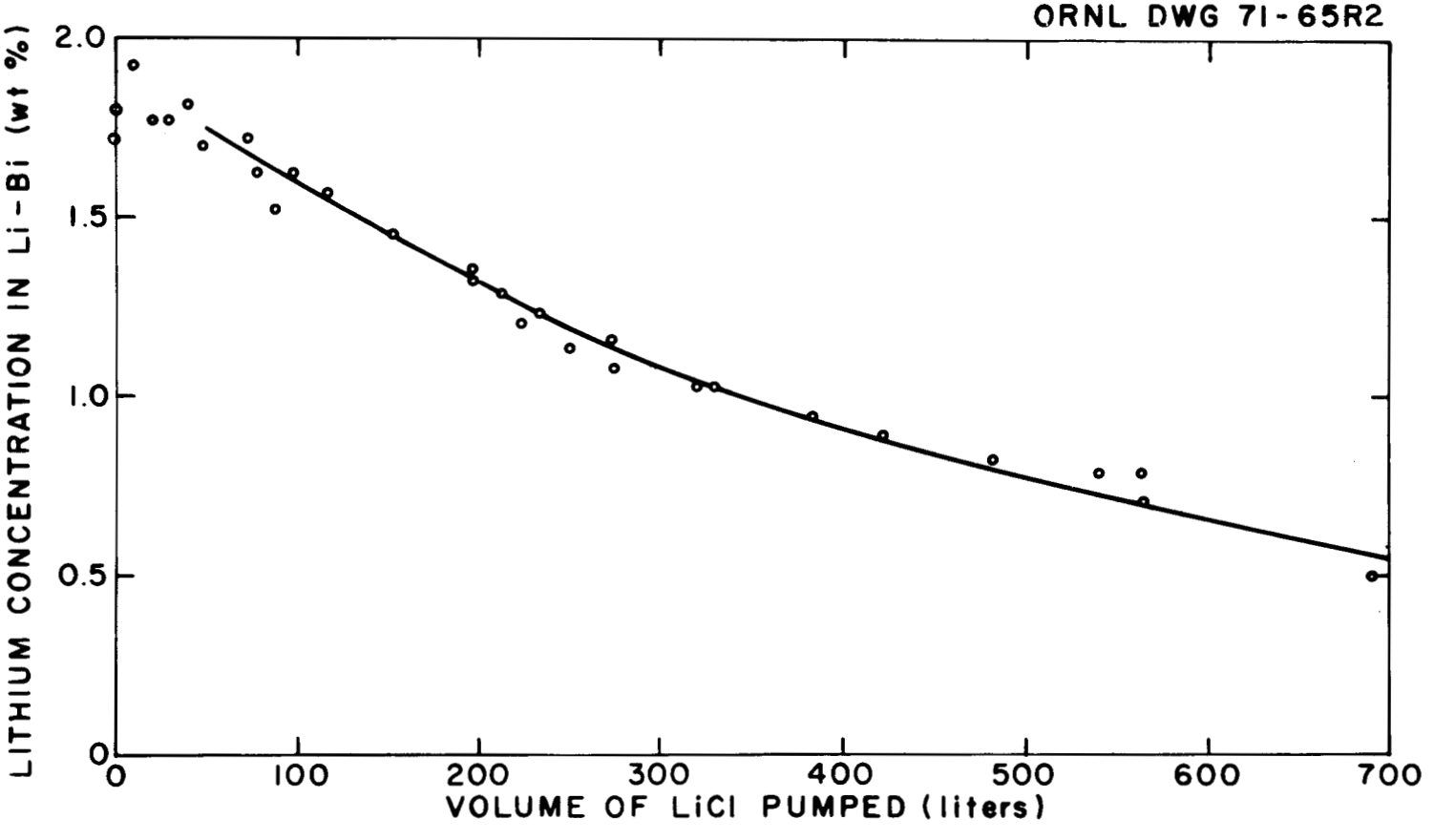

Fig. 72. Variation of Lithium Concentration in the Li-Bi Solution with Time During Metal Transfer Experiment MTE-2.

Table 49. Variation of the Distribution of Radium with Time During Metal Transfer Experiment MTE-2

Pumping Time (hr)	Volume of LiCl Circulated (liters)	Radium Conc. in Fluoride Salt (cpm/g)[a]	Radium Conc. in LiCl (cpm/g)[a]	Radium Conc. in Li-Bi (cpm/g)[a]	Pumping Time (hr)	Volume of LiCl Circulated (liters)	Radium Conc. in Fluoride Salt (cpm/g)[a]	Radium Conc. in LiCl (cpm/g)[a]	Radium Conc. in Li-Bi (cpm/g)[a]
0	0	537	1565	0	143.5	218.2	166	1028	901
3	4.7	487	1300	103	150.1	226.5	152	1107	964
6	9.6	451	1410	216	156.1	233.4	136	1103	885
9	14.7	453	--	285	162.6	241.2	154	1010	856
12	19.6	422	1511	406	175.9	258.5	97	1241	997
15	24.5	348	1311	384	185.3	273.9	115	--	907
18	29.1	409	1540	508	250.5	384.3	182.3	898	771
21	33.9	349	1506	513	250.5	384.3	--	1372[b]	--
24	39.0	--	1361	621	250.5	384.3	187.4	1846	977
27	44.0	365	1310	617	250.5	384.3	--	1309[b]	--
30	48.8	318	1508	--	273.5	421.0	63	1356	733
33	54.1	316	1371	692	273.5	421.0	52	1177	700
36	59.0	275	1029	1100	302.7	471.2	--	1163	631
39	63.9	--	907	1057	309.7	482.8	--	1176	628
44.5	73.2	278	950	1235	309.7	482.8	--	1135[b]	--
47.5	77.9	96	966	1261	343.9	538.8	--	1296	684
50.5	82.7	197	1388	1184	343.9	538.8	--	1362[b]	--
53.5	87.6	188	825	1213	343.9	538.8	--	1486	665
56.5	92.3	200	916	1154	343.9	538.8	--	1419[b]	--
59.5	97.1	185	701	1131	358.1	563.2	--	1311	640
62.5	102.1	226	979	1117	358.1	563.2	--	1676[b]	--
65.5	107.0	227	850	1160	358.1	563.2	--	1463	696
80.0	130.4	183	1032	1286	358.1	563.2	--	1570[b]	--
94.5	153.2	153	1019	1197	391.1	619.1	--	1367	511
108.2	173.8	77	1084	1084	391.1	619.1	--	1318[b]	--
114.9	183.5	57	1186	1134	413.3	656.0	--	1549[c]	457
124.2	195.3	92	1220	1097	413.3	656.0	--	1739[c]	--
130.7	202.5	80	1117	1123	413.3	656.0	--	1424[c]	--
137.6	211.2	--	1069	1029	419.2	665.2	--	1378[c]	498

[a] Counts per minute per gram.

[b] Samples taken from Li-Bi alloy container.

[c] After 1 vol % fluoride salt was added to LiCl.

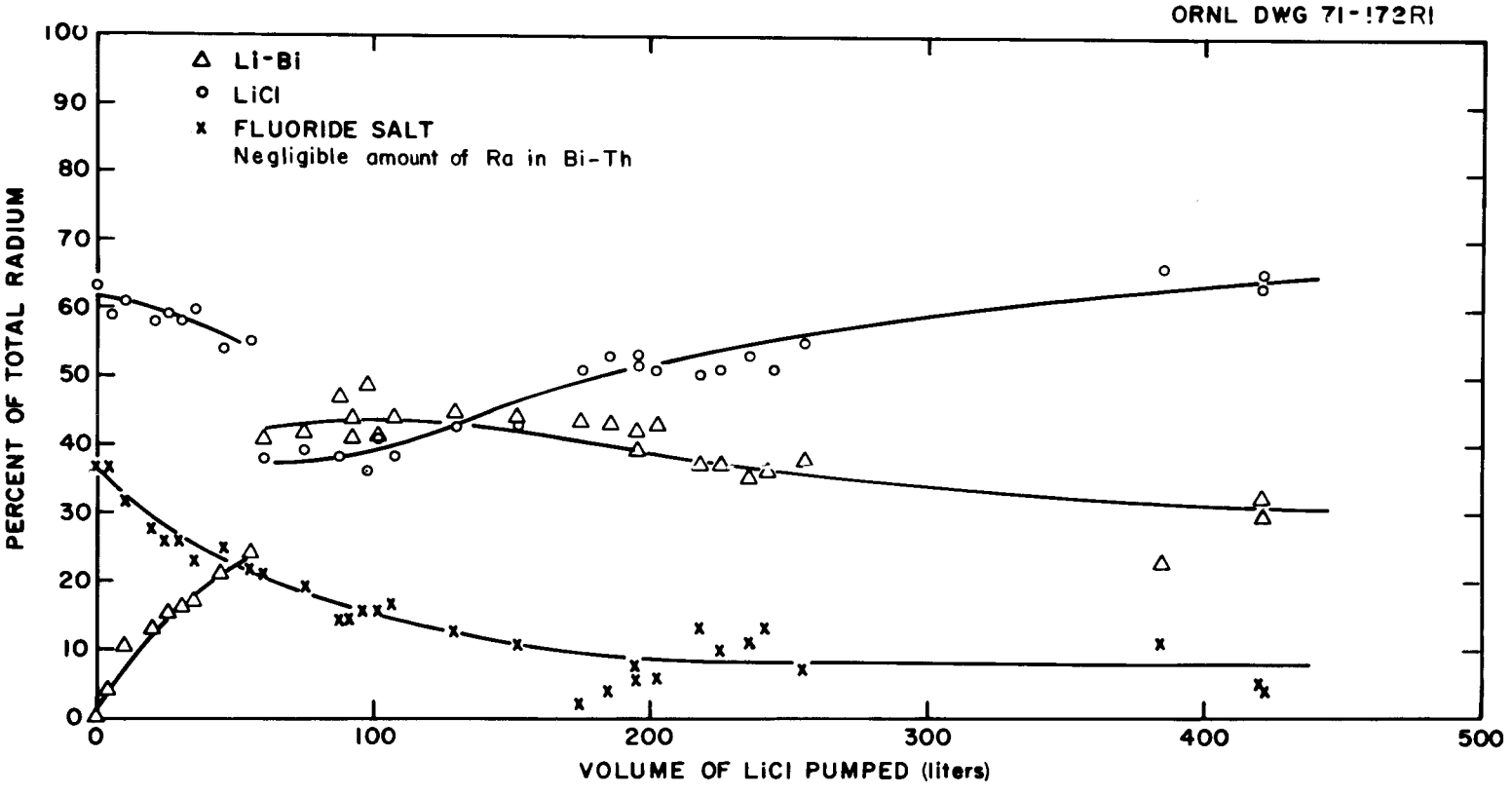

Fig. 73. Variation of the Distribution of Radium with Time in the Salt and Metal Phases in Metal Transfer Experiment MTE-2.

Addition of Fluoride Salt to the LiCl. — During operation of the metal transfer process, it is possible that small quantities of fluoride salt will be transferred to the LiCl by entrainment of salt in the bismuth that contacts these salt streams. It has been determined previously that the thorium distribution ratio between the LiCl and the bismuth is quite sensitive to the concentration of fluoride in the LiCl, and hence that the thorium--rare-earth separation factor in the process decreases markedly as the concentration of fluoride in the LiCl is increased. Throughout the experiment, very little fluoride was transferred to the LiCl, as indicated in Table 50; a final fluoride concentration of 1174 ppm was noted. Eight days before the end of the experiment, 1 vol % fluoride salt (72-16-12 mole % $LiF-BeF_2-ThF_4$) was added to the LiCl in order to simulate entrainment of fluoride salt in the circulating bismuth. The concentrations of beryllium, thorium, and fluoride in the LiCl were determined periodically after the addition of the fuel carrier salt, as shown in Table 51. During the 93-hr period in which the LiCl was not circulated through the Li-Bi container, the beryllium concentration remained constant at the initial value of 490 ppm and the thorium concentration decreased, as expected, from the initial value of 9480 ppm to a value of 644 ppm because of transfer of thorium into the Th-Bi solution. When circulation of the LiCl was resumed, the beryllium concentration in the LiCl began to decrease, probably because of reduction of Be^{2+} by the Li-Bi solution. After 27 hr of LiCl circulation, a beryllium concentration of 135 was observed in the LiCl. The thorium concentration in the LiCl was 171 ppm at this time.

Table 50. Variation of the Fluoride Concentration in the LiCl and the Chloride Concentration in the Fluoride Salt During Metal Transfer Experiment MTE-2

Pumping Time (hr)	Volume of LiCl Circulated (liters)	Chloride Concentration in Fluoride Salt (ppm)	Fluoride Concentration in LiCl (ppm)
0	0	--	77
9	14.7	175	530
56.5	92.3	121	--
101.3	164.0	--	517
273.5	421.0	392	205
413.3	656.0	--	1174

Table 51. Variation of Beryllium, Thorium, and Fluoride Concentrations in the LiCl After Addition of 1 vol % Fuel Carrier Salt

Time After Addition (hr)	Pumping Time (hr)	Fluoride (wt %)	Beryllium (ppm)	Thorium (ppm)
0	0	0.98[a]	490[a]	9480[a]
19.8	0	1.49	490	7200
45.4	0	1.08	500	1100
69.7	0	1.81	320	--
93	0	2.03	490	644
115.9	5.9	2.34	470	--
163.9	20.3	1.07	120	1400
188.8	27.4	0.91	--	350
188.8	27.4	1.7[b]	135[b]	171[b]

[a]Calculated values based on the amount of fluoride salt added.

[b]Salt taken from vessel after experiment was concluded.

12. DEVELOPMENT OF THE METAL TRANSFER PROCESS: DESIGN OF EXPERIMENT MTE-3

L. E. McNeese E. L. Nicholson
W. F. Schaffer, Jr. E. L. Youngblood
H. O. Weeren

It has been found that rare earths distribute selectively into molten LiCl from bismuth solutions containing rare earths and thorium, and an improved rare-earth removal process based on this observation has been devised. We are currently engaged in experiments designed to demonstrate all phases of the improved rare-earth removal method, which is known as the metal transfer process. In a previous engineering experiment (MTE-1),[46] we studied the removal of rare earths from single-fluid MSBR fuel salt by this process. During the experiment, approximately 50% of the lanthanum and 25% of the neodymium originally present in fluoride salt were removed at about the predicted rate. Surprisingly, however, the lanthanum and neodymium that were removed from the fluoride salt did not accumulate in the Li-Bi solution used for removing these materials from the LiCl. Reaction of impurities in the system with the rare earths is believed to have caused this unexpected behavior. A second engineering experiment (MTE-2) has been designed and put into operation (see Sect. 11). The design of the third engineering experiment is currently under way. The third experiment (MTE-3) will use salt and bismuth flow rates that are about 1% of the estimated flow rates required for processing a 1000-MW(e) reactor. In the two previous experiments, the salt and bismuth phases were only slightly agitated, resulting in a low rate of transfer of rare earths from the fuel carrier salt to the Li-Bi solution. In experiment MTE-3, the salt and metal phases will be mechanically agitated in order to increase the rate of transfer of materials between the phases. In the remainder of this section, results from a mathematical analysis carried out for estimating the performance of the system are presented and the experiment is briefly described.

12.1 Mathematical Analysis of Metal Transfer Experiment MTE-3

A mathematical analysis of experiment MTE-3 was performed in order to determine the approximate operating conditions for the system and to aid in setting values for parameters such as flow rates, solution volumes, etc. In considering the conceptual design for the experiment, it was concluded that the salt-metal contactor should be of the two-compartmented, stirred-interface type. As pointed out in the following section of this report (Sect. 13), such a contactor is of interest because, with it, adequate mass transfer rates can apparently be achieved without dispersal of either the salt or bismuth phases. Contact of the salt and metal streams without dispersion of the phases should considerably diminish the problem of entrainment of bismuth in the processed fuel carrier salt and the subsequent transfer of bismuth to the reactor, which is constructed of a nickel-base alloy that is subject to damage by metallic bismuth. The bismuth in a salt-metal contactor of the type being considered would be a near-isothermal, internally circulated phase, which is a desirable condition. Also, it is believed that a processing system employing this type of contactor may be more easily fabricated from molybdenum and graphite than one employing packed columns. The major equipment items considered in the mathematical analysis are shown in Fig. 74. Fuel carrier salt (72-16-12 mole % $LiF-BeF_2-ThF_4$) containing rare-earth fluorides would be circulated between the fluoride salt surge tank and the side of the salt-metal contactor containing fluoride salt. Lithium fluoride would be circulated between the other side of the contactor and a vessel containing a Li-Bi solution having a lithium concentration of about 5 at. %. During operation of the system, the rare earths would be extracted from the fluoride salt and would accumulate in the Li-Bi solution.

In carrying out the mathematical analysis, it was assumed that the salt and bismuth phases in the salt-metal contactor remain at equilibrium at all times. Although this condition will clearly not be met during operation of the experiment, such an assumption will allow a useful representation of the salt-metal contactor. The concentrations of a rare earth in the salt and bismuth phases in the salt-metal contactor at time t are then related by the following expressions:

ORNL DWG. 73-44

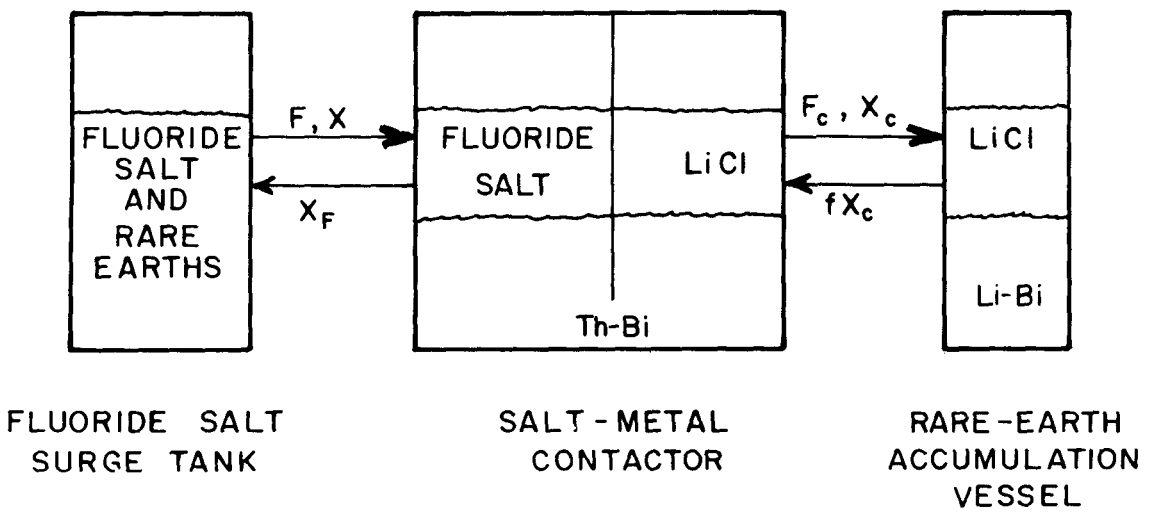

Fig. 74. Equipment Representation and Nomenclature Used for Mathematical Analysis of Experiment MTE-3.

$$D_F = \frac{x_{Bi}}{x_F} \quad , \tag{52}$$

where

D_F = rare-earth distribution ratio between fluoride salt and bismuth containing reductant at time t,

x_{Bi} = equilibrium concentration of rare earth in bismuth in contactor at time t, mole fraction,

x_F = equilibrium concentration of rare earth in fluoride salt in contactor at time t, mole fraction,

and

$$D_c = \frac{x_{Bi}}{x_c} \quad , \tag{53}$$

where

D_c = rare-earth distribution ratio between LiCl and bismuth containing reductant at time t,

x_c = equilibrium concentration of rare earth in LiCl in contactor at time t, mole fraction.

Combination of Eqs. (52) and (53) yields the following expression:

$$x_F = \frac{D_c}{D_F} x_c \quad , \tag{54}$$

which relates the concentration of rare earth in the fluoride salt to that in the LiCl in the contactor at time t. The rate at which the rare earth is transferred through the contactor is then given by the expression

$$\text{rate} = F_c \, x_c \, (1 - f) \quad , \tag{55}$$

where

F_c = flow rate of LiCl between the contactor and the vessel containing the Li-Bi solution, moles/sec,

f = fraction of rare earth removed from LiCl during its passage through the vessel containing the Li-Bi solution.

The rate of transfer is also equal to the instantaneous rate at which rare earths are removed from the fluoride salt surge tank, which is given by the expression

$$\text{rate} = F(x - x_F) \quad , \tag{56}$$

where

F = flow rate of fluoride salt between the contactor and the fluoride salt surge tank, moles/sec,

x = concentration of rare earth in fluoride salt surge tank at time t, mole fraction.

If it is assumed that the rate of accumulation of rare earth in the salt and metal phases in the salt-metal contactor is negligible, Eqs. (55) and (56) can be equated. Substituting Eq. (54) in the resulting relation and solving for x_F, the concentration of rare earth in the fluoride salt in the contactor at time t, yields the following expression:

$$x_F = \frac{x}{1 + \frac{F_c}{F}\frac{D_F}{D_c}(1 - f)} \quad . \tag{57}$$

A material balance on the rare earth in the fluoride salt surge tank yields the following relation:

$$-V\frac{dx}{dt} = F(x - x_F) \quad , \tag{58}$$

where

V = volume of fluoride salt in the surge tank, moles.

Combination of Eqs. (57) and (58) yields the following differential equation:

$$\int_{x_o}^{x} \frac{dx}{x} = -\frac{F}{V}\,\frac{\frac{F_c}{F}\frac{D_F}{D_c}(1 - f)}{1 + \frac{F_c}{F}\frac{D_F}{D_c}(1 - f)} \int_0^t dt \tag{59}$$

where

x_o = initial concentration of rare-earth fluoride in fluoride salt surge tank, mole fraction.

This equation can be integrated between the indicated limits to yield the following expression for the concentration of rare-earth fluoride in the fluoride salt surge tank at time t:

$$\frac{x}{x_o} = e^{-\kappa t} \quad , \tag{60}$$

where

$$\kappa = \frac{F}{V} \frac{\frac{F_c}{F}\frac{D_F}{D_c}(1-f)}{1+\frac{F_c}{F}\frac{D_F}{D_c}(1-f)} \quad .$$

If it assumed that the flow rates for the fluoride salt and the LiCl are, in each case, 1% of the expected flow rates required for removing rare earths from a 1000-MW(e) MSBR (see Sect. 3) and if the concentration of reductant in the bismuth in the salt-metal contactor corresponds to a thorium concentration equal to 90% of the solubility of thorium in bismuth at the operating temperature of 640°C, the following values are obtained for the parameters in Eq. (60) for the transfer of neodymium:

$$D_F = 0.0564 \quad ,$$

$$D_c = 3.5 \quad , \text{ and}$$

$$\frac{F_c}{F} = 25.1 \quad .$$

If it assumed that 50% of the neodymium is extracted from the LiCl as it passes through the vessel containing the Li-Bi solution, the expression for the quantity κ can be written as:

$$\kappa = 0.168 \frac{F}{V} \quad . \tag{61}$$

If it is desired to reduce the concentration of neodymium in the fluoride salt surge tank by 20% during a 24-hr operating period, the quantity κ must have the value 0.223, which then sets the value for the quantity V/F

at 0.753 day. The resulting volume of the fluoride salt in the surge tank is 36.1 liters. Table 52 summarizes the resulting design parameters which are dependent on the following assumptions: (1) the salt and metal phases in the salt-metal contactor remain at equilibrium at all times, (2) salt and metal flow rates equal to 1% of the expected rates required for processing a 1000-MW(e) MSBR are used, (3) neodymium is the transferring rare earth, and (4) the concentration of neodymium fluoride in the fluoride salt surge tank is to be reduced by 20% during a 24-hr operating period.

Table 52. Calculated Values of the Design Parameters for Experiment MTE-3

Quantity	Value
D_F	0.0564
D_c	3.5
F	33 cm^3/min
F_c	1.25 liters/min
V	36.1 liters

12.2 Preliminary Design of Metal Transfer Experiment MTE-3

The planned experiment, shown schematically in Fig. 75, will use mechanical agitators to promote efficient contact of the salt and metal phases. Fuel carrier salt containing rare-earth fluorides will be circulated between one side of the salt-metal contactor and a fluoride salt reservoir. Lithium chloride containing rare-earth chlorides will be circulated between the other side of the salt-metal contactor and a rare-earth stripper, where the rare earths will be extracted into a Li-Bi solution.

The experiment will use approximately 35 liters of MSBR fuel carrier salt, 6 liters of Th-Bi solution, 6 liters of LiCl, and about 5 liters of Li-Bi solution having an initial lithium content of about 5 at. %.

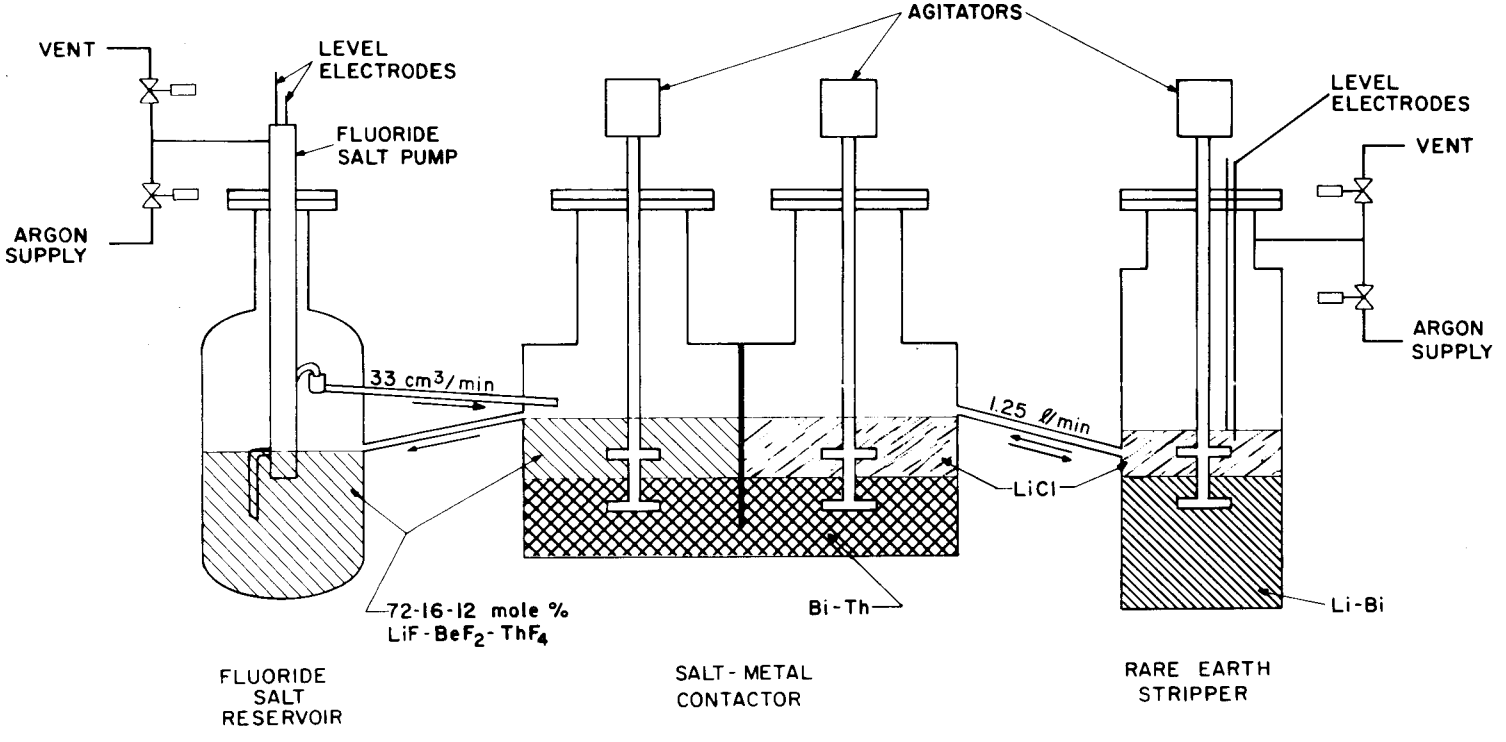

Fig. 75. Flow Diagram for Metal Transfer Experiment MTE-3.

The system will require three process vessels, each of which will be made of carbon steel. The largest vessel will be the fluoride salt reservoir, which will contain approximately 32 liters of fuel carrier salt. The remaining 3 liters of fluoride salt will be contained in the salt-metal contactor. The fluoride salt will be recirculated continuously from the reservoir to the contactor at the rate of about 33 cm^3/min by a pump similar to the one used in the second metal transfer experiment.[48] The salt-metal contactor will be a 10-in.-diam, two-compartmented vessel having a mechanical agitator in each compartment. The agitator will consist of two paddles mounted on a common shaft with a paddle operating in each of the salt and metal phases in a manner such that neither of the phases is dispersed. Each paddle will consist of 4 blades that are canted at a 45° angle in a manner such that the salt and bismuth will be forced to flow toward the salt-metal interface in the area around the agitator shaft. The Th-Bi solution will be captive in the salt-metal contactor and will form a seal to isolate the fluoride salt from the LiCl. The Th-Bi solution will be recirculated between the two compartments of the salt-metal contactor by utilizing the pumping capability of the agitators. The third vessel, which will be similar in design to one compartment of the salt-metal contactor, will contain the Li-Bi solution. The LiCl will be circulated between the salt-metal contactor and the rare-earth stripper at the rate of about 1.25 liters/min by varying the gas pressure above the LiCl in the rare-earth stripper. All of the vessels will be operated at 650°C. The carbon steel used for fabricating the system will be protected from external air oxidation by the use of a nickel aluminide coating.

13. DEVELOPMENT OF MECHANICALLY AGITATED SALT-METAL CONTACTORS

H. O. Weeren L. E. McNeese
J. S. Watson

A program has been initiated for the development of mechanically agitated salt-metal contactors as an alternative to packed columns presently under consideration for MSBR processing systems. This type of contactor is of particular interest for the metal transfer process since designs can be envisioned in which the bismuth phase would be a near-isothermal, internally recirculated, captive phase. It is believed that such designs will require a less highly developed technology for molybdenum fabrication than would a counterpart system based on packed columns. During this report period, we carried out preliminary tests on the hydrodynamics of mechanically agitated salt-metal contactors using water and mercury and reviewed information in the literature relative to mass transfer rates in contactors in which the phases are not dispersed. Results of work in these areas are summarized in the remainder of this section.

13.1 Hydrodynamic Studies

Studies of the hydrodynamics of mechanically agitated salt-metal contactors carried out thus far have been concerned primarily with the selection of a contactor design for experiment MTE-3 (discussed in Sect. 12), which will have salt and bismuth flow rates that are about 1% of the estimated rates for processing a 1000-MW(e) MSBR. Several scouting tests were carried out with water and mercury in 4- to 7-in.-diam vessels, and a mockup of the contactor proposed for experiment MTE-3 was built for additional study with mercury and water. The mockup consists of an 8-in.-diam vessel having a central partition that extends to within 1/2 in. of the bottom of the vessel. The first tests with the mockup were made with a flat, four-bladed paddle located in the mercury-water interface. The paddle, 1.5 in. in diameter, was located inside a 3-in.-diam, 3-in.-high shroud containing four 0.3-in.-wide, 3-in.-long baffles. The design of the proposed contactor was chosen to maximize

the extent of dispersion of the mercury in the water, thereby maximizing the interfacial area between the two phases. The mockup of the MTE-3 system was tested with agitator speeds up to 1600 rpm. It was found that a stable dispersion of very small mercury droplets was frequently formed under these operating conditions. Also, a dispersion of water droplets was formed in the mercury at all but the lowest mixer speeds, and these droplets were pumped from one chamber of the contactor to the other. Such pumping of molten salt solutions cannot be tolerated in the metal transfer process since it would lead to mixing of the chloride and fluoride salts. The tendency of the salt-bismuth system to form emulsions may be quite different from that of the water-mercury system; however, it was concluded that the contactor should operate under conditions that minimize the likelihood of emulsion formation.

The contactor design that has the greatest potential for achieving effective mass transfer rates with minimum dispersion of the phases appears to be the Lewis cell.[49] This contactor has a paddle in each phase, located well away from the interface as shown in Fig. 76. Each agitator is operated in a manner such that the phases are agitated as vigorously as possible without actually dispersing one phase in the other. The contactor cell mockup described previously was modified in order to study the hydrodynamics of this type of contactor. The shroud was removed, and paddles having a range of diameters were tested at several positions in baffled cells and also in cells containing no baffles. A significant amount of entrainment of water via circulation of the mercury between the compartments was noted at agitator speeds above 180 rpm when 3-in.-diam, four-bladed vertical paddles were used. The agitator speed at which entrainment began to occur could be increased slightly (to about 220 rpm) when baffles were used in the cell, when the lower paddle was located within 0.25 in. of the bottom of the cell, or when the depth of the mercury in the cell was increased by about 0.5 in. When smaller-diameter agitators were used, the speed at which entrainment was noted increased; however, the Reynolds number based on the paddle diameter was almost the same in each case.

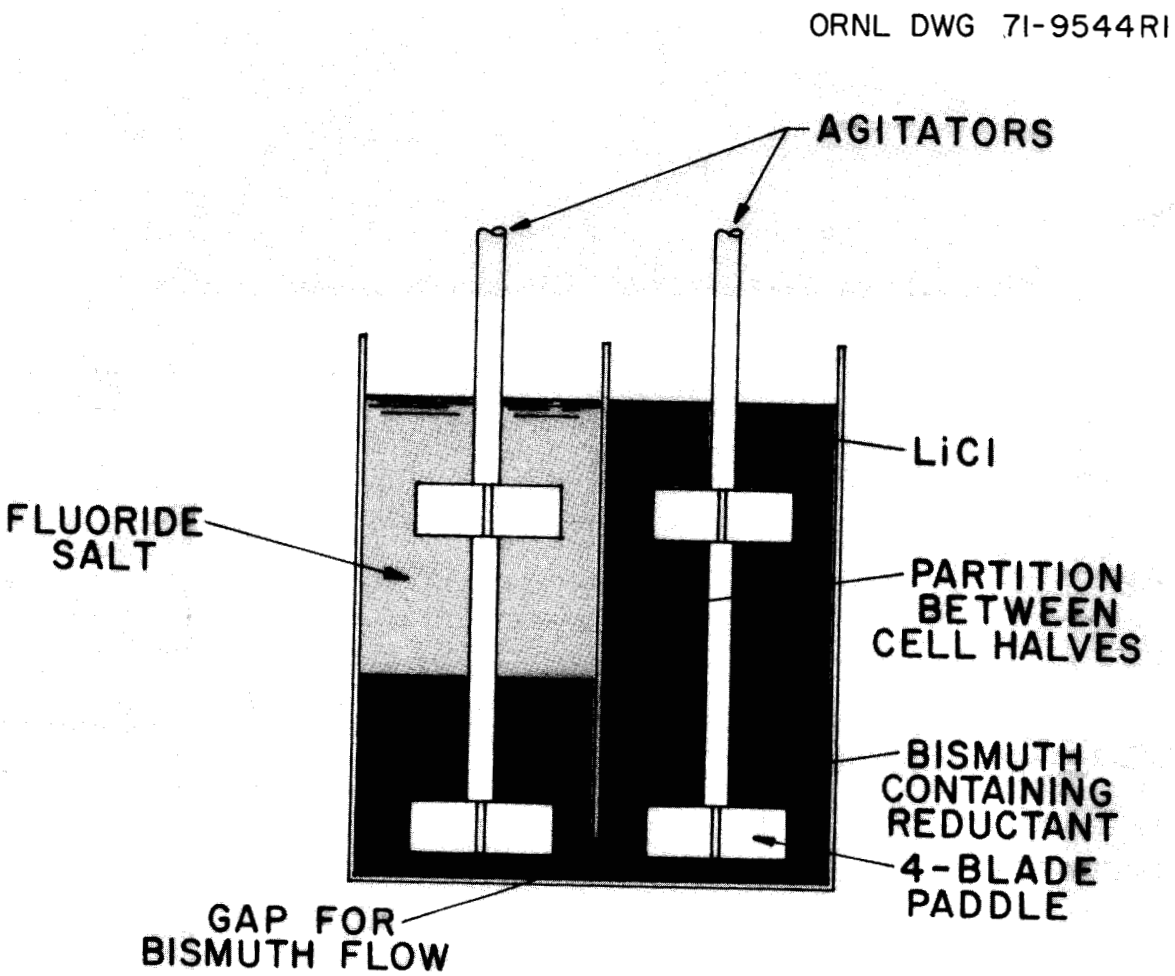

Fig. 76. Mechanically Agitated Salt-Metal Contactor Proposed for Use with Metal Transfer Experiment MTE-3.

Investigation showed that use of a 3-in.-diam, four-bladed paddle having blades canted at a 45° angle did not result in entrainment of water until an agitator speed of 400 rpm was reached. It is believed that the flow patterns in the water and mercury that are created by the use of canted blades inhibit the formation of a vortex around the agitator shaft and thereby reduce the extent of dispersion of water in the mercury phase.

13.2 Survey of Literature Relative to Mechanically Agitated, Nondispersing Salt-Metal Contactors

Various investigations have been carried out for determining the rate of mass transfer between aqueous and organic phases in mechanically agitated contactors in which the phases are not dispersed. Lewis[49] has investigated mass transfer rates in six solvent-water systems and two nonaqueous systems. The solvents used were aniline, ethyl acetate, ethyl acetoacetate, ethyl formate, furfural, and isobutanol; formic acid--benzene and aniline-cyclohexane were the nonaqueous systems. A sketch of the apparatus used, with reported dimensions, is given in Fig. 77. The speed and direction of rotation of the agitators were controlled individually; most of the data were taken with the agitators contrarotating, but it was stated that the relative direction of rotation made little difference. Lewis correlated his data by the expression:

$$\frac{60\ k_1}{\nu_1} = 6.76 \times 10^{-6} \left(Re_1 + Re_2 \frac{\mu_2}{\mu_1} \right)^{1.65} + 1 , \qquad (62)$$

where

k_1 = individual mass transfer coefficient, cm/sec,
ν_1 = kinematic viscosity (μ/ρ), cm^2/sec,
Re = nd^2/ν, dimensionless,
μ = viscosity, poises,
ρ = density, g/cm^3,
d = agitator diameter, cm, and
n = agitator speed, rps.

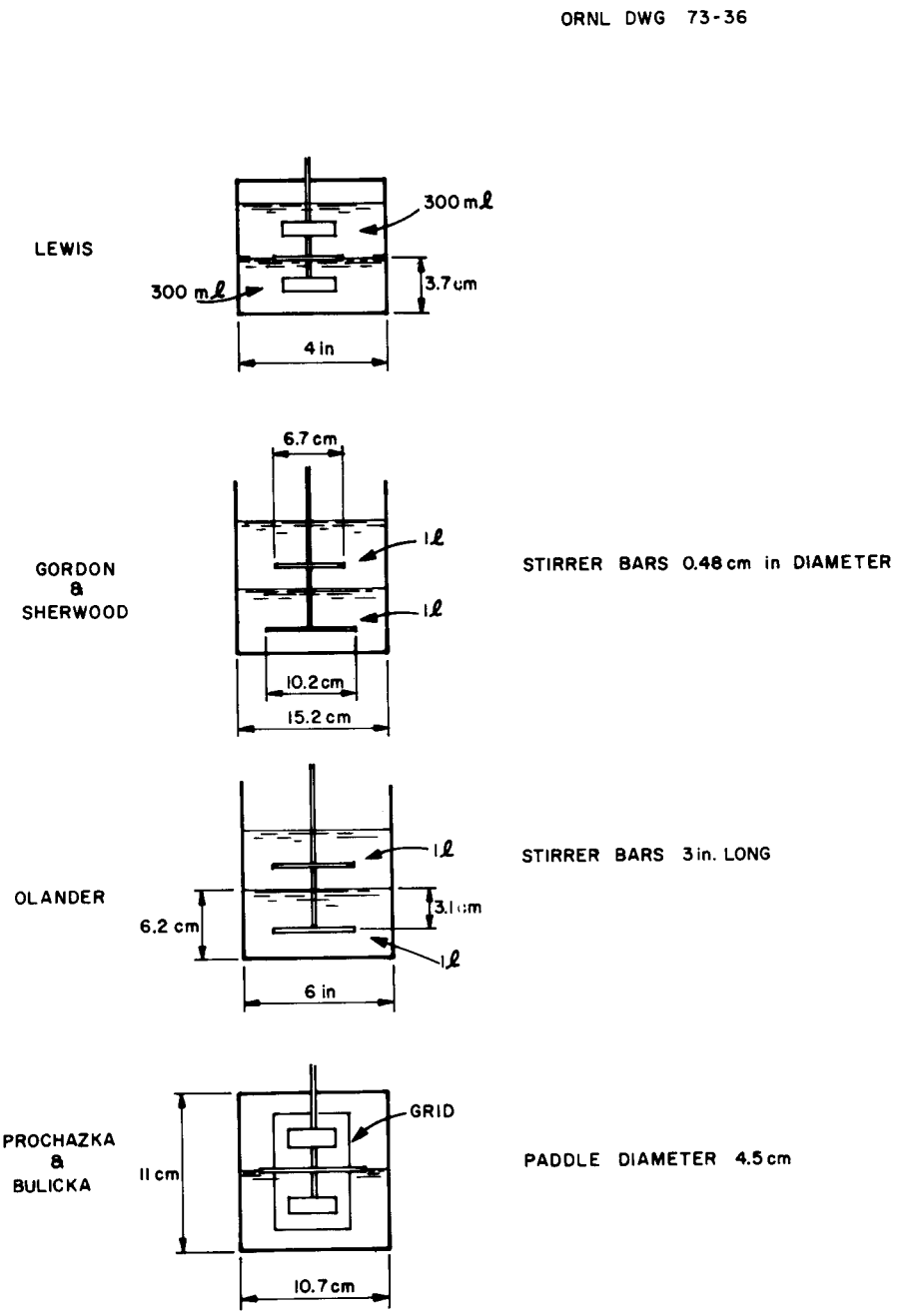

Fig. 77. Schematic Diagrams of Equipment Used By Various Investigators for Measuring Mass Transfer Coefficients in Stirred Interface Contactors.

The subscripts 1 and 2 refer to phases 1 and 2, respectively. In a subsequent paper, Lewis[50] reported results for the rate of transfer of a third component between the two phases of several solvent-water systems. He stated that the relation given by Eq. (62) also correlated the data on the rate of transfer of the third component.

McManamey[51] correlated Lewis' results and his own data (obtained in a cell similar to that used by Lewis) by the expression:

$$\frac{60\ k_1}{v_1} = 0.1\ \text{cm}^{-1} \left(\frac{\nu}{D}\right)_1^{-0.3} (\text{Re}_1)^{0.9} \left(1 + \frac{\mu_2}{\mu_1} \frac{\text{Re}_2}{\text{Re}_1}\right), \qquad (63)$$

where

D = diffusivity of the transferable material in the phase indicated, cm^2/sec.

Mayers[52] correlated Lewis' results and his own data (obtained in a cell similar to that used by Lewis) by the expression:

$$\frac{k_1 d}{D_1} = 0.00316 \left(\frac{\mu_2}{\mu_1}\right)^{1.9} \left(0.6 + \frac{\mu_2}{\mu_1}\right)^{-2.4} (\text{Re}_1\ \text{Re}_2)^{1/2} \left(\frac{\nu_1}{D_1}\right)^{5/6}. \qquad (64)$$

Gordon and Sherwood[53] determined individual mass transfer coefficients in the system isobutanol-water with and without a third solute. A sketch of their apparatus is given in Fig. 77. The agitators in each phase were mounted on a common shaft. No correlation was suggested.

Olander[54] determined mass transfer coefficient values in several solvent-water systems (many of which were identical to those used by Lewis) in the apparatus shown in Fig. 77. The agitators for each phase were mounted on a common shaft. The suggested correlation was:

$$\left(\frac{k_1}{v_1}\right)\left(\frac{\nu_1}{D_1}\right)^{0.44} = 0.046 \left(\frac{\omega}{\nu_1}\right)^{0.67}, \qquad (65)$$

where

ω = agitator speed, radians/sec.

Prochazka and Bulicka[55] determined mass transfer coefficient values in water--ethyl acetate and water-isobutanol systems. A sketch of their apparatus is shown in Fig. 77. The agitators were controlled separately, and the agitator blades were canted at an angle of 45°. The suggested correlation for their mass transfer coefficient data was:

$$\frac{k_1 d}{D_1} \propto \left(\frac{\nu_1}{D_1}\right)^{1/2} (Re_1)^{3/4} \left[\frac{1 + \left(\frac{n_2}{n_1}\right)^3 \left(\frac{d_2}{d_1}\right)^2 \left(\frac{\nu_2}{\nu_1}\right) \left(\frac{\rho_2}{\rho_1}\right)^{3/2}}{1 + \left(\frac{\rho_1}{\rho_2}\right)^{1/2}}\right]^{1/4} . \quad (66)$$

The magnitudes of the individual mass transfer coefficients obtained by most of the investigators were approximately the same -- from about 0.007 cm/sec for ethyl acetate--water systems to about 0.001 cm/sec for isobutanol-water systems. The values for the individual mass transfer coefficients reported by Prochazka and Bulicka, however, were two orders of magnitude greater -- from about 1.1 cm/sec for ethyl acetate--water systems to about 0.1 cm/sec for isobutanol-water systems. It was later found that a decimal point has been misplaced in their literature article.[56] After the appropriate correction had been made, the reported results were found to be consistent with the data of other investigators.

Although the magnitudes of the individual mass transfer coefficients obtained by different investigators were about the same, the reported dependence of the mass transfer coefficient on the agitator speed varied widely. Part of this difference is apparently due to the different relations used to correlate the data, and part is due to a different degree of interfacial turbulence created in the various pieces of equipment at a given agitator speed. The scatter in the reported data is shown in Figs. 78-80. In Fig. 78 the data from all the investigators are plotted in the manner suggested by Lewis; in Fig. 79 the data are plotted according to the correlation suggested by Olander; and in Fig. 80 the data are plotted as suggested by Prochazka and Bulicka.

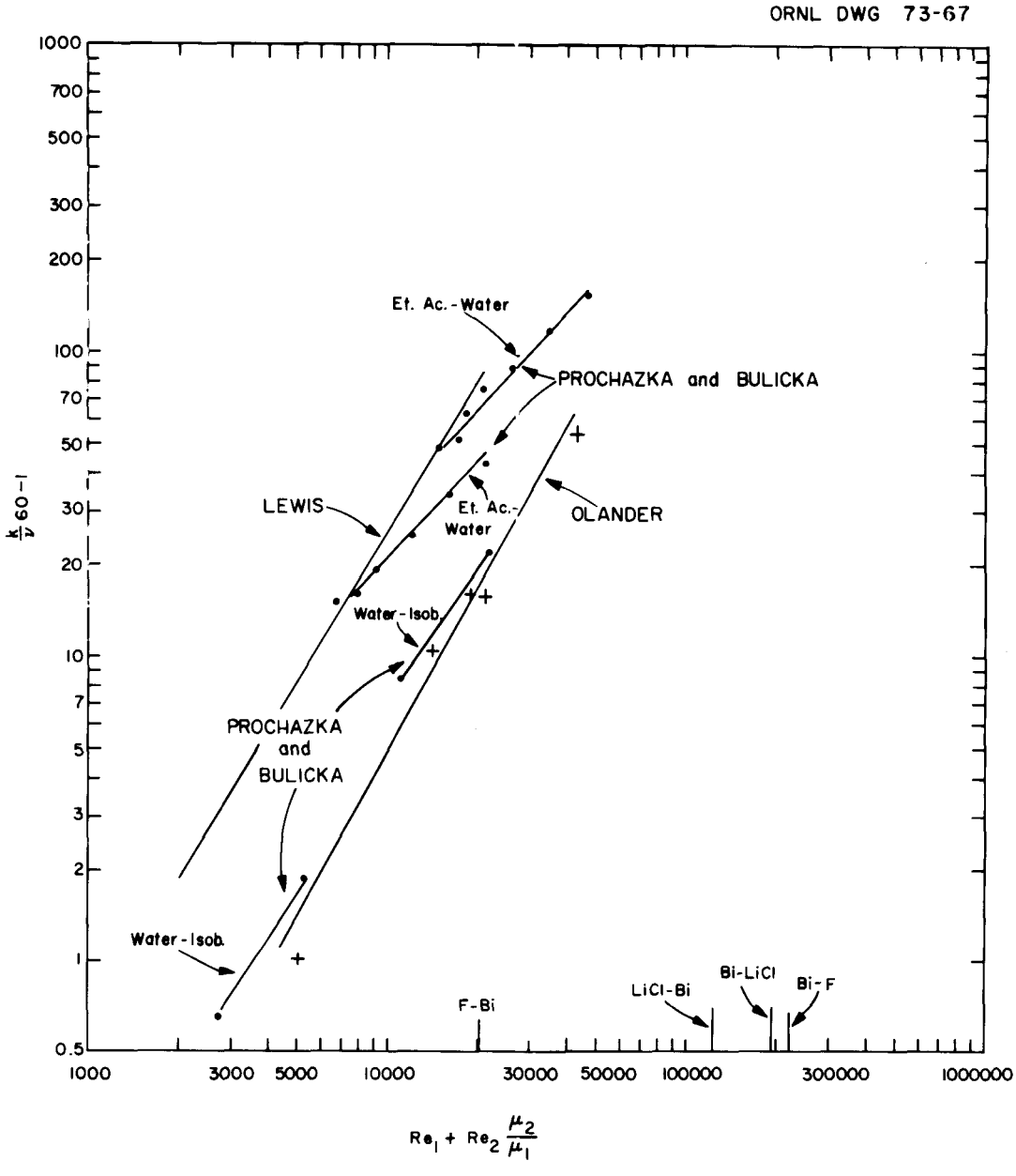

Fig. 78. Correlation of Data on Mass Transfer Coefficients in Stirred-Interface Contactors in the Manner Suggested by Lewis. The operating conditions that will be obtained at the various interfaces in metal transfer experiment MTE-3 with an agitator speed of 3 rps are shown on the abscissa. The notation F-Bi denotes transfer from fluoride salt to a bismuth phase; LiCl-Bi, transfer from molten LiCl to a bismuth phase; Bi-LiCl, transfer from a bismuth phase to molten LiCl; and Bi-F, transfer from a bismuth phase to fluoride salt.

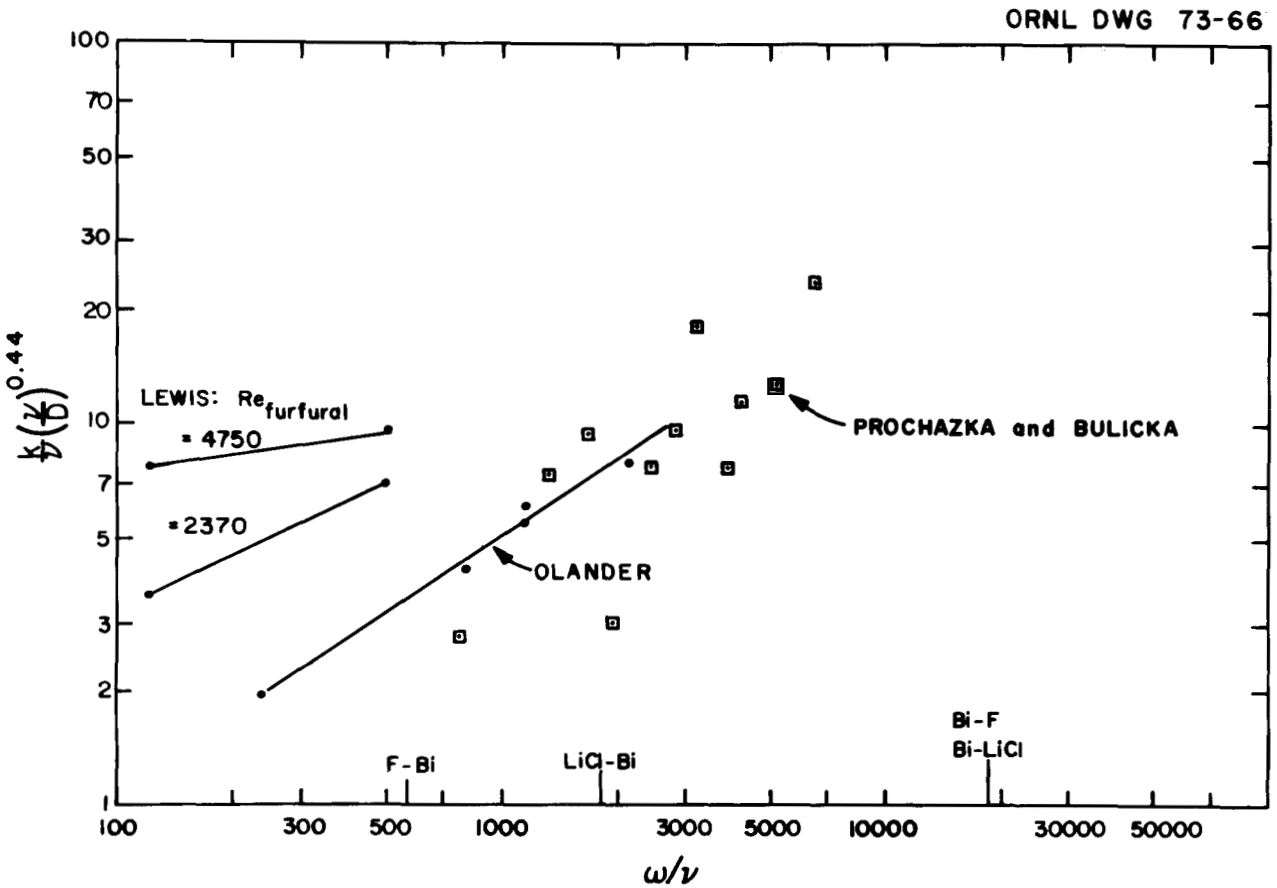

Fig. 79. Correlation of Data on Mass Transfer Coefficients in Stirred Interface Contactors in the Manner Suggested by Olander. The operating conditions that will be obtained at the various interfaces in metal transfer experiment MTE-3 with an agitator speed of 3 rps are shown on the abscissa. The notation F-Bi denotes transfer from fluoride salt to a bismuth phase; LiCl-Bi, transfer from molten LiCl to a bismuth phase; Bi-LiCl, transfer from a bismuth phase to molten LiCl; and Bi-F, transfer from a bismuth phase to fluoride salt.

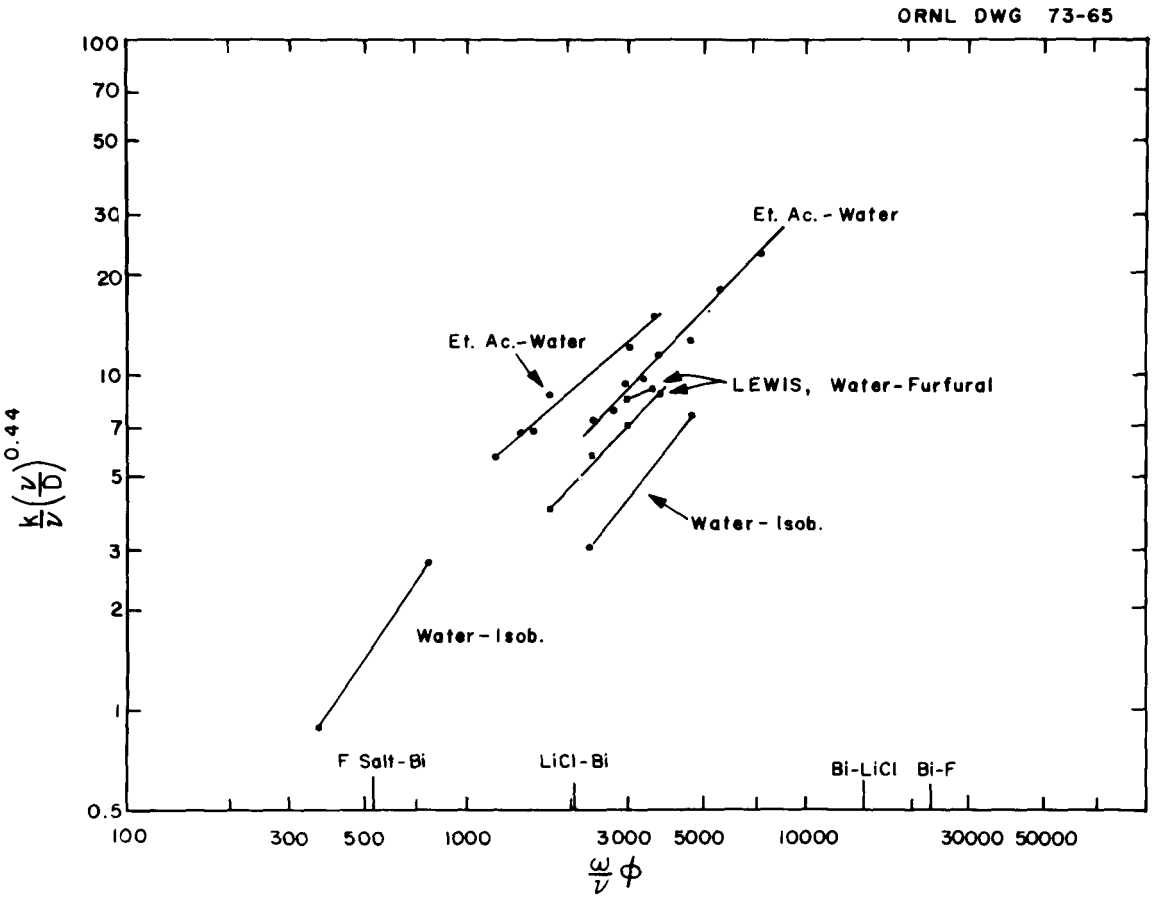

Fig. 80. Correlation of Data on Mass Transfer Coefficients in Stirred Interface Contactors in the Manner Suggested by Prochazka and Bulicka. The operating conditions that will be obtained at the various interfaces in metal transfer experiment MTE-3 with an agitator speed of 3 rps are shown on the abscissa. The notation F-Bi denotes transfer from fluoride salt to a bismuth phase; LiCl-Bi, transfer from molten LiCl to a bismuth phase; Bi-LiCl, transfer from a bismuth phase to molten LiCl; and Bi-F, transfer from a bismuth phase to fluoride salt.

Examination of the three methods for correlating the data shows that the Olander correlation has serious shortcomings. This correlation assumes that the individual mass transfer coefficient in one phase is independent of the level of turbulence in the second phase. However, data of Lewis and data of Prochazka and Bulicka show that the individual mass transfer coefficient in one phase is definitely dependent on the level of turbulence in the other phase. The Prochazka-Bulicka relationship does not seem to adequately correlate data from different systems; for instance, the data for water-isobutanol and isobutanol-water do not fall on the same line. Of the three correlations, the Lewis correlation seems to represent the data best.

The operating conditions that will be obtained with an agitator speed of 3 rps for the phases to be used in experiment MTE-3 are indicated along the abscissas of the figures for the three correlations. The values for the Reynolds-number grouping lie outside the range of the data obtained by Lewis but inside the range of the data obtained by Prochazka and Bulicka. The Prochazka-Bulicka correlation indicates a probable value for the individual mass transfer coefficient in the fluoride salt of about 0.0015 cm/sec; extrapolation of the Lewis correlation indicates a probable value of 0.05 cm/sec. Estimates of the individual mass transfer coefficients from the MTE-2 experiment indicated a coefficient of about 0.001 cm/sec under conditions where practically no agitation occurred. The value obtained from the Lewis correlation seems much more likely to reflect operating conditions that will be used in experiment MTE-3.

14. HYDRODYNAMICS OF PACKED-COLUMN OPERATION WITH HIGH-DENSITY FLUIDS

J. S. Watson L. E. McNeese

The hydrodynamics of packed-column operation with fluids having high densities and a large density difference is being studied in order to evaluate and to design countercurrent contactors for use in MSBR processing systems based on reductive extraction. Mercury and water are being used to simulate bismuth and molten salt in these studies. Earlier experiments[57] carried out with 1/8- and 1/4-in. solid cylinders and with 3/16- and 1/4-in. Raschig rings in a 1-in.-ID column demonstrated that a transition in mode of flow of the dispersed phase occurs between the packing sizes of 3/16 and 1/4 in. This transition appeared to be a function of the packing size only and was not related to packing shape (solid cylinders or Raschig rings). With the larger packing the mercury was dispersed into small droplets, which produced a large interfacial area. With the smaller packing, the mercury flowed down the column in continuous channels and resulted in a much smaller interfacial area. A large interfacial area (and hence large-sized packing) is desired in order to obtain high mass transfer rates between the salt and metal phases. A 2-in.-diam column was installed in the experimental system in order to carry out studies with packing of larger sizes, and measurements were made of flooding rates, dispersed-phase holdup, and pressure drop with 1/4-in. solid cylinders and with 3/8- and 1/2-in. Raschig rings.[58] The results of these studies have shown that the dispersed-phase holdup and the column throughputs at flooding can be correlated[58] on the basis of a constant superficial slip velocity in the following manner:

$$\frac{V_c}{1-X} + \frac{V_d}{X} = V_s \,, \tag{67}$$

$$V_{c,f}^{1/2} + V_{d,f}^{1/2} = V_s^{1/2} \,, \tag{68}$$

where

V_c = superficial velocity of continuous phase, ft/hr,
V_d = superficial velocity of dispersed phase, ft/hr,
V_s = superficial slip velocity, ft/hr, and
X = dispersed-phase holdup.

The subscript f denotes conditions at flooding.

These relations were previously[58] extended to cover dispersed-phase holdup and throughput at flooding with salt-bismuth systems by assuming that, for a given packing size, the slip velocity was (1) independent of the viscosity of the continuous phase, (2) proportional to the difference in the densities of the phases, and (3) proportional to the packing void fraction. Although the resulting relations predicted flooding rates that were in excellent agreement with flooding rates measured with molten salt and bismuth, it was realized that the agreement did not constitute verification of the assumed effects of the continuous-phase viscosity and the difference in the densities of the phases.

During this reporting period, data showing the dependence of slip velocity on continuous-phase viscosity were obtained by a group of students from the MIT Practice School.[59] A 2-in.-diam, 24-in.-long column packed with 3/8-in. Teflon Raschig rings, which were not wetted by either the continuous phase or the dispersed phase, was used in the study. Results of this study and the development of an improved relation for predicting packed column performance during the countercurrent flow of molten salt and bismuth are discussed later in this section. Studies for evaluating the effect of wetting of the packing by the nominally dispersed phase were also carried out.

14.1 Equipment and Experimental Technique

The experimental facility used in the present study has been described previously.[58] However, the system (shown in Fig. 81) was modified for the present studies so that water or water-glycerin solutions could be circulated through the column at constant temperature by installation of a heat exchanger and aqueous-phase surge tank. During the study in which the effect of the viscosity of the continuous

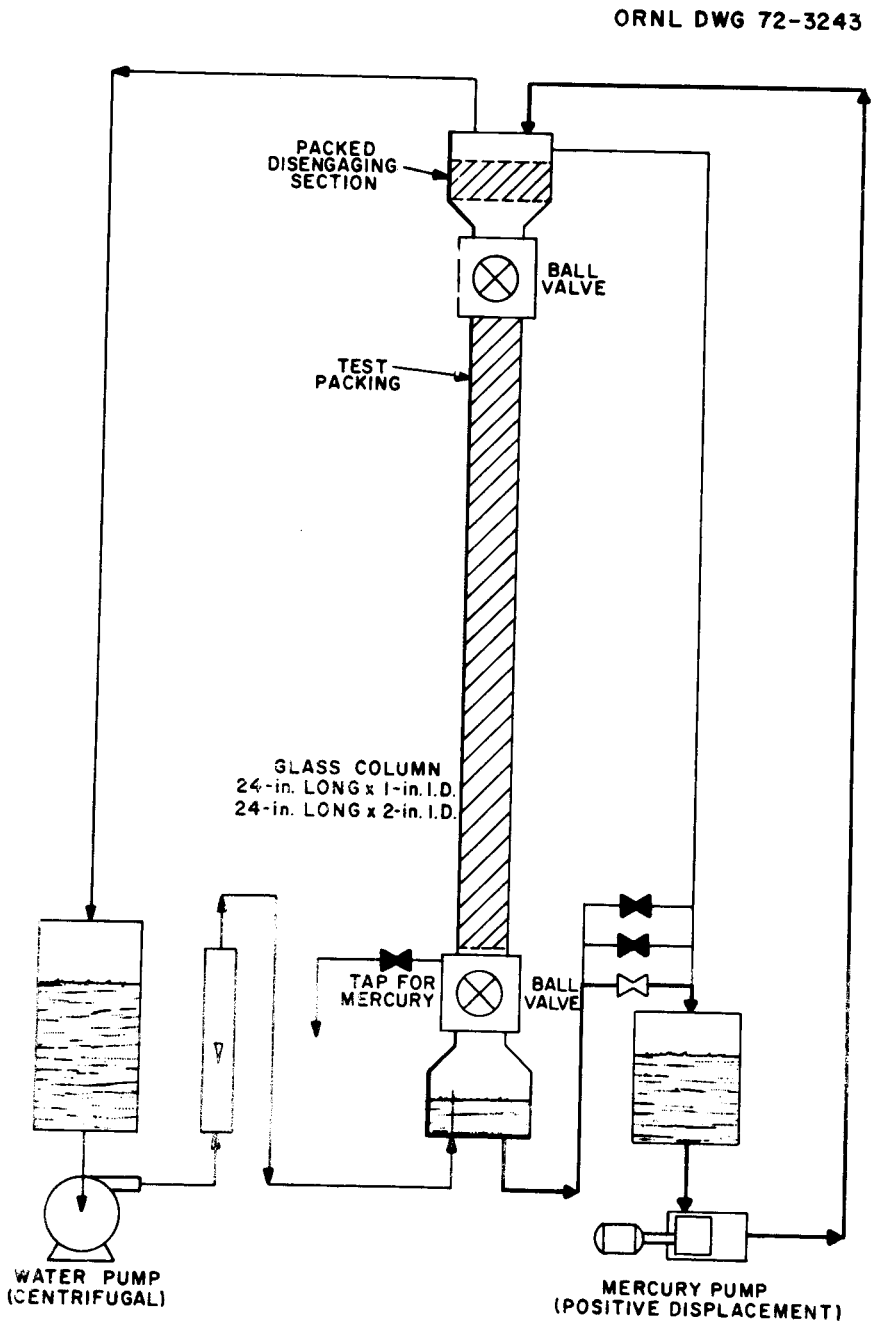

Fig. 81. Flow Diagram of Equipment Used for Determining Dispersed-Phase Holdup, Flooding Rate, and Pressure Drop in a Packed Column During the Countercurrent Flow of Mercury and Aqueous Solutions.

phase on slip velocity was determined, the column consisted of a 2-in.-ID, 24-in.-long glass tube that was packed with 3/8-in. polyethylene Raschig rings having a void fraction of 0.66. During subsequent tests for determining the effect of wetting of the packing by the nominally dispersed phase, the column was packed with 3/8-in. copper Raschig rings (void fraction, 0.81) that had been treated with nitric acid in order to promote wetting of the packing by the mercury. A 6-in.-long section above the column was packed with 0.5-in. Raschig rings in order to distribute the mercury uniformly over the column cross section. Ball valves having internal diameters equal to that of the column were provided above and below the column for use during measurements of dispersed-phase holdup. The holdup measurements were effected by simultaneously closing both ball valves and subsequently draining the mercury into a graduated cylinder. It was found that approximately 35 ml of mercury remained in the column during the draining operation. The mercury flow rate was measured during the studies by closing the lower ball valve and determining the time required for filling a 10-in.-long section of the column which had been calibrated.

During the flooding measurements, the water flow rate was increased incrementally with a fixed mercury flow rate until flooding was observed. Steady-state conditions were normally reached within 30 min after each adjustment of the aqueous-phase flow rate. The column was considered to be flooded when it became impossible to maintain fixed flow rates without a constantly increasing pressure drop. With the particular equipment used in this experiment, the continuous-phase flow rate and the pressure drop across the column fluctuated widely under "flooding" conditions. Mercury could be seen accumulating in the column until the water flow was essentially blocked. Mercury would then drain from the column, and the water flow rate would return to the desired value. This behavior was repeated in a cyclic manner.

14.2 Results

Data were obtained on dispersed-phase holdup, column pressure drop, and flooding, using viscosities of 1, 7.5, and 15 cP for the continuous phase. Tables 53-55 and Figs. 82-84 present data on holdup and pressure

Table 53. Experimentally Determined Values for Dispersed-Phase Holdup and Pressure Drop During Countercurrent Flow of Mercury and Water Through a 2-in.-diam Column Packed with 3/8-in. Teflon Raschig Rings

Continuous-phase viscosity, 1 cP

Superficial Velocity (ft/hr)		Dispersed-Phase Holdup	Pressure Drop (mm Hg-mm H_2O)[a]
Dispersed Phase	Continuous Phase		
0	36.3	--	~0
0	50.3	--	1
0	65.4	--	1
0	144	--	2
0	206	--	3
0	272	--	4
0	340	--	6
71	0	0.0506	18
71	67	0.0678	18
71	144	0.0826	16
71	205.7	0.0838	19
71	271	0.0666	24
71	339	0.0801	35
145	0	0.136	35
145	144	0.183	26
145	205.7	0.160	39
145	271	0.174	50
145	339	0.183	52
188	0	0.183	49
188	144	0.206	39
188	206	0.217	52
188	271	0.247	79
188	339	0.271	102

[a]Millimeters of liquid having a density of 12.6 g/cm^3.

drop for a range of values of the continuous-phase superficial velocity. The points at which flooding was observed are indicated in the figures. Table 56 and Fig. 85 give values of holdup and pressure drop obtained during operation with a continuous-phase viscosity of 1 cP for the case in which the packing was wet by the dispersed phase. Data on flooding are presented in Figs. 86-89, where the square root of the dispersed-phase

Table 54. Experimentally Determined Values for Dispersed-Phase Holdup and Pressure Drop During Countercurrent Flow of Mercury and a Water-Glycerin Solution Through a 2-in.-diam Column Packed with 3/8-in. Teflon Raschig Rings

Continuous-phase viscosity, 7.5 cP

Superficial Velocity (ft/hr)		Dispersed-Phase Holdup	Pressure Drop (mm Hg-mm H_2O)[a]
Dispersed Phase	Continuous Phase		
0	13.9	--	1
0	24.1	--	1.5
0	33.9	--	2
0	81.1	--	3
0	136.2	--	4
0	198.4	--	5-7
0	259.5	--	8-13
0	303	--	11-14
0	373	--	15-18
0	431.5	--	22-25
0	484	--	31
0	568	--	37
67	0	0.0716	28
67	81.1	0.0900	33
67	136.2	0.0998	40
67	198.4	0.0839	48
67	172	0.0962	43
67	218	0.122	61
67	259	0.131	70
67	284	0.128	60
107	0	0.154	26
107	81.1	0.154	44
107	33.9	0.148	27
107	136.2	0.168	33.5
107	198.4	0.143	63
107	160	0.138	50
107	150	0.127	38
107	230	0.181	67
124	0	0.154	40
124	33.9	0.174	61
124	81.1	0.181	50
124	136.2	0.192	65
124	172	0.211	72

[a]Millimeters of liquid having a density of 12.6 g/cm^3.

Table 55. Experimentally Determined Values for Dispersed-Phase Holdup and Pressure Drop During Countercurrent Flow of Mercury and a Water-Glycerin Solution Through a 2-in.-diam Column Packed with 3/8-in. Teflon Raschig Rings

Continuous-phase viscosity, 15 cP

Superficial Velocity (ft/hr)		Dispersed-Phase Holdup	Pressure Drop (mm Hg-mm H_2O)[a]
Dispersed Phase	Continuous Phase		
0	22.4	--	~0
0	51.2	--	1
0	116.5	--	9
0	167	--	12
0	216.2	--	15
0	270	--	19
0	330	--	24
0	397	--	28
71	0	0.107	5
71	100	0.109	9.5
71	200	0.141	12
71	220	0.174	62
85	0	0.131	0
85	22.4	0.157	--
85	51.2	0.143	--
85	110.5	0.158	--
85	167	0.181	--
85	196	0.220	--
85	228	0.253	--
126	0	0.204	31
126	22.4	0.195	33
126	51.2	0.197	36
126	110.5	0.217	57

[a]Millimeters of liquid having a density of 12.6 g/cm^3.

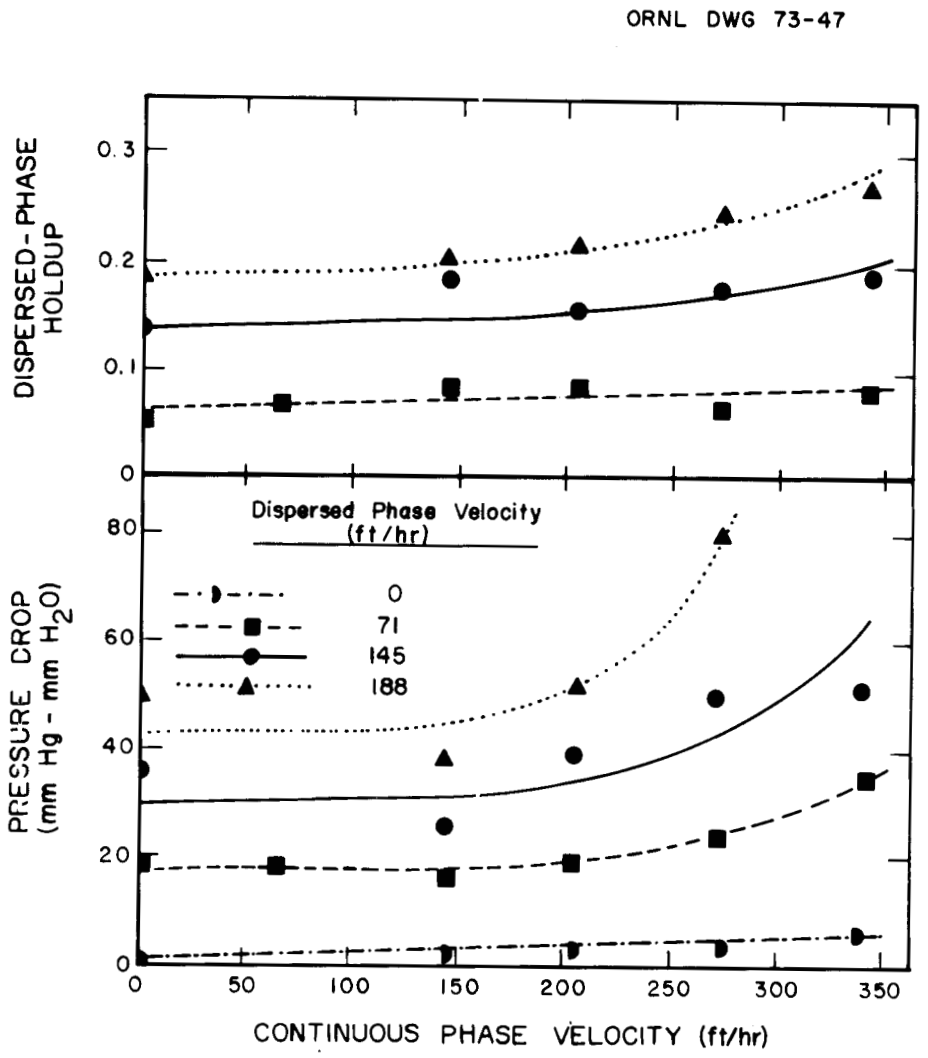

Fig. 82. Variation of Dispersed-Phase Holdup and Column Pressure Drop During the Countercurrent Flow of Mercury and Water in a 2-in.-ID, 24-in.-long Column Packed with 3/8-in. Teflon Raschig Rings.

ORNL DWG. 73-35RI

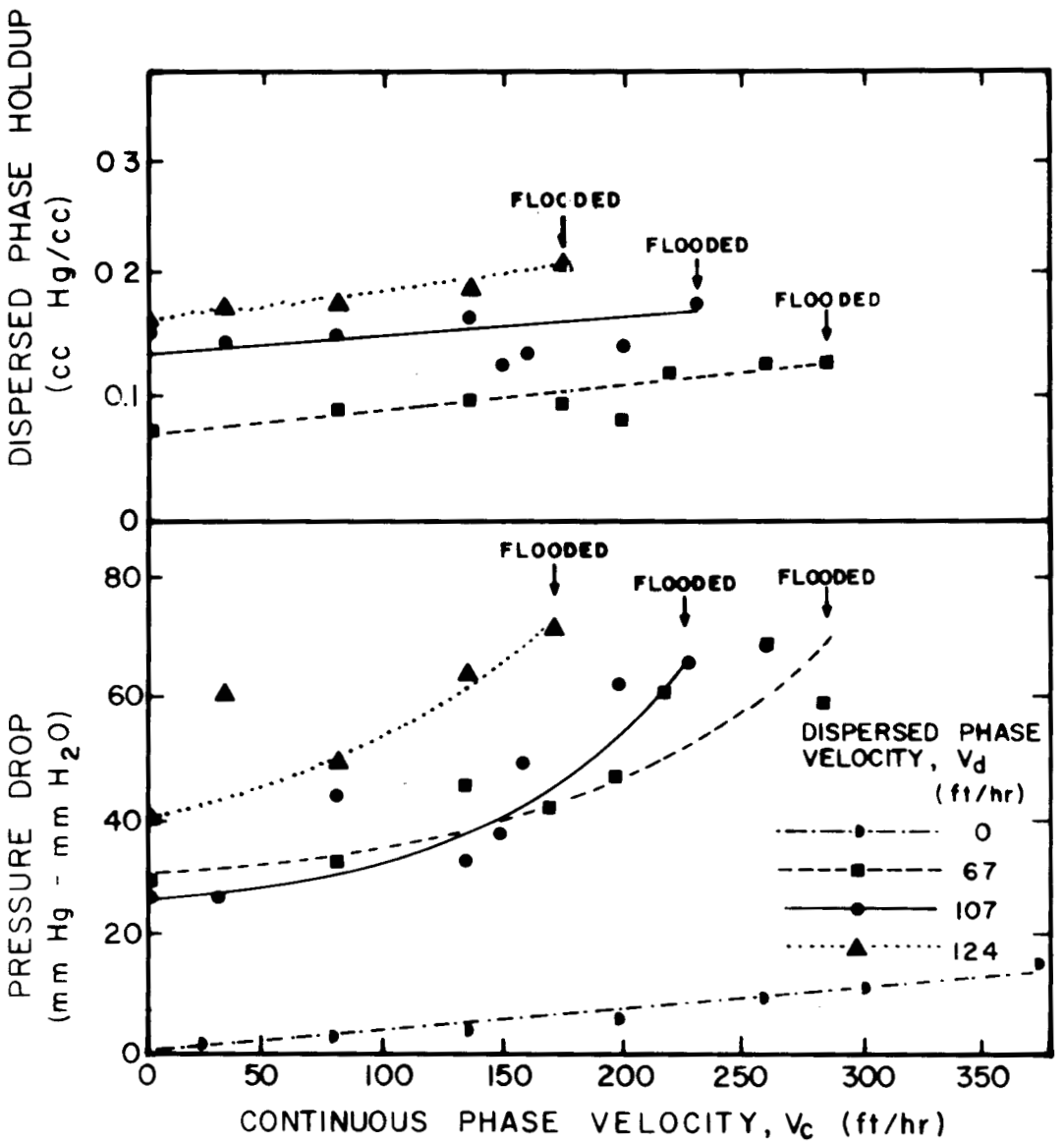

Fig. 83. Variation of Dispersed-Phase Holdup and Column Pressure Drop During the Countercurrent Flow of Mercury and a Water-Glycerin Solution in a 2-in.-ID, 24-in.-long Column Packed with 3/8-in. Teflon Raschig Rings. The viscosity of the continuous (aqueous) phase was 7.5 cP.

ORNL DWG. 73-37

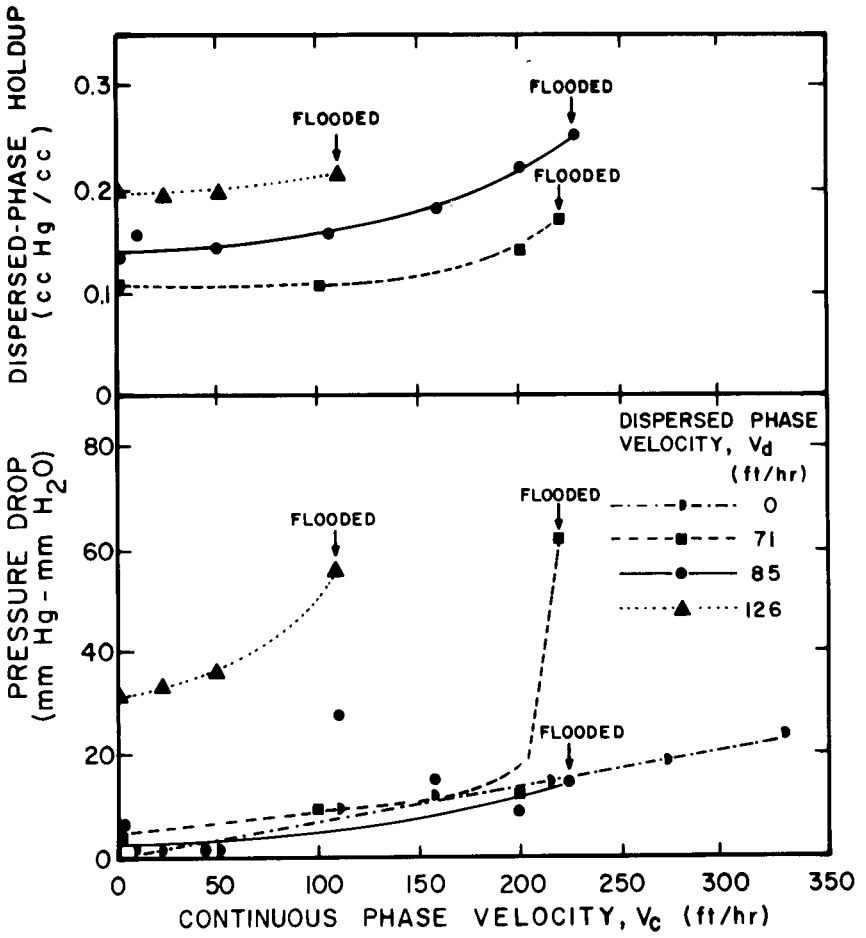

Fig. 84. Variation of Dispersed-Phase Holdup and Column Pressure Drop During the Countercurrent Flow of Mercury and a Water-Glycerin Solution in a 2-in.-ID, 24-in.-long Column Packed with 3/8-in. Teflon Raschig Rings. The viscosity of the continuous (aqueous) phase was 15 cP.

Table 56. Experimentally Determined Values for Dispersed-Phase Holdup and Pressure Drop During Countercurrent Flow of Mercury and Water Through a 2-in.-diam Column Packed with 3/8-in. Copper Raschig Rings

Continuous-phase viscosity, 1 cP

Superficial Velocity (ft/hr)		Dispersed-Phase Holdup	Pressure Drop[a] (mm Hg-mm H_2O)
Dispersed Phase	Continuous Phase		
113	0	0.108	15
113	144	0.106	46
113	272	0.113	40
113	406	0.119	14
315	0	0.201	33
315	144	0.204	36
315	206	0.194	--
315	339	0.215	41-50
315	406	0.270	75
315	440	0.308	103
315	380	0.233	58

[a]Millimeters of liquid having a density of 12.6 g/cm^3.

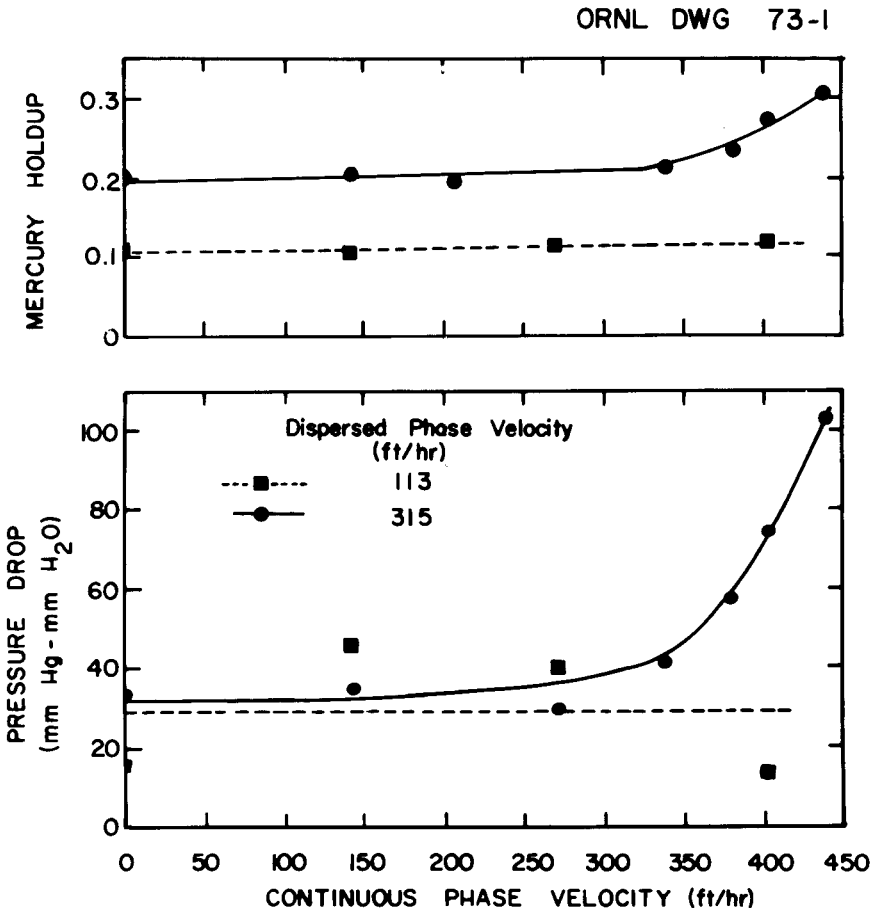

Fig. 85. Variation of Mercury Holdup and Column Pressure Drop During the Countercurrent Flow of Mercury and Water in a 2-in.-ID, 24-in.-long Column Packed with 3/8-in. Copper Raschig Rings. The packing was wet by the mercury.

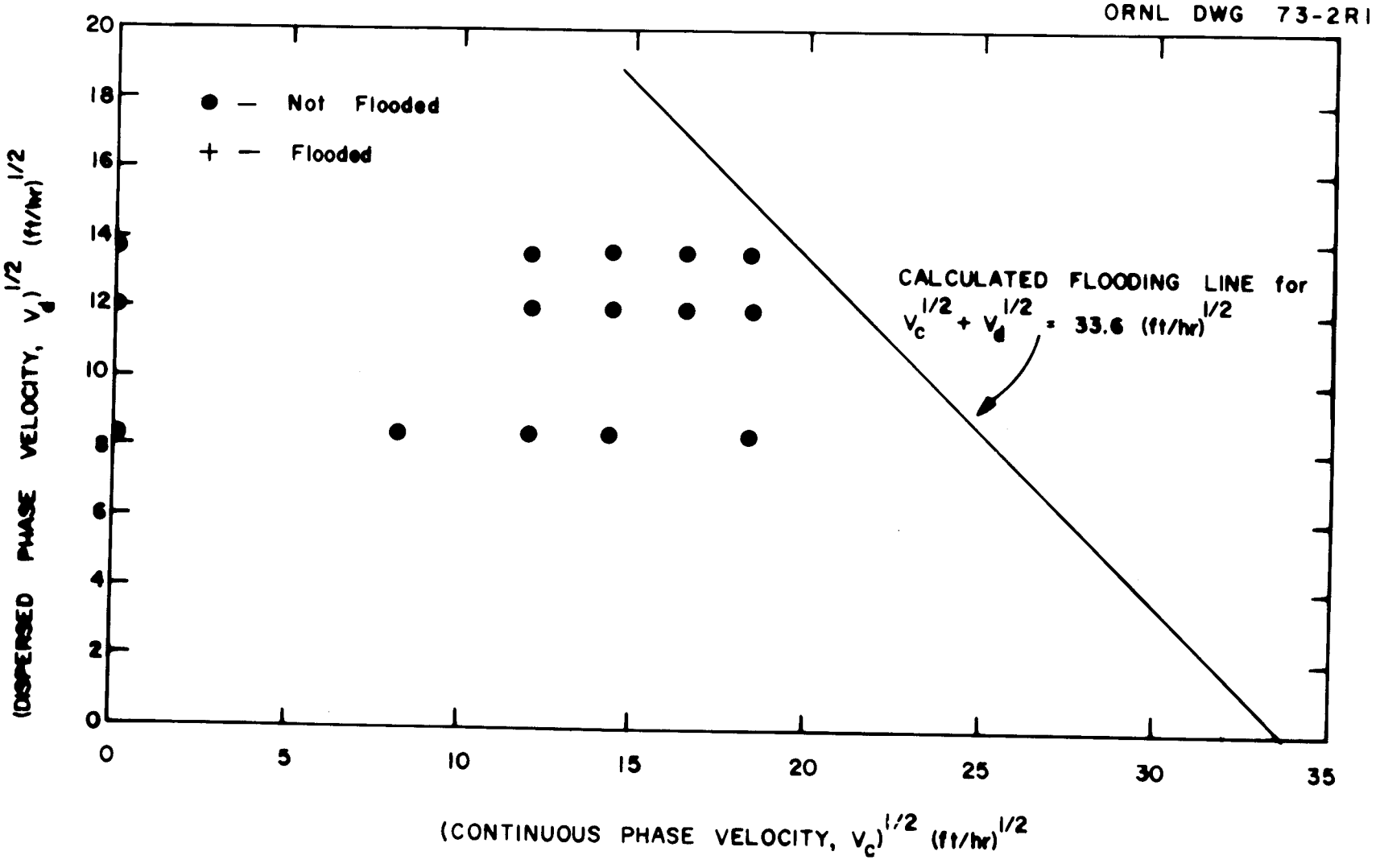

Fig. 86. Flooding Data Obtained During the Countercurrent Flow of Mercury and Water Through a 2-in.-ID, 24-in.-long Column Packed with 3/8-in. Teflon Raschig Rings.

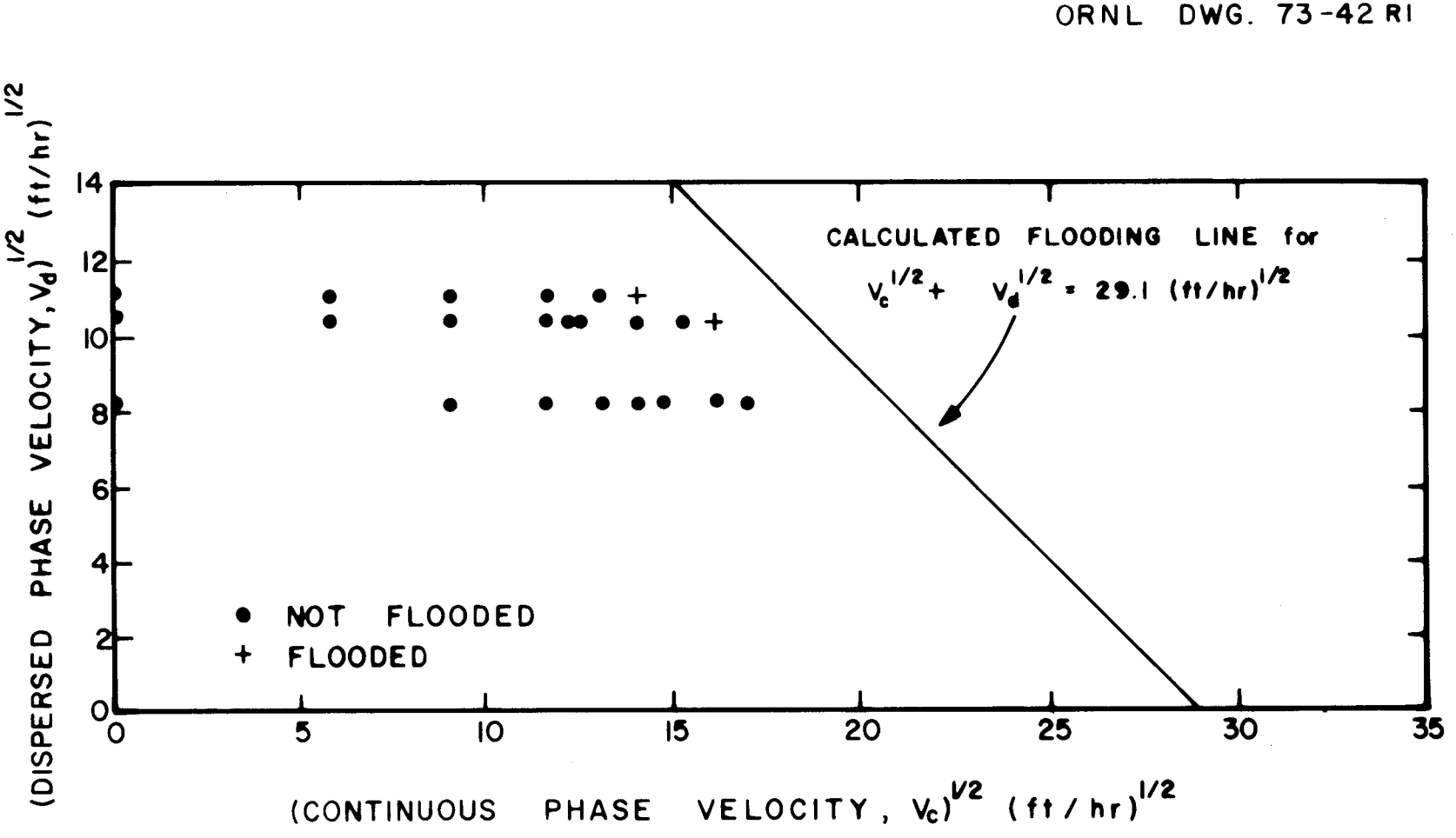

Fig. 87. Flooding Data Obtained During the Countercurrent Flow of Mercury and a Glycerin-Water Solution Through a 2-in.-ID, 24-in.-long Column Packed with 3/8-in. Teflon Raschig Rings. The viscosity of the continuous (aqueous) phase was 7.5 cP.

ORNL DWG. 73-43

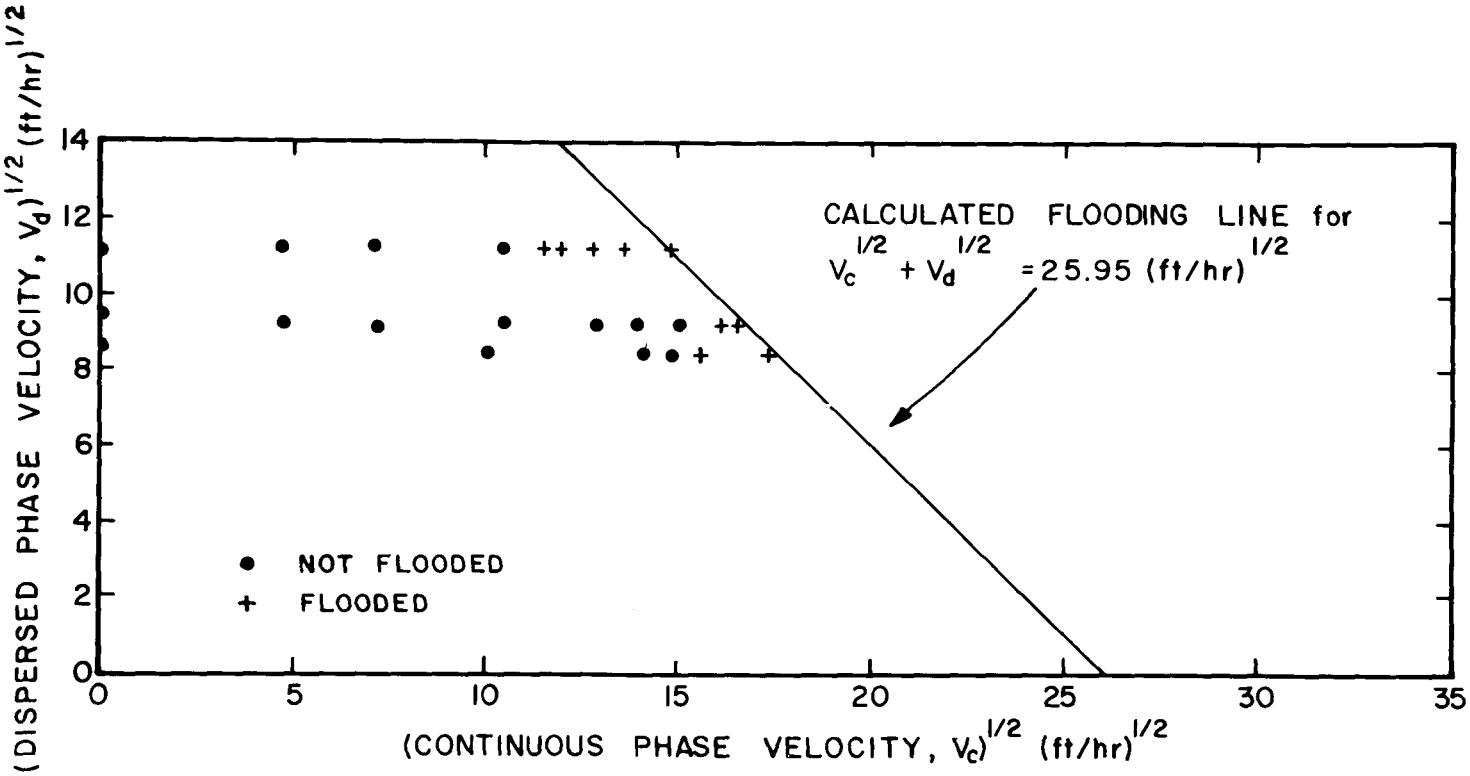

Fig. 88. Flooding Data Obtained During the Countercurrent Flow of Mercury and a Glycerin-Water Solution Through a 2-in.-ID, 24-in.-long Column Packed with 3/8-in. Teflon Raschig Rings. The viscosity of the continuous (aqueous) phase was 15 cP.

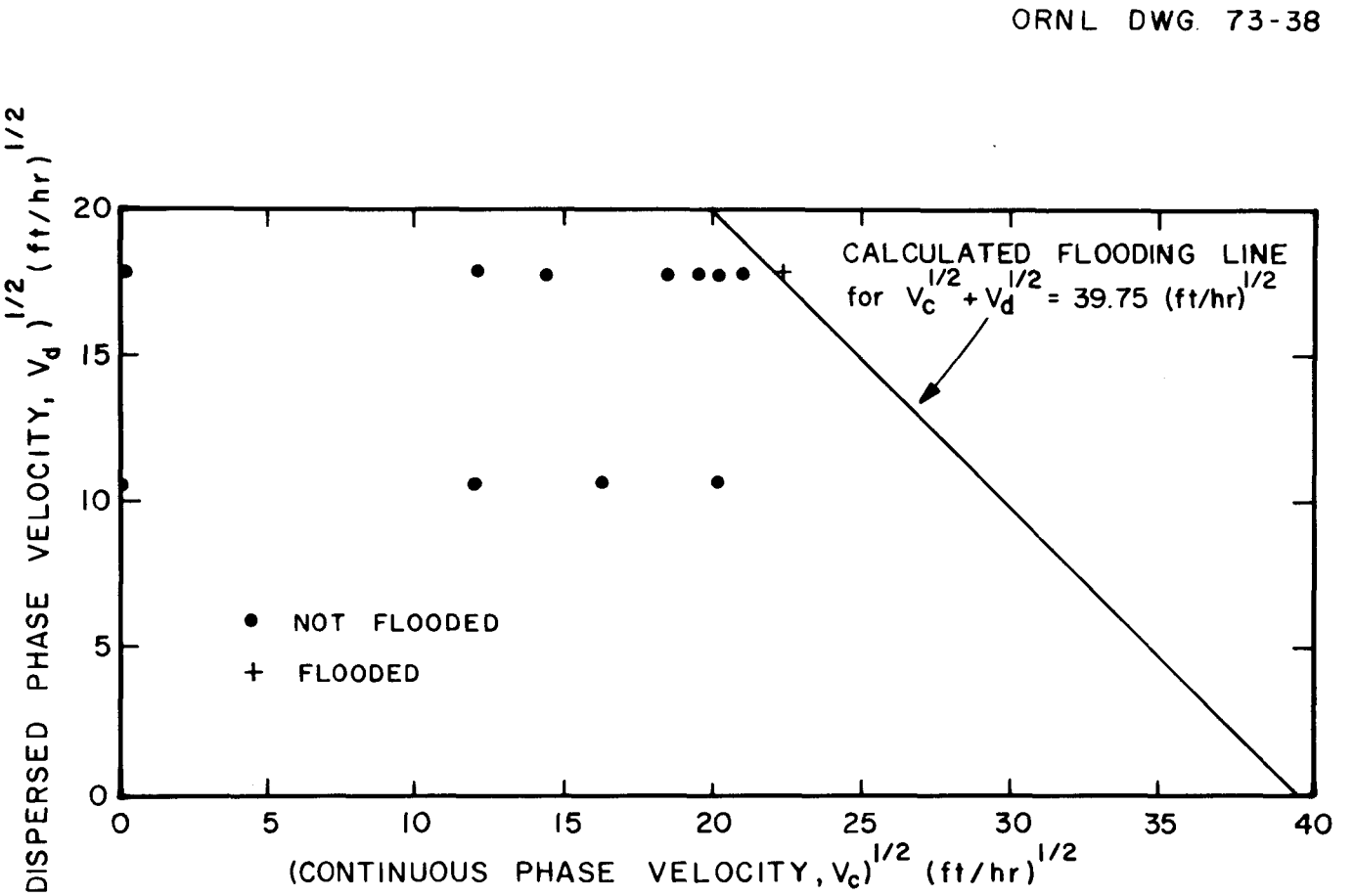

Fig. 89. Flooding Data Obtained During the Countercurrent Flow of Mercury and Water in a 2-in.-ID, 24-in.-long Column Packed with 3/8-in. Copper Raschig Rings. The packing was wet by the mercury.

superficial velocity is plotted vs the square root of the continuous-phase superficial velocity. The conditions for which the system was operated in a nonflooded state, as well as conditions for which flooding was observed, are indicated. The results obtained during this study were similar to those observed previously for mercury and water. The data on dispersed-phase holdup involving nonwetted packing could be correlated in terms of a constant superficial slip velocity, as shown in Table 57. The relative standard deviations for the slip velocities were about ±10%; no dependence of slip velocity on the flow rate of either phase was noted. The variation of slip velocity with the continuous-phase viscosity is shown in Fig. 90, which indicates that the superficial slip velocity is proportional to the -0.167 power of the continuous-phase viscosity. As expected, the dependence is not large; however, neglect of this effect was significant in the earlier extrapolation of data from a mercury-water system to a salt-bismuth system since the continuous-phase viscosity differs by a factor of 12.

The effect of wetting of the packing by the metal phase on dispersed-phase holdup, flooding, and pressure drop was also evaluated by packing the column with 3/8-in. copper Raschig rings that had been etched with nitric acid (to promote wetting of the packing by the mercury). Complete wetting of the packing was obtained. Although the mercury was saturated with copper, the solubility of copper in mercury is quite low and no important changes in other physical properties should occur. After a few hours of operation, solids were observed at the water-mercury interface below the column; these solids were believed to be copper oxide that was formed as the result of the reaction of dissolved copper with oxygen in the water. Periodic additions of nitric acid to the aqueous phase quickly removed the solids.

The interfacial area between the aqueous and mercury phases was decreased substantially when the packing was wetted by the mercury, as noted by comparing Figs. 91 and 92, which show operation with nonwetted and wetted packing respectively. No dispersion of the mercury was observed with the wetted packing, and the interfacial area was essentially equal to the packing surface area. The superficial slip velocity (and hence the flooding rates) was considerably greater with wetted packing

Table 57. Variation of Superficial Slip Velocity with Continuous-Phase Viscosity and Wetting of the Packing for a Column Packed with 3/8-in. Raschig Rings

Type of Packing	Continuous-Phase Viscosity (cP)	Packing Void Fraction, ϵ	Slip Velocity, V_s (ft/hr)	Standard Deviation, σ (ft/hr)	Percent Deviation, σ/V_s
Nonwetted	1	0.66	1129	$\pm$105	$\pm$9.3
Nonwetted	7.5	0.66	848	$\pm$88	$\pm$10.4
Nonwetted	15	0.66	674	$\pm$49	$\pm$7.3
Wetted	1	0.82	1583	$\pm$268	$\pm$16.9

than with nonwetted packing, as shown in Table 57. It was not clear whether the data on metal-phase holdup with wetted packing could be correlated on the basis of a constant superficial slip velocity. Only nine metal holdup measurements were made, and a quantitative analysis of the relation between mercury holdup and the water and mercury superficial velocities was not possible.

14.3 Prediction of Flooding Rates and Dispersed-Phase Holdup in Packed Columns

After the dependence of slip velocity on the continuous-phase viscosity had been determined, it was possible to reevaluate the dependence of slip velocity on the difference of the densities of the two phases by using the two data points afforded by the mercury-water data and salt-bismuth data. The salt-bismuth data indicated a superficial slip velocity of 388 ft/hr with a continuous-phase viscosity of 12.1 cP, a density difference of 6.28 g/cm^3, and a packing void fraction of 0.84. It was assumed that the dependence of slip velocity on the difference in densities is a power-type dependence, and the resulting power value was 0.5. This result is interesting because it is the same as the dependence of

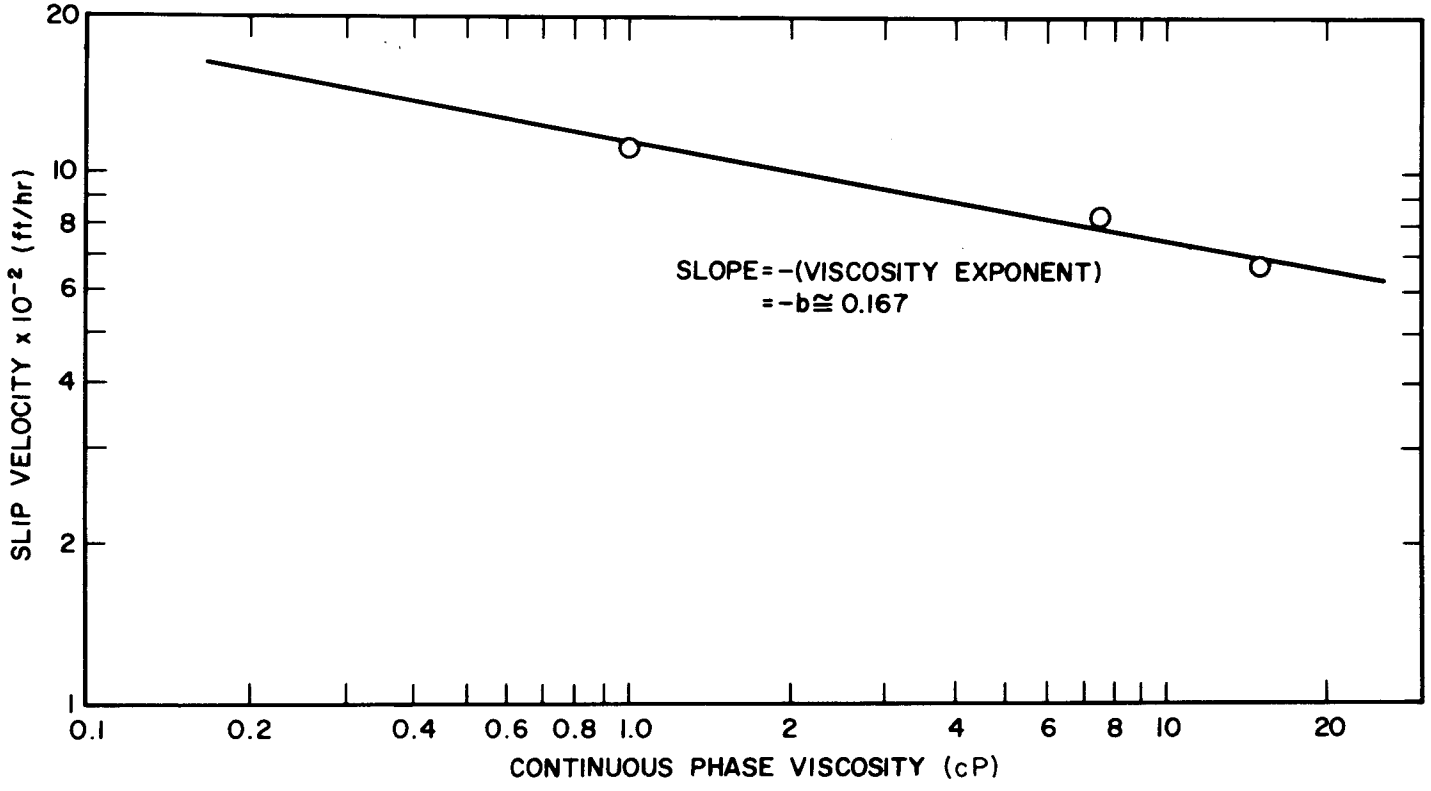

Fig. 90. Variation of Superficial Slip Velocity with Continuous-Phase Viscosity in a 2-in.-diam Column Packed with 3/8-in. Teflon Raschig Rings.

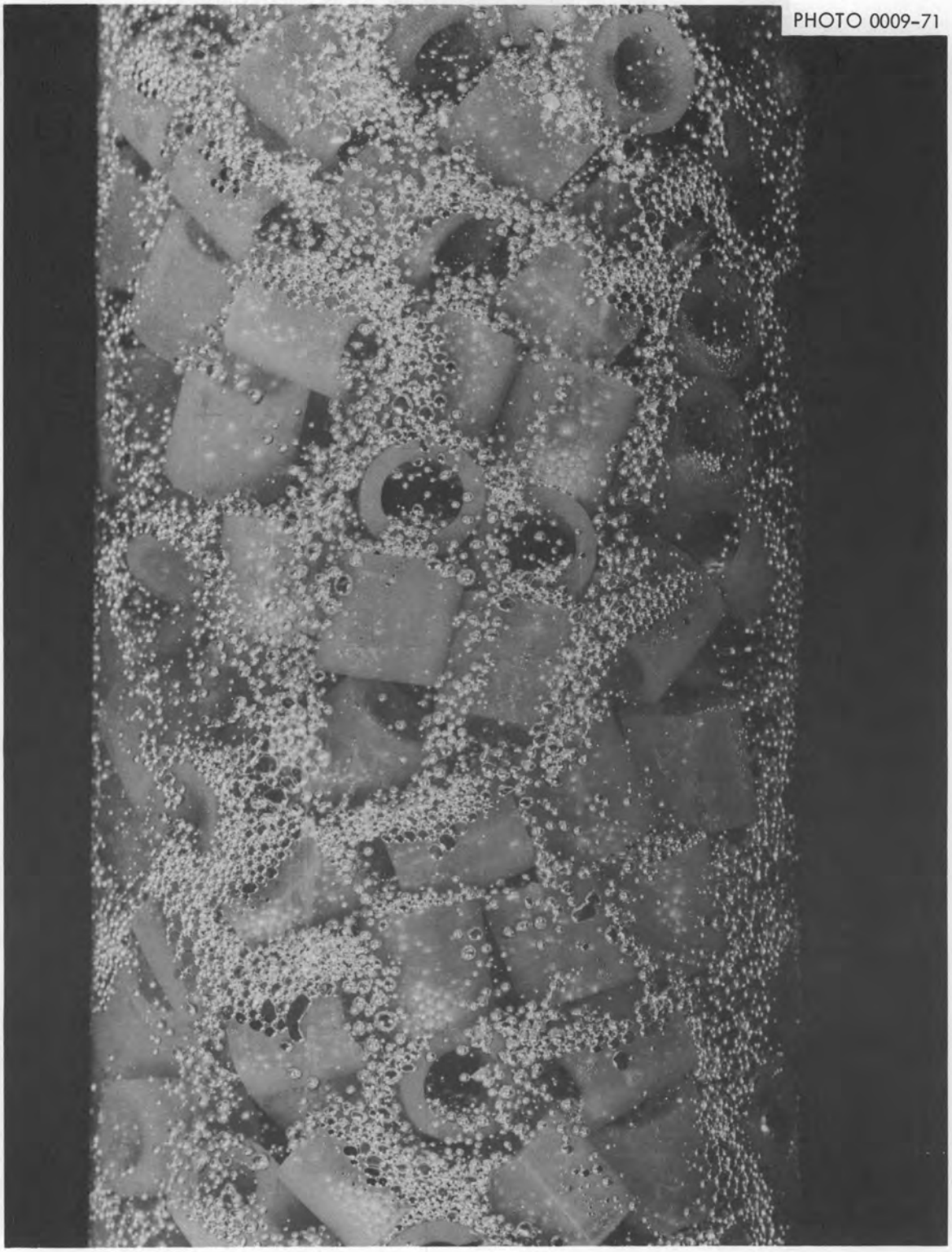

Fig. 91. Countercurrent Flow of Mercury and Water in a 2-in.-diam Column Packed with 3/8-in. Teflon Raschig Rings. The packing is not wetted by the metal phase, and the interfacial area is much greater than the surface area of the packing.

Fig. 92. Countercurrent Flow of Mercury and Water in a 2-in.-diam Column Packed with 3/8-in. Copper Raschig Rings. The packing is wetted by the metal phase, and the interfacial area is essentially equal to the surface area of the packing.

drop terminal velocity on the difference in densities for conditions under which inertial forces predominate and the drag coefficient is essentially constant. The final relation for predicting the variation of superficial slip velocity with packing void fraction, the difference in the densities of the phases, and the continuous-phase viscosity is, then:

$$V_s = V_{s,Hg\text{-}H_2O} \left(\frac{\epsilon}{\epsilon_{Ref}}\right)\left(\frac{\mu}{\mu_{H_2O}}\right)^{-0.167}\left(\frac{\Delta\rho}{\Delta\rho_{Hg\text{-}H_2O}}\right)^{0.5}, \qquad (69)$$

where

V_s = superficial slip velocity,

$V_{s,Hg\text{-}H_2O}$ = slip velocity for mercury-water for the packing size being used,

ϵ = packing void fraction,

ϵ_{Ref} = void fraction for packing for which $V_{s,Hg\text{-}H_2O}$ was determined,

μ = viscosity of continuous phase,

μ_{H_2O} = viscosity of water at 20°C,

$\Delta\rho$ = difference in the densities of the phases, and

$\Delta\rho_{Hg\text{-}H_2O}$ = difference in the densities of mercury and water at 20°C.

Slip velocity values calculated from Eq. (69) can be used with Eqs. (67) and (68) for determining both the dispersed-phase holdup and throughputs of the continuous and dispersed phases at flooding.

15. ANALYSIS OF MULTICOMPONENT MASS TRANSFER BETWEEN MOLTEN SALTS AND LIQUID BISMUTH DURING COUNTERCURRENT FLOW IN PACKED COLUMNS

C. P. Tung J. S. Watson

Reductive extraction, an important operation in the removal of protactinium and rare earths from MSBR fuel salt, involves the exchange of metal ions in the salt phase with neutral (reduced) metal atoms in the bismuth phase. Since no net electric current flows between the salt and metal phases, the rate at which metal ions are reduced must equal the rate at which metal atoms are oxidized (taking into consideration differences in the charges of the ions involved). In the bismuth phase, the fluxes of the transferring atoms are dependent only on concentration gradients. However, in the salt phase, electric potential gradients are generated near the salt-metal interface as the result of differences in the mobilities and/or charges of the various diffusing ions. This results in a condition where the fluxes of the transferring ions are dependent on both concentration gradients and electric potential gradients. These effects greatly complicate the mass transfer process and make the design of continuous (differential) reductive extraction columns difficult. We have begun a mathematical analysis of mass transfer during reductive extraction processes to facilitate interpretation of the results from present and proposed experiments in packed columns, and as an aid in using these data for the design of larger reductive extraction systems. The results from this study will also be applicable to several other solvent extraction operations that involve exchange reactions between uncharged species in a solvent and ions in an electrolyte. The extraction of metals from aqueous solutions by use of "liquid ion exchange" solvents such as amines is a typical example of such an operation.

15.1 Literature Review

It has been recognized for some time[60] that the diffusion of ions in a liquid is inherently different from the diffusion of uncharged species. The interdiffusion of charged species as a result of concentration gradients produces an electric potential gradient, which, in turn, alters the ionic fluxes and prevents further deviation from electroneutrality. An electrical potential gradient in an electrolyte will produce a flux of

ion i, which depends on the concentration of the ion in the electrolyte and on the valence and mobility of the ion, as indicated by the relation

$$J_i = u_i Z_i C_i \text{ grad } \phi \ ,$$

where

J_i = flux of ion i,
u_i = mobility of ion i in electrolyte,
Z_i = valence of ion i,
C_i = concentration of ion i, and
grad ϕ = electrical potential gradient.

The mobility of an ion is related to its diffusion coefficient in the electrolyte by the Nernst-Einstein equation as follows:

$$u_i = \frac{D_i F}{RT} \ ,$$

where

D_i = diffusion coefficient of ion i in the electrolyte,
F = Faraday constant,
R = gas constant, and
T = absolute temperature.

If a concentration gradient is also present in the electrolyte, an additional flux, which is described by Fick's First Law, is produced; the flux resulting from this effect is given by the relation

$$J_i = -D_i \text{ grad } C_i \ .$$

The net flux of ion i will be the sum of these contributions, which is known as the Nernst-Planck equation:

$$J_i = -D_i \left(\text{grad } C_i + \frac{Z_i C_i F}{RT} \text{ grad } \phi\right) \ .$$

Several studies related to mass transfer during reductive extraction operations have been reported in the literature. The effects of electric fields on the rate of diffusion of ions were considered by Schlögl and Helfferich.[60] Copeland, Henderson, and Marchello[61] derived an analytical solution for the rate of transfer of ions through the liquid film surrounding solid ion exchange resin beads for the case in which the

exchanging ions have the same charge. Turner and Snowdon[62] extended these results to cover the case in which the exchanging ions have different valences. Kataoka, Sato, Nishiki, and Ueyama[63] studied systems involving two different coions (e.g., ions having electric charges opposite in sign to that of the exchanging ions). This study will attempt to extend the previous studies in three important ways:

1. Countercurrent liquid-liquid columns will be treated rather than portions of fixed beds.
2. Diffusion resistances may exist in both phases. Previous studies have treated either resistance to diffusion in solid ion exchange resins or resistance to diffusion through a liquid film surrounding the resin. The case for which significant resistance occurs in each phase is considerably more complex than either of these.
3. Any number of transferring ions may be considered. The results will not be limited to the case in which only one ion exchanges for another ion. The method that will be developed will be general, and any number of ions can be treated. However, provisions are being made for only as many as ten ions in computer programs that are being developed.

15.2 Mathematical Analysis

The model selected for the mathematical analysis in the present study is based on a model similar to the Whitman two-film model; that is, an effectively stagnant film of liquid is assumed to exist on both sides of the interface, and all concentration gradients and all electric potential gradients are assumed to lie within these two films. The phases are assumed to be in chemical equilibrium at the interface. The rates of diffusion of species in the solvent film are controlled by Fick's First Law since the transferring materials have no electric charge in the solvent (bismuth). Thus, at a point within a packed column, the flux of component i across the solvent film is given by the relation

$$J_{si} = \frac{D_{si}}{\delta_s} (C_{siI} - C_{siB}) , \qquad (70)$$

where

J_{si} = flux of component i across the solvent film,

D_{si} = diffusion coefficient of component i in solvent phase,

δ_s = thickness of the solvent film,

C_{siB} = concentration of component i in the bulk solvent, and

C_{siI} = concentration of component i in the solvent phase at the interface.

The rate of transfer of ions in the electrolyte film, however, involves electrical transference as well as diffusion, and both concentration and electrical potential gradients are important. For this case, the flux is given by the Nernst-Planck equation:

$$J_{ei} = -D_{ei}\left[\text{grad } C_{ei} + \frac{Z_i C_{ei} F}{RT} \text{grad } \phi\right] , \tag{71}$$

where

Z_i = valence (electric charge) of component i,

ϕ = electric potential in the electrolyte phase,

D = diffusion coefficient of transferring component,

F = Faraday constant,

C = concentration of transferring component,

R = gas constant, and

T = absolute temperature.

The subscript i refers to component i, and the subscript e denotes the electrolyte phase.

Since the films are thin, it is assumed that the rate of accumulation of materials in the films is negligible in comparison with the flux of the materials through the films. Thus, the flux of component i is constant across the films so that

$$J_{ei} = J_{si} . \tag{72}$$

The fluxes, however, will vary with axial position in the column; this effect will be considered subsequently. There is no net transfer of electric charge between phases (e.g., no net electric current); this is expressed by the relation

$$\sum_i J_{ei} Z_i = \sum_i J_{si} Z_i = 0 . \tag{73}$$

Also, the accumulation of electric charge at any point can be neglected,

so that at all points in the electrolyte film

$$\sum_i C_{ei} Z_i = -Z_Y C_Y \quad , \tag{74}$$

where the subscript Y refers to the nontransferring ion. If the transferring ions have a positive charge (as is the case with reductive extraction), at least one other ion in the electrolyte phase must have an opposite (negative) charge. (Ions that are charged oppositely to the transferring ions are referred to as coions.) If the transferring ions are negatively charged, the coions would be positively charged. The rate of transfer of coions between the phases is assumed to be negligible.

It will be convenient to develop two general expressions from Eqs. (71) and (74) which will be used subsequently. Multiplication of Eq. (71) by the quantity $Z_i D_{ei}$ and summation of the resulting expression over the i transferring ions yields

$$\sum_i \frac{J_{ei} Z_i}{D_{ei}} = - \sum_i Z_i \text{ grad } C_{ei} - \sum_i \frac{Z_i^2 C_{ei} F}{RT} \text{ grad } \phi \quad . \tag{75}$$

Taking the gradient of Eq. (74) yields

$$\sum_i Z_i \text{ grad } C_{ei} = - Z_Y \text{ grad } C_Y \quad . \tag{76}$$

For most aqueous solutions, the concentrations of all ions will be small compared to the concentration of water molecules; hence it is assumed that no solubility limits are reached at any point in the electrolyte phase. For this case, the coion concentration will vary across the electrolyte film, but there will be no net transfer of coions. This condition is described by the relation

$$J_Y = 0 = -D_{eY} \left(\text{grad } C_{eY} + \frac{Z_Y C_{eY} F}{RT} \text{ grad } \phi \right) \quad , \tag{77a}$$

where the subscript Y refers to the coion. Thus, the concentration profile for coion Y is independent of the diffusion coefficient of the coion. Kataoka, Sato, and Ueyama have solved Eqs. (71), (73), (74), and (77a) analytically for the case where there are two different cations

(transferring ions).[63] Combination of Eqs. (76) and (77a) yields the relation

$$\sum_i Z_i \text{ grad } C_{ei} = \frac{Z_Y^2 C_Y F}{RT} \text{ grad } \phi \ , \qquad (78)$$

and substitution of Eq. (78) into Eq. (75) yields the final relation which describes the electric potential gradient in the electrolyte film. The resulting relation is

$$\frac{F}{RT} \text{ grad } \phi = - \frac{\sum_i \frac{J_{ei} Z_i}{D_{ei}}}{Z_Y^2 C_Y + \sum_i Z_i^2 C_{ei}} \ . \qquad (79a)$$

For the case in which there are more than two transferring ions, Eq. (71) must be integrated numerically for each ion.

If the electrolyte phase is a molten salt, the concentration of transferring ions in the electrolyte film relative to the total concentration of ions can be high, and the volume of each ion should be taken into account. For molten salt systems of immediate interest, this effect can be treated approximately by a simple technique In the case of MSBR fuel salt, the electrolyte phase will consist of a mixture of the fluorides of Th, Li, Be, U, Pa, Zr, and rare earths. In reductive extraction operations involving molten LiCl, the electrolyte phase will consist of a mixture of the chlorides of these materials (except for beryllium) and of the rare-earth and alkaline-earth fission products. In both cases, only cations will exchange between the bismuth and salt phases. As shown in Tables 58 and 59, the equivalent volumes of most of the salts in each individual group are approximately the same (12.1 cm^3/equiv for fluorides and 27.1 cm^3/equiv for chlorides). It has also been found that the equivalent volumes are linearly additive for fluoride mixtures containing the elements of interest.[64] In view of these factors, the concentration of fluoride (or chloride) ion will be assumed to be constant throughout the electrolyte film. Thus

$$C_Y = \text{constant} = 1/\upsilon \ , \qquad (77b)$$

Table 58. Empirical Molar and Equivalent Volumes of Fluorides at 600°C[a]

Material	Molar Volume (cm^3/mole)	Equivalent Volume (cm^3/equiv)
LiF	13.46	13.46
BeF_2	23.6	11.8
ThF_4	46.6	11.65
UF_4	45.5	11.38
ZrF_4	47	11.75
YF_3	34.6	11.53
LaF_3	37.7	12.57
CeF_3	36.3	12.1
PrF_3	36.6	12.2
SmF_3	39.0	13.0
SrF_2	30.4	15.2
BaF_2	35.8	17.9

[a]Data taken from ref. 64.

Table 59. Molar and Equivalent Volumes for Chlorides at 650°C

Material	Molar Volume (cm^3/mole)	Equivalent Volume (cm^3/equiv)
LiCl	28.6	28.6
$SrCl_2$	55.5	27.8
$BaCl_2$	61.5	30.7
YCl_3	76.7	25.6
$LaCl_3$	72.7	24.3
$CeCl_3$	72.5	24.2
$ThCl_4$	112.6	28.2

where υ = equivalent volume of salt, cm^3/equiv. This assumption will not be universally valid for all molten salt systems, but it is believed to be reasonable for cation exchange between molten salt and bismuth since the anions in this instance will usually be much larger than the cations. Equations (75), (76), and (77b) may be combined to obtain an expression that describes the electric potential gradient for the case where the electrolyte is a molten salt. The resulting relation is

$$\frac{F}{RT} \text{ grad } \phi = - \frac{\sum_i \frac{J_{ei} Z_i}{D_{ei}}}{\sum_i Z_i^2 C_{ei}} \quad . \tag{79b}$$

In summary, the relations which define the rate at which components transfer between an aqueous and an organic phase are as follows:

$$J_{si} = \frac{D_{si}}{\delta_s} \left(C_{siI} - C_{siB} \right) , \tag{70}$$

$$J_{ei} = -D_{ei} \left[\text{grad } C_{ei} + \frac{Z_i C_{ei} F}{RT} \text{ grad } \phi \right] , \tag{71}$$

$$J_{ei} = J_{si} , \tag{72}$$

$$\sum_i J_{ei} Z_i = \sum_i J_{si} Z_i , \tag{73}$$

and

$$\frac{F}{RT} \text{ grad } \phi = - \frac{\sum_i \frac{J_{ei} Z_i}{D_{ei}}}{Z_Y^2 C_Y + \sum_i Z_i^2 C_{ei}} \quad . \tag{79a}$$

Similarly, the relations which define the rate at which components transfer between a molten salt and bismuth phase consist of Eqs. (70), (71), (72), (73), and the relation

$$\frac{F}{RT} \text{ grad } \Phi = - \frac{\sum_i \frac{J_{ei} Z_i}{D_{ei}}}{\sum_i Z_i^2 C_{ei}} \quad . \tag{79b}$$

Equilibrium relations for the distribution of solutes between salt-metal or aqueous-organic phases can take many forms, and in principle, almost any type could be used with the calculational procedure being considered. A mass action type of equilibrium relation was chosen, which can be expressed as

$$\frac{C_{ei}}{C_{si}} \left(\frac{C_{sr}}{C_{er}} \right)^{\frac{Z_i}{Z_r}} = Q_i \ , \tag{80}$$

where Q_1 is the equilibrium constant and the subscript r refers to a reference component. Ferris and co-workers[65] have measured the equilibrium distributions of several materials between molten salts and bismuth. Their studies have shown that the activity coefficients for the species in both phases are essentially independent of composition; hence, the equilibrium quotients Q_i are essentially constant. Equation (80) is believed to be appropriate for several aqueous systems also.

15.3 Calculational Procedure

The rates of transfer of materials between two liquid phases at a given axial position in a packed column are calculated by a trial-and-error integration of Eq. (71) across the electrolyte film. When only two transferring ions are present, the integration can be made analytically in a manner similar to that shown by Kataoka, Sato, and Ueyama.[63] When more than two transferring ions are present, a numerical procedure such as the one discussed below is recommended. The bulk concentrations of the transferring materials in both phases, the mass transfer coefficient (D_i/δ_s) for each component in both phases, and the equilibrium constants [defined by Eq. (80)] are required for the calculations. The transfer rate for each ion and the concentration of each ion in the electrolyte at the interface are computed by the following procedure:

1. A value is assumed for the flux of each transferring ion through the electrolyte film.

2. The electrolyte film is divided into several thin increments. Equations (79b) and (71) are used to calculate the electric potential gradient and concentration gradients of all components in the increment adjacent to the region where the bulk concentrations occur.

3. The concentrations of the transferring materials at the boundary between the first and second increments of the electrolyte film are calculated using the calculated values for the concentration gradient.

4. Steps 2 and 3 are repeated until values for the concentrations of the transferring materials are established throughout the electrolyte film.

5. A value is assumed for the concentration of the reference component (which can be any one of the transferring ions) in the solvent phase at the interface. Equation (80) and the concentrations of the transferring materials in the electrolyte phase at the interface (from step 4) are used to calculate concentrations of all other transferring materials in the solvent phase at the interface.

6. The rate of transfer of each ion across the solvent film is calculated using Eq. (70). The sum of the products of the transfer rates and the valences of the components should be zero, as shown in Eq. (73). In general, this will not be the case for the first value assumed for the concentration of the reference component in the solvent phase at the interface. The next value for the concentration of the reference component is obtained by using Newton's method with Eqs. (73) and (80), as follows. For the expression

$$f = \sum_i Z_i D_{si} (C_{siB} - C_{siI}) , \tag{81}$$

f should have the value of zero when the proper value of C_{srI} is found. The derivative of f with respect to C_{srI} is:

$$f' = \sum_i Z_i^2 D_{si} \frac{C_{siI}}{Z_r C_{srI}} . \tag{82}$$

The next value to be assumed for C_{srI} is then given by the relation

$$(C_{srI})_{n+1} = (C_{srI})_n - \frac{f'}{f} . \tag{83}$$

7. Steps 5 and 6 are repeated until the concentration of the reference component in the solvent phase at the interface is known within the specified convergence criterion (10^{-6} has been used thus far in this study).

8. The calculated values for the flux of each transferring component across the solvent film are compared with the assumed values for the respective fluxes across the electrolyte film. If the values are not equal, a new set of values is assumed for the fluxes of the transferring materials through the electrolyte film. The new value for the flux of component i is taken to be the arithmetic average of the previously assumed value and the flux of component i across the solvent film that was calculated using this value. Steps 1 through 7 are repeated until the difference between the values for each material is less than a specified quantity (1% of the average of the flux values has been used thus far in this study).

The calculational procedure outlined above was found to converge rapidly; however, it is not necessarily the optimum procedure for solving Eqs. (70)-(80).

After a procedure had been developed for calculating the concentrations and fluxes for the transferring components in the electrolyte and solvent phases at a given axial location in a packed column, it was necessary to develop a calculational procedure that could be used throughout the column. The column was divided axially into a number of increments; the concentration of each component was assumed to be constant throughout a given increment. It was assumed that the electrolyte and solvent phases were in constant volumetric flow throughout the column and that no dispersion occurred in either phase. The interfacial area per unit column volume and the values for the film thickness in the solvent and electrolyte phases were assumed to be constant throughout the column. Material balances for each phase in a given column increment then resulted in the following relations:

$$\frac{d\,C_{si}(Z)}{dZ} = -\frac{Sa}{V_s}\,J_i(Z)\,, \tag{84}$$

$$\frac{d\,C_{ei}(Z)}{dZ} = -\frac{Sa}{V_e}\,J_i(Z)\,, \tag{85}$$

where

$C_{si}(Z)$ = concentration of component i in the solvent at height Z in the column,

$C_{ei}(Z)$ = concentration of component i in the electrolyte at height Z in the column,

V_s = volumetric flow rate of solvent,

V_e = volumetric flow rate of electrolyte,

S = cross-sectional area of column, and

a = interfacial area per unit column volume.

In deriving these relations, it was assumed that transfer of material from the solvent phase to the electrolyte phase resulted in a positive value for the flux. These relations can be expressed in finite difference form as follows:

$$C_{si}(0) - C_{si}(L) = \sum_{j=0}^{n-1} \frac{A_t}{V_s} \frac{1}{n} J_{ij}(j\Delta Z) \quad , \tag{86}$$

$$C_{ei}(0) - C_{ei}(L) = \sum_{j=0}^{n-1} \frac{A_t}{V_e} \frac{1}{n} J_{ij}(j\Delta Z) \quad , \tag{87}$$

where

A_t = SaL, total interfacial area in column,

j = column increment number, (j = 0, ...n),

n = number of increments in column

= $L/\Delta Z$,

ΔZ = height of column increment, and

J_{ij} = flux of component i in increment j.

These relations were used in the following manner for calculating concentrations and fluxes for the transferring materials throughout a column:

(1) Values were assumed for the concentration of each component in the solvent phase in the increment from which the solvent phase exits the column. Equations (70)-(79) were used for

calculating the fluxes of the transferring materials between the solvent and electrolyte phases in the increment.

(2) Equations (86) and (87) were used for calculating the concentrations of the transferring materials in the solvent and electrolyte phases in the next increment of the column. The fluxes of the transferring components were again calculated in this increment, using Eqs. (74)-(79). This procedure was repeated until concentrations and fluxes for each transferring material had been calculated in each increment of the column.

(3) The calculated values for the concentrations of the transferring components in the solvent phase entering the column were compared with values that were specified by the operating conditions. Usually, differences between the calculated and specified values were observed. When the difference was greater than desired, a new set of values was assumed for the concentrations of the transferring materials in the solvent stream leaving the column. Each new value was calculated by summing the values for the concentrations of component i in the exit solvent stream with one-half of the difference between the specified concentration of component i in the inlet solvent stream and the calculated value for the concentration of component i in the inlet solvent stream from the last iteration. This procedure was repeated until the calculated and the specified values for the concentrations of transferring materials in the inlet solvent stream were in agreement.

In the future, work will be carried out for calculating rates of mass transfer between solvent and electrolyte phases for a range of operating conditions. Particular attention will be paid to the influence of the electric field on the rate of mass transfer, and to the differences that result from the case where mass transfer rates are assumed to be dependent only on concentration gradients.

16. STUDY OF THE PURIFICATION OF SALT BY CONTINUOUS METHODS

R. B. Lindauer L. E. McNeese

We have previously described equipment for studying the purification of salt by continuous methods.[66] Initial work with this system was directed at the measurement of the flooding rates in a 1.25-in.-diam, 7-ft-long column packed with 1/4-in. nickel Raschig rings. Flooding data were obtained during the countercurrent flow of molten salt (66-34 mole % $LiF-BeF_2$) and hydrogen or argon.[67] The objective of the present work is to study the continuous reduction of iron fluoride in molten salt by countercurrent contact of the salt with hydrogen in a packed column. We reported previously[68] on the first two iron fluoride reduction runs (runs 1 and 2), which were carried out at a temperature of 700°C. Reasonable values for the mass transfer coefficient for the transfer of iron fluoride from the bulk salt to the gas-salt interface were obtained. Operation of the column during these runs was erratic, and the pressure drop across it increased to twice the initial value. The increased restriction was believed to have resulted from precipitation of BeO on the column packing as the result of an accumulation of oxide in the system.

During this report period, salt purification studies using 66-34 mole % $LiF-BeF_2$ were terminated because of leaks that resulted in the loss of about half of the 14-liter salt charge. The composition of the remaining salt was adjusted to the approximate composition of the proposed MSBR fuel salt (72-16-12 mole % $LiF-BeF_2-ThF_4$) by addition of sufficient quantities of salt having the composition 72.6-27.4 mole % $LiF-ThF_4$ and LiF powder to produce 17 liters of salt having the composition 72.0-14.4-13.6 mole % $LiF-BeF_2-ThF_4$. The newly prepared $LiF-BeF_2-ThF_4$ salt was then countercurrently contacted with a H_2--10% HF mixture in the column in order to remove oxide from the salt. Although considerable oxide was removed, the pressure drop across the packed column was reduced only slightly. This indicated that a significant quantity of oxide still remained in the column. Two flooding runs and

one iron fluoride reduction run were then made. During these runs, the pressure drop across the column increased to the point where operation of the system became difficult. The packed column was then filled with molten salt, and an HF-H_2 stream was allowed to contact the static salt charge for a period of 18 hr in order to remove the oxide from the column. This operation was successful in reducing the pressure drop across the column to approximately the value observed after the first two iron fluoride reduction runs. Eight additional iron fluoride reduction runs were subsequently completed. During these runs, operation of the system was smooth, and there was no increase in pressure drop. The results obtained by analyzing salt samples from the runs for iron were inconsistent, probably because of the low iron concentration in the system although sample contamination was suspected in some cases. These operations are described in greater detail in the remainder of this section.

16.1 Removal of Oxide from Salt by Countercurrent Contact with an HF-H_2 Gas Stream

We have found that routine measurement of the pressure drop across the packed column is a useful means for detecting the buildup of materials such as metallic iron or insoluble oxides in the column. As shown in Fig. 93, the pressure drop across the column with an argon flow rate of 5 liters/min increased from 5.6 in. H_2O to 12.0 in. H_2O during previously reported[68] experiments with the LiF-BeF_2 salt (flooding runs No. 3-10). Since less than 6 g of iron would have been reduced during this time, the restriction is believed to have been due mainly to an accumulation of insoluble BeO on the column packing. The oxide in the salt could have originated from several sources. Although the gas purification and supply equipment for the hydrogen and argon was used throughout all the experiments, the purification traps were not regenerated before the experimental work was initiated. Instrumentation for monitoring the moisture content of the gases was installed after 1 month of operation, and an oxygen analyzer was installed 3 months after operation of the system began. Typical water and oxygen contents of the unpurified gases were 15 ppm and 2 ppm, respectively, and are much

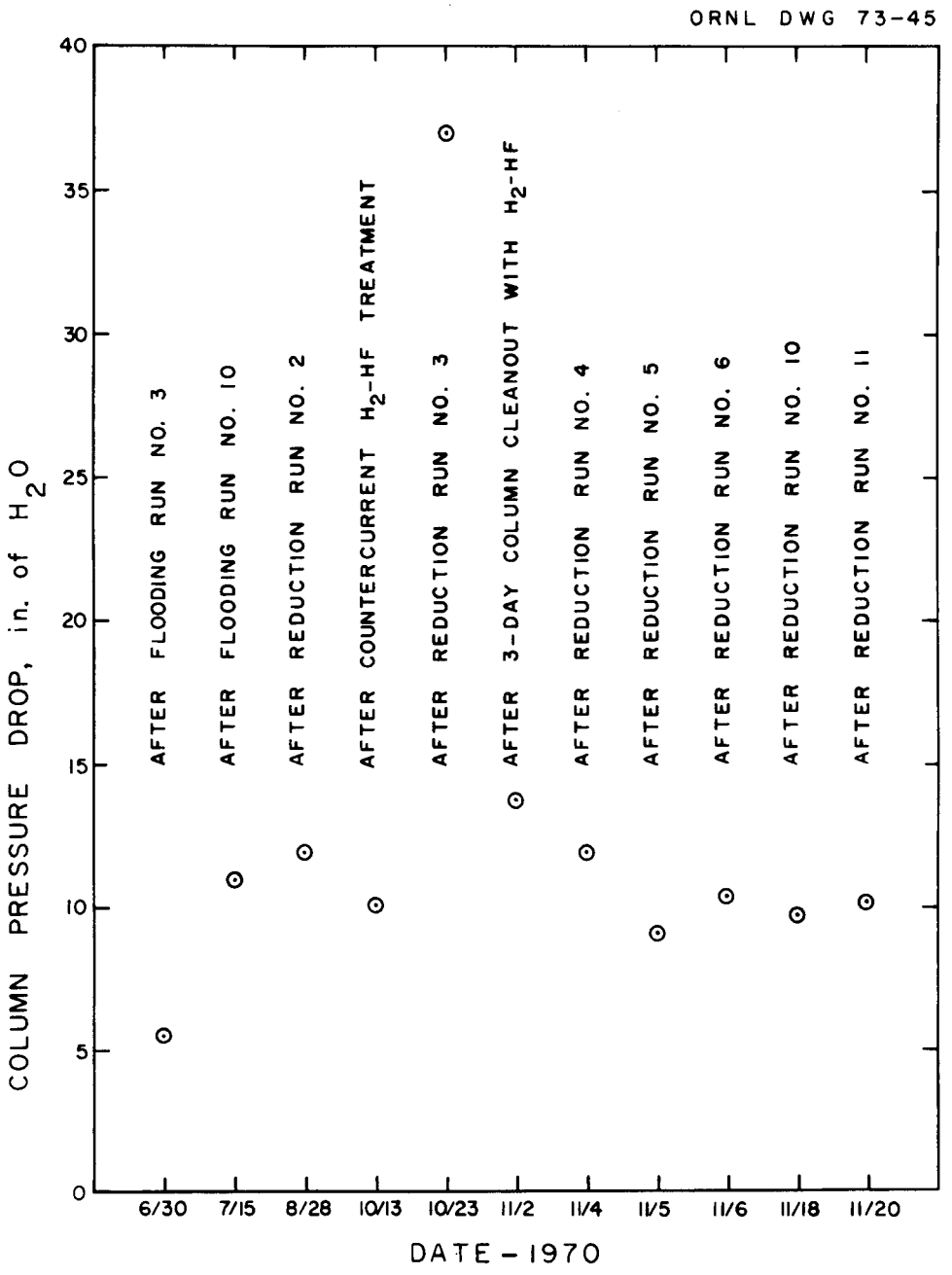

Fig. 93. Column Pressure Drop with an Argon Flow Rate of 5 liters/min.

too low to account for the quantity of oxide (several hundred ppm) that had accumulated in the salt during the six months of operation. Some contamination undoubtedly occurred during repair of plugged vent lines and possibly as the result of insufficient purge rates when the system was vented to the atmosphere between runs. Recent practice has been to close the system vent valve between experiments, while maintaining a sufficient purge rate to keep the system at a few psi of positive pressure (a small amount of gas leakage occurs through the vent valve).

In order to remove the oxide that had accumulated in the salt, the salt was contacted with a 10-90 mole % $HF-H_2$ gas stream for 165 min at average salt and gas flow rates of 103 cm^3/min and 5 liters/min respectively. Some difficulty was experienced in maintaining a constant gas sample flow rate to the analyzer used for determining the concentration of H_2O in the gas stream leaving the column; however, during a period of steady flow near the end of the run, the analyzer indicated that 100 ppm of oxide was being removed from the salt as it passed through the column. The HF utilization at this point was 15%. Treatment of the salt with the $HF-H_2$ stream reduced the pressure drop across the column from 12.0 in. H_2O to 10.3 in. H_2O with an argon flow rate of 5 liters/min, which indicated that the column still contained an appreciable quantity of oxide.

16.2 Removal of Oxide from Column

Following the countercurrent contact of the salt with an H_2-HF gas stream, two flooding runs and one iron fluoride reduction run (No. 3) were carried out. During the second flooding run, it was necessary to heat the molten salt (downstream from the column) to a much higher temperature (650°C on the bottom of the filter housing) than usual in order to maintain the flow of salt through the filter. This could have been due to the presence of oxide in the salt since the solubility of BeO in salt increases as the temperature is increased. During the reduction run, the pressure drop across the column increased, as had been observed in the two previous runs made with salt having the

composition 66-34 mole % $LiF-BeF_2$. However, a test with argon after reduction run No. 3 showed an even higher column pressure drop (see Fig. 93) than had been observed during the run. An $HF-H_2$ gas stream was then passed through a static charge of molten salt in the column in order to provide more opportunity for the dissolution and hydrofluorination of insoluble oxide. The column was filled with salt to the top of the packing (about 1-1/2 liters) by observing the hydrostatic pressure at the bottom of the column. For the first 6.5 hr, the column was held at 650°C and a 29-71 mole % $HF-H_2$ gas mixture was passed through the column at the rate of 8.3 liters/min. The concentration of HF in the stream was higher than planned because of an error in the size of the capillary used for measuring the HF flow rate (2.4 liters/min). Only about 1.5% of the HF was utilized at this HF flow rate, and oxide was removed from the column at the rate of 0.024 mole/hr. Passage of the $HF-H_2$ stream through the column was continued for 6.5 hr, after which it was terminated at the end of the day shift. When the treatment was resumed the following day, the column was cooled to 590°C in order to increase the concentration of HF in the salt, and the HF flow rate was reduced to 750 cm^3/min. The oxide removal rate (as indicated by the water analyzer in the off-gas stream) was about the same as had been observed previously, and the HF utilization increased to about 5%. This compares favorably with the value obtained during countercurrent flow of salt and gas through the column (i.e., 15%). The treatment was resumed on the third day with a column temperature of 700°C to facilitate the dissolution of any remaining oxide. The output from the water analyzer decreased to a value below the reference value, which indicated that the NaF trap in the sample stream had become saturated and was allowing HF to reach the sample electrode. Since the rate of oxide removal could no longer be measured, the oxide removal operation was terminated after the salt had been contacted with the $HF-H_2$ gas stream for a total of 18 hr. The remainder of the batch of salt was then passed countercurrent to a 10-90 mole % $HF-H_2$ gas stream in the column. On completion of these operations, the pressure drop across the column had been reduced to 14.8 in. H_2O. After two additional iron

fluoride reduction runs (runs No. 4 and 5), the column pressure drop had decreased to 9 to 10 in. H_2O (probably from dissolution of insoluble oxide remaining on the packing) and remained in this range for the rest of the report period.

16.3 Iron Fluoride Reduction Runs

During this report period, nine iron fluoride reduction runs were carried out with salt having the composition 72.0-14.4-13.6 mole % LiF-BeF_2-ThF_4. Table 60 summarizes the data from these runs, along with the data from the two previous reduction runs (Nos. 1 and 2) made with salt having the composition 66-34 mole % LiF-BeF_2. During the nine current runs, the concentration of iron fluoride in the salt was decreased from 220 ppm to 70 ppm or less. Operation of the equipment was satisfactory following run 3 (after removal of oxide from the column); however, analyses of the resulting salt samples for iron produced inconsistent data. The reported data for four of the last eight runs showed an increase in the iron fluoride content of the salt. Two of the reported values exceeded the total iron concentration believed to be possible (276 ppm). These unusually high analyses may have been caused by contamination of the samples during their removal from the nickel samplers or by the diminished accuracy of the analytical method as the iron concentration is decreased.

16.4 Calculated Values for the Mass Transfer Coefficient and the Reaction Rate Constant During the Reduction of Iron Fluoride

The rate of reduction of FeF_2 by reaction with hydrogen can be affected by a number of factors. One of the objectives of the present work is to determine the rate-controlling steps involved in the reduction of FeF_2 in a packed column, and to evaluate the associated rate constants. We have previously[68] carried out mathematical analyses for two limiting cases:

Table 60. Data From Iron Fluoride Reduction Runs

Column Temperature, 700°C

Run No.	Date	Gas Flow Rate (std. liters/min) H_2	Gas Flow Rate (std. liters/min) Ar	Salt Flow Rate[a] (cm^3/min)	Analyses of Filtered Samples (ppm iron) Feed	Analyses of Filtered Samples (ppm iron) Product	Percent of Batch Contacted
1	7/27	20.0	--	100	425	307	68.5
2	7/28	13.5	--	100	307	228	27.6
3	10/22	16.6	--	100	220	158	75.3
4	11/3	14.6	--	210	158	373	84.7
5	11/4	18.2	--	161	373	137	68.8
6	11/5	4.5	4.5	106	137	110	81.8
7	11/6	3.9	3.9	142	110	70	81.8
8	11/9	24.0	--	103	70	75	86.5
9A	11/13	4.5	4.5	93	75	55[b]	79.4[c]
9B	11/13	3.5	3.5	136			
10	11/17	14.1	--	105	69[d]	77[b]	81.8
11	11/19	3.1	4.5	117	207	339	81.2
						104[b]	

[a]The first two runs used LiF-BeF_2 salt; the remaining runs used LiF-BeF_2-ThF_4 salt.

[b]Average of flowing-stream samples.

[c]A value of 100% is used in calculating $k_\ell a$ since samples are of flowing-stream type.

[d]Calculated from flowing-stream samples from previous run.

(1) the case in which the rate of reduction is limited by the rate of transfer of FeF_2 to the gas-salt interface from the bulk salt, and

(2) the case in which the rate of reduction is limited by the rate of reaction between H_2 and FeF_2 dissolved in the salt at the gas-salt interface.

The associated rate constants can be evaluated by the relations given below. For the case in which the rate of reduction is limited by the rate of transfer of FeF_2 from the bulk salt to the gas-salt interface, the product of the mass transfer coefficient k_ℓ and the interfacial area a (which is not known) is given as:

$$k_\ell a = \frac{L}{AH} \ln \frac{X_i}{X_o} \quad , \tag{88}$$

where

k_ℓ = mass transfer coefficient for the transfer of FeF_2 from the bulk salt to the salt-gas interface, moles/sec·cm^2,

a = gas-salt interfacial area per unit column volume, cm^2/cm^3,

A = cross-sectional area of the column, cm^2,

L = salt flow rate, moles/sec,

H = column height, cm,

X_i = concentration of FeF_2 in salt fed to column, mole fraction,

X_o = concentration of FeF_2 in salt leaving column, mole fraction.

This relation is valid only under conditions such that the concentration of FeF_2 in salt that would be in equilibrium with the HF-H_2 mixture adjacent to the salt being considered (X*) is small in comparison with the concentration of FeF_2 in the bulk salt in the region being considered. For the case in which the rate of reduction is limited by the rate of reaction between FeF_2 in molten salt and H_2 in the gas at the gas-salt interface, the rate constant is given by the relation

$$k_s = \frac{L}{K_H HA\, p_{H_2}} \ln \frac{X_i}{X_o} \quad , \tag{89}$$

where

k_s = reaction rate constant, sec^{-1},

K_H = Henry's law constant for hydrogen in salt, $moles/cm^3 \cdot atm$,

p_{H_2} = partial pressure of hydrogen in gas, atm,

and the other quantities are as defined above.

Values for the mass transfer coefficient and the reaction rate constant were calculated for the current runs for which meaningful results could be obtained. These values, along with values from the two runs reported previously, are summarized in Table 61.

Since the value for X* is negligible compared with the FeF_2 concentration in the bulk of the salt for the runs considered, the expression used for calculating $k_\ell a$ should be valid. Also, since the partial pressure of hydrogen (p_{H_2}) is nearly constant throughout the column, the expression given above for calculating k_s should be valid. Although the inlet hydrogen partial pressure was reduced to 0.5 atm in the last three runs for which rate constants are shown, the variation in the calculated constants is not sufficiently large to determine whether the rate of iron fluoride reduction is controlled by the rate of transfer of FeF_2 to the gas-salt interface or by the rate of reaction between FeF_2 and hydrogen at the interface. This question will be resolved after additional data are obtained.

Table 61. Calculated Values for the Mass Transfer Coefficient and the Reaction Rate Constant for Runs R-1 and R-2

Run No.	FeF_2 Concentration ($\times 10^4$) mole fraction		Mass Transfer Controlled		Reaction Rate Controlled			
	X_i	X_o	$k_\ell a$ (moles/sec·cm^3 $\times 10^5$)	X^* (mole fraction $\times 10^4$)[a]	k_s (sec^{-1} $\times 10^4$)	p_{H_2} (atm) Inlet	Exit	Equilibrium[b]
R-1	5.13	3.70	2.4	0.033	2.4	1.0	0.9987	0.9850
R-2	3.70	2.75	5.4	0.198	5.4	1.0	0.9967	0.9959
R-3	2.65	1.90	1.9	0.035	1.9	1.0	0.9993	0.9974
R-6	1.65	1.33	1.2	0.042	2.5	0.5	0.4995	0.4969
R-7	1.33	0.84	2.9	0.170	5.7	0.5	0.4989	0.4975
R-9A	0.90	0.66	1.8	0.032	3.7	0.5	0.4995	0.4978

[a]Calculated from the composition of the exit gas.

[b]Calculated from the FeF_2 composition in the salt leaving the column.

17. REFERENCES

1. R. G. Ross, C. E. Bamberger, and C. F. Baes, Jr., MSR Program Semiann. Progr. Rept. Aug. 31, 1970, ORNL-4622, pp. 92-95.

2. J. C. Mailen, MSR Program Semiann. Progr. Rept. Feb. 28, 1971, ORNL-4676, pp. 245-48.

3. C. E. Bamberger and C. F. Baes, Jr., J. Nucl. Mater. 35, 177 (1970).

4. M. J. Bell and L. E. McNeese, MSR Program Semiann. Progr. Rept. Aug. 31, 1970, ORNL-4622, pp. 202-8.

5. L. E. McNeese, Engineering Development Studies for Molten-Salt Breeder Reactor Processing No. 5, ORNL-TM-3140 (October 1971), pp. 2-15.

6. L. E. McNeese, Engineering Development Studies for Molten-Salt Breeder Reactor Processing No. 6, ORNL-TM-3141 (December 1971), pp. 4-13.

7. L. E. McNeese, Engineering Development Studies for Molten-Salt Breeder Reactor Processing No. 8, ORNL-TM-3258 (May 1972), pp. 3-21.

8. L. E. McNeese, MSR Program Semiann. Progr. Rept. Feb. 28, 1970, ORNL-4548, pp. 282-88.

9. M. J. Bell and L. E. McNeese, MSR Program Semiann. Progr. Rept. Aug. 31, 1970, ORNL-4622, pp. 199-202.

10. F. J. Smith and C. T. Thompson, Ibid., pp. 207-8.

11. L. E. McNeese, Engineering Development Studies for Molten-Salt Breeder Reactor Processing No. 7, ORNL-TM-3257 (February 1972), pp. 16-29.

12. L. E. McNeese, Engineering Development Studies for Molten-Salt Breeder Reactor Processing No. 8, ORNL-TM-3258 (May 1972), pp. 24-30.

13. R. L. Jarry, W. H. Gunther, and J. Fischer, The Mechanism and Kinetics of the Reaction Between Nickel and Fluorine, ANL-6684 (August 1963).

14. W. H. Gunther and M. J. Steindler, Laboratory Investigations in Support of Fluid-Bed Fluoride Volatility Processes. Part XIV. The Corrosion of Nickel and Nickel Alloys by Fluorine, Uranium Hexafluoride, and Selected Volatile Fission Product Fluorides at 500°C, ANL-7241 (December 1966).

15. Chemical Engineering Division Summary Report, July-September, 1958, ANL-5924 (1958).

16. Chemical Engineering Div. Semiann. Rept., January-June, 1964, ANL-6900 (August 1964).

17. P. D. Miller and W. E. Berry, A Survey of Corrosion in the Fluidized-Bed Volatility Process, BMI-X-362 (November 1965).

18. F. T. Miles et al., Progress Report of the Reactor Science and Engineering Department, BNL-176 (March 1952), pp. 17-18.

19. L. E. McNeese, Engineering Development Studies for Molten-Salt Breeder Reactor Processing No. 2, ORNL-TM-3137 (February 1971), pp. 22-43.

20. MSR Program Semiann. Progr. Rept. Feb. 29, 1968, ORNL-4254, pp. 260-63.

21. H. F. Bauman, ORNL, personal communication, August 1970.

22. L. E. McNeese, Engineering Development Studies for Molten-Salt Breeder Reactor Processing No. 5, ORNL-TM-3140 (October 1971), pp. 15-22.

23. L. E. McNeese, Engineering Development Studies for Molten-Salt Breeder Reactor Processing No. 6, ORNL-TM-3141 (December 1971), pp. 23-39.

24. L. E. McNeese, Engineering Development Studies for Molten-Salt Breeder Reactor Processing No. 8, ORNL-TM-3258 (May 1972), pp. 3-21.

25. L. E. McNeese, Engineering Development Studies for Molten-Salt Breeder Reactor Processing No. 4, ORNL-TM-3139 (August 1971), pp. 38-83.

26. L. E. McNeese, Engineering Development Studies for Molten-Salt Breeder Reactor Processing No. 5, ORNL-TM-3140 (October 1971), pp. 22-30.

27. L. E. McNeese, Engineering Development Studies for Molten-Salt Breeder Reactor Processing No. 6, ORNL-TM-3141 (December 1971), pp. 13-23.

28. L. E. McNeese, Engineering Development Studies for Molten-Salt Breeder Reactor Processing No. 8, ORNL-TM-3258 (May 1972), pp. 31-58.

29. M. E. Whatley et al., Unit Operations Section Quarterly Progress Report, April-June 1968, ORNL-4365 (February 1970), pp. 33-45.

30. V. G. Levich, Physiochemical Hydrodynamics, pp. 47-52, translated by Scripta Technica, Inc., Prentice-Hall, Englewood Cliffs, N. J., 1962.

31. H. P. Meissner, Process and Systems in Industrial Chemistry, Chap. 9, Prentice-Hall, Englewood Cliffs, N. J., 1971.

32. G. D. Towell, C. P. Strand, and G. H. Ackerman, "Mixing and Mass Transfer in Large Diameter Bubble Columns," A.I.Ch.E. J., Chem. Eng. Symp. Ser., No. 10, p. 97 (1965).

33. Y. Aoyama, O. Katsunori, K. Koide, and H. Kubota, "Liquid Mixing in Concurrent Bubble Columns," J. Chem. Eng. Japan 1(2), 158 (1968).

34. K. Imafuku, T. Wang, K. Koide, and H. Kubosta, "The Behavior of Suspended Solid Particles in the Bubble Column," J. Chem. Eng. Japan 1 (2), 153 (1968).

35. Y. Ohki and H. Inoue, "Longitudinal Mixing of the Liquid Phase in Bubble Columns," Chem. Eng. Sci. 25, 1 (1970).

36. K. B. Bischoff and J. B. Phillips, "Longitudinal Mixing in Orifice Plate Gas-Liquid Reactors," Ind. Eng. Chem., Process Design Develop. 5(4), 416 (1966).

37. S. H. Eissa, M. M. El-Halwagi, and M. A. Saleh, "Axial and Radial Mixing in a Cocurrent Bubble Column," Ind. Eng. Chem., Process Design Develop. 10(1), 31 (1971).

38. T. Reith, S. Reuken, and B. A. Israel, "Gas Holdup and Axial Mixing in the Fluid Phase of Bubble Columns," Chem. Eng. Sci. 23, 619 (1968).

39. L. E. McNeese, Engineering Development Studies for Molten-Salt Breeder Reactor Processing No. 1, ORNL-TM-3053 (November 1970), pp. 1-14.

40. L. E. McNeese, Engineering Development Studies for Molten-Salt Breeder Reactor Processing No. 6, ORNL-TM-3141 (December 1971), pp. 73-79.

41. L. E. McNeese, Engineering Development Studies for Molten-Salt Breeder Reactor Processing No. 7, ORNL-TM-3257 (February 1972), pp. 52-58.

42. L. E. McNeese, Engineering Development Studies for Molten-Salt Breeder Reactor Processing No. 8, ORNL-TM-3258 (May 1972), pp. 64-89.

43. D. T. Goldman and J. R. Roesser, "Chart of the Nuclides," 9th ed., 1966.

44. N. E. Holden and F. W. Walker, "Chart of the Nuclides," 10th ed., 1968.

45. H. E. McCoy, personal communication to L. E. McNeese (February 1971).

46. L. E. McNeese, Engineering Development Studies for Molten-Salt Breeder Reactor Processing No. 7, ORNL-TM-3257 (February 1972), pp. 29-46.

47. L. E. McNeese, Engineering Development Studies for Molten-Salt Breeder Reactor Processing No. 8, ORNL-TM-3258 (May 1972), pp. 58-63.

48. Ibid., p. 61.

49. J. B. Lewis, Chem. Eng. Sci. 3, 248-59 (1954).

50. J. B. Lewis, Chem. Eng. Sci. 3, 260-78 (1954).

51. W. J. McManamey, Chem. Eng. Sci. 15, 251-54 (1961).

52. G. R. A. Mayers, Chem. Eng. Sci. 16, 16-75 (1966).

53. K. F. Gordon and T. K. Sherwood, Chem. Eng. Progr., Symp. Ser. 50(10), 15-23 (1954).

54. D. R. Olander, Nucl. Sci. Eng. 14, 287-94 (1962).

55. J. Prochazka and J. Bulicka, Session VA: Transport and Interfacial Phenomena, Inst. Chem. Proc. Fund. Prague, Czechoslovakia (April 1971).

56. Jaroslav Prochazka, personal communication to H. O. Weeren (Mar. 24, 1972).

57. J. S. Watson and L. E. McNeese, Unit Operations Section Quarterly Progress Report, July-September 1968, ORNL-4366 (April 1970), pp. 57-98.

58. L. E. McNeese, Engineering Development Studies for Molten-Salt Breeder Reactor Processing No. 5, ORNL-TM-3140 (October 1971), pp. 102-3.

59. P. A. Carroad and A. C. Meyerer, Flooding Characteristics of a Countercurrent Mercury-Water Packed Column, ORNL-MIT-115 (Nov. 18, 1970).

60. R. Schlögl and F. Helfferich, J. Chem. Phys. 26, 5 (1957).

61. J. P. Copeland, C. L. Henderson, and J. M. Marchello, A.I.Ch.E. J. 13, 449 (1967).

62. J. C. R. Turner and C. B. Snowdon, Chem. Eng. Sci. 23, 1009 (1968).

63. T. Kataoka, M. Sato, T. Nishiki, and K. Ueyama, Chem. Eng. Japan 33, 59 (1966).

64. S. Cantor, Reactor Chem. Div. Ann. Progr. Rept., Dec. 31, 1965, ORNL-3913, pp. 27-29.

65. L. M. Ferris, J. C. Mailen, J. J. Lawrance, F. J. Smith, and E. D. Nogueira, J. Inorg. Nucl. Chem. 32, 2019-35 (1970).

66. L. E. McNeese, Engineering Development Studies for Molten-Salt Breeder Reactor Processing No. 6, ORNL-TM-3141 (December 1971), pp. 59-72.

67. L. E. McNeese, Engineering Development Studies for Molten-Salt Breeder Reactor Processing No. 7, ORNL-TM-3257 (February 1972), pp. 46-52.

68. L. E. McNeese, Engineering Development Studies for Molten-Salt Breeder Reactor Processing No. 8, ORNL-TM-3258 (May 1972), pp. 97-106.

INTERNAL DISTRIBUTION

1. S. E. Beall
2. M. R. Bennett
3. R. E. Blanco
4. R. E. Brooksbank
5. K. B. Brown
6. W. L. Carter
7. H. D. Cochran, Jr.
8. F. L. Culler
9. D. E. Ferguson
10. L. M. Ferris
11. W. R. Grimes
12. P. A. Haas
13. B. A. Hannaford
14. J. R. Hightower, Jr.
15. C. W. Kee
16. J. A. Klein
17. R. B. Lindauer
18. H. G. MacPherson
19-34. L. E. McNeese
35. J. P. Nichols
36. E. L. Nicholson
37. J. H. Pashley (K-25)
38-39. M. W. Rosenthal
40. A. D. Ryon
41. W. F. Schaffer, Jr.
42. J. H. Shaffer
43. M. J. Skinner
44. Martha Stewart
45. O. K. Tallent
46. D. B. Trauger
47. W. E. Unger
48. C. D. Watson
49. J. S. Watson
50. A. M. Weinberg
51. W. M. Woods
52. R. G. Wymer
53. E. L. Youngblood
54-55. Central Research Library
56. Document Reference Section
57-59. Laboratory Records
60. Laboratory Records, RC
61. Y-12 Document Reference Section
62. ORNL Patent Office

EXTERNAL DISTRIBUTION

63. J. A. Accairri, Continental Oil Co., Ponca City, Oklahoma 74601
64. M. J. Bell, Effluent Treatment Systems Branch, USAEC, Washington, D. C. 20545 Mail Station Beth. 008
65. Delonde R. DeBoisblanc, Ebasco Services, Inc., 2 Rector Street, New York, New York 10006
66. Norton Haberman, USAEC, RDT, Washington, D. C. 20545
67. T. R. Johnson, Argonne National Laboratory, 9700 S. Cass Avenue, Argonne, Illinois 60439
68. R. D. Pierce, Argonne National Laboratory, 9700 S. Cass Avenue, Argonne, Illinois 60439
69. J. Roth, Combustion Engineering Inc., Prospect Hill Road, Windsor, Connecticut 06095
70. D. D. Sood, Radiochemistry Division, Bhabha Atomic Research Center, Bombay 85, India
71. N. Srinivasan, Head, Fuel Reprocessing Division, Bhabha Atomic Research Center, Trombay, Bombay 74, India
72-73. TIC, Oak Ridge, Tennessee
74. Research and Technical Support Division, AEC, ORO